Alma Mater Studiorum - Università di Bologna

DOTTORATO DI RICERCA IN

Scienze della Terra

Ciclo XXVI

Settore Concorsuale di afferenza: 04/A1

Settore Scientifico disciplinare: GEO06

AB INITIO QUANTUM MECHANICAL INVESTIGATION OF STRUCTURAL AND CHEMICAL-PHYSICAL PROPERTIES OF SELECTED MINERALS FOR MINERO-PETROLOGICAL, STRUCTURAL CERAMIC AND BIOMATERIAL APPLICATIONS

Presentata da: Gianfranco Ulian

Coordinatore Dottorato	**Relatore**
Prof. Vincenzo Picotti	Prof. Giovanni Valdrè

Esame finale anno 2014

Abstract

The purpose of this thesis is the atomic-scale simulation of the crystal-chemical and physical (phonon, energetic) properties of some strategically important minerals for structural ceramics, biomedical and petrological applications. These properties affect the thermodynamic stability and rule the mineral - environment interface phenomena, with important economical, (bio)technological, petrological and environmental implications. The minerals of interest belong to the family of phyllosilicates (talc, pyrophyllite and muscovite) and apatite (OHAp), chosen for their importance in industrial and bio-medical applications (structural ceramics) and petrophysics.

In this thesis work we have applicated quantum mechanics methods, formulas and knowledge to the resolution of mineralogical problems ("Quantum Mineralogy"). The chosen theoretical approach is the Density Functional Theory (DFT), along with periodic boundary conditions to limit the portion of the mineral in analysis to the crystallographic cell and the hybrid functional B3LYP. The crystalline orbitals were simulated by a linear combination of Gaussian functions (GTO). The dispersive forces, which are important for the structural determination of phyllosilicates and not properly considered in pure DFT method, have been included by means of a semi-empirical correction.

The phonon and the mechanical properties were also calculated. The equation of state, both in athermal conditions and in a wide temperature range, has been obtained by means of variations in the volume of the cell and quasi-harmonic approximation. Some thermo-chemical properties of the minerals (isochoric and isobaric thermal capacity) were calculated, because of their considerable applicative importance. For the first time three-dimensional charts related to the structural, thermo-chemical and thermo-mechanical properties at different pressures and temperatures were provided.

The hydroxylapatite has been studied from the standpoint of structural and phonon properties for its biotechnological role. In fact, biological apatite represents the inorganic phase of vertebrate hard tissues. Numerous carbonated (hydroxyl)apatite structures were modelled by QM to cover the broadest spectrum of possible biological structural variations to fulfil bioceramics applications.

The results obtained are generally in good agreement with the theoretical and experimental literature. The proposed method is able to predict the behaviour of minerals in PTV conditions still not easily accessible in modern experimental settings.

Riassunto

Scopo della presente tesi di dottorato è la simulazione su scala atomica delle proprietà cristallochimiche e fisiche di alcuni minerali di importanza strategica per applicazioni ceramiche strutturali, biomediche e petrologiche. Tali proprietà influenzano le caratteristiche di stabilità termodinamica e guidano fenomeni all'interfaccia minerale-ambiente, con importanti ricadute economiche, (bio)tecnologiche, petrologiche e ambientali. I minerali di interesse appartengono alla famiglia dei fillosilicati (talco, pirofillite e muscovite) e delle apatiti (idrossiapatite), scelti per la loro importanza in ambito industriale, biomedico e petrofisico.

In questo lavoro di tesi abbiamo applicato metodi, formule e conoscenze della meccanica quantistica a problemi di natura mineralogica ("Mineralogica Quantistica"). L'approccio teorico scelto è la Teoria del Funzionale della Densità (DFT), adoperata insieme a condizioni periodiche al contorno per limitare la porzione di minerale in analisi alla sola cella cristallografica e al funzionale ibrido B3LYP. Gli orbitali cristallini sono stati simulati mediante una combinazione lineare di funzioni gaussiane (GTO). Le forze dispersive, importanti per la determinazione strutturale dei fillosilicati e non propriamente considerate dal metodo DFT puro, sono state incluse mediante una correzione semi-empirica.

Inoltre, sono state calcolate le proprietà fononiche e meccaniche. L'equazione di stato, sia in condizioni atermiche, sia in un ampio intervallo di temperature, è stata ricavata mediante variazioni dei volumi di cella e approssimazione quasi-armonica. Alcune proprietà termo-chimiche dei minerali (capacità termiche isocora e isobara) sono state calcolate, in quanto di notevole importanza in ambito applicativo. Per la prima volta sono forniti grafici tridimensionali relativi alle proprietà strutturali e termo-chimiche e termo-meccaniche a diverse pressioni e temperature.

L'idrossiapatite è stata studiata dal punto di vista strutturale e fononico per il ruolo ricoperto dal minerale in ambito biotecnologico. Infatti, l'apatite biologica rappresenta la fase inorganica dei tessuti duri degli organismi vertebrati. Sono stati realizzati numerosi modelli di (idrossi)apatite carbonatata per coprire il più ampio spettro di possibili variazioni strutturali biologiche per applicazioni biocera-miche.

I risultati ottenuti sono generalmente in ottimo accordo con la letteratura teorica e sperimentale e il metodo proposto è in grado di prevedere il comportamento dei minerali in condizioni P-T-V ancora non facilmente accessibili nelle moderne condizioni sperimentali.

Index

CHAPTER 1 – General introduction

1.1 Ceramic Materials

The word ceramic is derived from the Greek *keramos*, which means "potter's clay" or "pottery", which in turn originates from the Sanskrit meaning "to burn". Indeed, "ceramic" describes products obtained by heating clay-containing materials and included all products made from fired clay, for example, bricks, fireclay refractories, sanitaryware, and tableware. As a broader definition, "most solid materials that are not metal, plastic, or derived from plants or animals are ceramics" (Carter and Norton, 2013). The majority of ceramic materials are compounds of metals or metalloids and non-metals; most frequently they are oxides, nitrides, and carbides. However, a wide variety of minerals can be classified as ceramics, which are usually associated with "mixed" bonding, *i.e.* a combination of covalent, ionic, and sometimes metallic. They consist of arrays of interconnected atoms, no isolated molecules are present in the structure. For example, iodine crystals, composed by discrete I_2 molecules, and paraffin wax, made of long-chain alkane molecules, can not be considered as ceramics. According to the previous definition, even diamond and graphite are ceramics, because these form of carbon are inorganic, they were not prepared from living organisms.

Ceramics generally have specific properties associated with them although some material in this class may behave in atypical manner.

- *Brittleness*. This probably comes from personal experiences such as dropping a glass beaker or a dinner plate. The mixed ionic-covalent bonding between the atoms is the reason behind the brittle behaviour of ceramic materials. Temperature plays an important role in determine the material brittleness, since it behaves as a viscous liquid above the glass transition temperature. That is why it is easy to form glass into intricate shapes. In general, most ceramics are brittle at room temperature but not necessarily at elevated temperatures.
- *Poor electrical and thermal conduction*. This property is again bound to the presence of covalent and ionic bonds within the material structure. In ceramics the valence electrons are not free because of the bonds, whereas in metals they are free to move (the electron sea). The electron mobility determines many of the electrical and thermal properties of the materials. However, some ceramics may exhibits high electrical conductivity, such as the oxide ReO_3, the mixed oxide $YBa_2Cu_3O_{7-x}$ and sulphide MoS_2 (Klinovaja and Loss, 2013) which are high-temperature superconductors (they have zero resistivity below 92 K).

- *Compressive strength*. Ceramics exhibit stronger resistance to compressive stress than to tensile one, whereas metals have comparable tensile and compressive strengths. This is an important difference, which must be kept into account when using ceramic components for load-bearing applications. Ceramics generally have low toughness, although combining them in composites can dramatically improve this property.
- *Chemical stability*. Ceramic materials structure and composition are usually insensitive to both harsh chemical and thermal environments. Pyrex glass is used widely in chemistry laboratories specifically because it is resistant to many corrosive chemicals, stable at high temperatures (it does not soften until 1100 K), and is resistant to thermal shock because of its low coefficient of thermal expansion ($33\times10-7K-1$). It is also widely used in bakeware.
- *Optically transparent*. Many ceramics are transparent because they have a large percent of light transmission, such as watch covers, and optical fibers.

Phyllosilicate minerals answer positively to all previous points, so they fully belong to the ceramic materials class. These minerals usually form as the result of magmatic (biotite) and metamorphic processes (serpentine, muscovite) and of chemical weathering of other silicate minerals at the surface of Earth. Phyllosilicates compose a wide mineral family, in which at least two structural units are recognizable (Pauling, 1930):

- a continuous tetrahedral layer ("T") made by silica tetrahedra ($[SiO_4]^{4-}$), each one bound to three neighboring tetrahedral via three basal bridging oxygens;
- a continuous octahedral sheet ("O") made by divalent (Mg^{2+}, Fe^{2+}) or trivalent (Al^{3+}) cations, the apical oxygens of the T-layer and hydroxyl (OH) groups (e.g. $[AlO_3(OH)_3]^{6-}$).

According to the classification of Martin et al. (Martin et al., 1991), phyllosilicates can be divided in subclasses by the characteristics of layer type (1:1, or 2:1), the magnitude of net layer charge per formula unit, and the type of interlayer species: (1) kaolin-serpentine, (2) pyrophyllite-talc, (3) smectite, (4) vermiculite, (5) mica, (6) chlorite, (7) interstratified clay minerals (Table 1.1).

The building ceramic parts, such as bricks and roofing tiles, sanitary ceramics, easily washable tiles for exteriors and interiors, are manufactured from raw phyllosilicate minerals (Konta, 1995). Besides manufacturing, phyllosilicates are used in the calcined form as fillers, carriers, extenders and grogs.

Technological properties of phyllosilicate raw materials mainly depend on the properties of the mineral present, total mineral composition, size distribution, degree of consolidation and processing conditions. Their recognition is always fundamental because many mineral properties can be largely derived from their crystal structures and crystal chemistry. In this sense, cation substitution, which in

phyllosilicates is a special form of natural isomorphous substitution of a higher charged cation by a lower charged one (for example, Mg^{2+} replacing Al^{3+} , or Al^{3+} replacing Si^{4+}), may affect several properties of the minerals. The negative layer charge resulting from cation substitution is often called structural or permanent charge, the latter because the particle charge is not dependent on the pH. An example is provided in a recent study, where it was shown by both experimental and theoretical means that the surface potential of chlorite is dramatically affected by the presence of atomic substitutions in the tetrahedral layer, leading to the formation of acidic Brønsted sites similar to those found in zeolites (Valdre et al., 2011).

Table 1.1. Structural classification of phyllosilicate minerals

Strutcure	**Interlayer Charge**	**Trioctahedral (M^{2+})**	**Dioctahedral (M^{3+})**
O (not silicate)	≈ 0	Brucite, Portlandite	Gibbsite
TO	≈ 0	Serpentine	Kaolinite
TOT	≈ 0	Talc	Pyrophyllite
TOT O TOT	≈ 0	(trioctahedral) Clinochlore (tri,dioctahedral) none	(dioctahedral) Donbassite (di, trioctahedral) Cookeite
TOT (X^+, X^{2+}, H_2O) TOT Expandable clay	≈ 0.2 – 0.6	Saponite (smectite)	Montmorillonite (smectite)
	≈ 0.6 – 0.9	Trioctahedral Vermiculite	Dioctahedral Vermiculite
TOT (X^+, X^{2+}) TOT Non-expandable clay	≈ 0.5 – 0.75	Wonesite	-
TOT X^+ TOT True mica	+1	Phlogopite, Biotite	Muscovite, Paragonite
TOT X^{2+} TOT Brittle mica	+2	Clintonite	Margarite

Notes: M indicates the divalent or trivalent ion in the octahedral sheet.

There is an ongoing interest in phyllosilicates thermo-mechanical properties, both in geophysical and technological applications. From the ceramic industry point of view, properties of interest are obviously plasticity and moldability, but also color, refractoriness, solubility and corrosion resistance, electrical properties and the many possible variations on these and other properties afforded by the essentially two-dimensional morphology of the individual platelets. A great attention was paid to study the possible changes of the nanosize-dependent properties of these minerals due to mechanical grinding because the changes in the physico-chemical, structural and thermal properties can be exploited in new industrial applications. For example, controlled ball milling experiments of talc showed that at very low load an increase of flattening lamination and texturing of the talc platelets took place, while at high load it was observed TOT layer disruption, OH thermal loss anticipation and fracturation of particles (Dellisanti et al., 2011). Practical applications can profit from these results, as layer flattening and texturing is required for polymer nucleation in talc-polymers composites

(Zanetti et al., 2000), whereas the significant anticipation of thermo-dehydroxylation and the recrystallisation of talc in enstatite could be exploited in ceramic composites, refractories and in the production of non-hydrous silicates.

From the geological and geophysical points of view, the interest in phyllosilicates is focused on processes that take place in subduction zones, where mineral dehydration is responsible for earthquakes and explosive volcanism. The high-pressure stability, and thus the mechanical properties, of hydrous phases determines the depth to which water can be recycled into the Earth's mantle and the amount of recycling that can take place.

In general, the characterization of the mechanical properties of a mineral requires the equation of state (EOS), i.e., the P- and T-dependence of its unit-cell volume and the second order elastic constants (SOEC) tensor for geological and technological applications, respectively. Nonetheless, only few studies by in situ high-pressure and/or high-temperature experiments on phyllosilicates are available in literature (Comodi et al., 2002; Gatta et al., 2013; Pawley et al., 2002) and they often led to discordant results.

1.2 Bioceramics

In vertebrates calcium orthophosphates occur as the principal inorganic constituent of normal (bones, teeth, fish enameloid, deer antlers and some species of shells) and pathological (dental and urinary calculus and stones, atherosclerotic lesions, etc.) calcified tissues (LeGeros, 1991; LeGeros, 2002). Considering the human body, all hard tissues but a small portion of the inner ear are formed of calcium orthophosphates, mainly hydroxylapatite [$Ca_{10}(PO4)_6(OH)_2$,OHAp]. Structurally, pure OHAp is a hexagonal crystal (space group $P6_3/m$), in which tetrahedral phosphate groups are coordinated by Ca^{2+} ions network. The OH groups are sited in a hexagonal channel (as seen from the [001] direction) formed by calcium ions. However, the mineral phase of hard tissues occurs mainly as poorly crystallized non-stoichiometric sodium-, magnesium- and carbonate-containing hydroxyapatite (often called biological apatite or dahllite). The main constituents of human bones are calcium orthophosphates (~ 60 – 70 wt%), collagen (~ 20 – 30 wt%) and water (up to 10 wt%) (Dorozhkin, 2009c). In Figure 1.1 the bone hierarchy in vertebrates is reported .

Biomaterials can be both natural or synthetic materials which have applications to health care, especially to reconstructive surgery. More into details, ceramics and glasses have been used for a long time in the health care industry for eyeglasses, diagnostic instruments, chemical ware, thermometers, tissue culture flasks and fiber optics for endoscopy. As a definition, bioceramics are ceramic materials

developed for skeletal repair and reconstruction. Prior to them, the typical implants used for biomedical and orthopaedical applications were made from metals, but their use was associated to some biocompatibility problems, such as inflammatory response and rejection from the host. The development of bioceramics, which began in the first 1920s (Albee, 1920) and appeared in the late 1960s (Arcos and Vallet-Regi, 2013), was then intended to overcome these issues.

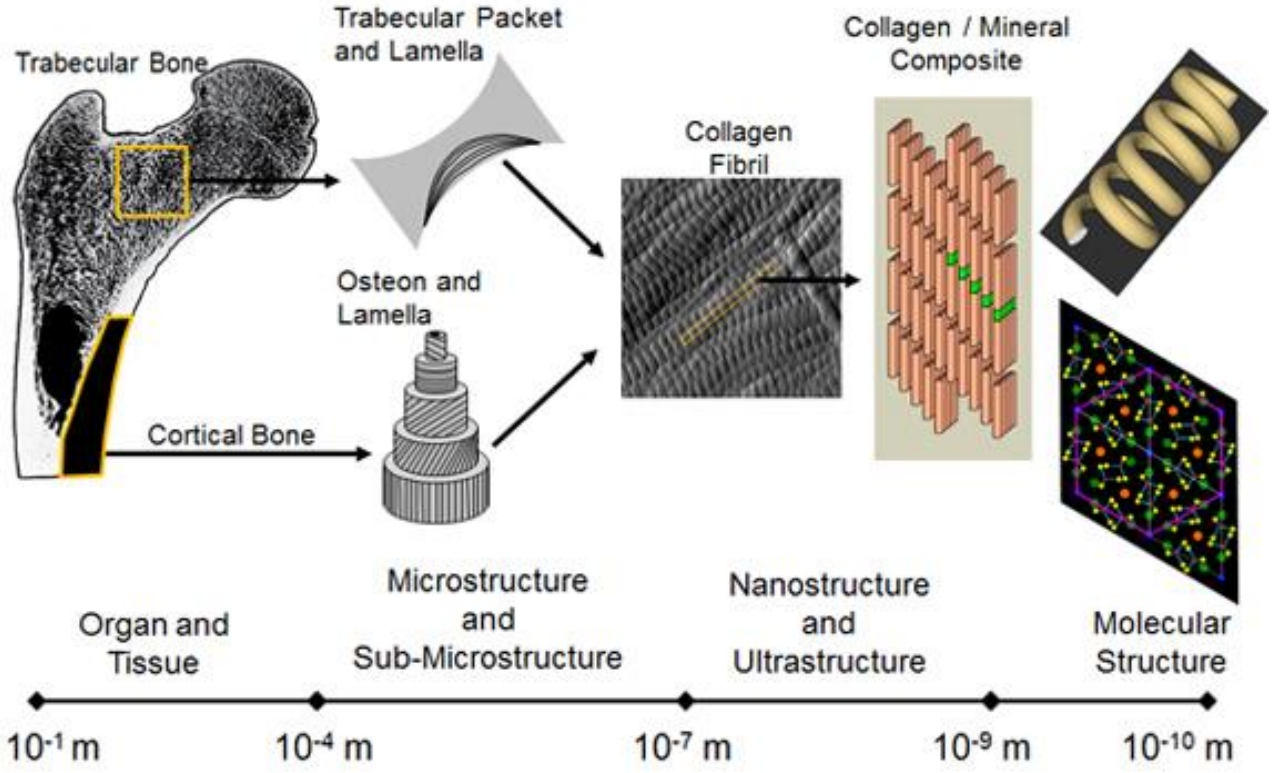

Figure 1.1. Bone hierarchy, from macroscopic to sub-nanometric (atomic) scale. Picture taken from http://www.iupui.edu/~bbml/boneintro.shtml.

Bioceramic-based implants are required to replace and restore the function of diseased or damaged hard tissues, i.e. bone and teeth. The rise in life expectancy and the social need to provide a better quality of life led to an increased demand for new restoring and augmenting materials. An ideal bone graft should be reabsorbable and should guide the patient's bone tissue towards regeneration (Hench and Polak, 2002). Moreover, the graft should exhibit mechanical properties appropriate to the implantation site, especially when implanted as a solid piece or as porous scaffolds (Langer and Vacanti, 1993). Bioactive (or second generation) bioceramics bond to and integrate with living bone in the body without forming fibrous tissue around them or promoting inflammation or toxicity. Hydroxyapatite (OHAp), calcium phosphate-based cements (CPCs) and silica-based bioactive glasses are the most representative bioceramics of this second generation. The high reactivity of these materials is

the main advantage for their application in periodontal repair and bone augmentation, since the reaction products lead to crystallization into an apatite-like phase, similar to the inorganic component of bones in vertebrate species.

Although there is an expansion in the range of medical application of this kind of materials, it is interesting to note that the chemical elements used in their production form a very narrow set of the whole periodic table. The biomaterial ceramic class, which is the most close to the original human (and animal) hard tissues, is given by calcium-phosphate-based ceramics. They are widely used in medicine as bone substitutes, implants, and coatings on dental and orthopaedic prostheses (Dorozhkin, 2009a; Dorozhkin, 2009b; Dorozhkin, 2009c; Dorozhkin, 2009d). Nowadays, biomedical applications include replacements for hips, knees and teeth, as well as repair for periodontal disease, maxillofacial reconstruction, augmentation and stabilization of the jawbone, spinal fusion and bone fillers after tumor surgery (Dorozhkin, 2010). Due to their chemical and structural similarities to the human bone inorganic phase, hydroxyapatite and other calcium phosphates such as α- or β-tricalcium phosphate (α- or β-TCP) show excellent biocompatibility. In the last ten years, OHAp/β-TCP biphasic materials (Bouler et al., 2000) as well as silicon-substituted hydroxylapatite (Gibson and Bonfield, 2002; Vallet-Regì and Gonzàlez-Calbet, 2004) have been incorporated into clinical practice. Most of the relevant application properties of these materials, including their biological influence on tissues and especially their biodegradation behavior, are determined by their special chemical composition, morphology and surface topology. As an example, it has been shown that the OHAp surface properties and porosity induce specialization in stem cells, a result that suggests the possibility to regrow, and not only substitute, hard tissues (Dangaria et al., 2011).

Therefore, proper material design offers numerous possibilities for the use of calcium phosphate materials in hard tissue replacement and regeneration. In particular, there is a growing interest in obtaining a replacing material with composition closer to human bone inorganic phase than pure OHAp. The biological apatite composition is already known (Dorozhkin, 2009a), but there are still some uncertainties on the effect of OHAp substituent in the crystalline framework. For example, the carbonate ion could substitute both hydroxyl (type A defect) and phosphate (type B defect) groups, but there are contradictory results in literature on its position and spatial orientation within the unit-cell. A clear knowledge on this matter could lead to a tailored bioceramic that answer for specific structural needs and completely biocompatible within the host.

1.3 The investigation method

1.3.1 Experimental Techniques

In recent decades instrumental techniques have improved enormously, reaching close to nanoscale resolutions, especially with recent trends in which atomic-scale measurements are being made at synchrotron and other high-energy source facilities throughout the world. Such analytical methods and facilities have matured to such an extent that mineralogists and geochemists routinely probe Earth materials to evaluate bulk, surface, defect, intergranular, compositional, isotopic, long-range, local, order-disorder, electronic, and magnetic structures.

Single-crystal X-Ray Diffraction (sc-XRD) is a technique that exploits the fact that X-rays are diffracted by crystals. It is not an imaging technique. X-rays have the proper wavelength (in the Ångström range, $\sim 10^{-10}$ m) to be scattered by the electron cloud of an atom of comparable size. The interaction of the incindent rays with the sample produces constructive interference when conditions satisfy the Bragg's Law:

$$n\lambda = 2d \sin\theta \qquad (1.1)$$

where λ is the X-rays wavelength, θ is the incident angle, d is the spacing between diffracting planes and n is an integer (1, 2, …). Based on the diffraction pattern obtained from X-ray scattering off the periodic assembly of molecules or atoms in the crystal, the electron density can be reconstructed. Additional phase information must be extracted either from the diffraction data or from supplementing diffraction experiments to complete the reconstruction (the phase problem in crystallography). A model is then progressively built into the experimental electron density, refined against the data and the result is a quite accurate molecular structure.

Alongside single-crystal analysis, it is possible to study powdered samples with XRD. In such samples, every possible crystalline orientation is represented equally. This rotational averaging implies that the three-dimensional reciprocal space (studied in sc-XRD) is projected on a single dimension and the collected data are smooth diffraction rings around the beam axis, rather than the discrete Laue spots observed in single crystal diffraction. The angle between the beam axis and the ring is called the scattering angle, always denoted as 2θ in X-ray crystallography. In accordance with Bragg's law, each ring corresponds to a particular reciprocal lattice vector G in the sample crystal. The diffractogram obtained for a particular sample shows the diffracted intensity as a function of the scattering angle and can be used to identify and quantify different solid phases, phase transitions, the crystallinity, the lattice and some mechanical properties of the sample.

In recent years, both sc-XRD and Powder Diffraction has been coupled with sample cells, such as a diamond anvil cell, to allow the investigation of structural deformation with increasing pressure and temperature.

Fourier Transform Infrared (FTIR) spectroscopy is well-established experimental technique that relies on detection of molecular vibrations. The spectrum of a given substance (both as gaseous, liquid or solid phase) is like its "fingerprint", and then can be used for qualitative mineral identification. In recent years it is also being developed for quantitative mineralogy. Mineral identification is possible because minerals have characteristic absorption bands in the mid-range of the infrared (4000 to 400 cm^{-1}). The concentration of a mineral in a sample can be extracted from the FTIR spectrum because the absorbance of the mixture is proportional to the concentration of each mineral. This is given by Beers Law:

$$A = \sum_{i=1}^{n} \varepsilon_i \cdot l \cdot c_i \qquad (1.2)$$

with A the absorbance of a mineral mixture at a given wavenumber, n the number of mineral components, ε_i the absorptivity of component i, l the absorption path length, and c_i the concentration of component i. All multicomponent analyses are based on Beers law, the absorbance at a specific wavenumber is the sum of the absorbance of all sample components that absorb at that wavenumber.

Regarding mineral surfaces, the scanning probe microscopy (SPM) is one of the powerful modern investigation techniques that allow to study the morphology and the local properties with nanometric resolution. Within SPM, the analysis of a surface is performed by specially prepared tips with different shapes, such as cones, pyramids or needles. The size of the tip apex, which is the working part, is about ten nanometers. The usual tip - surface distance in probe microscopes is between 0.1 – 10 nanometers. Various types of interaction of the tip with the surface are exploited in different types of probe microscopes. As an example, the tunnel microscope is based on the phenomenon of a tunneling current between a metal needle and a conducting sample. In other types of SPM techniques, such as atomic force, magnetic force and electric force microscopes, different interactive forces are exploited and underlie the working mechanism. A feedback system controlled by a parameter. which measure the interaction between the tip and the sample, monitor their reciprocal distance (**z**-axis) with high accuracy (about 0.01Å). During tip scanning along the sample surface (**x**-axis and **y**-axis) the sample topography induces changes in the interaction parameter. The feedback system restores the preset value of the tip-sample distance in real time, so that when the tip is moved to a point *x,y* over the sample, the registered signal *V(x,y)* is proportional to the local departure of the sample surface from

the ideal plane *X,Y(z = 0)*. This makes possible to use the values *V(x,y)* to map the surface topography, and to obtain an SPM image. Alongside with investigation of the sample topography, probe microscopes allow to study various properties of a surface: mechanical, electric, magnetic, optical and many others.

1.3.2 The Theoretical Approach

Despite the impressive improvements in experimental characterization of minerals, in some systems with relatively small particle sizes and significant internal disorder, as in the case of the layered phyllosilicates and oxides/hydroxides minerals, it is difficult to interpret some experimental data with respect to the origin of their behaviour at the atomic and molecular level. Some instrument can reach atomic-scale, e.g. atomic force microscopes (AFMs), but they require very expensive equipment to achieve this goal. Regarding the structure, it is difficult to assign unequivocally hydrogen atom positions in the crystal lattice from sc-XRD results, because they have smaller electron density than heavier atoms. A solution to the light atoms problem is provided by Neutron Diffraction methods, but this involves the use of another complex instrument. The interpretation of FTIR and Raman spectra of both natural and synthetic samples can be complicated by several factors, for instance:

- the presence of impurities from preliminary treatments and the synthesis process of the sample;
- the nature and the morphology of the samples (powders or single crystals);
- the presence of overtones and/or combination peaks;
- band broadening and overlap of signals.

In this context, theoretical methods provide a powerful complement for the experimentalist to study different systems at nanoscale and sub-nanoscale (atomic) levels. Computational modelling theory provides a means to help interpret the field and experimental observation, and to discriminate among various competing models to explain the macroscopic observation.

In the last twenty years, many works have been made coupling the macro- and microscopic knowledge in mineralogy with several computational methods. The application of these approaches to the different phenomena related to mineralogy is known as ‘computational mineralogy’, an inter- and multi-disciplinary subject where different aspects of computing science, physics, chemistry, geology and mathematics meet. Within this field of research, it is possible to reproduce and interpret experimental results and allow the researchers to explore the behavior of mineral systems in extreme conditions of temperature and pressure, deep ocean conditions, geological periods of time, strato-

sphere and interplanetary conditions, where experiments require a complex, cumbersome and expensive instrumentation and methods. The rapid growth in computing power and the development of parallel and massively parallel codes for intensive calculations allowed extension of the use of theoretical simulations to systems of increasing complexity. There are several excellent comprehensive reviews in literature of the methods that can be used in computational mineralogy, which represents also a sort of "story-line" of the development of this field of research (Bleam, 1993; Cygan et al., 2009; Dovesi et al., 2005).

In the present thesis the work has been conducted using a full *ab initio* quantum-mechanics approach, which is based on solving the Schrödinger equation:

$$\hat{H}\Psi = E\Psi \tag{1.3}$$

where $\hat{H}$ is the Hamiltonian operator, Ψ is the wavefunction (dependent on the spatial coordinates of electrons and nuclei) and E is the total energy of the system. The Hamiltonian contains kinetic and potential energy terms, that are classic mechanics analogous:

$$\hat{H} = -\frac{1}{2}\left(\frac{h}{2\pi}\right)^2 \sum_i \frac{1}{m_i}\nabla^2 + \sum_{i \neq j} \frac{e_i e_j}{r_{ij}} \tag{1.4}$$

In Eq. 1.4 h is the Planck's constant, ∇^2 is the Laplacian operator, m and e are the mass and the charge of the electrons or nuclei, respectively, and r_{ij} is the distance between the particles.

The solution of Eq. 1.3 for systems that contain more than one electron is only possible by adopting some approximations. The first one is the Born-Oppenheimer approximation, which decouples the motions of the nuclei and electrons because of the great mass difference between them. The second one is the Density Functional Theory (DFT). With this approach, the total energy of a system can be expressed in terms of functionals of the electronic charge density (3 coordinates), in place of the atomic orbitals of each electron ($3 \times n$ coordinates, where n is the number of electrons in the system). The energy calculated by the DFT method should be exact in principle, but there is a difference from the true total energy, known as the exchange-correlation energy in the Khon-Sham scheme. All DFT methods attempt to calculate this energy with some approximations, such as the local density approximation (LDA) or the generalized gradient approximation (GGA) including the gradient of the charge density. Additional parameterizations for the correlation functional have been developed for LDA (VWN, PW92, etc.) and GGA (PBE, rPBE, BLYP, etc.). However, in this thesis we adopted a hybrid method, the B3LYP functional, which combines Hartree-Fock (HF) exchange with DFT exchange-correlation, including parameterizations from empirical thermodynamic data:

$$E_{xc}^{B3LYP} = (1-a_0-a_x)E_x^{LSDA} + (a_0+a_x)a_0E_x^{HF} + aE_x^{B88} + (1-a_c)E_c^{VWN} + a_cE_c^{LYP} \quad (1.5)$$

where $a_0 = 0.20$, $a_x = 0.72$ and $a_c = 0.81$. It is worth noting that the exchange contribution is described by the Becke's three parameters, with 20% of the Hartee-Fock exact exchange (Becke, 1993) and the correlation by the LYP (GGA) functional (Lee et al., 1988).

All the system presented in this work has been calculated by using periodic boundary conditions (PBC). This means, we simulated the minerals by modelling a small part (the crystal lattice) far from its surface (the bulk of the solid system), applying Bloch's theorem where the wavefunction is expressed by the vectors of the reciprocal space of the Bravais lattice (Payne et al., 1992). This method allows the calculation of properties that depend directly on the crystal structure, e.g. crystallographic properties, elastic constants, cation ordering, equation of-state, surface features, etc.

The electron density used in the DFT approach can be described as plane-waves (PW) or as a linear combination of atomic orbitals (LCAO). We mainly adopted the latter choice for it's high accuracy level and for reasons explained in the next chapters.

For the sake of completeness and clarity, the quantum mechanics approach comes with some issues. While experimental techniques have the merit of dealing with real materials (samples), theoretical methods applied to minerals deal mainly with "idealized" models, i.e. the considered structures are free of any defect. However, it is possible to add them, but this causes a reduction of the system symmetry and an increase of computational costs. The modelling method also explains why theoretical results are closer to sc-XRD analysis than Powder Diffraction ones: indeed, in *ab initio* quantum mineralogy it is not yet possible to study random lattice orientations typical of polycrystals.

1.4 Scope and contents of the present work

In Sections 1.1 and 1.2 two main problems in the ceramic and bioceramic fields have been presented. On one side, the need of accurate data on the thermo-mechanical properties of phyllosilicates, that can be used for structural ceramics technological applications. On the other side, the interest on the structural, chemical and physical properties of biological apatites for their use in bioceramic material design. We decided to consider both issues in this work, related to the ceramic field, by consistent *ab initio* theoretical approach.

For the phyllosilicate case, due to the numerous members of this family, the number of cases in analysis was limited to those of upmost importance. Talc and pyrophyllite were the first considered minerals, because they are respectively the tri-octahedral and di-octahedral end-members of the TOT classification.

Chapter 2 introduces the basis of the *ab initio* methods adopted in this work. Phyllosilicate structure presents strong bonds (covalent and ionic) within the TOT (or TO) layers and weak interactions (van der Waals forces) that hold the layers together. This feature represents a very interesting challenge for quantum mineralogy, because a correct description of both strong and weak bonds is mandatory. Given the many theoretical approaches available within Density Functional Theory, a comparison between has been made using some of the most preferred methods and considering talc as a model system of the phyllosilicate family. The results have aided the choice of one method that will be adopted in the whole work.

In **Chapters 3** the mechanical properties of talc were calculated and reported. We calculated the second-order elastic constants (SOECs) and the equation of state (EOS) of the mineral in athermal conditions (T = 0 K), which are both important quantities useful to understand the talc mechanical response under stresses. The temperature dependence on talc EOS has been reported in **Chapter 4**. The results were obtained by the quasi-harmonic approximation (Anderson, 1995), a very difficult and computationally expensive task. The calculations made in Chapters 2-4 were made also for pyrophyllite (**Chapter 5**), for which the knowledge of the thermo-physical and thermo-chemical properties of this kind of minerals is very scarce in literature. In **Chapter 6** muscovite was considered. It is an important mineral in both mineralogy and ceramic industry, which, differently from pyrophyllite, presents a monovalent cation (K^+) in the interlayer. The structure and both athermal and thermal EOS were calculated and discussed.

In **Chapters 7 – 9** the focus is on bioceramic materials, in particular hydroxylapatite (OHAp) and its carbonate-defective structures. The aim is obtaining a better understanding of the carbonate ion effects and location in the OHAp lattice. The CO_3^{2-} ion can substitute two anion: the hydroxyl group (type A defect) or the phosphate ion (type B defect), both as single or mixed substitutions (type A-B defect). A deep structural analysis has been performed to find the most probable orientation of the carbonate ion. Furthermore, the phonon properties of the investigated structures have been reported to ease the interpretation of experimental spectra. Since the CO_3^{2-} ion is the most abundant substituent of OHAp in biological hard tissues, the obtained knowledge could improve both the development and the controls on the production of bioceramics for prosthetic implants.

Finally, in **Chapter 10** the obtained results have been discussed and summarized.

REFERENCES CITED

Albee, F.H. (1920) Studies in bone growth – triple calcium phosphate as stimulus to osteogenesis. Ann. Surg., 71, 32-39.

Anderson, O.L. (1995) Equation of state of solids for geophysics and ceramic science. 405 p. Oxford University Press, New York, US.

Arcos, D., and Vallet-Regi, M. (2013) Bioceramics for drug delivery. Acta Materialia, 61(3), 890-911.

Becke, A.D. (1993) A New Mixing of Hartree-Fock and Local Density-Functional Theories. Journal of Chemical Physics, 98(2), 1372-1377.

Bleam, W.F. (1993) Atomic theories of phyllosilicates: quantum chemistry, statistical mechanics, electrostatic theory, and crystal chemistry. Reviews of Geophysics, 31(1), 51-73.

Bouler, J.M., LeGeros, R.Z., and Daculsi, G. (2000) Biphasic calcium phosphates: Influence of three synthesis parameters on the HA/beta-TCP ratio. Journal of Biomedical Materials Research, 51(4), 680-684.

Carter, C.B., and Norton, M.G. (2013) Ceramic Materials: Science and Engineering. Springer.

Comodi, P., Gatta, G.D., Zanazzi, P.F., Levy, D., and Crichton, W. (2002) Thermal equations of state of dioctahedral micas on the join muscovite-paragonite. Physics and Chemistry of Minerals, 29(8), 538-544.

Cygan, R.T., Greathouse, J.A., Heinz, H., and Kalinichev, A.G. (2009) Molecular models and simulations of layered materials. Journal of Materials Chemistry, 19(17), 2470-2481.

Dangaria, S.J., Ito, Y., Yin, L.L., Valdre, G., Luan, X.H., and Diekwisch, T.G.H. (2011) Apatite Microtopographies Instruct Signaling Tapestries for Progenitor-Driven New Attachment of Teeth. Tissue Engineering Part A, 17(3-4), 279-290.

Dellisanti, F., Minguzzi, V., and Valdre, G. (2011) Mechanical and thermal properties of a nanopowder talc compound produced by controlled ball milling. Journal of Nanoparticle Research, 13(11), 5919-5926.

Dorozhkin, S.V. (2009a) Calcium orthophosphate-based biocomposites and hybrid biomaterials. Journal of Materials Science, 44(9), 2343-2387.

-. (2009b) Calcium Orthophosphate Cements and Concretes. Materials, 2, 221-291.

-. (2009c) Calcium Orthophosphates in Nature, Biology and Medicine. Materials, 2, 399-398.

-. (2009d) Nanodimensional and Nanocrystalline Apatites and Other Calcium Orthophosphates in Biomedical Engineering, Biology and Medicine. Materials, 2, 1975-2045.

-. (2010) Bioceramics of calcium orthophosphates. Biomaterials, 31, 1465-1485.

Dovesi, R., Civalleri, B., Orlando, R., Roetti, C., and Saunders, V.R. (2005) Ab initio quantum simulation in solid state chemistry. In K.B. Lipkowitz, R. Larter, and T.R. Cundari, Eds. Reviews in Computational Chemistry, 21, p. 1-125. Wiley, New York.

Gatta, G.D., Merlini, M., Valdre, G., Liermann, H.-P., Nenert, G., Rothkirch, A., Kahlenberg, V., and Pavese, A. (2013) On the crystal structure and compressional behavior of talc: a mineral of interest in petrology and material science. Physics and Chemistry of Minerals, 40(2), 145-156.

Gibson, I.R., and Bonfield, W. (2002) Novel synthesis and characterization of an AB-type carbonate-substituted hydroxyapatite. Journal of Biomedical Materials Research, 59(4), 697-708.

Hench, L.L., and Polak, J.M. (2002) Third-generation biomedical materials. Science, 295(5557), 1014-+.

Klinovaja, J., and Loss, D. (2013) Spintronics in MoS2 monolayer quantum wires. Physical Review B, 88(7).

Konta, J. (1995) CLAY AND MAN - CLAY RAW-MATERIALS IN THE SERVICE OF MAN. Applied Clay Science, 10(4), 275-335.

Langer, R., and Vacanti, J.P. (1993) Tissue Engineering. Science, 260(5110), 920-926.

Lee, C.T., Yang, W.T., and Parr, R.G. (1988) Development of the Colle-Salvetti Correlation-Energy Formula into a Functional of the Electron-Density. Physical Review B, 37(2), 785-789.

LeGeros, R.Z. (1991) Calcium phosphates in oral biology and medicine. Monographs in Oral Science, 15, 1-201.

-. (2002) Properties of osteoconductive biomaterials: Calcium phosphates. Clinical Orthopaedics and Related Research, 395, 81-98.

Martin, R.T., Bailey, S.W., Eberl, D.D., Fanning, D.S., Guggenheim, S., Kodama, H., Pevear, D.R., Srodon, J., and Wicks, F.J. (1991) Report of the Clay-Minerals-Society Nomenclature Committee - Revised Classification of Clay Materials. Clays and Clay Minerals, 39(3), 333-335.

Pauling, L. (1930) The structure of the micas and related minerals. Proceedings of the National Academy of Sciences of the United States of America, 16, 123-129.

Pawley, A.R., Clark, S.M., and Chinnery, N.J. (2002) Equation of state measurements of chlorite, pyrophyllite, and talc. American Mineralogist, 87(8-9), 1172-1182.

Payne, M.C., Teter, M.P., Allan, D.C., Arias, T.A., and Joannopoulos, J.D. (1992) Iterative minimization techniques for ab initio total-energy calculations: molecular dynamics and conjugate gradients. Reviews of Modern Physics, 64(4), 1045-1097.

Valdre, G., Tosoni, S., and Moro, D. (2011) Zeolitic-type 'Bronsted-Lowry sites distribution imaged on clinochlore. American Mineralogist, 96(10), 1461-1466.

Vallet-Regì, M., and Gonzàlez-Calbet, J.M. (2004) Calcium phosphates as substitution of bone tissues. Progress in Solid State Chemistry, 32, 1-31.
Zanetti, M., Lomakin, S., and Camino, G. (2000) Polymer layered silicate nanocomposites. Macromolecular Materials and Engineering, 279(6), 1-9.

CHAPTER 2 – Comparison between Gaussian-type Orbitals and Plane Wave *ab initio* Density Functional Theory modeling of layer silicates: Talc [$Mg_3Si_4O_{10}(OH)_2$] as model system.[1]

Abstract

The quantum chemical characterization of solid state systems is conducted with many different approaches, among which the adoption of periodic boundary conditions to deal with three-dimensional infinite condensed systems. This method, coupled to the Density Functional Theory (DFT), has been proved successful in simulating a huge variety of solids. Only in relatively recent years this *ab initio* quantum-mechanic approach has been used for the investigation of layer silicate structures and minerals. In the present work a systematic comparison of different DFT functionals (GGA-PBEsol and hybrid B3LYP) and basis sets (plane waves and all-electron Gaussian-type orbitals) on the geometry, energy and phonon properties of a model layer silicate, talc [$Mg_3Si_4O_{10}(OH)_2$], is presented. Long range dispersion is taken into account by DFT+D method. Results are in agreement with experimental data reported in literature, with minimal deviation given by the GTO/B3LYP-D* method regarding both axial lattice parameters and interaction energy and by PW/PBE-D for the unit-cell volume and angular values. All the considered methods adequately describe the experimental talc infrared spectrum.

2.1 Introduction

The computational treatment of solid state systems can be accomplished by two different approaches: cluster modelling or periodic boundary conditions (PBC). In the first one only a small, but representative portion of the whole mineral is described at a quantum mechanical level, as a molecule or as an aggregate. The mechanical strength that the whole crystal enforces on the quantum zone, as well as the electrostatic and polarization effects, are, in this approach, neglected. A strategy to overcome this problem, is to surround the cluster by a periodic arrangement of point charges according to the Ewald lattice sum (Parry, 1975). Many researches of the properties of minerals have been successfully conducted with this approach (Bleam, 1990a; Bleam, 1990b; Tunega et al., 1994). Its main advantage is that it allows to adopt for a great variety of methods, from Density Functional (DFT) to post Hartree

[1] This chapter consists a paper by Gianfranco Ulian, Sergio Tosoni and Giovanni Valdrè, "Comparison between Gaussian-type Orbitals and Plane Wave *ab initio* Density Functional Theory modeling of layer silicates: Talc [Mg3Si4O10(OH)2] as model system.", published in the *Journal of Chemical Physics*, **139** (20), 204101.

Fock (HF) correlated schemes. The main drawback is that the limited quantum region may not be physically representative of the whole crystal and boundary effects may bias the calculations. The computational cost, moreover, tends to grow very rapidly with the size of the cluster and it can be hard to reach convergence on the properties of interest with respect to the size of the quantum zone.

However, an appealing possibility is to deal with real infinite condensed systems via PBC. In this kind of simulation, the wave function of a finite unit cell is replicated in the space, accounting for all short range and long range interactions that take place in a real solid. The main drawback of this approach is that the choice of the method is limited for technical reasons to Hartree Fock and Density Functional Theory, even though it must be mentioned that there is ingoing effort toward the implementation of correlated methods such as second-order Møller-Plesset (MP2) within PBC (Katouda and Nagase, 2010).

Concerning the choice of the method of calculation, i.e. the definition of a Hamiltonian, a compromise between accuracy and computational feasibility has to be reached. Hartree Fock is based on the solution of the equation of motions of the electron in the mean field of the other electrons. This accounts for coulombic and quantum exchange interactions, but neglects correlation effects. The so-called post Hartree Fock techniques, such as Configuration Interaction, MP2 or Coupled Cluster, address the issue of correlation by including electronically excited configuration in the calculation (Huang and Carter, 2008). The clear improvement in accuracy compared to Hartree Fock is however hindered by the drastic augment of required computer resources and by arising of technical difficulties in implementing these methods for solid state simulations, as mentioned above. An appealing alternative is represented by methods based on the Density Functional Theory (Parr and Yang, 1989). These methods are based on a theorem stating the total energy of a generic system is a function of the total electron density. This allows for a drastic simplification of the problem because the electron density is a function of three spatial coordinates only, while HF and post-HF systems expand the total energy as a function of 3N variables, where N is the total number of electrons. However, in DFT the explicit functional dependency of the energy from the electron density is unknown and then DFT reduces to the implementation of an approximated functional. Several attempts to formulate density functionals have been carried out over many years, leading to a hierarchy of more and more accurate methods, starting from the Local Density Approximation (LDA), to the Generalized Gradient Approximation (GGA) and the so-called hybrid methods, which consist in mixing a given percentage of exact Hartree Fock exchange with the exchange arising from DFT. The implementation of DFT in many codes designed for solid state simulations led to several important papers concerning the simulations of

minerals, among which some of layer silicates and their surfaces (Bruno et al., 2006; Molina-Montes et al., 2008a; Molina-Montes et al., 2008b; Refson et al., 2003; Sainz-Diaz et al., 2011).

All the aforementioned classes of DFT methods, LDA, GGA and hybrids, have a well-documented problem in describing long range, dispersive forces, which are often the driving force in weak interactions. For this reason, when dealing with weakly bound systems, such as layer silicates or non-polar surface-molecules interactions, it is recommendable to profit of some semiempiric corrections, such as the DFT+D (Grimme, 2006). Details on the DFT+D approach adopted in the present paper are provided in the next section.

In case of solid state simulation, the choice of the basis set is an important technical issue to be addressed; it is possible to either exploit a linear combination of plane waves (PW) or local atomic orbitals, usually represented as Gaussian-type orbitals (GTO). The pros and cons of GTO and PW approaches can be shortly summarized as follows:

- With plane waves basis sets, calculations are intrinsically periodic in three dimensions: the system is always defined in a 3D box which is uniformly filled with plane waves, regardless of having a molecule, a two dimensional slab or a real 3D crystal. When dealing with non-three-dimensional systems, it is necessary to expand the cell along the finite direction (for example, *z* for a bi-dimensional surface) to create a sufficiently large void space between replicas, thus decoupling their interactions (Blochl, 1995). In GTO simulations the true dimensionality of the system is always obeyed, *i.e.*, molecules, polymers, 2D slabs and 3D crystals are treated without spurious effects due to artificial replicated images. This is obtained because of the local nature of Gaussian functions.
- The issue of quality and completeness of the basis set is more complicated for GTOs than for PWs. Indeed, the quality of PW basis sets is specified by a single parameter: the electronic kinetic energy cutoff E_{kin}. The higher the E_{kin}, the better is the basis set. Standard GTO basis sets of increased quality have been designed for cluster calculations for almost all atomic elements since the early days of quantum chemistry. However, at the state of the art, their transferability to periodic systems is limited. In particular, basis sets including very diffuse Gaussian functions are critical for periodic systems, and exponents of the more diffuse Gaussian functions should be properly adjusted (Dovesi et al., 2005).
- Within both GTO and PW approaches, core electrons can be treated implicitly, their presence accounted by pseudopotentials (Schwerdtfeger, 2011). This represents an approximation, but also a considerable speedup when the system in analysis is large. Moreover, the heavier the atom, the higher is the kinetic energy of the inner orbital electrons, and the larger are the

relativistic effects on the electron motions: the pseudopotentials take into account also for relativistic effects.

- Exact Fock-exchange with hybrid functionals (*i.e.*, B3LYP, PBE0) are known to work better than GGA in predicting electronic properties and vibrational features. This approach is currently adopted with both GTO (Tosoni et al., 2005; Ugliengo et al., 2004; Valenzano et al., 2007) and plane waves (Goumans et al., 2007; Hernandez-Rivera and Castillo-Chara, 2010; Hu et al., 2010; Wang et al., 2011) basis sets. However, the hybrid-PW method has extremely high computational cost, while with Gaussian-type orbitals the required resources are only 1.5 times those of the non-hybrid simulations.
- Plane waves are usually faster both for energy and gradient calculations than GTO, in particular for solid state systems, albeit they require much more main memory when using norm-conserving pseudopotentials.
- The calculation of atomic forces is simpler with PW because only Hellmann-Feynman forces are present, while in GTO it is much more time-consuming, and also their coding is more involved.
- Gaussian-type orbital basis sets suffer from the basis set superposition error (BSSE). This is a consequence of the finite expansion of basis functions describing the orbitals which affects relative energies when configuration with different number of bonds are compared. Namely, the energy of two interacting fragments (A and B) spuriously benefit from the contribution of basis functions centred in B in describing the wave function of A and vice versa. Corrections for BSSE are usually made with the well-known counterpoise method (Alagona et al., 1987; Boys and Bernardi, 1970; Cammi et al., 1985; Collins and Gallup, 1986). An extremely appealing feature of PW calculations is the absence of BSSE, which is particularly convenient when studying the interactions between layers in layer silicates and adsorption of molecules on solid surfaces. PW are BSSE free because they are spatially organized in a lattice independently from the ions position, thus allowing to treat interacting and isolated fragments at a consistent basis set quality, provided that the lattice is the same.

Because of the above reported differences in the simulating methods, the aim of the present work is to compare various theoretical approaches within PBC, PW and GTO basis sets with different DFT functionals for the quantum mechanical analysis of layered crystal structures, presenting ionic and covalent bonding within the layer (intralayer bonding) and van der Waals/weak electrostatic (dispersive) forces between the layers (interlayer bonding).

To this aim we have selected talc mineral [$Mg_3Si_4O_{10}(OH)_2$] as a model system for comparing the simulations. In fact, the structure of talc is the well-known TOT layer configuration consisting of a octahedrally Mg-coordinated sheet (O) sandwiched between two tetrahedrally Si-coordinated sheets (T). The final bulk layered talc structure can be described by a stacking of weakly bounded tetrahedral-octahedral-tetrahedral (TOT) layers.

In addition, the knowledge of the details of the talc structure is important also for the following different reasons:

i. From the mineralogical point of view, talc is very common on the earth crust and one of the example of TOT end-member crystal structure (Perdikatsis and Burzlaff, 1981).
ii. Talc plays an important role in petrology because it is responsible of water transport to the Earth's mantle in the subduction zones, where H_2O may trigger partial melting, magma generation and could affect the seismic/rheological properties of fluids or minerals (Pawley et al., 1995; Pawley and Wood, 1995).
iii. Talc is widely used in several industrial products such as paper, paints, rubbers, polymers, ceramics, etc. because of its inertness, whiteness, low thermal and electrical conductivity and adsorption capacity of organic substances (D'Haese et al., 2011; Dellisanti et al., 2011; Dellisanti and Valdre, 2010; Dellisanti and Valdre, 2012; Dellisanti et al., 2009; Jahani, 2011; Kalendova et al., 2010).

An adequate quantum-mechanical simulation method is required to characterize the talc structure, and in general layer silicate minerals, providing a better understanding of geometrical, electric, magnetic, mechanical and surface data experimentally obtained. Furthermore, the theoretical approach could be a predictive tool of upmost importance in areas where setting up an experiment is very difficult, such as obtaining the high pressure-thermal behaviour of the mineral model.

In this work, a clear description of the computational parameters adopted for the simulations is reported. The evaluation of the different modelling approaches will be made by comparison with the experimental data of the single-crystal X-Ray Diffraction (XRD) refinement (Perdikatsis and Burzlaff, 1981) and Fourier-Transform Infrared (FTIR) analysis (Dellisanti et al., 2009). The provided data can be helpful to researchers when choosing a method to investigate layer silicate minerals.

2.2 Computational details

The simulations reported in this work have been done with CRYSTAL09 (Dovesi et al., 2009) and VASP 5.2 (Kresse and Furthmuller, 1996; Kresse and Hafner, 1993) codes, which rely on Gaussian-type orbitals and plane waves, respectively. Visualization and structure editing were done with the software Moldraw (Ugliengo et al., 1993) and VESTA (Momma and Izumi, 2008).

Model structures

The talc structure was taken from XRD refinement data (Perdikatsis and Burzlaff, 1981). The unit cell belongs to $P\bar{1}$ space group. Since hydrogen atoms location has not been characterized by crystallographic studies, they have been oriented with O-H bond parallel to the [001] direction. Oxygen atoms are subdivided in three groups: apical [O^a or O(a)] shared between Si and Mg; hydroxyl [O^h or O(h)]; basal [O^b or O(b)] shared between silica tetrahedrons. See the stick and ball model reported in Figure 2.1 for a graphical representation.

Localized Gaussian-type Orbitals (GTO) simulations

The three-parameter (B3LYP) hybrid exchange functional (Becke, 1993b; Lee et al., 1988) and the generalized gradient approximation (GGA) functional PBE (Perdew et al., 1996), with both its original and modified version for solid state calculations (PBEsol) (Perdew et al., 2008), have been adopted for all calculations. The exchange–correlation contribution is performed over a grid of points and is the result of a numerical integration of the electron density and its gradient. The adopted pruned grid is given by 75 points and 974 angular points (XLGRID) and obtained from the Gauss–Legendre quadrature and Lebedev schemes (Prencipe et al., 2004). This is a good compromise between accuracy and cost of calculation for geometry optimization and vibrational frequencies. The values of the tolerances that control the Coulomb and exchange series are the default provided by CRYSTAL09 (*ITOL1* to *ITOL4* = 6), but we increased the pseudo-overlap parameter (*ITOL5*) from 12 to 14 (Dovesi et al., 2009). The Hamiltonian matrix has been diagonalized (Monkhorst and Pack, 1976) using a shrinking factor of *IS* = 4 (Dovesi et al., 2009), that leads to 36 reciprocal lattice points (k-points).

Within the CRYSTAL code, multi-electron wave functions are described by linear combination of crystalline orbitals (CO), expanded in terms of Gaussian-type orbital (GTO) basis sets. The basis setshave been chosen from optimized ones used by other authors for the investigations of similar structures. For all the calculations, magnesium and oxygen have been described by a 8-511d1G and

a 8-411d11G basis sets, respectively (Valenzano et al., 2006), silicon by a 88-31G* (Nada et al., 1996) and hydrogen by a 3-1p1G basis set (Gatti et al., 1994).

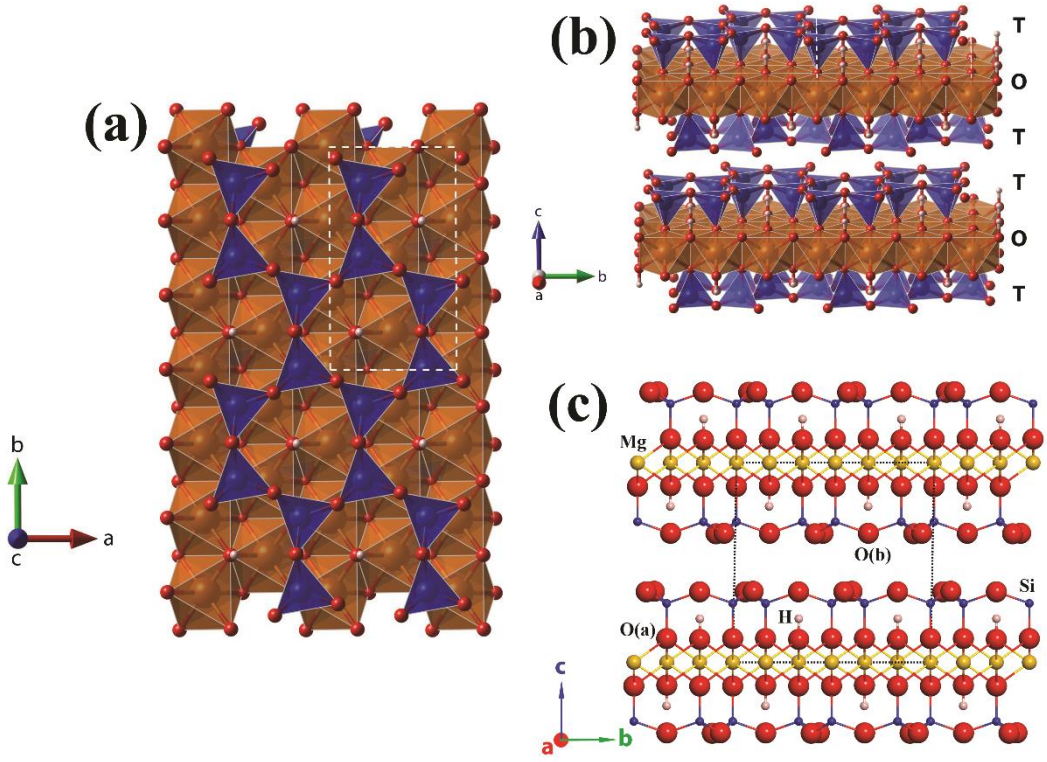

Figure 2.1. Talc polyhedral and stick-and-ball models of talc. (a) View from the [001] direction, the white dashed line is referred to a single unit-cell; (b) view from a slightly rotated [100] direction; (c) seen from the [100] direction. Apical and basal oxygen atoms are labelled as O(a) and O(b), respectively.

Lattice constants and internal coordinates have been optimized within the same run using the analytical gradient method for the atomic positions and a numerical gradient for the unit-cell parameters. The Hessian matrix is upgraded with the Broyden–Fletcher–Goldfarb–Shanno algorithm (Broyden, 1970a; Broyden, 1970b; Fletcher, 1970; Goldfarb, 1970; Shanno, 1970). The tolerances for the maximum allowed gradient and the maximum atomic displacement for considering the geometry as converged have been set to 0.00006 hartree bohr^{-1} and 0.00012 bohr, respectively.

Plane Wave (PW) simulations

All simulations were performed adopting both the PBE and the PBEsol functionals (Perdew et al., 1996; Perdew et al., 2008). The projected augmented planewave basis set (PAW) is expanded within a cutoff of 400 eV (Blochl, 1994; Kresse and Joubert, 1999). The geometry optimizations were performed with the PBE functional modified for solid state calculations, using the conjugated gradient

algorithm, with a tolerance of 10^{-2} eV/Å. The parameters considered for the cell optimization are the k-point Monkhorst-Pack mesh and the kinetic energy cutoff (E_{kin}) of the basis set. To provide an adequate sampling in the first Brillouin zone, a 6×3×3 k-mesh has been considered. Generally, when dealing with cell parameters optimization, it is necessary to raise E_{kin} from the usually assigned 400 eV to at least 550-600 eV to increase the accuracy of the calculation. In this work the kinetic energy cutoff was set to 600 eV and 800 eV to test which provides results in better agreement with experimental data. For the IR spectrum simulation, the E_{kin} was set at the standard value of 400 eV.

Correction for dispersive forces

As previously mentioned, Density Functional Theory often fails to adequately describe long-range dispersive interactions. To overcome this problem, dispersive forces are evaluated according to the semiempirical approach (DFT+D) suggested by Grimme (2006), which adds the following contribution to the calculated DFT energy:

$$E_{DISP} = -s_6 \sum_{\mathbf{g}} \sum_{i \neq j} f_{dump}\left(R_{ij,\mathbf{g}}^6\right) \frac{C_6^i C_6^j}{R_{ij,\mathbf{g}}^6} \tag{2.1}$$

The summation is over all atom pairs *ij* and **g** lattice vectors, excluding the self- interaction contribution ($i = j$) for every **g**, C_6^i is the dispersion coefficient for the atom *i*, s_6 is a scaling factor that depends on the adopted functional (0.75 and 1.05 for PBE and B3LYP, respectively) and $R_{ij,\mathbf{g}}$ is the interatomic distance between atom *i* in the reference cell and atom *j* in the neighbouring cells at distance |**g**|. f_{dump} is a dumping function used to avoid double counting of short-range contributions to the energy:

$$f_{dump} = \frac{1}{1 + e^{-d\left(R_{ij,\mathbf{g}}/R_{vdw} - 1\right)}} \tag{2.2}$$

where R_{vdw} is the sum of atomic van der Waals radii and *d* determines the steepness of the damping function (d = 20). In practice, pairwise dispersive contributions are damped out if the distance between atoms i and j is smaller than the sum of the respective Van der Waals radii.

This approach has been widely used for both GGA and hybrid models and the correction was implemented in both CRYSTAL09 and VASP 5.2 codes.

However, it must be stated that C_6 and Van der Waals radii have been defined for organic molecules and metallorganic complexes. It is therefore not granted that they will provide equally accurate results when applied to solids with a relevant ionic character, such as layer silicates. In particular, a general tendency toward the overestimation of the cohesive energies has been reported and it could affect the

geometry optimization of the crystalline structure leading to underestimated lattice parameters. This effect can be explained by considering two aspects. On one hand, in solid phases the intermolecular contacts are shorter and the overlap between charge density distributions is larger. This feature is controlled by the damping function that is probably too short-range for crystalline systems. On the other hand, the original parametrization by Grimme contains the s_6 scaling factor that rescales the whole contribution that, for B3LYP, is increased by a factor of 1.05. Civalleri and co-workers (Civalleri et al., 2008) proposed a modification to the parameters of the damping function. The empirical parameters of the original B3LYP+D have been modified, setting s_6 to 1.00 and R_{vdw}(H) to 1.30 and the heavier atom van der Waals radii were scaled by a factor of 1.05 (method called B3LYP-D*). Proposed scaling factors were determined from a manual procedure by progressively increasing the atomic van der Waals radii and trying to find the best agreement between computed and experimental data for urea molecular crystal. Some interesting results in this way have been reported in literature for organic crystals (Tosoni et al., 2007).

Vibrational features

In periodic systems and within the harmonic approximation, the phonon frequencies at Γ point are evaluated diagonalising the central zone (k = 0) mass-weighted Hessian matrix:

$$W_{ij}(k=0) = \sum_G \frac{H_{ij}^{0G}}{\sqrt{M_i M_j}} \tag{2.3}$$

H_{ij}^{0G} represents the second derivative of the electronic and nuclear repulsion energy E evaluated at equilibrium **u=0** with respect to the displacement of atom A in cell 0 ($u_i = x_i - x_i^*$) and displacement of atom B in cell G ($u_j = x_j - x_j^*$) from their equilibrium position x_i^*, x_j^*:

$$\sum_G H_{ij}^{0G} = \sum_G \left[\frac{\partial^2 E}{\partial u_i^0 \partial u_j^G}\right]_0 \qquad i = 1,...,3N; \quad j = 1,...,3N \tag{2.4}$$

The calculation of the Hessian at equilibrium is made by the analytical evaluation of the energy first derivatives, Φ_j of E with respect to the atomic displacements:

$$\Phi_j = \sum_G v_j^G = \sum_G \frac{\partial E}{\partial u_j^G} \quad j = 1,...,3N \tag{2.5}$$

while second derivatives at **u = 0** (where all first derivatives are zero) are calculated numerically using a "two-point" formula:

$$\left[\frac{\partial \Phi_j}{\partial u_i^0}\right]_0 \approx \frac{\Phi_j\left(0,...,u_i^0,...,0\right) - \Phi_j\left(0,...,u_i^0,...,0\right)}{u_i^0} \qquad (2.6)$$
$$i = 1,...,3N; \quad j = 1,...,3N$$

More details on the vibrational calculation made by CRYSTAL can be found in literature (Pascale et al., 2004; Tosoni et al., 2005). The Hessian matrix eigenvalues provide the normal harmonic frequencies ω_h and it is obtained with 3N+1 SCF and gradient calculation. This method can be quite demanding for large unit cells, but point symmetry facilitates a remarkable time saving, because only the lines of the Hessian matrix referring to irreducible atoms need to be generated. The tolerances were increased to obtain better results, TOLDEE = 10 for CRYSTAL09 and "high" precision with VASP 5.2.

2.3 Results and discussion

Talc geometry

Table 2.1 reports the geometrical optimization results obtained by using localized Gaussian-type orbitals and plane wave basis sets, in conjunction with different DFT functionals as deviation from the XRD refinement (Perdikatsis and Burzlaff, 1981). To ease the comparison between theoretical and experimental data plots of the relative difference $\Delta x = 100 \times \left(x_{calc} - x_{\exp}\right) \Big/ x_{calc}$ are provided in Figure 2.2, where *x* represents unit-cell parameters and mean bond lengths (internal geometry).

All the proposed methods provided a unit-cell smaller when compared to the experimental one, with a range that spans from 0.5% (PW/PBE-D 800eV) to 3.0% (GTO/B3LYP-D). An exception is given by the PBEsol functional with plane wave basis set, which resulted in a significant expansion of the cell of about 3.0%.

Considering the hybrid functional, the original Grimme's dispersion correction caused an overestimation of the van der Waals forces that hold the TOT together. The adoption of the modified dispersion parameters (B3LYP-D*) provided a better agreement with experimental data, with only a small underestimation of the cell volume (1.2%). This is an important improvement of the standard B3LYP-D method and confirms the adequacy of the B3LYP-D* for different solid phases (Civalleri et al., 2008). The best result in the volumetric dimension was obtained by PBE-D approach in both GTO and PW simulations, with the smallest contraction on the unit-cell (< 1.0%). Considering the plane

wave simulations, increasing the kinetic energy cutoff from 600 eV to 800 eV leaded to a systematic cell expansion with both functionals of about 2.5-3.0%.

Table 2.1. Deviation of the Talc optimized geometry obtained by DFT/GTO basis set.

		GTO				PW			
	XRD[a]	PBE-D	PBEsol	B3LYP-D	B3LYP-D*	PBE-D 600eV	PBE-D 800eV	PBEsol 600eV	PBEsol 800eV
Lattice									
a (Å)	5.290	-0.005	-0.023	-0.033	-0.001	-0.002	+0.002	+0.021	+0.023
b (Å)	9.173	-0.014	-0.043	-0.067	-0.003	-0.001	+0.005	+0.032	+0.035
c (Å)	9.460	-0.065	+0.030	-0.155	-0.044	-0.087	-0.049	+0.151	+0.204
α (°)	90.46	+0.51	+0.48	+0.43	+0.56	-0.037	+0.054	+0.016	-0.060
β (°)	98.68	+2.36	+1.45	+2.36	+2.09	+0.787	+0.727	+0.009	-0.073
γ (°)	90.09	+0.03	-0.01	+0.03	+0.03	+0.050	+0.036	-0.018	-0.037
d spacing (Å)	9.351	-0.130	-0.009	-0.218	-0.101	-0.106	-0.067	+0.150	+0.204
V_{cc} (Å^3)	453.790	-7.528	-4.623	-16.674	-5.243	-5.352	-2.901	+10.666	+13.693
Density (g cm^{-3})	2.80	+0.012	+0.005	+0.071	-0.003	+0.009	-0.006	-0.088	-0.105
Mean bond lenghts (Å)									
Si–O[b]	1.625	+0.022	+0.001	+0.009	+0.010	+0.013	+0.014	+0.011	+0.011
Si–O[a]	1.612	+0.027	+0.013	+0.016	+0.021	+0.021	+0.021	+0.021	+0.021
Mg–O	2.080	-0.004	-0.015	-0.013	+0.001	+0.000	+0.002	+0.004	+0.005
Mg–O[h]	2.053	+0.002	-0.009	-0.004	+0.006	+0.003	+0.003	+0.006	+0.006
O–H	-	0.9673	0.9599	0.9570	0.9577	0.9680	0.9684	0.9748	0.9746

Notes: V_{cc} is the volume of the crystallographic cell. Simulation results are reported as difference from XRD data. The results for PW simulations are subdivided according to the functional (PBE-D and PBEsol) and the energy cutoff (600eV and 800eV).
[a] (Perdikatsis and Burzlaff, 1981)

The deviations of the calculated talc volume from experiment is noticeable from the individual contribution of lattice parameters. Each combination of basis set/functional adequately describes the **a**- and **b**-axis ($|\Delta l| < 0.5\%$), which are dominated by strong covalent bonds. However, greater variations were observed for the **c**-axis, which all the DFT+D functionals underestimated, especially the GTO/B3LYP-D method. An opposite behaviour was observed for the PBEsol functional and, when adopted with GTO basis set, provided the best description of the *c* parameter ($\Delta l \approx 0.32\%$). Worth to be noted, in plane waves simulations the PBEsol overestimation of the *c* direction is significantly increased. Excellent results for each lattice parameter in comparison with XRD data were obtained with PBE-D (both GTO and PW) and GTO/B3LYP-D* approaches.

Unit-cell angles α, β and γ also concur in the description of the unit-cell volume deviations. Angular values were almost consistent within all simulations with localized Gaussian basis set, with negligible variations changing the functional ($0.03\% < \Delta\theta < 0.20\%$). However, the GTO results exhibit a systematic overestimation when compared to the experiments, in particular the β angle ($\Delta\beta > 2.0\%$).

On the other hand, plane waves simulations, in particular the PBEsol functional, provided excellent angular data ($\Delta\theta < 0.05\%$), with only a small overestimation of the β angle with PBE-D ($\Delta\beta < 0.4\%$).

Si – O and Mg – O mean bond lengths follow the trends PBEsol < B3LYP-D < B3LYP-D* < PBE-D and B3LYP-D* < PBE-D < B3LYP-D < PBEsol, respectively. OH bond length is almost the same, but is slightly larger with the GGA functional than with the B3LYP one.

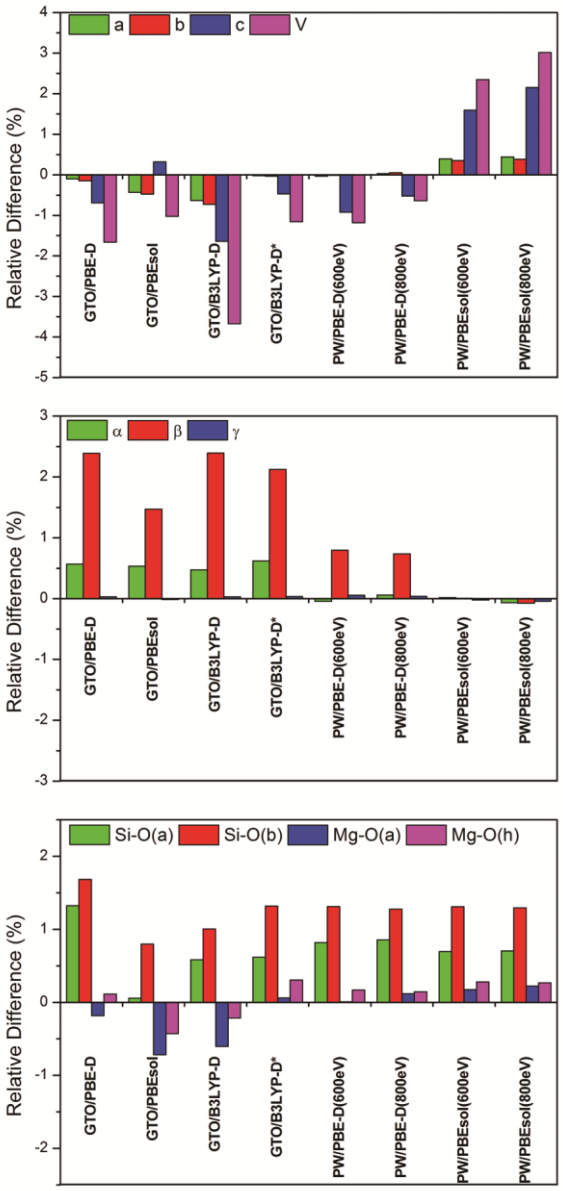

Figure 2.2. Relative difference of talc unit cell parameters and bond lengths with respect to experimental data.

In general, mean Si-O[a] and Si-O[b] bond lenghts are over-estimated by 0.5 – 1.0% by all the proposed basis set/DFT functional combinations. Mg-O bonds exhibit smaller deviations than Si-O bonds, a result in good agreement with previous observations made by PW methods (Tunega et al., 2012).

The calculated OH bond lengths are about 0.960-0.970 Å with each approach, slightly shorter for the GTO/B3LYP-D(*) and longer in the PW/PBEsol case. However, a comparison with experiment is difficult because of XRD methods do not determine the position of hydrogen atoms with adequate accuracy. For this reason, we considered the most recent theoretical result (Tunega et al., 2012), which are very close to the one here reported.

Compared to the PW results of Tunega and co-workers (2012), our data with the same kinetic energy cutoff (E_{kin} = 600 eV) and functionals are very close to those reported in literature. The observed small differences can be explained by the different sampling k-meshes adopted. It can be observed that increasing the quality of the plane wave basis set, *i.e.* the kinetic energy cutoff from 600 eV to 800 eV improved also the structure description, compared to both experimental (Perdikatsis and Burzlaff, 1981) and theoretical (Tunega et al., 2012) data.

While the unit-cell of a phyllosilicate mineral defines the whole structure and in particular the interlayer interactions, the internal angles describe the geometric features within TOT layers. A bond angle classification based on five general groups within the talc structure has been considered: O-Mg-O,

Mg-O-Mg, Si-O-Mg, Si-O-Si, and O-Si-O. Each group is further subdivided on the basis of the oxygen atom types in the triad, basal and apical. The deviation from the XRD refinement (Perdikatsis and Burzlaff, 1981) are reported in Table 2.2.

Table 2.2. Mean calculated talc internal angles with different methods.

		Experimental	Localized GTO				PW	
Angle		XRD	PBE-D	PBEsol	B3LYP-D	B3LYP-D*	PBE-D	PBEsol
O – M – O	*O(a)-Mg-O(a)*	83.5	1.3	1.4	1.7	1.9	1.8	1.5
		96.4	-1.8	-1.5	-1.9	-1.9	-1.8	-1.5
		178.2	1.8	1.8	1.8	1.8	1.8	1.8
	O(a)-Mg-O(h)	83.3	1.6	1.3	1.7	1.6	1.6	1.2
		95.4	-0.2	0.1	-0.3	-0.3	-0.3	0.1
		178.3	1.3	1.0	1.3	0.7	0.7	0.7
	O(h)-Mg-O(h)	82.9	1.7	1.2	1.7	1.3	1.4	1.0
		180.0	0.0	0.0	0.0	0.0	0.0	0.0
M – O – H		-	121.2	120.9	121.3	121.0	121.0	120.5
M – O – M	*Mg-O(a)-Mg*	96.3	-1.6	-1.3	-1.7	-1.8	-1.7	-1.4
	Mg-O(h)-Mg	97.5	-2.0	-1.5	-2.0	-1.7	-1.7	-1.3
Si – O – M	*Si-O(b)-Si*	141.3	-5.7	-2.8	-4.9	-3.1	-3.6	-2.1
	Si-O(a)-Mg	120.7	1.1	1.0	1.2	1.3	1.3	1.1
	O(b)-Si-O(a)	108.9	0.4	0.4	0.4	0.4	0.8	1.0
	O(b)-Si-(Ob)	110.0	-0.3	-0.4	-0.3	-0.4	-0.7	-0.8

Notes: All the angular values are in degrees (°). Simulated results have been reported as deviation from the experimental data.

Differently from the other angles, O-Mg-O values are very different and a direct mean on them is not suitable. According to previous works (Larentzos et al., 2007; Perdikatsis and Burzlaff, 1981), the distributions of the angular values were calculated, finding three components for O^a-Mg-O^a and O^a-Mg-O^h and two components for O^h-Mg-O^h. There are negligible differences (±0.2°) between the different DFT functionals used with GTO basis set on the angular values. The major deviation is on the Si-O^b-Si angle, which increases as PBE-D < B3LYP-D < B3LYP-D* < PBEsol. Plane wave simulations gave results consistent with localized GTO basis set ones, same trends were observed for each angular class. Furthermore, the theoretical data are in good agreement with the experimental ones.

Interaction Energy

An interesting property to investigate in phyllosilicates is the energy that holds together the TOT layers. Its amount is an index of the strength of the whole mineral and affects many mechanical properties, such as the resistance to stress and shear forces. Within PBC approach, the simplest method to calculate the talc interaction energy is considering two infinite bi-dimensional TOT monolayers

which interact at the same distance found in the bulk. With this description, the interaction energy per unit cell between talc layers can be defined in the following way:

$$\Delta E_{interaction} = E_{BL}^{opt} - 2E_{ML}^{opt} \quad (2.7)$$

where E_{BL}^{opt} and E_{ML}^{opt} are the energies of the fully relaxed unit cells of the bilayer and the monolayer structures of talc, respectively. The cohesion energy that arises between a TOT layer and its neighbours (one up and one down) is simply the double of the interaction energy:

$$\Delta E_{cohesive} = 2\Delta E_{interaction} \quad (2.8)$$

A negative value indicates attraction between the layers, while positive means repulsion. In the case of calculations with localized GTO, these values must include the basis set superposition error (BSSE), which has been computed with the counterpoise method (Alagona et al., 1987; Cammi et al., 1985; Collins and Gallup, 1986).

The interaction and cohesive energies between layers ($\Delta E_{interaction}$ and $\Delta E_{cohesive}$, respectively) have been reported in Table 2.3.

Table 2.3. Cohesive and interaction energies (J m^{-2}) evaluated with different methods.

	GTO				PW	
	PBE-D	PBEsol	B3LYP-D	B3LYP-D*	PBE-D	PBEsol
with dispersion effects						
$\Delta E_{cohesive}$	-0.563	-	-0.724	-0.627	-	-
$\Delta E_{interaction}$	-0.282	-	-0.362	-0.314	-	-
$\Delta E_{cohesive}^{C}$	-0.450	-	-0.617	-0.520	-0.317	-0.016
$\Delta E_{interaction}^{C}$	-0.225	-	-0.308	-0.260	-0.158	-0.008
without dipersion effects						
$\Delta E_{cohesive}$	0.001	-0.129	0.049	0.022	-	-
$\Delta E_{interaction}$	0.000	-0.065	0.024	0.011	-	-
$\Delta E_{cohesive}^{C}$	0.141	-0.041	0.128	0.117	0.078	-
$\Delta E_{interaction}^{C}$	0.071	-0.020	0.064	0.059	0.039	-

Notes: ΔE^{C} represents energy corrected by counterpoise method. PW results are BSSE free and the comparison was made with the corrected localized GTO energies.

As expected, the talc structure is held together due to dispersion forces. When this factor was not taken into account, the TOT sheets shows a small repulsion, which is in contrast with experimental evidences. Also, the BSSE correction brought more repulsion between the layers, as it is more visible for the GTO/PBE (without dispersion effects) calculation. The energies evaluated within the localized GTO basis set are comparable with that obtained with plane wave pseudopotential ($\Delta E_{GTO} \approx 1.5\Delta E_{PW}$).

Furthermore, within the Gaussian basis set the attraction between talc layers is follows the trend B3LYP-D > B3LYP-D* > PBE-D > PBEsol, which corresponds to the opposite trend of the optimized lattice parameter *c*, i.e. shorter *c* corresponds to higher energies. The results obtained with the hybrid functional and modified dispersion correction parameters are in agreement with the geometrical features reported in the previous section. When the dispersive forces for layered solids were not considered, the TOTs exhibited repulsive behaviour, which can be directly in agreement with the theoretical structure results obtained with the uncorrected DFT functionals (Tosoni et al., 2007). It is also worth to be noted that the PBEsol functional gives a small attraction between the layers, even without the correction for dispersive forces and after subtracting the BSSE contribution.

These results have been compared to the talc surface energy γ_S obtained via solid-water interface interactions (Helmy et al., 2005). The simulated interaction energies are very close to the experimentally obtained value of 0.217 J m^{-2} reported in literature. It is worth noting that the calculated results with bare DFT would even have the wrong sign and only DFT+D reproduces satisfactorily the experiment.

Simulated Infrared Spectroscopy

The talc unit-cell contains N = 42 atoms and due to the $P\bar{1}$ symmetry its 126 normal modes are subdivided in:

$$\Gamma_{tot} = 63A_u + 63A_g$$

The A_u modes are IR active, while the A_g ones are Raman active. Three A_u modes are relative to atom traslations in the cell (acoustic modes), while the other 123 are optic modes. In the following we will focus only on the IR vibrational frequencies of most intense peaks.

The simulated and experimental (Dellisanti et al., 2009) IR vibrational modes are reported in Table 2.4.

The talc IR spectra evaluated with GTO basis set and different DFT functionals present very similar features in the 300-800 cm^{-1} range. Compared to the B3LYP results, the PBE-D spectrum is systematically red shifted of about 15 cm^{-1} for the low-frequency modes (O^h-Mg-O^h , O-Si-O, Mg-O^a-Si and O-Mg-O bendings) and 40 cm^{-1} in the high frequency region. The reason of the behaviour of the GGA functional lies in its electrostatic description, which exhibits less repulsion than the B3LYP. The modified PBEsol functional provided phonon frequencies very close to the B3LYP-D* ones in the

range 300-600 cm^{-1}, but the OH libration mode is red shifted ($\Delta\nu = -54\,cm^{-1}$) and the stretching modes, both Si-O and O-H, are blue shifted ($\Delta\nu = +30\,cm^{-1}$).

Table 2.4. Simulated and experimental IR vibrational modes.

GTO				PW		FTIR[a]	Assignment
PBE-D	PBEsol	B3LYP-D	B3LYP-D*	PBE-D	PBEsol		
374	404	414	408	391	384		δ O^h-Mg-O^h
410	413	418	411	418	413	425	
430	435	444	438	435	428	449	δ O-Si-O
444	455	462	459	437	430		
447	458	464	461	456	446		δ Si-O^a-Mg
469	474	484	480	479	472		
491	500	510	504	509	501	536	ν Mg-O
677	696	710	749	635	626	669	O-H libration
684	702	716	756	637	631		
929	973	953	940	923	931	1020	ν Si-O^a
976	1048	1020	1017	987	1001	1060	ν Si-O^b
980	1049	1024	1021	990	1002		
3860	3886	3871	3853	3796	3743		ν O-H (harmonic)
3707	3733	3727	3713			3676	ν O-H (anharmonic)

Notes: All the values reported are in wavenumbers (cm^{-1}). δ and ν refer to bending and stretching modes, respectively.
[a] (Dellisanti et al., 2009)

The comparison between hybrid functional results with standard and modified dispersion correction parameters is very interesting. B3LYP-D* calculated frequencies are very close to those of standard B3LYP-D and presents only a discrepancy on the OH libration (+30 cm^{-1}) and stretching (-14 cm^{-1}). This effect is probably due to the increased hydrogen atomic radius R_0 in the dispersive correction.

In the 400-600 cm^{-1} range the vibrational spectra obtained by PW/PBE-D and PW/PBEsol are very similar to the GTO counterparts. There are some differences on the OH libration and stretching modes, which are at lower wavenumbers of about 40 cm^{-1} than GTO/PBE-D. The Si-O stretching signals are slightly blue-shifted with the PBE-D functional ($\Delta\nu = +10\,cm^{-1}$), but they are red-shifted in the PBEsol case ($\Delta\nu = -40\,cm^{-1}$). The overall frequency shifts of the vibrational modes, in particular for the Si-O stretching, are probably linked to the different interaction energies. Indeed, the $\Delta E^{C}_{interaction}$ value increases as GTO/PBE-D < GTO/B3LYP-D < PW/PBE-D < GTO/B3LYP-D*, which is approximately also the red shift trend.

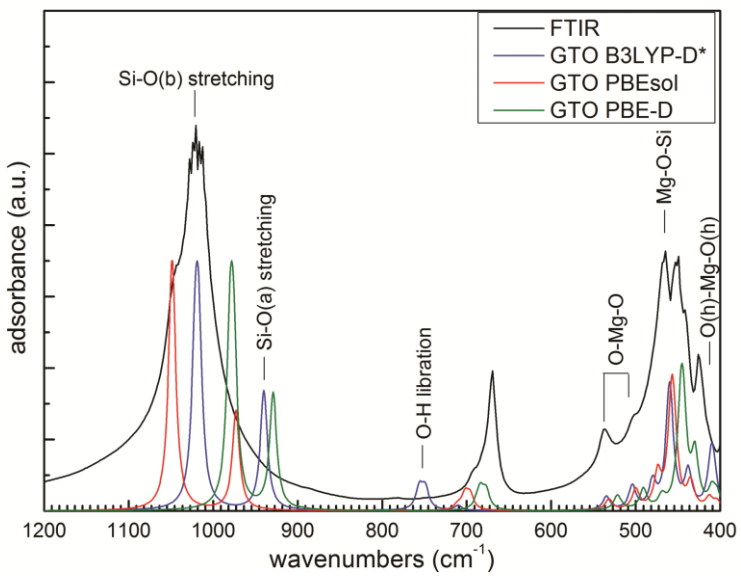

Figure 2.3. Simulated IR spectra obtained with GTO basis set.

The simulated spectra, both with Gaussian-type orbitals and plane waves basis sets are in acceptable agreement with earlier experimental results (Dellisanti et al., 2009). Differences between theoretical and FTIR results are mainly due to peak positions, intensities and band broadening. As an example, Figure 2.3 reports the superposition of simulated spectra, obtained with GTO basis sets, and experimental FTIR spectrum of talc.

The simulations well reproduced the bending modes in low-wavenumber range. The hydroxyl libration mode is at 669 cm^{-1} in the experimental spectrum, while it falls at higher wave numbers in all our simulations. Furthermore, the region relative to the stretching modes of silicon and oxygen atoms ($Si\text{-}O^a$ and $Si\text{-}O^b$ between 900-1200 cm^{-1}) presents many differences. In the experimental spectrum there is a single, broad band centred at 1020 cm^{-1}, with a shoulder at about 1060 cm^{-1}. However, in the experimental investigation of Nkoumbou and co-workers (Nkoumbou et al., 2008) there are two acceptably resolved peaks at 1000 and 1060 cm^{-1}. In the simulated spectra the Si-O stretching modes are slightly underestimated (40 cm^{-1}) and their intensities seem opposite to the FTIR ones. Worth to be noted that better agreement with experimental data was obtained by the PBEsol functional. Despite this difference, the separation between the two peaks is in quite good agreement with experimental data, about 60 cm^{-1} for the GTO and 40 cm^{-1} for the PW simulations. The observed deviations can be caused by atomic substitutions, impurities and mechanical defects in the experimental sample which is made in form of a mechanically powdered material. Geologically, talc mineral is usually found with these kinds of defects, which drastically modify the chemical environment and affect the whole vibrational character of the material, while our model is for a stoichiometrically pure $Mg_3Si_4O_{10}(OH)_2$ talc structure.

The OH stretching modes (not shown in Figure 2.3) are generally overestimated, even after applying the anharmonic correction, because of the sensitiveness of the H atom to the chemical environment.

2.4 Conclusions

Different *ab initio* quantum mechanics QM methods to study layered silicates dominated by both weak interlayer and strong intralayer bondings were investigated and compared in details. To this aim talc mineral has been chosen as model system because of its TOT layer structure and also for the minero-petrological and industrial importance. The proposed QM methods are within the Density Functional Theory and take into account different atomic descriptions (GTO and PW), dispersive corrected functionals (PBE and B3LYP) and a specific functional designed for solid phases (PBEsol). The chosen approaches fit and extend those reported in a previous work (Tunega et al., 2012).

As mentioned, when dealing with layered silicates, a proper description of the weak interaction forces is mandatory. Standard DFT functionals correctly describe covalent and ionic bonds, but not dispersive forces. The adoption of a semi-empirical correction, such as DFT-D, or a specifically designed functional, such as PBEsol, is strongly recommended. The use of the DFT-D approach is tightly linked to the choice of the functional, because of the different proposed parameterizations.

The kinetic energy cutoff in PW simulations and the richness and balance of the atomic basis set for Gaussian-type orbital calculations are extremely important parameters. Adopting full-potential GTO basis set and increasing the E_{kin} from 1.5 to 2.0 times the suggested value for PW simulations are recommended.

Considering the different DFT functionals, the best results were provided by the hybrid B3LYP-D* and the PBE-D functionals, using Gaussian-type Orbitals and plane waves basis sets, respectively. However, the adoption of hybrid functionals such as B3LYP is practically limited to GTO calculations because its use with plane waves basis set requires a large amount of computational resources.

The choice of the basis set/functional combination used to characterize and predict layered silicates properties is then driven by the scientific interest and the available computational resources. On one hand plane waves simulations are less demanding than GTO ones, especially when surface modelling and adsorption/interaction processes are involved because plane waves are BSSE free. On the other hand the reported results suggest that, whenever finer energy data are required, the investigations are much more accurate with full-potential Gaussian-type orbital basis set and hybrid functionals. GTO basis sets are also preferable when energy *vs* volume calculations are involved, such as in the equation of state prediction, because they are unaffected by cell shape variations.

A final note regards the PBEsol functional that provided a fairly good description of the talc structure. When used with GTO basis set, the results are in good agreement for the cell vectors, but they are over-estimated for the cell angular values; vice versa in the case of the PW/PBEsol approach. The

calculated energy values show attraction between the TOT layers, but they are highly under-estimated when compared to experimental results. This DFT functional is promising for the description of layered silicate structures and it could be improved using a rescaled DFT-D correction, not yet present in literature.

REFERENCES CITED

Alagona, G., Ghio, C., Cammi, R., and Tomasi, J. (1987) The effect of full and limited counterpoise corrections with different basis-set on the energy and the equilibrium distance of hydrogen-bonded dimers. International Journal of Quantum Chemistry, 32(2), 207-226.

Becke, A.D. (1993) A New Mixing of Hartree-Fock and Local Density-Functional Theories. Journal of Chemical Physics, 98(2), 1372-1377.

Bleam, W.F. (1990a) Electrostatic potential at the basal (001) surface of talc and Pyrophillite as related to tetrahedral sheet distortions. Clays and Clay Minerals, 38(5), 522-526.

-. (1990b) The nature of cation-substitution sites in phyllosilicates. Clays and Clay Minerals, 38(5), 527-536.

Blochl, P.E. (1994) Projector augmented-wave method. Physical Review B, 50(24), 17953-17979.

-. (1995) Electrostatic decoupling of periodic images of plane-wave-expanded densities and derived atomic point charges. Journal of Chemical Physics, 103(17), 7422-7428.

Boys, S.F., and Bernardi, F. (1970) The calculation of small molecular interactions by the differences of separate total energies. Some procedures with reduced errors. Molecular Physics, 19(4), 553-566.

Broyden, C.G. (1970a) The convergence of a class of double-rank minimization algorithms 1. General considerations. IMA Journal of Applied Mathematics (Institute of Mathematics and Its Applications), 6(1), 76-90.

-. (1970b) The convergence of a class of double-rank minimization algorithms: 2. The new algorithm. IMA Journal of Applied Mathematics (Institute of Mathematics and Its Applications), 6(3), 222-231.

Bruno, M., Prencipe, M., and Valdre, G. (2006) Ab initio quantum-mechanical modeling of pyrophyllite Al2Si4O10(OH)(2) and talc Mg3Si4O10(OH)(2) surfaces. Physics and Chemistry of Minerals, 33(1), 63-71.

Cammi, R., Bonaccorsi, R., and Tomasi, J. (1985) Counterpoise corrections to the interaction energy components in bimolecular complexes. Theoretica Chimica Acta, 68(4), 271-283.

Civalleri, B., Zicovich-Wilson, C.M., Valenzano, L., and Ugliengo, P. (2008) B3LYP augmented with an empirical dispersion term (B3LYP-D*) as applied to molecular crystals. Crystengcomm, 10(4), 405-410.

Collins, J.R., and Gallup, G.A. (1986) The full versus the virtual counterpoise correction for basis set superposition error in self-consistent field calculations. Chemical Physics Letters, 123(1-2), 56-61.

D'Haese, M., Goderis, B., and Van Puyvelde, P. (2011) The Influence of Calcium-Stearate-Coated Calcium Carbonate and Talc on the Quiescent and Flow-Induced Crystallization of Isotactic Poly(propylene). Macromolecular Materials and Engineering, 296(7), 603-616.

Dellisanti, F., Minguzzi, V., and Valdre, G. (2011) Mechanical and thermal properties of a nanopowder talc compound produced by controlled ball milling. Journal of Nanoparticle Research, 13(11), 5919-5926.

Dellisanti, F., and Valdre, G. (2010) On the high-temperature structural behaviour of talc (Mg3Si4O10(OH)2) to 1600 degrees C: Effect of mechanical deformation and strain. Philosophical Magazine, 90(17-18), 2443-2457.

Dellisanti, F., and Valdre, G. (2012) The role of microstrain on the thermostructural behaviour of industrial kaolin deformed by ball milling at low mechanical load. International Journal of Mineral Processing, 102, 69-77.

Dellisanti, F., Valdre, G., and Mondonico, M. (2009) Changes of the main physical and technological properties of talc due to mechanical strain. Applied Clay Science, 42(3-4), 398-404.

Dovesi, R., Civalleri, B., Orlando, R., Roetti, C., and Saunders, V.R. (2005) Ab initio quantum simulation in solid mate chemistry. In K.B. Lipkowitz, R. Larter, and T.R. Cundari, Eds. Reviews in Computational Chemistry, 21, p. 1-125. Wiley, New York.

Dovesi, R., Saunders, V.R., Roetti, C., Orlando, R., Zicovich-Wilson, C.M., Pascale, F., Civalleri, B., Doll, K., Harrison, N.M., Bush, I.J., D'Arco, P., and Llunell, M. (2009) CRYSTAL09 User's Manual. University of Torino, Torino.

Fletcher, R. (1970) A new approach to variable metric algorithms. The Computer Journal, 13(3), 317-322.

Gatti, C., Saunders, V.R., and Roetti, C. (1994) Crystal-field effects on the topological properties of the electron-density in molecular-crystals - the case of urea. Journal of Chemical Physics, 101(12), 10686-10696.

Goldfarb, D. (1970) A family of variable-metric methods derived by variational means. Mathematics of Computation, 24, 23-26.

Goumans, T.P.M., Wander, A., Brown, W.A., and Catlow, C.R.A. (2007) Structure and stability of the (001) alpha-quartz surface. Physical Chemistry Chemical Physics, 9(17), 2146-2152.

Grimme, S. (2006) Semiempirical GGA-type density functional constructed with a long-range dispersion correction. Journal of Computational Chemistry, 27(15), 1787-1799.

Helmy, A.K., Ferreiro, E.A., and de Bussetti, S.G. (2005) The surface energy of talc. Journal of Colloid and Interface Science, 285(1), 314-317.

Hernandez-Rivera, S.P., and Castillo-Chara, J. (2010) Ab initio, DFT calculation and vibrational analysis of 2,4,6-trinitrotoluene. Vibrational Spectroscopy, 53(2), 248-259.

Hu, X., Zhang, Y., Zhuang, N., and Li, J. (2010) Density functional theory predictions for blue luminescence and nonlinear optical properties of carbon-doped gallium nitride. Journal of Solid State Chemistry, 183(12), 2741-2745.

Huang, P., and Carter, E.A. (2008) Advances in correlated electronic structure methods for solids, surfaces, and nanostructures. Annual Review of Physical Chemistry, 59, p. 261-290. Annual Reviews, Palo Alto, CA.

Jahani, Y. (2011) Comparison of the effect of mica and talc and chemical coupling on the rheology, morphology, and mechanical properties of polypropylene composites. Polymers for Advanced Technologies, 22(6), 942-950.

Kalendova, A., Vesely, D., and Kalenda, P. (2010) Properties of paints with hematite coated muscovite and talc particles. Applied Clay Science, 48(4), 581-588.

Katouda, M., and Nagase, S. (2010) Application of second-order Moller-Plesset perturbation theory with resolution-of-identity approximation to periodic systems. Journal of Chemical Physics, 133(18).

Kresse, G., and Furthmuller, J. (1996) Efficiency of ab-initio total energy calculations for metals and semiconductors using a plane-wave basis set. Computational Materials Science, 6(1), 15-50.

Kresse, G., and Hafner, J. (1993) Ab-initio molecular-dynamics for open-shell transition-metals. Physical Review B, 48(17), 13115-13118.

Kresse, G., and Joubert, D. (1999) From ultrasoft pseudopotentials to the projector augmented-wave method. Physical Review B, 59(3), 1758-1775.

Larentzos, J.P., Greathouse, J.A., and Cygan, R.T. (2007) An ab initio and classical molecular dynamics investigation of the structural and vibrational properties of talc and pyrophyllite. Journal of Physical Chemistry C, 111(34), 12752-12759.

Lee, C.T., Yang, W.T., and Parr, R.G. (1988) Development of the Colle-Salvetti Correlation-Energy Formula into a Functional of the Electron-Density. Physical Review B, 37(2), 785-789.

Molina-Montes, E., Donadio, D., Hernandez-Laguna, A., and Sainz-Diaz, C.I. (2008a) DFT research on the dehydroxylation reaction of pyrophyllite - 2. Characterization of reactants, intermediates, and transition states along the reaction path. Journal of Physical Chemistry A, 112(28), 6373-6383.

Molina-Montes, E., Donadio, D., Hernandez-Laguna, A., Sainz-Diaz, C.I., and Parrinello, M. (2008b) DFT research on the dehydroxylation reaction of pyrophyllite 1. First-principle molecular dynamics simulations. Journal of Physical Chemistry B, 112(23), 7051-7060.

Momma, K., and Izumi, F. (2008) VESTA: a three-dimensional visualization system for electronic and structural analysis. Journal of Applied Crystallography, 41, 653-658.

Monkhorst, H.J., and Pack, J.D. (1976) Special points for Brillouin-zone integrations. Physical Review B, 8, 5188-5192.

Nada, R., Nicholas, J.B., McCarthy, M.I., and Hess, A.C. (1996) Basis sets for ab initio periodic Hartree-Fock studies of zeolite/adsorbate interactions: He, Ne, and Ar in silica sodalite. International Journal of Quantum Chemistry, 60(4), 809-820.

Nkoumbou, C., Villieras, F., Njopwouo, D., Ngoune, C.Y., Barres, O., Pelletier, M., Razafitianamaharavo, A., and Yvon, J. (2008) Physicochemical properties of talc ore from three deposits of Lamal Pougue area (Yaounde Pan-African Belt, Cameroon), in relation to industrial uses. Applied Clay Science, 41(3-4), 113-132.

Parr, R.G., and Yang, W. (1989) Density Functional Theory of Atoms and Molecules. Oxford University Press, Oxford, UK.

Parry, D.E. (1975) Electrostatic potential in surface region of an ionic-crystal. Surface Science, 49(2), 433-440.

Pascale, F., Zicovich-Wilson, C.M., Gejo, F.L., Civalleri, B., Orlando, R., and Dovesi, R. (2004) The calculation of the vibrational frequencies of crystalline compounds and its implementation in the CRYSTAL code. Journal of Computational Chemistry, 25(6), 888-897.

Pawley, A.R., Redfern, S.A.T., and Wood, B.J. (1995) Thermal expansivities and compressibilities of hydrous phases in the system MgO-SiO2-H2O: Talc, phase A and 10-angstrom phase. Contributions to Mineralogy and Petrology, 122(3), 301-307.

Pawley, A.R., and Wood, B.J. (1995) The High-Pressure Stability of Talc and 10 Angstrom Phase - Potential Storage Sites for H_2O in Subduction Zones. American Mineralogist, 80(9-10), 998-1003.

Perdew, J.P., Burke, K., and Ernzerhof, M. (1996) Generalized gradient approximation made simple. Physical Review Letters, 77(18), 3865-3868.

Perdew, J.P., Ruzsinszky, A., Csonka, G.I., Vydrov, O.A., Scuseria, G.E., Constantin, L.A., Zhou, X.L., and Burke, K. (2008) Restoring the density-gradient expansion for exchange in solids and surfaces. Physical Review Letters, 100(13).

Perdikatsis, B., and Burzlaff, H. (1981) Structural refinement of talc $Mg_3(OH)Si_4O_{10}$. Zeitschrift Fur Kristallographie, 156(3-4), 177-186.

Prencipe, M., Pascale, F., Zicovich-Wilson, C.M., Saunders, V.R., Orlando, R., and Dovesi, R. (2004) The vibrational spectrum of calcite (CaCO3): an ab initio quantum-mechanical calculation. Physics and Chemistry of Minerals, 31(8), 559-564.

Refson, K., Park, S.H., and Sposito, G. (2003) Ab initio computational crystallography of 2 : 1 clay minerals: 1. Pyrophyllite-1Tc. Journal of Physical Chemistry B, 107(48), 13376-13383.

Sainz-Diaz, C.I., Francisco-Marquez, M., and Vivier-Bunge, A. (2011) Adsorption of polyaromatic heterocycles on pyrophyllite surface by means of different theoretical approaches. Environmental Chemistry, 8(4), 429-440.

Schwerdtfeger, P. (2011) The Pseudopotential Approximation in Electronic Structure Theory. Chemphyschem, 12(17), 3143-3155.

Shanno, D.F. (1970) Conditioning of quasi-Newton methods for function minimization. Mathematics of Computation, 24, 647-656.

Tosoni, S., Pascale, F., Ugliengo, P., Orlando, R., Saunders, V.R., and Dovesi, R. (2005) Quantum mechanical calculation of the OH vibrational frequency in crystalline solids. Molecular Physics, 103(18), 2549-2558.

Tosoni, S., Tuma, C., Sauer, J., Civalleri, B., and Ugliengo, P. (2007) A comparison between plane wave and Gaussian-type orbital basis sets for hydrogen bonded systems: Formic acid as a test case. Journal of Chemical Physics, 127(15).

Tunega, D., Bucko, T., and Zaoui, A. (2012) Assessment of ten DFT methods in predicting structures of sheet silicates: Importance of dispersion corrections. Journal of Chemical Physics, 137(11).

Tunega, D., Nagy, L.T., and Varga, S. (1994) Comparative study of the electrostatic potential obtained with various atomic basis sets for the cluster model of the tetrahedral sheet $[Si_2O_5H_2]$ infinity. Ceramics-Silikaty, 38(3-4), 167-172.

Ugliengo, P., Pascale, F., Merawa, M., Labeguerie, P., Tosoni, S., and Dovesi, R. (2004) Infrared spectra of hydrogen-bonded ionic crystals: Ab initio study of Mg(OH)(2) and beta-Be(OH)(2). Journal of Physical Chemistry B, 108(36), 13632-13637.

Ugliengo, P., Viterbo, D., and Chiari, G. (1993) MOLDRAW: molecular graphic on a personal computer. Zeitschrift Fur Kristallographie, 207, 9-23.

Valenzano, L., Noel, Y., Orlando, R., Zicovich-Wilson, C.M., Ferrero, M., and Dovesi, R. (2007) Ab initio vibrational spectra and dielectric properties of carbonates: magnesite, calcite and dolomite. Theoretical Chemistry Accounts, 117(5-6), 991-1000.

Valenzano, L., Torres, F.J., Klaus, D., Pascale, F., Zicovich-Wilson, C.M., and Dovesi, R. (2006) Ab initio study of the vibrational spectrum and related properties of crystalline compounds; the case of CaCO3 calcite. Zeitschrift Fur Physikalische Chemie-International Journal of Research in Physical Chemistry & Chemical Physics, 220(7), 893-912.

Wang, F., Di Valentin, C., and Pacchioni, G. (2011) Electronic and Structural Properties of WO3: A Systematic Hybrid DFT Study. Journal of Physical Chemistry C, 115(16), 8345-8353.

- This page was left blank -

CHAPTER 3 – The mechanical properties of talc [$Mg_3Si_4O_{10}(OH)2$]: a density functional theory contribution[2]

Abstract

In this work, we modelled the structure, the compressional behaviour and the physical properties of talc over a wide range of pressure using a quantum mechanical approach based on periodic boundary conditions. We adopted the density functional theory using the B3LYP-D* functional, which includes a correction for the dispersive forces and all-electron Gaussian-type orbitals basis sets. An atomic level description of the athermal pressure-induced structural modification of talc is provided. From the compression results we obtained the athermal (T = 0 K) bulk modulus (K_{T0}), its first derivative (K') and the athermal volume at zero pressure (V_0) by a third-order Birch-Murnaghan equation with parameters K_{T0} = 56.25 GPa, K' = 5.66 and V_0 = 450.34 Å^3. The mechanical behaviour is highly anisotropic, as observed by the axial compressibility. The presented data are in very good agreement with recent experimental results obtained by single-crystal neutron and X-ray diffraction experiments.

3.1 Introduction

Talc, $Mg_3Si_4O_{10}(OH)_2$, is the product of metamorphism or hydrothermal alteration of ultramafic rocks (Evans and Guggenheim, 1988). This mineral is a 2:1 trioctahedral layered silicate whose structure is composed of a Mg-octahedral (brucite) sheet ("O") sandwiched between two Si-tetrahedral (siloxane) sheets ("T"), giving a structure called T-O-T. The adhesion between charge-neutral T-O-T layers talc slabs is due solely to van der Waals forces (Larentzos et al., 2007; Ulian et al., 2013a).

Talc commonly occurs on the seafloor surface as well as at a depth of about 150 km in subduction zones. It plays an important role in the transport and recycling of water to the Earth's mantle because of its water content of about 5 wt. % (Mysen et al., 1998). It is supposed that it releases water in the dehydration reaction to enstatite at ca 1.7 GPa and 660 °C, conditions that are usually found at about 60 km under the crust surface (Melekhova et al., 2006; Ulmer and Trommsdorff, 1995). The presence of H_2O in the mantle, even in small amounts, could trigger partial melting and magma generation and affect the seismic/rheological properties of fluids or minerals (Pawley et al., 1995). Knowledge of the stability of talc at high pressure and different temperatures is therefore important to determine the

[2] This chapter consists of a paper by Gianfranco Ulian, Sergio Tosoni and Giovanni Valdrè, "The compressional behaviour and the mechanical properties of talc [$Mg_3Si_4O_{10}(OH)_2$]: a density functional theory investigation", *Physics and Chemistry of Minerals*, Accepted.

capability of this mineral and other hydrothermally altered ultramafic rocks to store and transport water into the mantle.

Talc is also one of the most important industrial minerals because of its properties such as, for instance, low coefficient of friction, platyness, chemical inertness, affinity for organic chemicals and hydrophobicity. These characteristics allow its use in several technological applications, such as, paper coating, paint, ceramics, cosmetics and polymer industries. As an example, talc is used to create composite polymers, which exhibit tailored properties (hardness, chemical activity, etc.) from their "pure" counterparts (Butylina et al., 2012; Castillo et al., 2012; D'Haese et al., 2011; Mirabedini et al.. 2012). Because of its industrial importance, talc was subject of numerous experimental investigations of its thermophysical and thermochemical behavior after compaction and shear (Dellisanti et al., 2011; Dellisanti and Valdrè, 2010; Dellisanti et al., 2009).

Despite the above considerations, some issues about the crystal-chemical and mechanical properties of talc are still open questions and need further investigation and/or confirmation. For instance, the OH position in the structure and compressional behavior of talc. While the talc lattice parameters and Mg, Si and O positions within the unit-cell were described in the early 1930's (Gruner, 1934; Rayner and Brown, 1973), the first suggestion on the OH group position was proposed by Perdikatsis and Burzlaff after single-crystal X-Ray Diffraction (XRD) refinement of the talc structure (Perdikatsis and Burzlaff, 1981). The authors stated that the proton is placed near the centers of the six-member SiO_4^{4-} rings. Very recently, a combined experimental XRD and Neutron Diffraction refinement was in agreement with this observation, adding further information about the hydrogen-bonding scheme (Gatta et al., 2013). Our simulations aim to study the OH group in the talc structure.

Another issue is the high-pressure stability and compressional behavior of talc, as evidenced by conflicting results present in literature. For instance, there is a strong discordance on the elastic parameters of talc, *i.e.* axial and bulk modulus (K_{T0}) and the P-derivative of the bulk modulus (K') at room temperature (T = 298 K). With K_{T0} we indicate the isothermal bulk modulus calculated at P = 0 GPa.

Pawley et al. (1995) measured the structural changes of talc at room temperature in a range of pressure from 0.0 to 6 GPa using a X-Ray powder diffractometer equipped with a lever-arm diamond-anvil cell. They measured a powdered sample of talc with a non-dried 4:1 methanol:ethanol mixture as the pressure-transmitting fluid and with NaCl as internal pressure standard. The data were fitted with a Murnaghan equation (Murnaghan, 1937) to obtain K_{T0} = 41.6 GPa and K' = 6.5.

Gleason and co-workers (2008) used different pressure transmitting fluids (ethylciclohexane or water) to collect X-ray powder diffraction data from ambient pressure to 10 GPa. In this case the structural results were fitted with a third-order Birch-Murnaghan equation (Birch, 1947), which led to K_{T0}

= 44(2) GPa and K' = 18(1). The obtained bulk modulus is comparable to the one of Pawley et al. (1995), but K' presents differences probably because of the different pressure range studied, the non-hydrostaticity in the sample chamber and the different pressure transmitting fluid. More recently, Gatta et al. (2013) performed a single-crystal investigation combining Neutron Diffraction and X-Ray Diffraction techniques up to 15.5 GPa using a symmetric diamond-anvil cell with neon as hydrostatic pressure transmitting medium. The results were fitted with a third-order Birch-Murnaghan equation of state, with parameters V_0 = 454.7(10) Å^3, K_{T0} = 56(3) GPa and K' = 5.4(7). It is immediately evident how single-crystal and powder diffraction data led to discordant bulk modulus values, which may imply different behaviors of crystalline and powdered samples.

In recent years, a few *ab initio* quantum chemistry approaches were used to understand the talc compressional behavior at atomic level. For instance, Stixrude (2002) presented a theoretical talc model, calculated using Density Functional Theory (DFT), local density approximation (LDA) and plane wave basis set at 300 K in hydrostatic conditions from 0.0 to 29 GPa. The author employed a fourth-order Birch-Murnaghan equation of state to fit the structural data, with refined parameters K_{T0} = 37.8 GPa, K' = 13.6 in static conditions (T = 0 K). The bulk modulus is smaller and its pressure derivative higher than X-Ray powder diffraction data (Pawley et al. 1995).

Mainprice et al. (2008) reported a DFT simulation with generalized gradient approximation (GGA) and plane wave basis set of both talc equation of state and second-order elastic constants up to 12 GPa. The parameters of a fourth-order Birch-Murnaghan equation of state were K_{T0} = 32.1 GPa, K' = 17.4 at T = 0 K. The theoretical results of Mainprice and co-workers (2008) are consistent with those of Stixrude (2002), but both of them showed a less rigid structure than real samples, both as powdered (Gleason et al., 2008; Pawley et al., 2002; Pawley et al., 1995) and as single-crystal ones (Gatta et al., 2013). This discrepancy by the experimental results was explained by the authors (Mainprice et al., 2008; Stixrude, 2002) with the effects of strain compatibility in the polycrystalline laboratory sample. However, we note that both simulations lack of adequate description of weak dispersive forces, because it was still not available at that time. Dispersive forces are important for layer silicates because the structural layer units are bond together by weak interaction forces and influences the final geometry (Ulian et al., 2013a).

To overcome the above limitation, in the present work we modelled and optimized the talc geometry by an *ab initio* quantum mechanical approach based on the density functional theory (DFT) corrected for the dispersive forces. In addition, differently from above mentioned theoretical studies we used an all-electron localized Gaussian-type orbitals (GTO) and the B3LYP hybrid functional integrated with dispersive forces contribution. This combination provides more accurate energy results than

plane wave simulations, as shown in previous works (Ulian et al., 2013a; Ulian et al., 2013b; Ulian et al., 2013c). Starting from the XRD data of Perdikatsis and Burzlaff (1981), we optimized the talc structure of talc and investigated the mechanical properties of the mineral. First, in order to gain information on the compressional behavior of a pure talc model, we investigated the talc structure from 0 GPa to 10 GPa. A small range of negative pressures were also considered to explore the mineral behavior under the effect of an hydrostatic tensile stress. Then, we calculated the second-order elastic constants (SOEC), which provide other important information on the mechanical properties of materials and on their structural stability. These data were used to predict the equation of state, lattice and internal structural parameters of talc and were compared with previous theoretical and experimental results.

3.2 Computational details

CRYSTAL09 code (Dovesi et al., 2009), which implements the Hartree–Fock and Kohn–Sham self-consistent field method for the study of periodic systems, was used to perform all the simulations reported in the present work. The graphical drawings have been carried out with the molecular graphics software MOLDRAW (Ugliengo et al., 1993) and VESTA (Momma and Izumi, 2008).

Hamiltonian and computational parameters

The calculations have been performed within the Density Functional Theory, using the Becke, three-parameters (Becke, 1993), and the gradient-corrected correlation functional of Lee, Yang and Parr (Lee et al., 1988) hybrid exchange functional (B3LYP). The exchange–correlation contribution is calculated over a grid of points and is the result of a numerical integration of the electron density and its gradient. To improve the accuracy/computational costs ratio for geometry optimizations, a 75 points × 974 angular points pruned grid (XLGRID keyword) obtained from the Gauss–Legendre quadrature and Lebedev schemes (Prencipe et al., 2004) was used. The values of the tolerances that control the Coulomb and exchange series are the default provided by CRYSTAL09 (*ITOL1* to *ITOL4* = 6), but we increased the pseudo-overlap parameter (*ITOL5*) from 12 to 14 (Dovesi et al., 2009) to stabilize the self-consistent behaviour during unit-cell deformations. Differently from our previous work (Ulian et al., 2013a), the Hamiltonian matrix has been diagonalized (Monkhorst and Pack, 1976) using a shrinking factor (*IS*) = 4 (Dovesi et al., 2009), that leads to a 4×4×4 k-mesh and 36 k-points. This increased the energy sampling along the **c**-axis direction and the whole accuracy of the modelling.

Within the CRYSTAL code, multi-electron wave functions are described by linear combination of crystalline orbitals (CO), expanded in terms of Gaussian-type orbital (GTO) basis sets. The basis sets have been previously optimized by other authors for their investigations of similar structures. For all the calculations, magnesium and oxygen have been described by a 8-511d1G and a 8-411d11G basis sets, respectively (Valenzano et al., 2006), and silicon by a 88-31G* (Nada et al., 1996). Hydrogen was described by a standard 3-1p1G basis set with *p* polarization function exponent of 1.1 $Bohr^{-1}$, which was employed in previous simulations of urea crystals (Gatti et al., 1994) and silica surface (Civalleri et al., 1999). The chosen hydrogen atom basis set allows accurate calculations of hydrogen atoms in molecular and crystal structures without too high computational costs and it is well balanced with the other atomic basis sets used in talc structure.

Lattice constants and internal coordinates have been optimized within the same run using the analytical gradient method for the atomic positions and a numerical gradient for the unit-cell parameters. The Hessian matrix is upgraded with the Broyden–Fletcher–Goldfarb–Shanno algorithm (Broyden, 1970b, a; Fletcher, 1970; Goldfarb, 1970; Shanno, 1970). The tolerances for the maximum allowed gradient and the maximum atomic displacement for considering the geometry as converged have been set to $6 \cdot 10^{-5}$ hartree $bohr^{-1}$ and $1.2 \cdot 10^{-5}$ bohr, respectively. These values are stricter than the default ones provided by CRYSTAL09 (Dovesi et al., 2009), because mechanical properties evaluations require the structure in analysis as close as possible to the structure corresponding to the minimum of the potential energy.

As previously mentioned, GGA functionals, both standard and hybrid (such as B3LYP), often fails to provide adequate description of long-range dispersive interactions. We overcome this issue adopting the semiempirical approach (DFT+D) suggested by Grimme (Grimme, 2006), which adds the following contribution to the calculated DFT energy:

$$E_{DISP} = -s_6 \sum_{\mathbf{g}} \sum_{i \neq j} f_{dump}\left(R_{ij,\mathbf{g}}^6\right) \frac{C_6^i C_6^j}{R_{ij,\mathbf{g}}^6} \tag{3.1}$$

The summation over all atom pairs *ij* and **g** lattice vectors excludes the self- interaction contribution ($i = j$) for every $\mathbf{g}$. The parameters C_6^i represent the dispersive coefficient for the atom *i*, $R_{ij,\mathbf{g}}$ is the interatomic distance between atom *i* in the reference cell and atom *j* in the neighbouring cells at distance |**g**| and s_6 is a functional-dependent scaling factor. We employed the C_6^i parameters reported in the work of Grimme (2006), which were obtained from atomic ionization potentials (I_p) and static dipole polarizabilities (α) according to the formula $C_6^i = 0.05 N I_p^i \alpha^i$, where *N* depends on atom row in the periodic table. The function f_{dump} is used to dump the energy correction to avoid double counting

of short-range contributions and depends on the sum of atomic van der Waals radii and on a steepness parameter (d = 20). According to results previously reported in literature for urea crystals (Civalleri et al., 2008), showing that the E_{DISP} correction tends to overestimate cohesive energy in solid crystals, the original B3LYP-D parameters where modified setting s_6 to 1, the hydrogen atom van der Waals radius R_{vdw}(H) to 1.30 and the heavier atom van der Waals radii were scaled by a factor 1.05 (called B3LYP-D*).

3.3 Results

Talc structure

The modelled talc structure belongs to $P\bar{1}$ space group, corresponding to the 1Tc polytype described by single crystal XRD analysis (Evans and Guggenheim, 1988; Perdikatsis and Burzlaff, 1981). Oxygen atoms are subdivided in three groups: apical [O^a or O(a)] shared between Si and Mg; hydroxylic [O^h or O(h)]; basal [O^b or O(b)] shared between silica tetrahedrons. See the stick and ball model in Figure 3.1 for a graphical representation.

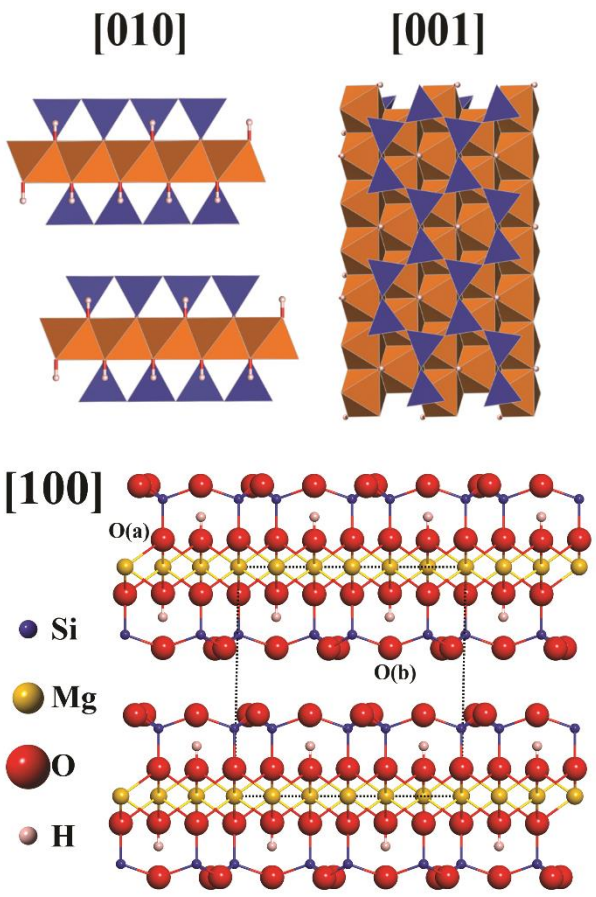

Figure 3.1. Polyhedral models of the talc structure as seen from the [010] and [001] directions. Stick and ball representation along the [100] direction was reported to clearly show the atomic arrangement within the mineral.

We adopted the conventional unit cell to facilitate a direct comparison between theoretical and experimental data. Thus in the structure there are two unit formula (Z = 2) of $Mg_3Si_4O_{10}(OH)_2$, for a total of 42 atoms. The results of the geometry optimization are listed in the following tables. For the sake of clearness, we have reported the lattice parameters in Table 3.1, the atomic fractional coordinates in Table 3.2 and bond lengths and polyhedron volumes in Table 3.3 with all data compared to experimental results from recent single-crystal neutron diffraction experiments (Gatta et al., 2013). In our simulations, the resulting structure has a volume V of 448.88 Å^3 (a = 5.2914 Å, b = 9.1729 Å, c = 9.4233 Å). In Table 1 we also reported the geometry optimization results of talc without the correction for dispersive forces (DFT/B3LYP). It

can be observed that the unit cell expands, in particular along the **c**-axis (+6%), because the hybrid GGA functional does not consider van der Waals forces that hold together the TOT layers. Thus, the inclusion of the semi-empirical correction of Grimme (2006) is of utmost importance when dealing with the structural and physical-chemical properties of layered minerals such as phyllosilicates (Ulian et al. 2013a).

Table 3.1. Experimental and theoretical refinement of talc structure

	Neutron Diffraction	**DFT B3LYP-D***	**DFT B3LYP**
a (Å)	5.299	5.2914	5.3322
b (Å)	9.165	9.1729	9.2405
c (Å)	9.484	9.4233	9.9799
α (°)	90.76	91.18	90.81
β (°)	100.39	101.00	99.56
γ (°)	90.16	90.12	90.03
Basal *d* spacing (Å)	9.328	9.250	9.841
V_{cc} (Å^3)	453.04	448.98	484.86

V_{cc} refers to the crystallographic cell. Very recent Neutron Diffraction (Gatta et al. 2013) data obtained at 20 K are reported for comparison. Theoretical refinement is made at 0.171 GPa and 0 K. DFT/B3LYP data are obtained without semi-empirical correction for dispersive forces.

Table 3.2. Atomic fractional coordinates of talc

	Neutron Diffraction			**DFT-B3LYP**		
	x/a	*y/b*	*z/c*	*x/a*	*y/b*	*z/c*
H	0.7311(5)	0.6693(3)	0.2170(1)	0.7401	0.6710	0.2183
Mg1	0.0000	0.0000	0.0000	0.0000	0.0000	0.0000
Mg2	0.5021(2)	0.8327(1)	1.0001(1)	0.5004	0.8332	0.9997
O(a)1	0.2053(2)	0.8357(1)	0.1186(1)	0.2081	0.8362	0.1191
O(a)2	0.2058(2)	0.5022(1)	0.1211(1)	0.2061	0.5024	0.1191
O(b)1	0.0371(2)	0.9339(1)	0.3465(1)	0.0563	0.9444	0.3534
O(b)2	0.5391(2)	0.9133(1)	0.3499(1)	0.5568	0.9051	0.3560
O(b)3	0.2536(2)	0.6739(1)	0.3506(1)	0.2470	0.6746	0.3535
O(h)	0.7037(2)	0.6704(1)	0.1110(1)	0.7051	0.6692	0.1146
Si1	0.2675(3)	0.5044(2)	0.2951(2)	0.2664	0.5065	0.2957
Si2	0.2560(3)	0.8392(2)	0.2946(2)	0.2674	0.8401	0.2957

Notes: Neutron Diffraction values are from the work of Gatta et al. (2013) and here reported for comparison with theoretical data.

Table 3.3. Experimental and theoretical bond distances (Å) and polyhedral volumes (Å^3)

	Neutron Diffraction	DFT B3LYP		Neutron Diffraction	DFT B3LYP
Si1–O(b)1	1.566(2)	1.6345	Mg2–O(h)	2.026(2)	2.0564
Si1–O(a)2	1.623(2)	1.6331	Mg2–O(h)'	2.030(2)	2.0583
Si1–O(b)3	1.639(2)	1.6346	Mg2–O(a)1	2.085(2)	2.079
Si1–O(b)2	1.631(2)	1.6358	Mg2–O(a)1'	2.090(2)	2.0819
<Si1–O>	1.6148	1.6345	Mg2–O(a)2	2.095(2)	2.0773
V($Si1O_4$)	2.16	2.240	Mg2–O(a)2'	2.102(2)	2.0808
			<Mg2–O>	2.071	2.0808
Si2–O(b)2	1.637(2)	1.6354	V($Mg2O_6$)	11.71	11.720
Si2–O(a)1	1.643(2)	1.6334			
Si2–O(b)3	1.613(2)	1.6337	O(h)–H	0.990(1)	0.9593
Si2–O(b)1	1.592(2)	1.6351	O(h)---O(b)1	3.360(2)	3.2859
<Si2-O>	1.621	1.6344	H---O(b)1	2.780(3)	2.7312
V($Si2O_4$)	2.19	2.241	O(h)–H---O(b)1	118.0(1)	117.4724
			O(h)---O(b)2	3.382(2)	3.3111
Mg1–O(h)	2.060(2)	2.0564	H---O(b)2	2.831(2)	2.7591
Mg1–O(a)2	2.094(2)	2.0843	O(h)–H---O(b)2	115.8(1)	117.0455
Mg1–O(a)1	2.080(2)	2.0815	O(h)---O(b)3	3.575(3)	3.6091
<Mg1–O>	2.078	2.0815	H---O(b)3	2.825(3)	2.7407
V($Mg1O_6$)	11.82	11.752	O2–H---O(b)3	116.4(1)	117.328

Neutron Diffraction values are from the work of Gatta et al. (2013) and here reported for comparison with theoretical data.

Talc compression and expansion

The description of the compressional behaviour of a solid phase within the periodic boundary conditions requires a series of steps, which were proposed firstly by Perger (2010) and here summarised. The first step is considering different unit-cell volumes of the crystal structure. A good accuracy of the whole method can be achieved by taking into account both smaller (compression) and larger (expansion) volumes than the equilibrium one. Then, the second step requires an optimization of the internal coordinates and lattice parameters for each selected volume, keeping that unit-cell volume constant, *i.e.* using the keyword CVOLOPT in CRYSTAL09 (Dovesi et al., 2009). Differently from the procedure known as "*symmetry preserving, variable cell-shape structure relaxation*" (Kiefer et al., 2001; Ottonello et al., 2009), we conducted the calculations removing the symmetry of the system (space group $P\bar{1} \rightarrow P1$). This approach allows the structure to freely relax and is used to find any possible drastic variation in the unit-cell due to high pressures. In our simulations the talc structure was optimized at twenty different volumes between 470.8 to 397.5 Å^3. Volumes and lattice parameters are reported in Table 3.4.

From the geometry optimization at constant volume V (Å^3) we calculated the total energy E of talc at that volume. We found that the relationship between the talc energy E at different volumes V, i.e.

E(V) curve, is well described by a 3rd-order polynomial equation as shown in Figure 3.2a. The static pressure (P_{st}) values for each selected volume can be obtained from the first derivative of the E(V) function, according to:

$$P_{st} = -\left(\frac{\partial E}{\partial V}\right)_{T=0} \tag{3.2}$$

A graphical representation of the $P_{st}(V)$ trend is shown in Figure 2b. These pressure values are labelled in Table 3.4 as P_{st} because atomic vibrational energy was not taken into account. This is also called "athermal" condition, because it is like studying "frozen" atoms at absolute zero (0 K).

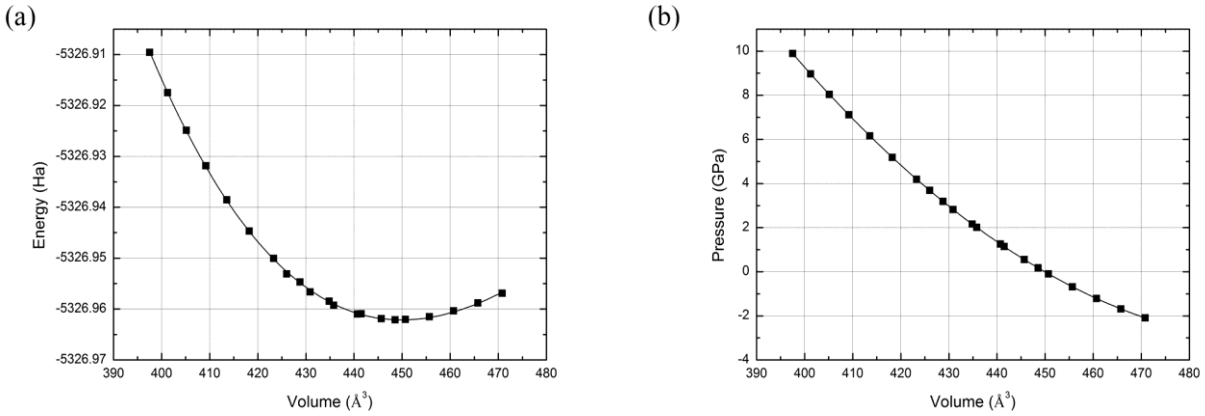

Figure 3.2. (a) Energy/Volume and (b) Pressure/Volume plots for talc cell compression and expansion.

In order to obtain the talc bulk modulus at 0 K (K_0), its pressure first derivative (K') and the volume at zero pressure (V_0), we fitted the volume *vs.* P_{st} data using a third-order finite strain isothermal Birch-Murnaghan Equation of State (III-BM EOS) (Birch, 1947). The III-BM EOS is defined as:

$$P_{st} = -\left(\frac{\partial E}{\partial V}\right)_{T=0} = \frac{3}{2}K_0\left[\eta^{-7/3} - \eta^{-5/3}\right]\left\{1 - \frac{3}{4}\left(4 - K'\right)\left(\eta^{-2/3} - 1\right)\right\} + P_0 \tag{3.3}$$

where $\eta = V/V_0$ is a dimensionless parameter called "dilaton" and P_0 is the reference pressure (P_0 = 0.0 GPa). The best fitting procedure was made using the EOS-FIT5.2 software (Angel, 2001), resulting in the refined elastic parameters: K_0 = 56.25 GPa, K' = 5.66 and V_0 = 450.34 Å^3 (R = 1.075%). The pressure values calculated by Eq.(3) are reported in Table 3.4 in the last column and labelled $P_{III\text{-}BM}$.

Figure 3.3 reports the evolution of talc volume and lattice parameters with pressure. The calculated trend is monotonic. It is clear from the graph in Figure 3b that the cell was deformed with a strong anisotropic behaviour, with *a* and *b* cell parameters only slightly affected by pressure, while the *c* one exhibited a great variation. In order to describe the observed anisotropy, the axial bulk moduli were calculated with a III-BM EOS fit of the lattice parameters values at different pressures. The obtained refined data for the *a*, *b* and *c* axis were, respectively: a_0 = 5.292 Å, $K_0(a)$ = 94.61 GPa and $K'(a)$ =

5.90; b_0 = 9.175 Å, $K_0(b)$ = 101.50 GPa and $K'(b)$ = 4.52; c_0 = 9.447 Å, $K_0(c)$ = 29.69 GPa and $K'(c)$ = 4.72. The axial compressibilities, described as $\beta = 1/3K_0$, are in ratio β(a): β(b): β(c) = 1.072 : 1.000 : 3.418. This result is not surprising because the covalent bonds in the TOT layers (*a* and *b* directions) are less compressible than interlayer (*c* direction), which is dominated by an interplay between van der Waals (attraction between layers) and Coulomb forces (repulsion between TOT).

Table 3.4. Lattice parameters and pressure values of talc at different volumes

Volume (Å^3)	a (Å)	b (Å)	c (Å)	α (°)	β (°)	γ (°)	P_{st}	$P_{III\text{-}BM}$
397.534	5.1432	8.9242	8.8272	90.2106	101.1328	90.2264	9.890	9.9783
401.264	5.1561	8.9464	8.8647	90.2619	101.0991	90.2380	8.966	8.9913
405.149	5.1687	8.9703	8.9036	90.3097	101.0578	90.2289	8.039	8.0193
409.192	5.1816	8.9929	8.9466	90.3622	101.0251	90.2331	7.113	7.0655
413.556	5.1959	9.0168	8.9936	90.4571	101.0380	90.2192	6.159	6.0977
418.233	5.2101	9.0403	9.0455	90.5326	100.9953	90.2142	5.187	5.1276
423.299	5.2249	9.0666	9.1019	90.6223	100.9672	90.2028	4.194	4.1492
426.014	5.2326	9.0799	9.1345	90.6887	100.9773	90.2039	3.687	3.6541
428.789	5.2404	9.0923	9.1662	90.7277	100.9511	90.1878	3.188	3.1681
430.890	5.2462	9.1021	9.1925	90.7876	100.9693	90.1888	2.822	2.8131
434.835	5.2567	9.1187	9.2400	90.8565	100.9612	90.1683	2.164	2.1754
435.795	5.2593	9.1231	9.2532	90.8937	100.9735	90.1713	2.010	2.0258
440.728	5.2718	9.1428	9.3161	91.0026	100.9846	90.1527	1.252	1.2894
441.518	5.2740	9.1457	9.3245	91.0067	100.9853	90.1453	1.136	1.1763
445.680	5.2836	9.1611	9.3821	91.1130	101.0108	90.1329	0.550	0.602
448.547	*5.2890*	*9.1701*	*9.4159*	*91.0235*	*100.7743*	*90.1225*	*0.171*	*0.2265*
450.667	5.2945	9.1776	9.4525	91.2320	101.0558	90.1121	-0.096	-0.0412
455.678	5.3043	9.1922	9.5270	91.3537	101.1086	90.0918	-0.685	-0.6415
460.705	5.3123	9.2042	9.6079	91.4797	101.1788	90.0726	-1.215	-1.2005
465.750	5.3184	9.2132	9.6954	91.6032	101.2467	90.0550	-1.685	-1.7208
470.807	5.3227	9.2194	9.7911	91.7615	101.3701	90.0402	-2.095	-2.2045

Notes: the static pressure values from both the polynomial fit (P_{st}) and the third-order Birch-Murnaghan fit equation of state are in GPa. Values in italic represent the minimum of the E/V function.

Upon compression, there is a significant variation in the size, shape and orientation of the coordination polyhedral, as shown in the visual representations in Figure 3.4 and 3.5. In general, the TOT thickness varies negligibly with compression (-1.7%), but the TOT – TOT distance shrinks of about 18% at 10 GPa. The increase of pressure produces a volume reduction in both SiO_4 tetrahedra and MgO_6 octahedra of about 2% and 7%, respectively. $\langle$Si-O$\rangle$ bond length is contracted by 0.6% in the 0 to 10 GPa pressure range. The reduction is more evident for the apical oxygen than for the basal ones. This effect produces an increase in the distortion of the tetrahedra, which consequently leads a corrugation of the T layer with non-coplanar basal oxygen atoms (see Figure 3.5). The same contraction

was observed for the $\langle$Mg-O$\rangle$ bond length (2.4%) at 10.0 GPa, but, differently from the SiO_4 tetrahedra, the distortion of the octahedra is reduced.

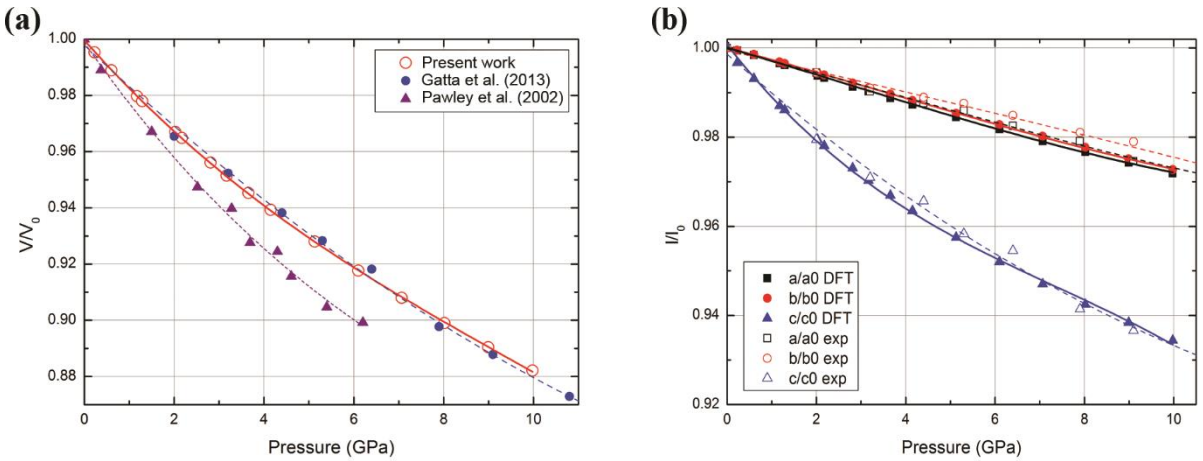

Figure 3.3. Relative compression of volume (a) and lattice parameters (b) of talc over the range 0-10 GPa. Values from experimental results have been reported for comparison. Lattice relative compression in figure 3b are related to the work of Gatta et al. (2013).

Another structural response to the compression is the increase of the tetrahedral rotation angle, which is defined as $\alpha = 1/2\left(\sum_{i=1}^{6}\left|\phi_i - 120°\right|\Big/6\right)$, where ϕ_i is the angle described by triples of basal oxygen atoms (Bailey, 1988). The predicted value of α varies from 7.8° at 0 GPa to 15.6° at 10 GPa (see Figures 3.4 and 3.5).

Worth to be noted that the O-H bond length do not vary in the pressure range investigated (0.959 Å at 0 GPa and 0.958 Å at 10 GPa) and it remains parallel to the [001] direction.

Calculation of elastic constants

Within periodic *ab initio* methods, the evaluation of the elastic constants is accomplished by using stress-strain relationships based on total energy calculations. In particular, the SOEC are related to the total energy of the crystal through a Taylor expansion in terms of the strain components truncated to the second order:

$$E(V,\varepsilon) = E(V_0) + V\sum_{\alpha}\sigma_{\alpha}\varepsilon_{\alpha} + \frac{V}{2}\sum_{\alpha\beta}C_{\alpha\beta}\varepsilon_{\alpha}\varepsilon_{\beta} + \ldots, \qquad (3.4)$$

where σ is the stress, ε is the strain, C are the second order elastic constants and V_0 is the volume at equilibrium. Note that the Voigt's notation (Nye, 1957) was used ($\alpha, \beta = 1,2,3,...6$). The adiabatic SOEC are related to the strain second derivatives of the total energy E according to:

$$C_{\alpha\beta} = \frac{1}{V}\frac{\partial^2 E}{\partial\varepsilon_\alpha \partial\varepsilon_\beta}\bigg|_0 \qquad (3.5)$$

Their discrete values may be evaluated by imposing a certain amount of strain ε along the crystallographic direction corresponding to the component of the dynamical matrix. The evaluation of elastic constants for an arbitrary crystal then requires to accurately calculate derivatives of the total energy as a function of crystal deformation. To ease obtaining the different energy vs strain curves and the SOEC, a fully automated numerical procedure was implemented in the CRYSTAL code, under the keyword ELASTCON. Briefly, the proposed algorithm uses the optimized structure and its space group to determine the necessary deformations in order to calculate the various elastic constants. For further details on the ELASTCON method we suggest the reader to refer to the work of Perger et al. (2009).

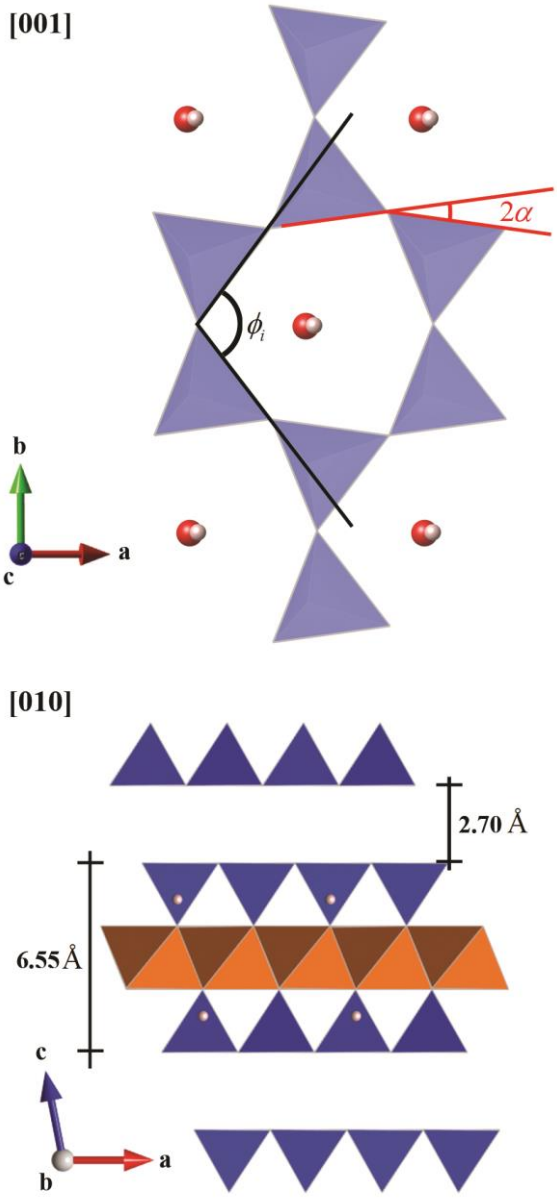

Figure 3.4. Theoretical structure of talc at 0 GPa, viewed from the [001] and [010] directions. TOT thickness is in Angstrom (Å).

The algorithm was successfully used in the calculation of the thermo-chemical and thermo-physical properties of $BaTiO_3$ and rutile TiO_2 (Narejo and Perger, 2010, 2011; Ottonello et al., 2010). In our work we chose to run the calculation with three points of displacement and a step of 0.010 Å, the default figure given by the code.

We report in Table 3.5 the results of the talc second order elastic constant tensor C, calculated at zero pressure and in athermal conditions (values are in GPa) together with those of Mainprice and coworkers (2008). The comparison is interesting because they used a different theoretical approach as mentionjed in the introduction.

The bulk (K) and shear (μ) moduli are related to the elements of the elastic constant tensor. For any crystal system, the bounds for bulk modulus (upper =K_V; lower = K_R) and shear modulus (upper = μ_V; lower = μ_R) are given by the Voigt and Reuss equations (Nye, 1957):

$$K_V = (1/9)\left[C_{11}+C_{22}+C_{33}+2\left(C_{12}+C_{13}+C_{23}\right)\right] = 78.95\,GPa \tag{3.6}$$

$$K_R = \left[S_{11}+S_{22}+S_{33}+2\left(S_{12}+S_{13}+S_{23}\right)\right]^{-1} = 55.30\,GPa \tag{3.7}$$

$$\mu_V = (1/15)\left[C_{11}+C_{22}+C_{33}+3\left(C_{44}+C_{55}+C_{66}\right)-\left(C_{12}+C_{13}+C_{23}\right)\right] = 58.52\,GPa \tag{3.8}$$

$$\mu_R = \frac{15}{4\left[S_{11}+S_{22}+S_{33}-\left(S_{12}+S_{13}+S_{23}\right)\right]+3\left(S_{44}+S_{55}+S_{66}\right)} = 20.92\,GPa \tag{3.9}$$

where $[S]=[C]^{-1}$, the compliance tensor, is the inverse of SOEC tensor C.

There is a significant separation between the upper and lower bounds for both bulk and shear moduli, which is typical for an anisotropic crystal such as talc. However, the bulk modulus K_0 obtained with the equation of state in the previous section is very close to that from the lower bound (Reuss equation). It is known that both bulk and shear moduli fall between the two bounds, according to the Voigt -Reuss-Hill averaging method (Hill, 1952):

$$\bar{K}_{VRH} = (1/2)\left(K_V + K_R\right) = 67.12\,GPa \tag{3.10}$$

$$\bar{\mu}_{VRH} = (1/2)\left(\mu_V + \mu_R\right) = 39.72\,GPa \tag{3.11}$$

where $\bar{K}_{VRH}$ and $\bar{\mu}_{VRH}$ are the Voigt-Reuss-Hill averages of the bulk and shear moduli, respectively.

There is a fairly good accordance between K_0 and $\bar{K}_{VRH}$, which means that there is a well self-consistency of the proposed simulation methods, but the isotropic calculation of the bulk and shear moduli for an anisotropic crystal suffers from an adequate consideration of all 21 independent elastic constants. With the obtained values it is possible to estimate the Young's modulus, E, and Poisson's ratio, ν_p, using the following expressions:

$$E = \frac{9K_0\bar{\mu}_{VRH}}{3K_0+\bar{\mu}_{VRH}} = 99.53\,GPa \tag{3.12}$$

$$\nu_p = \frac{3K_0-2\bar{\mu}_{VRH}}{2\left(3K_0+\bar{\mu}_{VRH}\right)} = 0.25. \tag{3.13}$$

The isotropic Voigt-Reuss-Hill average gives the mean shear and longitudinal wave velocities for hypothetical talc aggregates with random crystallographic preferred orientation, as

$$\bar{v}_s = \sqrt{(\bar{\mu}_{VRH}/\rho)} = 3.770\,{}^{km}/_{s} \quad (3.14)$$

$$\bar{v}_L = \sqrt{\frac{4K_0 + 3\bar{\mu}_{VRH}}{3\rho}} = 6.407\,{}^{km}/_{s} \quad (3.15)$$

where ρ is the density of the crystal. The v_L/v_s ratio is then 1.7. To understand the evolution of the seismic anisotropy of talc as a function of pressure, the seismic velocities for a given propagation direction are calculated from the SOEC elements and the density at each pressure using Christoffel's equation (Ottonello et al., 2010). In Table 3.6 the shear (v_{s1}, v_{s2}) and longitudinal (v_L) wave velocities for each relevant wave vector are reported.

Table 3.5 Calculated elastic constants, bulk (K) and shear (μ) moduli in GPa and mean shear and longitudinal wave velocities (km/s) at 0 GPa

Elastic Constants	GTO/B3LYP-D*	PW/PBE
C_{11}	242.156	219.83
C_{12}	57.944	59.66
C_{13}	4.766	-4.82
C_{14}	6.017	-0.82
C_{15}	-0.509	-33.87
C_{16}	2.066	-1.04
C_{22}	240.712	216.38
C_{23}	10.793	-3.67
C_{24}	5.256	1.79
C_{25}	-1.03	-16.51
C_{26}	1.613	-0.62
C_{33}	80.641	48.89
C_{34}	1.714	4.12
C_{35}	-0.337	-15.52
C_{36}	-5.344	-3.59
C_{44}	24.208	26.54
C_{45}	-11.015	-3.6
C_{46}	0.566	-6.41
C_{55}	12.817	22.85
C_{56}	1.106	-1.67
C_{66}	92.238	78.29
K_V	78.95	65.27
K_R	55.3	18.89
K_{VRH}	67.12	42.08
μ_V	58.52	54.46
μ_R	20.92	26.42
μ_{VRH}	39.72	40.44
v_s	3.770	3.81
v_l	6.407	5.87

PW/PBE data are relative to the work of Mainprice et al. (2008) obtained using plane wave (PW) basis set, here reported for comparison

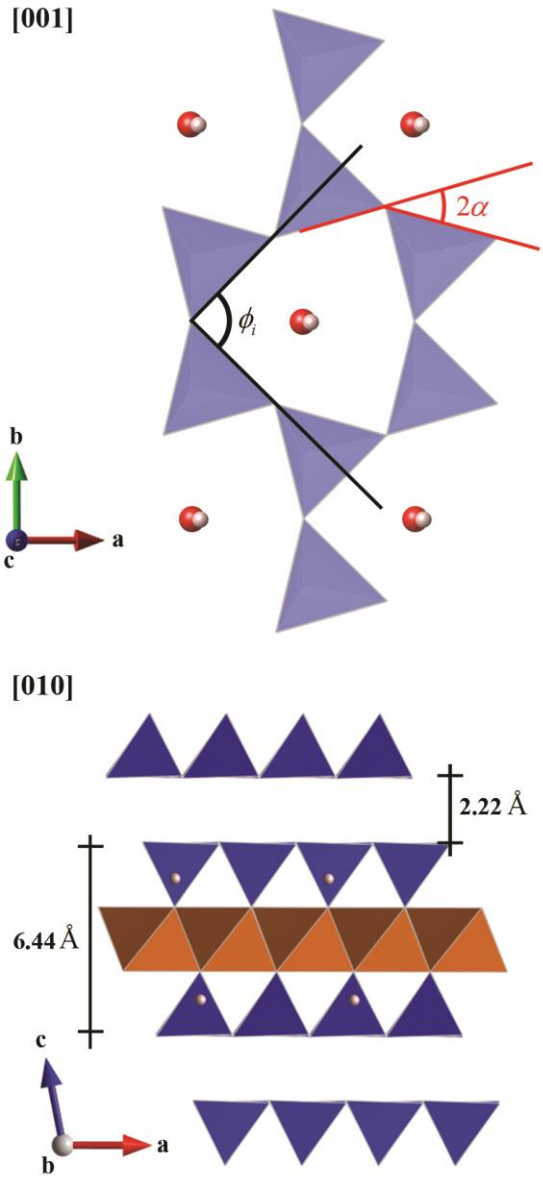

Figure 3.5. Theoretical structure of talc at 10 GPa, viewed from the [001] and [010] directions. TOT thickness is in Angstrom (Å).

Table 3.6. Calculated talc seismic wave velocities along different wave vectors

Wave vector	v_L (km/s)	v_{s1} (km/s)	v_{s2} (km/s)
[001]	1.478	3.323	5.373
[010]	5.744	9.282	2.935
[100]	9.308	5.744	2.14
[110]	9.375	5.729	1.631
[101]	6.763	4.654	3.904
[011]	3.955	7.16	4.573
[111]	5.049	7.807	3.381

3.4 Discussion and Conclusions

Regarding talc crystallography, the results provided in this work are in very good agreement with the experimental values obtained by synchrotron XRD and Neutron Diffraction methods on single crystal (Gatta et al., 2013; Perdikatsis and Burzlaff, 1981). There is a slight systematic contraction of the calculated talc unit-cell. This is a typical issue of the DFT approach, which causes a general volume reduction, albeit the B3LYP functional moderate this effect. The obtained atomic positions match well those reported in literature, with a maximum difference of about 4%. In particular, our theoretical data confirm the hydrogen atom position within talc unit-cell observed by Neutron Diffraction experiments. The simulated internal geometry in comparison with the detailed Neutron Diffraction data shown a slight expansion of the mean bond lengths and polyhedron volumes by 0.7% and 1.4%, respectively. Another small difference is the rotation angle α of the six-membered ring of tetrahedral, which is about 4° in experimental observations, while is $\alpha = 7.8°$ in our simulations. Worth noting that our end-member model has no defects in the structure.

The observed high anisotropic and monotonic compressional behaviour of talc is a general result obtained by both theoretical and experimental settings (Stixrude, 2002; Mainprice et al., 2008; Pawley et al., 2002; Pawley et al., 1995; Gatta et al., 2013). Our calculated talc equation of state is very close to that experimentally obtained by Gatta et al. (2013) on single-crystal experiments with the diamond anvil cell and Ne as hydrostatic pressure transmitting medium. In particular, our theoretical bulk modulus and axial compressibility are K_{T0} = 56.25 GPa, $K_{T0}(a)$ = 94.61, $K_{T0}(b)$ = 101.50 GPa and $K_{T0}(c)$ = 29.69 GPa, in very good agreement with the experimental data (K_{T0} = 57(3) GPa, $K_{T0}(a)$ = 95(13), $K_{T0}(b)$ = 99(5) GPa and $K_{T0}(c)$ = 31(4) GPa,). Both the computed and the experimental data show a talc mineral less compressible than the samples analysed with a multi anvil apparatus (Pawley et al., 2002). This difference could be due to some fraction of deviatoric stress, which has been found to be a problem at low temperature in other EOS measurements made in multi-anvil apparatus. This effect, induced by pressurization at low temperature, could be potentially a serious problem when the sample compressibility is strongly anisotropic, which is the case of layered silicates. In this case, it might be expected that the compression shows less anisotropy than predicted. The deviatoric stress could be removed by heating to ~600 K as suggested by (Weidner et al., 1992), but Pawley et al.

(2002) did not adopt this procedure for talc analysis. *In situ* powder experiments performed by Gleason et al. (2008) with water as P-transmitting media up to 11 GPa gave K_{T0} = 55(5) GPa and K' = 14(2). The anomalously high K' value could be due to several reasons: the non-hydrostatic regime of the experiments, the preferred orientations of platy crystallites in the compression chamber of the diamond anvil cell, the hydrophobicity of talc (Gleason et al., 2008) and the grinding-induced strain related to the powder sample preparation (Gatta et al., 2013). Furthermore, Gleason et al. (2008) suggested a talc – talc-II phase transformation at pressure of about 4-6 GPa and 298 K. Our theoretical data does not support this observation.

Compared to previous theoretical results, we noted a good accordance with the description of the talc structure at atomic level, but also a substantial difference in the compressional behaviour. The value of the athermal K_{T0} and K' constants obtained with a fourth-order Birch-Murnaghan fit were 37.8 GPa and 13.6 in the studies of Stixrude (2002) and 32.1 GPa 13.5 in the analysis of Mainprice and co-workers (2008). While the K_{T0} values were in quite well agreement with the experimental data of Pawley et al. (2002), they are discordant with our theoretical results and the recent single-crystal neutron diffraction data (Gatta et al., 2013). Furthermore, in contrast with the results obtained by Stixrude (2002), we did not observe a spinodal instability when we applied a tensile stress to the unit-cell (volume expansion of about 4.9%). In particular, the *b* lattice parameter do not shrink with the *c*-axis elongation, an issue that occurs when there is no interaction between TOT layers. Gatta et al. (2013) did not observe any spinodal instability, in agreement with our results.

These deviations are due to the adopted computational methods. In the previous theoretical works plane waves (PW) basis set was used for atoms descriptions, while in our work Gaussian-type orbitals (GTO) basis set was adopted. While PW provides accurate description of solid phases, it limits the adoption of hybrid functionals, such as B3LYP, because of their prohibitive computational costs (Ulian et al., 2013a). Stixrude (2002) adopted standard local-density approximation (LDA) DFT functional, which under static conditions under-estimated the talc volume by 5%. By using a generalized gradient approximation (GGA) functional the author observed a volume expansion in the equation of state of 9%. The overbinding effect of the LDA functional, which causes the volume contraction, and the high repulsive core-valence exchange in GGA, which increases the bulk lattice constants are well known. Mainprice and co-workers (2008) used PW basis set and PW91-GGA functional (Perdew and Wang, 1992) to calculate the talc equation of state and elastic constants. Their results are consistent with the use of a GGA functional, because it softens bonds and bulk moduli. Probably, another source of uncertainty was the use of a small kinetic energy cutoff (400 eV) used to optimize the geometry of talc under variable cell relaxation.

However, the lack of an adequate description of the dispersive forces, which held the layers together and was not available for solid phases simulations until late 2008, is probably the most critical point of previous simulations. In fact, while *a* and *b* parameters were quite accurately predicted, the **c**-axis description suffered both at zero pressure and under compression. This observation is further confirmed considering the elastic constants (see Table 3.5). C_{11} and C_{22} are very similar to the results of Mainprice et al. (2008), but the constant related to the **c**-axis (C_{33}) obtained in the present work is two times the one obtained without the correction for dispersive forces. The spinodal instability observed in the work of Stixrude (2002) may be due to the lack of the van der Waals contribution to the total energy of the mineral.

In the pressure range explored (0 – 10 GPa), we did not noticed any clear evidence of a talc-I to talc-II phase transformation (Gleason et al., 2008), high-pressure metastability or amorphization, despite our analysis excluded any symmetry constrain to the structure. Our observation is in accordance to synchrotron diffraction results of Gatta and co-workers (2013).

REFERENCES CITED

Angel, R.J. (2001) EOS-FIT6.0. Computer Program (http://www.rossangel.com).

Bailey, S.W. (1988) Introduction, Hydrous Phyllosilicates. Reviews in Mineralogy & Geochemistry, 19, 1-8.

Becke, A.D. (1993) Density-Functional Thermochemistry .3. The Role of Exact Exchange. Journal of Chemical Physics, 98(7), 5648-5652.

Birch, F. (1947) Finite elastic strain of cubic crystal. Physical Review, 71, 809-824.

Broyden, C.G. (1970a) The convergence of a class of double-rank minimization algorithms 1. General considerations. IMA Journal of Applied Mathematics (Institute of Mathematics and Its Applications), 6(1), 76-90.

-. (1970b) The convergence of a class of double-rank minimization algorithms: 2. The new algorithm. IMA Journal of Applied Mathematics (Institute of Mathematics and Its Applications), 6(3), 222-231.

Butylina, S., Hyvarinen, M., and Karki, T. (2012) Accelerated weathering of wood-polypropylene composites containing minerals. Composites Part A-Applied Science and Manufacturing, 43(11), 2087-2094.

Castillo, L.A., Barbosa, S.E., and Capiati, N.J. (2012) Influence of talc genesis and particle surface on the crystallization kinetics of polypropylene/talc composites. Journal of Applied Polymer Science, 126(5), 1763-1772.

Civalleri, B., Casassa, S., Garrone, E., Pisani, C., and Ugliengo, P. (1999) Quantum mechanical ab initio characterization of a simple periodic model of the silica surface. Journal of Physical Chemistry B, 103(12), 2165-2171.

Civalleri, B., Zicovich-Wilson, C.M., Valenzano, L., and Ugliengo, P. (2008) B3LYP augmented with an empirical dispersion term (B3LYP-D*) as applied to molecular crystals. Crystengcomm, 10(4), 405-410.

D'Haese, M., Goderis, B., and Van Puyvelde, P. (2011) The Influence of Calcium-Stearate-Coated Calcium Carbonate and Talc on the Quiescent and Flow-Induced Crystallization of Isotactic Poly(propylene). Macromolecular Materials and Engineering, 296(7), 603-616.

Dellisanti, F., Minguzzi, V., and Valdrè, G. (2011) Mechanical and thermal properties of a nanopowder talc compound produced by controlled ball milling. Journal of Nanoparticle Research, 13(11), 5919-5926.

Dellisanti, F., and Valdrè, G. (2010) On the high-temperature structural behaviour of talc (Mg3Si4O10(OH)2) to 1600 degrees C: Effect of mechanical deformation and strain. Philosophical Magazine, 90(17-18), 2443-2457.

Dellisanti, F., Valdrè, G., and Mondonico, M. (2009) Changes of the main physical and technological properties of talc due to mechanical strain. Applied Clay Science, 42(3-4), 398-404.

Dovesi, R., Saunders, V.R., Roetti, C., Orlando, R., Zicovich-Wilson, C.M., Pascale, F., Civalleri, B., Doll, K., Harrison, N.M., Bush, I.J., D'Arco, P., and Llunell, M. (2009) CRYSTAL09 User's Manual. University of Torino, Torino.

Evans, B.W., and Guggenheim, S. (1988) Talc, Pyrophyllite, and Related Minerals. Reviews in Mineralogy, 19, 225-294.
Fletcher, R. (1970) A new approach to variable metric algorithms. The Computer Journal, 13(3), 317-322.
Gatta, G.D., Merlini, M., Valdre, G., Liermann, H.-P., Nenert, G., Rothkirch, A., Kahlenberg, V., and Pavese, A. (2013) On the crystal structure and compressional behavior of talc: a mineral of interest in petrology and material science. Physics and Chemistry of Minerals, 40(2), 145-156.
Gatti, C., Saunders, V.R., and Roetti, C. (1994) Crystal-field effects on the topological properties of the electron-density in molecular-crystals - the case of urea. Journal of Chemical Physics, 101(12), 10686-10696.
Gleason, A.E., Parry, S.A., Pawley, A.R., Jeanloz, R., and Clark, S.M. (2008) Pressure-temperature studies of talc plus water using X-ray diffraction. American Mineralogist, 93(7), 1043-1050.
Goldfarb, D. (1970) A family of variable-metric methods derived by variational means. Mathematics of Computation, 24, 23-26.
Grimme, S. (2006) Semiempirical GGA-type density functional constructed with a long-range dispersion correction. Journal of Computational Chemistry, 27(15), 1787-1799.
Gruner, J.W. (1934) The crystal structures of talc and pyrophyllite. Zeitschrift Fur Kristallographie, 88, 412-419.
Hill, R. (1952) The elastic behaviour of a crystalline aggregate. Proceedings of the Physical Society, London, Section A, 65, 349-354.
Kiefer, B., Stixrude, L., Hafner, J., and Kresse, G. (2001) Structure and elasticity of wadsleyite at high pressures. American Mineralogist, 86(11-12), 1387-1395.
Larentzos, J.P., Greathouse, J.A., and Cygan, R.T. (2007) An ab initio and classical molecular dynamics investigation of the structural and vibrational properties of talc and pyrophyllite. Journal of Physical Chemistry C, 111(34), 12752-12759.
Lee, C.T., Yang, W.T., and Parr, R.G. (1988) Development of the Colle-Salvetti Correlation-Energy Formula into a Functional of the Electron-Density. Physical Review B, 37(2), 785-789.
Mainprice, D., Le Page, Y., Rodgers, J., and Jouanna, P. (2008) Ab initio elastic properties of talc from 0 to 12 GPa: Interpretation of seismic velocities at mantle pressures and prediction of auxetic behaviour at low pressure. Earth and Planetary Science Letters, 274(3-4), 327-338.
Melekhova, E., Schmidt, M.W., Ulmer, P., and Guggenbuhl, E. (2006) The reaction talc plus forsterite = enstatite plus H2O revisited: Application of conventional and novel experimental techniques and derivation of revised thermodynamic properties. American Mineralogist, 91(7), 1081-1088.
Mirabedini, S.M., Jamali, S.S., Haghayegh, M., Sharifi, M., Mirabedini, A.S., and Hashemi-Nasab, R. (2012) Application of mixture experimental design to optimize formulation and performance of thermoplastic road markings. Progress in Organic Coatings, 75(4), 549-559.
Momma, K., and Izumi, F. (2008) VESTA: a three-dimensional visualization system for electronic and structural analysis. Journal of Applied Crystallography, 41, 653-658.
Murnaghan, F.D. (1937) Finite deformations of an elastic solid. American Journal of Mathematics, 49, 235-260.
Mysen, B.O., Ulmer, P., Konzett, J., and Schmidt, M.W. (1998) The upper mantle near convergent plate boundaries. Ultrahigh-Pressure Mineralogy, 37, 97-138.
Nada, R., Nicholas, J.B., McCarthy, M.I., and Hess, A.C. (1996) Basis sets for ab initio periodic Hartree-Fock studies of zeolite/adsorbate interactions: He, Ne, and Ar in silica sodalite. International Journal of Quantum Chemistry, 60(4), 809-820.
Narejo, G., and Perger, W.F. (2010) First-principles computation of second-order elastic constants and equations of state for tetragonal BaTiO3. Chemical Physics Letters, 493(4-6), 263-268.
-. (2011) First principle computations of second-order elastic constants (SOEC) and equations of state of rutile TiO_2. Physics Research International, 2011, 7 pages.
Nye, J.F. (1957) Physical properties of crystals. Oxford University Press, Oxford.
Ottonello, G., Civalleri, B., Ganguly, J., Perger, W.F., Belmonte, D., and Zuccolini, M.V. (2010) Thermo-chemical and thermo-physical properties of the high-pressure phase anhydrous B ($Mg_{14}Si_5O_{24}$): An ab-initio all-electron investigation. American Mineralogist, 95(4), 563-573.
Ottonello, G., Civalleri, B., Ganguly, J., Zuccolini, M.V., and Noel, Y. (2009) Thermophysical properties of the alpha-beta-gamma polymorphs of Mg2SiO4: a computational study. Physics and Chemistry of Minerals, 36(2), 87-106.
Pawley, A.R., Clark, S.M., and Chinnery, N.J. (2002) Equation of state measurements of chlorite, pyrophyllite, and talc. American Mineralogist, 87(8-9), 1172-1182.
Pawley, A.R., Redfern, S.A.T., and Wood, B.J. (1995) Thermal expansivities and compressibilities of hydrous phases in the system MgO-SiO2-H2O: Talc, phase A and 10-angstrom phase. Contributions to Mineralogy and Petrology, 122(3), 301-307.
Perdikatsis, B., and Burzlaff, H. (1981) Structural refinement of talc $Mg_3(OH)Si_4O_{10}$. Zeitschrift Fur Kristallographie, 156(3-4), 177-186.

Perger, W.F. (2010) First-Principles Calculation of Second-Order Elastic Constants and Equations of State for Lithium Azide, LiN3, and Lead Azide, Pb(N-3)(2). International Journal of Quantum Chemistry, 110(10), 1916-1922.

Perger, W.F., Criswell, J., Civalleri, B., and Dovesi, R. (2009) Ab-initio calculation of elastic constants of crystalline systems with the CRYSTAL code. Computer Physics Communications, 180(10), 1753-1759.

Prencipe, M., Pascale, F., Zicovich-Wilson, C.M., Saunders, V.R., Orlando, R., and Dovesi, R. (2004) The vibrational spectrum of calcite (CaCO3): an ab initio quantum-mechanical calculation. Physics and Chemistry of Minerals, 31(8), 559-564.

Rayner, J.H., and Brown, G. (1973) The crystal structure of talc. Clays and Clay Minerals, 21, 103-114.

Shanno, D.F. (1970) Conditioning of quasi-Newton methods for function minimization. Mathematics of Computation, 24, 647-656.

Stixrude, L. (2002) Talc under tension and compression: Spinodal instability, elasticity, and structure. Journal of Geophysical Research-Solid Earth, 107(B12).

Ugliengo, P., Viterbo, D., and Chiari, G. (1993) MOLDRAW: molecular graphic on a personal computer. Zeitschrift Fur Kristallographie, 207, 9-23.

Ulian, G., Tosoni, S., and Valdrè, G. (2013a) Comparison between Gaussian-type Orbitals and Plane Wave *ab initio* DFT modeling of layered silicates: Talc mineral as model system. Journal of Chemical Physics, 139(20), 204101.

Ulian, G., Valdre, G., Corno, M., and Ugliengo, P. (2013b) Periodic ab initio bulk investigation of hydroxylapatite and type A carbonated apatite with both pseudopotential and all-electron basis sets for calcium atoms. American Mineralogist, 98(2-3), 410-416.

Ulian, G., Valdrè, G., Corno, M., and Ugliengo, P. (2013c) The vibrational features of hydroxylapatite and type A carbonated apatite: a first principle contribution. American Mineralogist, 98(4), 752-759.

Ulmer, P., and Trommsdorff, V. (1995) Serpentine Stability to Mantle Depths and Subduction-Related Magmatism. Science, 268(5212), 858-861.

Valenzano, L., Torres, F.J., Klaus, D., Pascale, F., Zicovich-Wilson, C.M., and Dovesi, R. (2006) Ab initio study of the vibrational spectrum and related properties of crystalline compounds; the case of CaCO3 calcite. Zeitschrift Fur Physikalische Chemie-International Journal of Research in Physical Chemistry & Chemical Physics, 220(7), 893-912.

Weidner, D.J., Vaughan, M.T., Ko, J., Wang, Y., Leinenweber, K., Liu, X., Yeganeh-Haeri, A., Pacalo, R.E., and Zhao, Y. (1992) Large volume high pressure research using the wiggler port at NSLS. High Pressure Research, 8(5-6), 617-623.

- This page was left blank -

CHAPTER 4 – Density Functional study on the thermo-physical and thermo-chemical properties of Talc [$Mg_3Si_4O_{10}(OH)_2$].[3]

Abstract

Talc is very important in mineralogy, petrology and geophysics as a hydrous phase which can recycle water into the Earth's mantle and in industrial applications. In both fields, the thermodynamic properties of this mineral are essential. However, very few works have been presented to fully characterize the thermodynamic properties of this mineral phase, especially at atomic-scale.

Starting from a previous work, we computed with the hybrid DFT/B3LYP density functional method and an all-electron Gaussian-type orbital basis set the *ab initio* thermo-chemical and thermo-physical properties of talc. The results of this kind of analysis can be adopted in the study of the thermodynamic properties of solid phases at physical conditions that are difficult to obtain in experimental procedures, especially controlled high temperatures.

4.1 Introduction

Geologically, talc plays and important role in the transport and recycling of water to the Earth's mantle because of its water content of about 5 wt. % (Mysen et al., 1998). The presence of H_2O in the mantle, even in small amounts, could trigger partial melting and magma generation and affect the seismic/rheological properties of fluids or minerals (Pawley et al., 1995). In ceramic and polymer industries, talc is one of the most appreciated mineral due to its low coefficient of friction, platyness, chemical inertness, affinity for organic chemicals and hydrophobicity. Talc mineral is commonly used in co-polymers with tailored hardness, chemical activity and other properties (Butylina et al., 2012; Castillo et al., 2012; D'Haese et al., 2011; Mirabedini et al., 2012). For this reason, Dellisanti and co-workers (Dellisanti et al., 2011; Dellisanti and Valdrè, 2010; Dellisanti et al., 2009) conducted a series of experiments to investigate talc thermophysical and thermochemical behavior after compaction and shear.

In our previous works we modelled the structure (Ulian et al., 2013a) and the mechanical behavior (Ulian et al., 2013b) of talc in athermal conditions (T = 0 K). The theoretical data were in good agreement with very recent results obtained by X-Ray and Neutron Diffraction techniques (Gatta et al., 2013). From the mineralogical point of view, talc is the product metamorphism or hydrothermal

[3] This chapter consists of a paper by Ulian G. and Valdrè G., "Density Functional study on the thermo-physical and thermo-chemical properties of Talc [$Mg_3Si_4O_{10}(OH)_2$]", in preparation for *Physics and Chemistry of Minerals*.

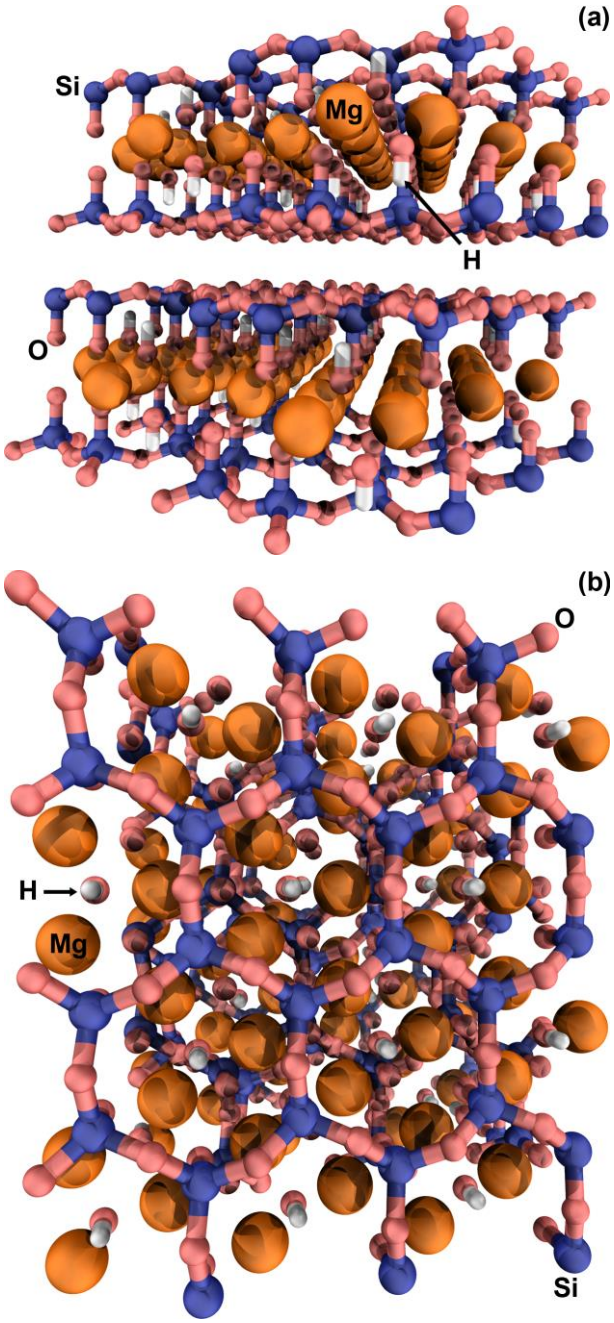

Figure 1. Talc model seen (a) from [110] and (b) from [001] directions. Blue tetrahedrons are related to SiO_4 groups and Orange octahedrons to $MgO_4(OH)_2$ ones. White circles are associated to hydrogen atoms.

alteration of ultramafic rocks (Evans and Guggenheim, 1988). This 2:1 trioctahedral mineral is composed by T-O-T layers, where the "O" is an Mg-octahedral (brucite-like) sheet sandwiched between two Si-tetrahedral sheets ("T"). Van der Waals forces are responsible of the adhesion between charge-neutral T-O-T layers talc slabs (Larentzos et al., 2007; Ulian et al., 2013a). A schematic model can be seen in Figure 4.1.

We did not include the thermal effects on the talc mechanical properties in our previous simulations because of limited publishing space and clearness of the text. Experimental equation of state data are obtained at specific temperature values, usually T = 298.15 K. In the case of talc, this is the operational temperature in the work of Gatta et al. (2013). To our knowledge, there is only one theoretical work (Stixrude, 2002) where the temperature variable on the talc mineral properties was considered. In that Density Functional Theory (DFT) simulation the author used plane waves basis set and local density approximation (LDA) functional. However, the influence of van der Waals forces was not considered because the correction to the DFT energy for weak interactions was not available at that time. We have shown in another work (Ulian et al., 2013a) that Gaussian-type orbitals (GTO) basis sets provide better energetic results than plane waves ones and that the dispersive forces may dramatically affect the talc mechanical properties. These observations are reflected in the simulations of the equation of state of the mineral: in fact, in the work of Stixrude (2002) the talc *V(P)* curve is slightly underestimated and the calculated athermal bulk modulus is lower than ours.

At the moment there are not any other works that analyze the elastic properties of talc at different *P-T* conditions. The scope of the present paper is to complete our previous investigation and modelling the thermal contribution. Starting from the athermal behavior in the pressure range 0 – 10 GPa, we included the temperature as variable to provide complete thermomechanical and thermochemical data (heat capacities and entropy). The thermal effects were considered by using the quasi-harmonic approximation (Anderson, 1995), which will be explained in the next section.

For the first time, three-dimensional plots of thermochemical results will be provided, which can be useful to both understand the metamorphic and igneous equilibriums and industrial applications. Thermochemical results will be compared to experimental investigations (Hemingway, 1991; Krupka et al., 1985) made by differential scanning calorimetry.

4.2 Computational details

All calculations have been performed on a Debian (Linux) Cluster with the CRYSTAL09 code (Dovesi et al., 2009), which implements the Hartree–Fock and Kohn–Sham self-consistent field method for the study of periodic systems.

Hamiltonian and computational parameters

The hybrid Becke, three-parameter (Becke, 1993), in combination with the gradient-corrected correlation functional of Lee, Yang, and Parr (Lee et al., 1988) was used for all simulations (B3LYP). The exchange–correlation contribution is calculated over a grid of points and is the result of a numerical integration of the electron density and its gradient. The adopted pruned grid is given by 75 points and 974 angular points and obtained from the Gauss–Legendre quadrature and Lebedev schemes.(Prencipe et al., 2004). The values of the tolerances that control the truncation criteria for the bielectronic Kohn-Sham integrals were set to the default values provided by CRYSTAL09 (Dovesi et al., 2009), but we increased the pseudo-overlap parameter from 12 to 14 to stabilize the self-consistent behaviour during unit-cell deformations. The Hamiltonian matrix has been diagonalized (Monkhorst and Pack, 1976) using a 4×4×4 k-mesh, resulting in 36 reciprocal lattice points (k-points).

Multi-electron wave functions are described by linear combination of crystalline orbitals (CO), expanded in terms of Gaussian-type orbital (GTO) basis sets. The basis sets have been previously optimized ones used by other authors for their investigations similar structures. For all the calculations, magnesium and oxygen have been described by a 8-511d1G and a 8-411d11G basis sets, respectively

(Valenzano et al., 2006), silicon by a 88-31G* (Nada et al., 1996) and hydrogen by a 3-1p1G basis set (Gatti et al., 1994). The chosen hydrogen atom basis set allows accurate calculations of hydrogen atoms in molecular and crystal structures without too high computational costs and it is well balanced with the other atomic basis sets used in talc structure.

Harmonic frequencies at Γ point were calculated with CRYSTAL code. An extensive discussion of the computational conditions and other numerical aspects concerning the calculation of the vibrational frequencies can be found in the literature (Pascale et al., 2004).

One drawback of DFT generalized gradient approximation functionals, including their hybrid forms, is their inadequate description of long-range dispersive (van der Waals) interactions. To overcome this problem, the energy contribution of dispersive forces has been added to the DFT energy according to the semiempirical approach (DFT+D) suggested by Grimme (Grimme, 2006):

$$E_{DISP} = -s_6 \sum_{\mathbf{g}} \sum_{i \neq j} f_{dump}\left(R^6_{ij,\mathbf{g}}\right) \frac{C_6^i C_6^j}{R^6_{ij,\mathbf{g}}}$$

$$f_{dump} = \frac{1}{1 + e^{-d\left(R_{ij,\mathbf{g}}/R_{vdw} - 1\right)}} \qquad (4.1)$$

The summation over all atom pairs *ij* and **g** lattice vectors excludes the self- interaction contribution ($i = j$) for every **g**. The parameters C_6^i represent the dispersion coefficient for the atom *i*, $R_{ij,\mathbf{g}}$ is the interatomic distance between atom *i* in the reference cell and atom *j* in the neighbouring cells at distance |**g**| and s_6 is a functional-dependent scaling factor. We employed the C_6^i parameters reported in the work of Grimme (2006), which were obtained from atomic ionization potentials (I_p) and static dipole polarizabilities (α) according to the formula $C_6^i = 0.05 N I_p^i \alpha^i$, where *N* depends on atom row in the periodic table. The function f_{dump} is used to dump the energy correction to avoid double counting of short-range contributions and depends on the sum of atomic van der Waals radii (R_{vdw}) and on a steepness parameter (d = 20). According to results previously reported in literature for urea crystals (Civalleri et al., 2008), showing that the E_{DISP} correction tends to overestimate cohesive energy in solid crystals, the original B3LYP-D parameters where modified setting s_6 to 1, the hydrogen atom van der Waals radius, R_{vdw}(H), to 1.30 and the heavier atom van der Waals radii were scaled by a factor 1.05. This modified method, called B3LYP-D*, has been adopted with good results in our previous works on talc (Ulian et al., 2013a; Ulian et al., 2013b).

Thermal contribution and thermomechanical properties

The Helmholtz energy *F* of a solid insulator is given by (Anderson, 1995)

$$F = E_{ST}(V) + F_{VIB}(V,T) \tag{4.2}$$

where E_{ST} is the potential of a static lattice at absolute zero (athermal limit), F_{VIB} is the vibrational energy related to the thermal motion of the atoms and E_{el} is the potential due to free electrons. The pressure can be obtained by the first derivative of Helmholtz free energy

$$P = -\left(\frac{\partial F}{\partial V}\right)_T = -\left(\frac{\partial E_{ST}}{\partial V}\right)_{T=0} + \left(\frac{\partial F_{VIB}}{\partial V}\right)_T \tag{4.3}$$

In statistical thermodynamics, the vibrational energy is given by

$$F_{VIB} = -kT \ln Z \tag{4.4}$$

with *Z* the partition function found by taking the sum of all quantum energy levels for each independent oscillators in the solid lattice

$$Z = \sum_i e^{-\varepsilon_i/kT} \tag{4.5}$$

The ε_i values are the eigenvalues of the energy operator, which can be used to define the partition function for each vibrational mode, Z_i.

$$\varepsilon_i = \frac{1}{2}\hbar\varpi_i, \frac{3}{2}\hbar\varpi_i \frac{5}{2}\hbar\varpi_i, etc... \tag{4.6}$$

$$Z_i = e^{-\hbar\varpi_i/2kT}\sum_{i=0}^{\infty} e^{-3\hbar\varpi_i/2kT} = \frac{e^{-\hbar\varpi_i/2kT}}{\left(1-e^{-\hbar\varpi_i/kT}\right)} \tag{4.7}$$

It is then possible to define the vibrational contribution to the Helmholtz given by each mode as:

$$F_{VIB_i} = -kT \ln Z_i = \frac{\hbar\varpi_i}{2kT} \ln\left(1-e^{\hbar\varpi_i/kT}\right) \tag{4.8}$$

which can then be summed over the *3n-3* oscillators (*n* the number of atoms in the unit-cell) in the considered lattice to obtain the whole thermal contribution to the free energy

$$F_{VIB} = \frac{1}{2}\sum_{i=1}^{3n-3}\hbar\varpi_i + kT\sum_{i=1}^{3n-3}\ln\left(1-e^{-\hbar\varpi_i/kT}\right) \tag{4.9}$$

where the first addendum represents the zero point energy (E_{ZP}) of the solid, unaffected by the temperature and the second term is the energy arising from excitation due to temperature (F_{TH}). The term $\hbar\varpi_i/kT$ can be substituted with X_i to simplify the expression

$$F_{VIB} = \frac{kT}{2}\sum_{i=1}^{3n-3} X_i + kT\sum_{i=1}^{3n-3}\ln\left(1-e^{-X_i}\right) \tag{4.10}$$

Applying Eq. (19) to Eq. (10) allows to find the pressure related to each volume transformation

$$P = -\left(\frac{\partial E_{ST}}{\partial V}\right)_{T=0} + \frac{kT}{2V}\sum_{i=1}^{3n-3}\gamma_i X_i + \frac{kT}{V}\sum_{i=1}^{3n-3} n_i\left(\nu_i, Y\right)\gamma_i X_i \tag{4.11}$$

where γ_i is the mode-gamma of each vibrational frequency, given by

$$\gamma_i = -\frac{\partial \ln \varpi_i}{\partial \ln V} = -\frac{V}{\varpi_i}\frac{\partial \varpi_i}{\partial V} \tag{4.12}$$

and X is the Bose-Einstein distribution

$$n_i\left(\nu_i, T\right) = \frac{1}{e^{X_i}-1} \tag{4.13}$$

In the quasiharmonic treatment the vibrational modes are dependent only on volume variations, but the thermodynamic properties are dependent on temperature by the second term of Eq. (9) (Anderson, 1995; Ottonello et al., 2009a; Ottonello et al., 2009b). Rewriting Eq. (11)

$$P = P_{ST} + P_{ZP} + P_{TH} = P_{T=0} + P_{TH} \tag{4.14}$$

the pressure evaluated in the previous section is corrected by the zero point energy (P_{ZP}) and by the thermal contribution (P_{TH}).

Following the quasi-harmonic treatment of vibrational frequencies (Anderson, 1995; Ottonello et al., 2009a), the thermal expansion coefficient at any given cell volume (pressure), as a function of T, can be obtained by the direct evaluation of the $\alpha_T K_T$ product:

$$\alpha_T K_T = \frac{R}{ZV}\sum_{i=4}^{3n}\gamma_i e^{X_i}\left(\frac{X_i}{e^{X_i}-1}\right)^2 \tag{4.15}$$

where K_T is the bulk modulus estimated at the given pressure and temperature.

Within the harmonic approximation, the isochoric heat capacity as a function of T of a solid insulator can be expressed as (Anderson, 1995)

$$C_V = \frac{3R}{Z}\left(\frac{2}{\pi}\right)^3\sum_{i=1}^{3}\int_0^{X_i}\frac{\left[\arcsin\left(X/X_i\right)\right]^2 X^2 e^X dX}{\left(X_i^2 - X^2\right)^{1/2}\left(e^X-1\right)^2} + \frac{R}{Z}\sum_{i=4}^{3n} e^{X_i}\left(\frac{X_i}{e^{X_i}-1}\right)^2 \tag{4.16}$$

where the first addendum represents the acoustic contribution represented in terms of a sine-wave dispersion relation (Kieffer, 1979a; Kieffer, 1979b; Kieffer, 1979c) and the second element is the optic contribution. The specific heat at constant pressure (C_P) can be obtained from the relationship

$$C_P = C_V + T\alpha_T^2 K_{T,P} V_{P,T} \quad (4.17)$$

where $V_{P,T}$ is the cell volume at pressure P and temperature T, respectively.

4.3 Results and discussion

Geometry optimizations and energy calculations of talc at the athermal ($T = 0K$) limit for a set of 15 different cell volumes in the range 471–398 Å^3 have been performed and discussed in a previous work (Ulian et al., 2013b). The equilibrium geometries previously obtained, summarised in Table 4.1, were used in the present work to calculate the vibrational frequencies at Γ point, needed to evaluate the thermo-mechanical properties.

Table 4.1. Lattice parameters and pressure values of talc at different volumes

Volume (Å^3)	a (Å)	b (Å)	c (Å)	α (°)	β (°)	γ (°)	$P_{III\text{-}BM}$
397.534	5.1432	8.9242	8.8272	90.2106	101.1328	90.2264	9.9783
401.264	5.1561	8.9464	8.8647	90.2619	101.0991	90.2380	8.9913
405.149	5.1687	8.9703	8.9036	90.3097	101.0578	90.2289	8.0193
409.192	5.1816	8.9929	8.9466	90.3622	101.0251	90.2331	7.0655
413.556	5.1959	9.0168	8.9936	90.4571	101.0380	90.2192	6.0977
418.233	5.2101	9.0403	9.0455	90.5326	100.9953	90.2142	5.1276
423.299	5.2249	9.0666	9.1019	90.6223	100.9672	90.2028	4.1492
426.014	5.2326	9.0799	9.1345	90.6887	100.9773	90.2039	3.6541
428.789	5.2404	9.0923	9.1662	90.7277	100.9511	90.1878	3.1681
430.890	5.2462	9.1021	9.1925	90.7876	100.9693	90.1888	2.8131
434.835	5.2567	9.1187	9.2400	90.8565	100.9612	90.1683	2.1754
435.795	5.2593	9.1231	9.2532	90.8937	100.9735	90.1713	2.0258
440.728	5.2718	9.1428	9.3161	91.0026	100.9846	90.1527	1.2894
441.518	5.2740	9.1457	9.3245	91.0067	100.9853	90.1453	1.1763
445.680	5.2836	9.1611	9.3821	91.1130	101.0108	90.1329	0.602
448.547	*5.2890*	*9.1701*	*9.4159*	*91.0235*	*100.7743*	*90.1225*	*0.2265*
450.667	5.2945	9.1776	9.4525	91.2320	101.0558	90.1121	-0.0412
455.678	5.3043	9.1922	9.5270	91.3537	101.1086	90.0918	-0.6415
460.705	5.3123	9.2042	9.6079	91.4797	101.1788	90.0726	-1.2005
465.750	5.3184	9.2132	9.6954	91.6032	101.2467	90.0550	-1.7208
470.807	5.3227	9.2194	9.7911	91.7615	101.3701	90.0402	-2.2045

Notes: the static pressure values from both the polynomial fit (P_{st}) and the third-order Birch-Murnaghan fit equation of state are in GPa. Values in italic represent the minimum of the E/V function.

The talc unit-cell contains n = 42 atoms and, because of the $P\bar{1}$ symmetry, its 3n = 126 normal modes are subdivided in:

$$\Gamma_{tot} = 66A_u + 66A_g$$

The A_u modes are IR active, while the A_g ones are Raman active. The first three A_u modes are relative to atom traslations of in the cell, while the other 123 are vibrational modes. For each normal mode, the Grüneisen's parameters γ_i was calculated according to Eq. (4.12) and reported in Table 4.2. Each

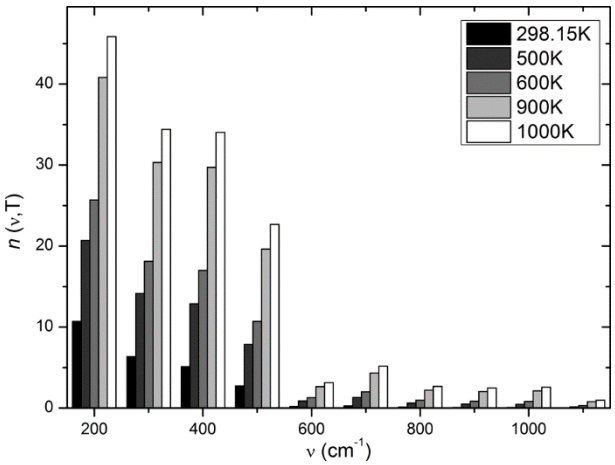

Figure 4.2 Bose-Einstein distributions of phonons at five different temperatures, as a function of the frequency of the corresponding normal modes.

optic phonon mode is associated with a positive Grüneisen's parameter, which means they all positively contribute to the vibrational pressure, as observed in Eq. (4.11). The average of all γ_i, $\overline{\gamma}$, for B3LYP calculations is 0.48.

Outside the athermal limit described in a previous work (Ulian et al., 2013b), a phonon gas is produced inside the crystal which contributes a thermal pressure whose value depends on several factors: the average number of phonons associated with each normal mode, the corresponding frequencies and the Grüneisen's parameters (Prencipe et al., 2011). We considered five different temperature values (298.15, 500, 600, 900 and 1000K) and calculated the Bose-Einstein distribution of phonons at zero pressure, as reported in Figure 4.2.

From the graph it is possible to see that at each temperature the main contribution to the vibrational pressure is due to the low-frequency modes (< 600 cm^{-1}), but at higher temperature values the amount of high-frequency modes and, consequently, their contribution increases. Low-frequency modes consist essentially of tilting of Mg-centre polyhedral associated with only minor variations of the Mg–O distances (the latter ones are nevertheless determinant for the decrease of the vibrational frequencies as the pressure increases).

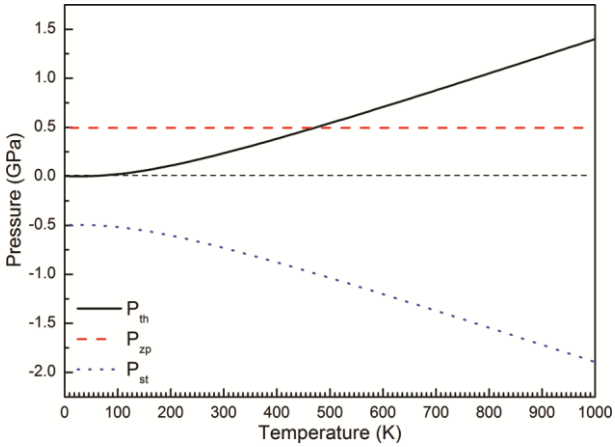

Figure 4.3 Static (P_{st}), zero point (P_{zp}) and thermal pressure (P_{th}) contributions to the zero total pressure in the T range 0 – 1000K.

The plot of the static (P_{st}), zero point (P_{zp}) and thermal pressures (P_{th}) contributions to the zero total pressure is shown in Figure 4.3. According to both the obtained Grüneisen's parameters and Eq. (4.11), the zero point contribution is constant in the temperature range considered (0 – 1000K), while the thermal pressure increases with T, almost linearly for T > 298.15K. As also observed in previous theoretical analysis, the static zero total pressure mirrors the thermal pressure, at the net of the zero point contribution (Prencipe et al., 2011).

Table 4.2. B3LYP phonon frequencies at Γ point of talc at equilibrium pressure and calculated Grüneisen's parameters

Mode	IR,Raman	ν (cm^{-1})	γ_i	Mode	IR,Raman	ν (cm^{-1})	γ_i	Mode	IR,Raman	ν (cm^{-1})	γ_i
Ac	A,I	101.9	-	43	I,A	362.4	0.5	85	I,A	694.3	0.1
Ac	A,I	101.9	-	44	A,I	365.1	0.6	86	I,A	697.5	0.1
Ac	A,I	173.2	-	45	I,A	380.9	0.4	87	A,I	708.5	0.1
4	A,I	100.0	1.8	46	A,I	383.9	0.5	88	A,I	710.4	0.2
5	I,A	111.0	1.7	47	A,I	388.3	0.5	89	I,A	725.2	0.1
6	I,A	114.5	1.7	48	A,I	390.8	0.5	90	A,I	742.7	0.0
7	I,A	125.4	2.1	49	A,I	393.6	0.4	91	A,I	748.6	0.0
8	A,I	134.1	2.6	50	I,A	395.3	0.5	92	I,A	756.1	0.0
9	I,A	145.3	3.1	51	I,A	400.3	0.4	93	A,I	756.2	0.0
10	A,I	156.7	1.6	52	I,A	402.8	0.4	94	I,A	761.3	0.2
11	I,A	174.7	0.8	53	A,I	407.8	0.6	95	I,A	780.4	0.0
12	A,I	182.0	1.3	54	A,I	410.6	0.6	96	A,I	794.2	0.0
13	A,I	187.6	1.4	55	I,A	411.2	0.7	97	A,I	800.2	0.3
14	I,A	211.5	1.0	56	A,I	416.1	0.8	98	I,A	803.4	0.3
15	I,A	214.1	0.7	57	I,A	431.6	0.6	99	A,I	805.9	0.3
16	A,I	221.7	0.8	58	A,I	435.4	0.6	100	I,A	810.0	0.3
17	I,A	234.7	0.7	59	A,I	437.8	0.6	101	A,I	851.5	0.2
18	A,I	236.6	0.6	60	I,A	438.4	0.6	102	I,A	852.3	0.3
19	I,A	245.9	0.3	61	A,I	444.7	0.5	103	I,A	906.7	0.3
20	A,I	247.2	0.3	62	I,A	447.0	0.5	104	A,I	907.0	0.3
21	I,A	247.5	0.4	63	I,A	451.4	0.4	105	I,A	909.1	0.3
22	A,I	255.1	0.3	64	I,A	455.6	0.5	106	A,I	919.9	0.3
23	A,I	263.8	0.5	65	A,I	458.8	0.5	107	A,I	940.1	0.2
24	A,I	275.7	0.4	66	A,I	459.9	0.5	108	A,I	969.9	0.3
25	A,I	284.4	0.3	67	A,I	461.3	0.6	109	I,A	989.0	0.3
26	A,I	289.2	0.3	68	I,A	472.4	0.7	110	A,I	1015.8	0.2
27	I,A	290.4	0.3	69	A,I	480.5	0.6	111	I,A	1016.8	0.2
28	I,A	295.5	0.4	70	I,A	490.6	0.6	112	I,A	1017.0	0.2
29	I,A	300.6	0.3	71	A,I	503.9	0.4	113	A,I	1017.1	0.2
30	A,I	303.4	0.5	72	A,I	510.1	0.3	114	A,I	1021.0	0.2
31	A,I	304.0	0.6	73	A,I	525.7	0.4	115	I,A	1024.7	0.3
32	I,A	317.1	0.5	74	I,A	526.1	0.5	116	I,A	1063.0	0.2
33	I,A	320.3	0.6	75	I,A	527.2	0.5	117	I,A	1090.8	0.0
34	I,A	328.4	0.5	76	A,I	530.9	0.5	118	A,I	1091.4	0.0
35	I,A	329.0	0.5	77	A,I	533.7	0.5	119	A,I	1113.4	0.0
36	A,I	329.9	0.5	78	A,I	534.5	0.5	120	I,A	1114.5	0.0
37	A,I	333.1	0.5	79	I,A	537.5	0.5	121	A,I	1145.6	0.1
38	I,A	340.0	0.5	80	I,A	541.2	0.4	122	I,A	1152.3	0.1
39	A,I	343.8	0.5	81	I,A	592.5	0.3	123	A,I	3851.9	0.0
40	I,A	348.1	0.6	82	A,I	609.4	0.3	124	I,A	3852.3	0.0
41	I,A	357.2	0.4	83	A,I	651.0	0.3	125	A,I	3852.7	0.1
42	A,I	360.5	0.5	84	I,A	669.0	0.2	126	I,A	3853.8	0.1

Ac refers to acoustic modes. Ir and Raman modes are reported as active (A) and inactive (I).

The total pressure was then calculated from each contribution (static, zero point and thermal) for every compressional state at different temperatures. In particular, data at room temperature (298.15K) were collected and compared to the experimental results recently obtained by Gatta and co-workers (Gatta et al., 2013) by diamond anvil cell on single-crystal X-Ray Diffraction (XRD). The results are

plotted in Figure 4.4a, alongside data obtained at the athermal limit (Ulian et al., 2013b). Furthermore, we reported the isobaric volume as a function of temperature and the *V(P,T)* plot is reported in Figures 4.4b,c, respectively.

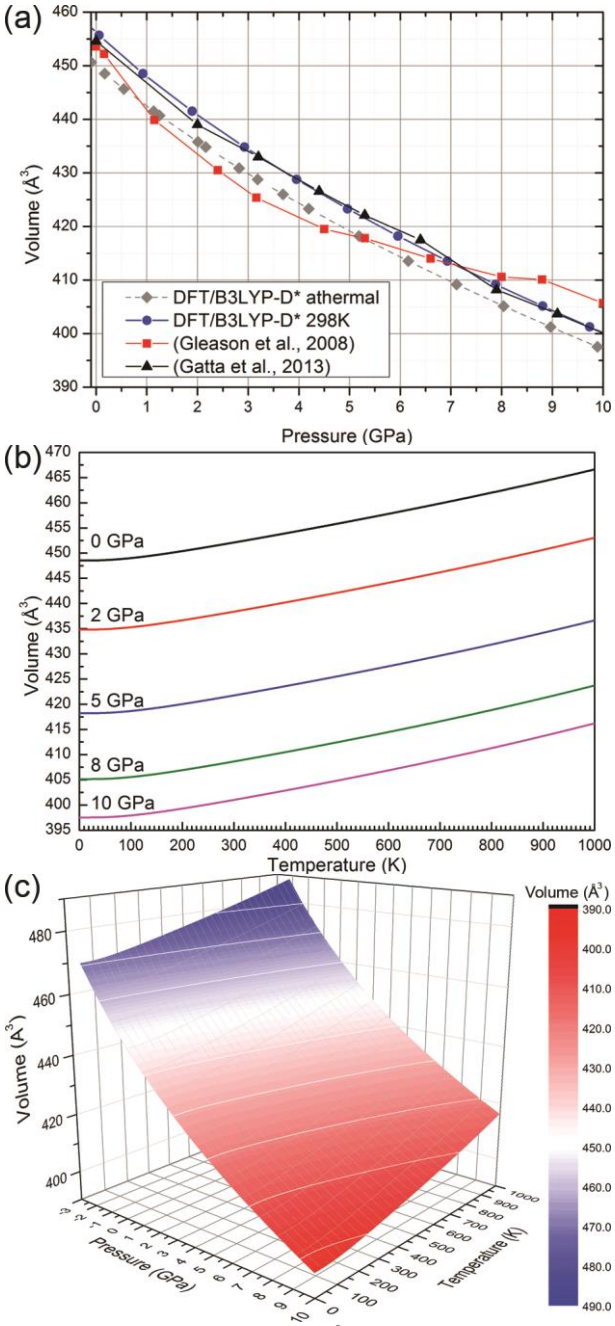

Figure 4.4 (a) Talc Volume (Å^3) vs Pressure (GPa) plot obtained with DFT/B3LYP approach at athermal limit (grey triangles) and at 298.15K (black squares), compared to both single-crystal (Gatta et al., 2013) and powder XRD data (Gleason et al. 2008). (b) Isobaric variations of volume (Å^3) as a function of temperature (K). (c) Three-dimensional surface map of talc *V(P,T)* data obtained in the range 0 – 1000 K.

There is an excellent agreement between the density functional theory approach and the experimental results, with negligible deviations. The pressure *vs.* volume data were fitted using a third-order finite strain isothermal Birch-Murnaghan Equation of State (III-BM EOS) (Birch, 1947):

$$P = \frac{3}{2} K_T \left[\eta^{-7/3} - \eta^{-5/3}\right] \times \left\{1 - \frac{3}{4}\left(4 - K'\right)\left(\eta^{-2/3} - 1\right)\right\} + P_0 \quad (4.18)$$

where $\eta = V/V_0$ is a dimensionless parameter and V_0 is the volume at reference pressure P_0. The best fitting procedure was made by least-square method implemented in the EOS-FIT5.2 software (Angel, 2001), resulting in the refined elastic parameters: V_0 = 456.336 Å^3, K_{T0} = 52.96 GPa and K' = 5.663 at T = 298.15K. With K_{T0} we indicate the bulk modulus at P = 0 GPa at specific isotherm, in this case room temperature. As expected, the volume at zero pressure is larger and the bulk modulus is lower than those obtained in static conditions (Ulian et al., 2013b). Again, there is a very good agreement with the results obtained by neutron diffraction experiments, where $\Delta V_0 = +1.636$ Å^3, $\Delta K_T = -3.04$ GPa and $\Delta K' = +0.263$ (Gatta et al., 2013). The *ab initio* results are also in satisfactionary agreement with the experimental results reported by Gleason and co-workers (Gleason et al., 2008), but there is a small deviation on the bulk modulus

value (44 GPa) and on its first derivative (18) at T = 298 K. Probably the difference between the experimental results of Gatta et al. (2013) and of Gleason et al. (2008) are mainly due to the nature of the analyzed sample, single-crystal and powder of talc, respectively. Then, it is expectable that the results obtained from our model, an "ideal" talc single crystal, fit better with those obtained on a similar "sample" than with the other.

In our talc model there is a correct evaluation of the weak van der Waals forces acting between the TOT layers of talc, which is also passed to the phonon calculation. For the latter case, it was noted that the DFT/B3LYP-D* method correctly evaluated the IR spectrum of the mineral, but for the hydroxyl groups (Ulian et al., 2013a). We are aware that a further improvement to the results could be promoted by calculating the anharmonic correction for all the OH vibrational modes (not used in the present work), but (1) the CRYSTAL code allows to apply this correction only to the stretching modes and (2) according to Figure 4.3, phonon modes with $\nu > 600$ cm^{-1} have only a small contribution to the thermal pressure.

Concerning the theoretical results provided by Stixrude (2002), we observed that the LDA bulk modulus expresses a softer mineral behavior than our observations (K_{T0} = 29 GPa at 300 K). Furthermore, the first derivative of the bulk modulus is high (K' = 17), which is reflected in a greater contraction of the unit cell upon compression than the one observed by GTO/B3LYP-D* approach. Beside the different computational approach, this discordant results may be due for two critical reasons. On one hand, previous data were obtained without considering the contribution of weak interaction forces to the DFT energy. On the other hand, the thermal/vibrational contribution to the Helmholtz free energy was accounted by the Mie-Grüneisen equation of state, which considers all γ_i equal to each other and to γ ($\gamma_i = \gamma_{mg}$). This approximation is true only at very high temperatures, not at intermediate T (Anderson, 1995).

The quasi-harmonic mode gamma analysis of the $3n - 3$ optic modes of the $\alpha_T K_T$ product shows that it attains a value of $1.25 \cdot 10^{-3}$ GPa/K in the 298.5 – 800 K range and reach a constant value of $1.49 \cdot 10^{-3}$ GPa/K at $T \to \infty$. The thermal dependence of the bulk modulus was calculated, obtaining $\left(\partial K_T / \partial T\right)_P = -4.85 \cdot 10^{-3}$ GPa/K. The trends of the $\alpha_T K_T$ product at 0, 5 and 10 GPa are plotted in Figure 4.5a.

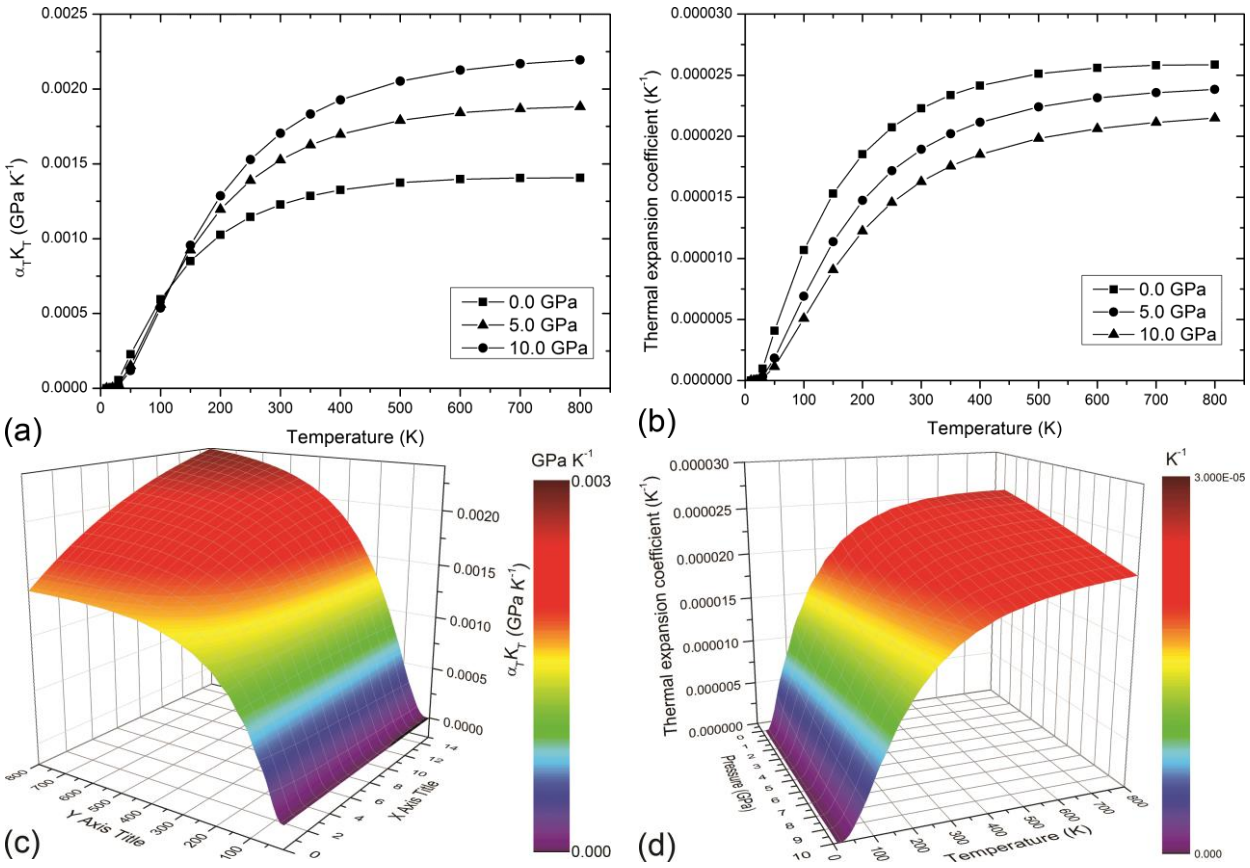

Figure 4.5 *Ab initio* $\alpha_T K_T$ product (a) and α_T (b) calculated for talc at selected pressures. 3D plots of $\alpha_T K_T$ product (c) and thermal expansion coefficients (d) in the temperature range 0 – 800 K.

The *ab initio* thermal expansion, which is plotted in Figure 4.5b for the previously cited compressional states, was calculated from the αK product with the isobaric temperature derivative. It can be observed that, at T = 300 K, α_T varied from 2.23 · 10^{-5} K^{-1} at P = *0* GPa to 1.63 · 10^{-5} K^{-1} at P =*10* GPa [$(\partial\alpha/\partial T)_P$ is -5.93 · 10^{-7} GPa^{-1} K^{-1}]. Unfortunately, only the thermal expansion coefficient is available in literature, which Gatta et al. (2013) estimated by combining the elastic parameters obtained in their study with the thermal data of talc reported by Pawley et al. (1995). The reported *P*-*T*-*V* EoS showed α = 2.15 · 10^{-5} K^{-1}, which is in good agreement with out theoretical result. We reported the results for different compressional states to help researchers in interpreting their results for eventual future works. The trend of both $\alpha_T K_T$ product and α_T plotted as a function of pressure and temperature in the three-dimensional plots of Figures 4.5c,d.

The isochoric and isobaric heat capacities, and, were calculated with Eqs. (4.16,4.17), respectively. It can be observed in Figure 4.6a that at high temperatures C_V attains the Dulong-Petit limit and there is a small decreasing of the heat capacity with increasing pressure. Similar trend was for the C_P data at different pressures, but at about 550K there is an inversion of the increasing ratio with increasing pressure. Calculated C_V and C_P data as a function of both pressure and temperature are plotted in

Figure 4.6b. The percentage of acoustic and optic contribution to heat capacity in the 0 – 800 K temperature range is reported in Figure 4.7. The influence of the acoustic modes is prominent at T < 100 K, but it decays rapidly with the temperature increase (< 5% at room temperature).

The C_P vs. T data are fitted between in the range 298.15–800K according to the form of a Haas–Fisher polynomial expression (Haas and Fisher, 1976), which is:

$$C_p = a + b \cdot T + c \cdot T^{-2} + d \cdot T^2 + e \cdot T^{-1/2} \quad (4.19)$$

The retrieved regression coefficients, listed in Table 4.3, reproduce computed heat capacities with a mean error of 0.326 J/(mol K). The summation of squared residuals over 72 values is $1.2 \cdot 10^{-3}$.

A comparison between theoretical data on isobaric heat capacity was performed considering the works of Krupka et al. (1985) and of Hemingway (1991), where both reported the isobaric heat capacities of talc. The *ab initio* C_P data nicely fit the differential scanning calorimetric results, but the theoretical method do not reproduce the small inflection experimentally observed at about T = 650K. According to literature, talc dehydroxylates in the temperature range 600 – 900 K (Dellisanti and Valdrè, 2010; Ptacek et al., 2013; Zhang et al., 2010). Thus, the temperature range explored in our simulations does not involve this process, but at temperature above 900 K. On one hand, in both the works of Krupka et al. (1985) and Hemingway et al. (1991) the talc sample presented Fe (0.4% wt.) and Al (0.2% wt.) substitu-

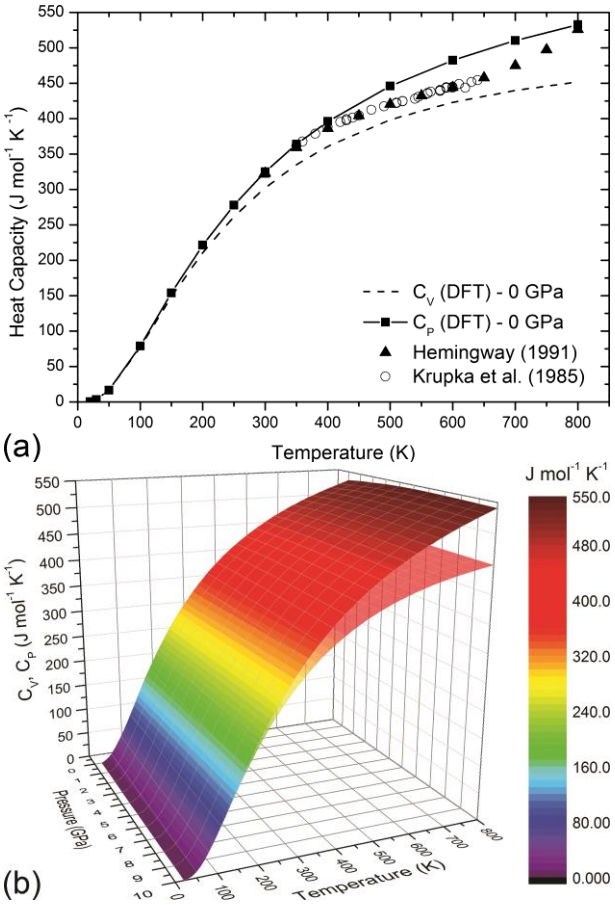

Figure 4.6 (a) Talc ab initio isochoric (dashed lines) and isobaric (solid lines) heat capacities, compared to experimental calorimetric data (Hemingway, 1991; Krupka et al., 1985). (b) Three-dimensional plot of heat capacities at different volumes and in the temperature range 10 – 800 K.

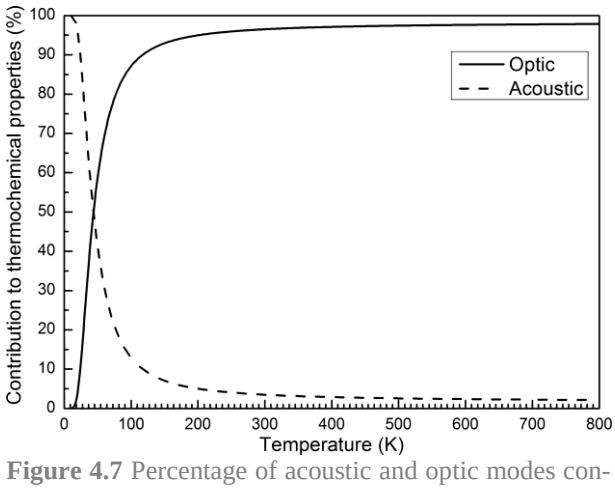

Figure 4.7 Percentage of acoustic and optic modes contributions to the thermochemical properties.

tions, which could alter the thermal behavior of the mineral. On the other hand, our model is a stochiometrically pure talc mineral. The different chemical composition may influence the thermochemical properties of the mineral.

In the absence of configurational disorder, the entropy of one mole of crystalline substance can be expressed by the following formula (Anderson, 1995; Kieffer, 1979c):

$$S(V,T)=\frac{3R}{Z}\left(\frac{2}{\pi}\right)^3\sum_{i=1}^{3}\int_0^{X_i}\frac{\left[\arcsin\left(X/X_i\right)\right]^2 XdX}{\left(X_i^2-X^2\right)^{1/2}\left(e^X-1\right)^2}-$$

$$\frac{3R}{Z}\left(\frac{2}{\pi}\right)^3\sum_{i=1}^{3}\int_0^{X_i}\frac{\left[\arcsin\left(X/X_i\right)\right]^2}{\left(X_i^2-X^2\right)^{1/2}}\ln\left(1-e^{-X}\right)dX+ \qquad (4.20)$$

$$N_A k\sum_{i=4}^{3n}\left[n_i\left(\nu_i,T\right)X_i-\ln\left(1-e^{-X_i}\right)\right]$$

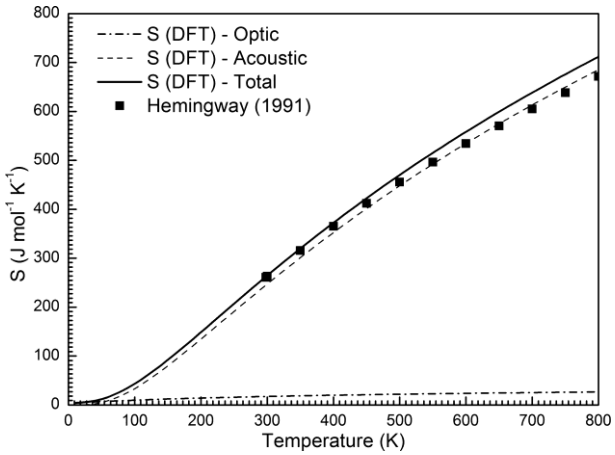

Figure 4.8 *Ab initio* bulk entropy of talc, compared to experimental calorimetric data (Hemingway, 1991)

where N_A is the Avogadro's number. The first two terms are related to the Kieffer model (Anderson, 1995; Kieffer, 1979b; Kieffer, 1979c), while the third one is the contribution of the optic modes (*3n -3*). We reported plotted the computed *S* as a function of temperature at *P* = 0.0 GPa in Figure 4.8, alongside the experimental data of Hemingway (1991). As it can be observed from the plot, the theoretical entropy is mainly given by the optic modes, while the acoustic phonons play a negligible role even at low temperatures.

The theoretical bulk entropy at *T* = 298.15 K (244.92 J mol^{-1} K^{-1}) is very close to the calorimetric value of 260.83 J mol^{-1} K^{-1} reported and there is also a good agreement at high temperatures.

4.4 Conclusions

The present results obtained with density functional theory approach on talc aim to study the thermomechanical behaviour of the mineral at different pressure and temperature conditions. The computations developed in this study were based on successful quantum chemical and geophysical approaches and provided an internally consistent set of references to compare with the various experiments. The provided data are of general interest and can be useful to both geochemists-geophysics in the study

of the mineral in Earth's mantle conditions and to application in ceramic industry. The use of all-electron calculations performed at the DFT/B3LYP level of theory (taking into account the dispersive forces) and appropriate computational parameters for both the self-consistent field equation and geometry optimization resulted in thermo-chemical and thermo-physical parameters with adequate accuracy for the study of layered silicates at different P-T conditions.

REFERENCES CITED

Anderson, O.L. (1995) Equation of state of solids for geophysics and ceramic science. 405 p. Oxford University Press, New York, US.

Angel, R.J. (2001) EOS-FIT6.0. Computer Program (http://www.rossangel.com).

Becke, A.D. (1993) Density-Functional Thermochemistry .3. The Role of Exact Exchange. Journal of Chemical Physics, 98(7), 5648-5652.

Birch, F. (1947) Finite elastic strain of cubic crystal. Physical Review, 71, 809-824.

Butylina, S., Hyvarinen, M., and Karki, T. (2012) Accelerated weathering of wood-polypropylene composites containing minerals. Composites Part A-Applied Science and Manufacturing, 43(11), 2087-2094.

Castillo, L.A., Barbosa, S.E., and Capiati, N.J. (2012) Influence of talc genesis and particle surface on the crystallization kinetics of polypropylene/talc composites. Journal of Applied Polymer Science, 126(5), 1763-1772.

Civalleri, B., Zicovich-Wilson, C.M., Valenzano, L., and Ugliengo, P. (2008) B3LYP augmented with an empirical dispersion term (B3LYP-D*) as applied to molecular crystals. Crystengcomm, 10(4), 405-410.

D'Haese, M., Goderis, B., and Van Puyvelde, P. (2011) The Influence of Calcium-Stearate-Coated Calcium Carbonate and Talc on the Quiescent and Flow-Induced Crystallization of Isotactic Poly(propylene). Macromolecular Materials and Engineering, 296(7), 603-616.

Dellisanti, F., Minguzzi, V., and Valdrè, G. (2011) Mechanical and thermal properties of a nanopowder talc compound produced by controlled ball milling. Journal of Nanoparticle Research, 13(11), 5919-5926.

Dellisanti, F., and Valdrè, G. (2010) On the high-temperature structural behaviour of talc (Mg3Si4O10(OH)2) to 1600 degrees C: Effect of mechanical deformation and strain. Philosophical Magazine, 90(17-18), 2443-2457.

Dellisanti, F., Valdrè, G., and Mondonico, M. (2009) Changes of the main physical and technological properties of talc due to mechanical strain. Applied Clay Science, 42(3-4), 398-404.

Dovesi, R., Saunders, V.R., Roetti, C., Orlando, R., Zicovich-Wilson, C.M., Pascale, F., Civalleri, B., Doll, K., Harrison, N.M., Bush, I.J., D'Arco, P., and Llunell, M. (2009) CRYSTAL09 User's Manual. University of Torino, Torino.

Evans, B.W., and Guggenheim, S. (1988) Talc, Pyrophyllite, and Related Minerals. Reviews in Mineralogy, 19, 225-294.

Gatta, G.D., Merlini, M., Valdre, G., Liermann, H.-P., Nenert, G., Rothkirch, A., Kahlenberg, V., and Pavese, A. (2013) On the crystal structure and compressional behavior of talc: a mineral of interest in petrology and material science. Physics and Chemistry of Minerals, 40(2), 145-156.

Gatti, C., Saunders, V.R., and Roetti, C. (1994) Crystal-field effects on the topological properties of the electron-density in molecular-crystals - the case of urea. Journal of Chemical Physics, 101(12), 10686-10696.

Gleason, A.E., Parry, S.A., Pawley, A.R., Jeanloz, R., and Clark, S.M. (2008) Pressure-temperature studies of talc plus water using X-ray diffraction. American Mineralogist, 93(7), 1043-1050.

Grimme, S. (2006) Semiempirical GGA-type density functional constructed with a long-range dispersion correction. Journal of Computational Chemistry, 27(15), 1787-1799.

Haas, J.L., and Fisher, J.R. (1976) Simultaneous evaluation and correlation of thermodynamic data. American Journal of Science, 276, 525-545.

Hemingway, B.S. (1991) Thermodynamic properties of anthophyllite and talc: Corrections and discussion of calorimetrlc data. American Mineralogist, 76(9-10), 1589-1596.

Kieffer, S.W. (1979a) Thermodynamics and lattice vibrations of minerals - 1. mineral heat capacities and their relationships to simple lattice vibrational models. Reviews of Geophysics and Space Physics, 17(1), 1-19.

-. (1979b) Thermodynamics and lattice vibrations of minerals - 2. vibrational characteristics of silicates. Reviews of Geophysics and Space Physics, 17(1), 20-34.

Kieffer, S.W. (1979c) Thermodynamics and lattice vibrations of minerals - 3. lattice dynamics and an approximation for minerals with application to simple substances and framework of silicates. Reviews of Geophysics and Space Physics, 17(1), 35-59.

Krupka, K.M., Hemingway, B.S., Borie, R.A., and Kerrick, D.M. (1985) High-temperature heat capacities and derived thermodynamic properties of anthophyllite, diopside, dolomite, enstatite, bronzite, talc, tremolite and wollastonite. American Mineralogist, 70(3-4), 261-271.

Larentzos, J.P., Greathouse, J.A., and Cygan, R.T. (2007) An ab initio and classical molecular dynamics investigation of the structural and vibrational properties of talc and pyrophyllite. Journal of Physical Chemistry C, 111(34), 12752-12759.

Lee, C.T., Yang, W.T., and Parr, R.G. (1988) Development of the Colle-Salvetti Correlation-Energy Formula into a Functional of the Electron-Density. Physical Review B, 37(2), 785-789.

Mirabedini, S.M., Jamali, S.S., Haghayegh, M., Sharifi, M., Mirabedini, A.S., and Hashemi-Nasab, R. (2012) Application of mixture experimental design to optimize formulation and performance of thermoplastic road markings. Progress in Organic Coatings, 75(4), 549-559.

Monkhorst, H.J., and Pack, J.D. (1976) Special points for Brillouin-zone integrations. Physical Review B, 8, 5188-5192.

Mysen, B.O., Ulmer, P., Konzett, J., and Schmidt, M.W. (1998) The upper mantle near convergent plate boundaries. Ultrahigh-Pressure Mineralogy, 37, 97-138.

Nada, R., Nicholas, J.B., McCarthy, M.I., and Hess, A.C. (1996) Basis sets for ab initio periodic Hartree-Fock studies of zeolite/adsorbate interactions: He, Ne, and Ar in silica sodalite. International Journal of Quantum Chemistry, 60(4), 809-820.

Ottonello, G., Civalleri, B., Ganguly, J., Zuccolini, M.V., and Noel, Y. (2009a) Thermophysical properties of the α–β–γ polymorphs of Mg2SiO4: a computational study. Physics and Chemistry of Minerals, 36(2), 87-106.

Ottonello, G., Zuccolini, M.V., and Civalleri, B. (2009b) Thermo-chemical and thermo-physical properties of stishovite: An ab-initio all-electron investigation. CALPHAD: Computer Coupling of Phase Diagrams and Thermochemistry, 33(3), 457-468.

Pascale, F., Zicovich-Wilson, C.M., Gejo, F.L., Civalleri, B., Orlando, R., and Dovesi, R. (2004) The calculation of the vibrational frequencies of crystalline compounds and its implementation in the CRYSTAL code. Journal of Computational Chemistry, 25(6), 888-897.

Pawley, A.R., Redfern, S.A.T., and Wood, B.J. (1995) Thermal expansivities and compressibilities of hydrous phases in the system MgO-SiO2-H2O: Talc, phase A and 10-angstrom phase. Contributions to Mineralogy and Petrology, 122(3), 301-307.

Prencipe, M., Pascale, F., Zicovich-Wilson, C.M., Saunders, V.R., Orlando, R., and Dovesi, R. (2004) The vibrational spectrum of calcite (CaCO3): an ab initio quantum-mechanical calculation. Physics and Chemistry of Minerals, 31(8), 559-564.

Prencipe, M., Scanavino, I., Nestola, F., Merlini, M., Civalleri, B., Bruno, M., and Dovesi, R. (2011) High-pressure thermo-elastic properties of beryl (Al4Be6Si12O36) from ab initio calculations, and observations about the source of thermal expansion. Physics and Chemistry of Minerals, 38(3), 223-239.

Ptacek, P., Opravil, T., Soukal, F., Havlica, J., Masilko, J., and Wasserbauer, J. (2013) Preparation of dehydroxylated and delaminated talc: Meta-talc. Ceramics International, 39(8), 9055-9061.

Stixrude, L. (2002) Talc under tension and compression: Spinodal instability, elasticity, and structure. Journal of Geophysical Research-Solid Earth, 107(B12).

Ulian, G., Tosoni, S., and Valdrè, G. (2013a) Comparison between Gaussian-type Orbitals and Plane Wave *ab initio* DFT modeling of layered silicates: Talc mineral as model system. Journal of Chemical Physics, 139(20), 204101.

-. (2013b) The compressional behaviour and the mechanical properties of talc [$Mg_3Si_4O_{10}(OH)_2$]: a density functional theory investigation. Physics and Chemistry of Minerals, Submitted.

Valenzano, L., Torres, F.J., Klaus, D., Pascale, F., Zicovich-Wilson, C.M., and Dovesi, R. (2006) Ab initio study of the vibrational spectrum and related properties of crystalline compounds; the case of CaCO3 calcite. Zeitschrift Fur Physikalische Chemie-International Journal of Research in Physical Chemistry & Chemical Physics, 220(7), 893-912.

Zhang, M., Redfern, S.A.T., Salje, E.K.H., Carpenter, M.A., and Wang, L. (2010) H_2O and the dehydroxylation of phyllosilicates: An infrared spectroscopic study. American Mineralogist, 95(11-12), 1686-1693.

CHAPTER 5 – Structural and thermo-physical properties of Pyrophyllite: a semi-empirical Density Functional contribution.[4]

Abstract

Pyrophyllite has a significant role in many industrial applications, such as petroleum engineering and civil engineering, and in geophysics as a hydrous phase which can recycle water into the Earth's mantle. However, very few works have been proposed to fully characterize the thermodynamic properties of this mineral phase.

Thermo-chemical and thermo-physical properties of pyrophyllite were computed with the hybrid DFT/B3LYP density functional method and taking into account a correction to include dispersive forces. The results of this kind of analysis can be adopted in the study of the thermodynamic properties of solid phases at physical conditions that are difficult to obtain in experimental procedures, especially controlled high temperatures. In particular, a set of thermodynamic properties of pyrophyllite at different *P-T* conditions are provided, which could be useful in both geophysical and technological applications of the mineral.

5.1 Introduction

Pyrophyllite ($[Al_2Si_4O_{10}(OH)_2]$; Figure 1a) is the dioctahedral term of the phyllosilicate group consisting of simple 2:1 tetrahedral-octahedral-tetrahedral layers, namely TOT (Bruno et al., 2006; Evans and Guggenheim, 1988). The tetrahedral sheet is composed by individual SiO_4 tetrahedra linked by sharing three oxygen atoms (basal oxygen, O^b) with SiO_4 neighbors to form infinite two-dimensional sheets with a hexagonal-based patterns of linked sixfold rings; the plane formed by the basal oxygen is usually named ''siloxanic basal plane''. The fourth corner (apical oxygen, O^a) does not link to other tetrahedral groups but it is shared with the Al octahedrum. The octahedrally-coordinated cations form a sheet, in which individual polyhedra are laterally linked by edge sharing. In pyrophyllite only 2/3 of the octahedral sites are occupied. The 2:1 layer is composed of two opposing tetrahedral sheets with the octahedral sheet in between. Since the TOT layer is electrically neutral, no interlayer cations exist in these structures. Pyrophyllite is commonly found in nature in three polytypic forms: a two layer monoclinic (2M), a one layer triclinic (1Tc) and a disordered form (Ghanaati et al., 2010; Sima

[4] This chapter consists of a paper by Gianfranco Ulian and Giovanni Valdrè, "Structural and thermo-physical properties of Pyrophyllite: a semi-empirical Density Functional contribution", in preparation for the *Journal of Chemical Physics*.

et al., 2010). The crystal structure of pyrophyllite-1Tc was determined by Lee and Guggenheim (Lee and Guggenheim, 1981) with a single crystal X-ray refinement.

From the geological point of view, pyrophyllite is one of the hydrous phases which in the last years have drawn a considerable interest in their high-pressure stability. Experimental studies have shown that some hydrous metamorphic minerals are stable to much greater depths in the Earth than previously evaluated (Pawley et al., 2002). Also, it seems that a range of new hydrous phases can be synthesized up to very high pressures. The main interest in these phases is focused on processes in subduction zones, where dehydration is responsible for explosive volcanism and earthquakes. In this prospective, the high-pressure stability of hydrous phases determines the depth to which water can be recycled into the Earth's mantle and the amount of recycling that can take place.

Studies on pyrophyllite have been carried out for its utilization in whiteware body as a replacement of quartz, clay or feldspar (Alimdzhanova et al., 1999; Bhasin et al., 2003; Lintz, 1938) and for its significant role in many industrial applications, such as petroleum engineering, civil engineering, food and cosmetic industry, heterogeneous catalysis, waste storage, etc. (Mazo et al., 2008). However, its use as a ceramic raw material is not yet widely accepted, probably because pyrophyllite seldom occurs in pure state like other silicates, such as kaolinite and the presente of associated minerals (quartz, kyanite, sericite, diaspore) in the aggregate structure can influence its properties and behaviour. For such reasons, there is still little information regarding thermal-mechanical transformation of pyrophyllite mineral, which could be of upmost importance due to depleting resources of standard alumino-silicate minerals. Few works in this prospective have been conducted recently on both pure pyrophyllite and pired-pyrophyllite for its utilization in ceramic and porcelain systems (Mukhopadhyay et al., 2011; Mukhopadhyay et al., 2010).

One of the most important thermodynamic parameters of a mineral is its equation of state (EOS), i.e., the pressure- and temperature-dependence of its unit-cell volume. This is essential for calculating the P-T conditions of mineral reactions. However, despite the importance of pyrophyllite in the water transport process in the Earth's mantle, very few works have been proposed to fully characterize the thermodynamic properties of this mineral phase. Furthermore, the results presented in literature are quite discordant.

A set of thermomechanical data for stoichiometric pyrophyllite was reported by Holland and Powell (1998), by deriving thermodynamic properties from equilibria involving pure end-members. The bulk modulus estimated at zero pressure and at 298K (K_{T0}) by a Murnaghan equation of state fit (Murnaghan, 1937) is 77 GPa, but its pressure derivative (K') was kept fixed at 4 during the fitting procedure. With K_{T0} we indicate the bulk moduli at 0 GPa at specific temperature.

More recently, Pawley et al. (2002) measured the structural changes of pyrophyllite following a *P-T* path in a range of pressure from 0 to 6.8 GPa between 300 – 700K using a X-Ray powder diffractometer equipped with a multi-anvil apparatus. They measured a powdered sample with NaCl as internal pressure standard. The data were fitted with a Murnaghan equation to obtain K_{T0} = 37 GPa and K' = 10. However, the authors did not make any high-temperature measurements at low-pressure on pyrophyllite, which limited the possibility to determine the thermal expansivity (α_T) of the mineral and the thermal dependence of the bulk modulus with the temperature ($\partial K_T/\partial T$).

Nowadays, the interpretation of both diffraction and thermodynamics properties of complex mineral phases, such as phyllosilicates, has been facilitated by a class of independent, first-principles (sometimes termed "ab initio") quantum-mechanical simulations. Regarding pyrophyllite, to our knowledge there is only one study aimed to obtain the elastic behavior of this mineral (Voora et al., 2011). This work reported an interesting comparison between different Density Functional Theory (DFT) methods, using a plane-wave basis set, in the analysis of the mechanical behavior of pyrophyllite. The theoretical bulk modulus and its first *P*-derivative fall between 38-41 GPa and 11-12, respectively. The authors observed a better agreement with experimental mechanical results when using a semi-empirical correction for dispersive forces (Grimme, 2006). In fact, while DFT-based approaches provide an adequate prediction of covalent bonding, they have a well-documented problem in describing long range dispersion, which is often the driving force in weak interactions. For this reason, when dealing with weakly bound systems, such as layered minerals, it is recommendable to profit of some semi-empiric correction scheme, such as the DFT+D proposed by Grimme. However, the theoretical results of Voora et al. (2011) are related only to athermal condition, as they did not include the temperature as a variable.

To overcome the thermal limitation, in the present work we the thermomechanical properties of pyrophyllite geometry by an *ab initio* quantum mechanical approach based on the density functional theory (DFT) corrected for the dispersive forces, including the thermal effects by the quasi-harmonic approximation (Anderson, 1995; Ulian and Valdrè, 2014). Differently from the work of Voora et al. (2011), we used an all-electron localized Gaussian-type orbitals (GTO) and the B3LYP hybrid functional integrated with dispersive forces contribution. We have shown in previous works (Ulian et al., 2013a; Ulian et al., 2013b) that this combination provides more accurate energy results than plane wave simulations. Starting from the XRD data of Wardle and Brindley (1972), we optimized the pyrophyllite unit-cell/internal geometry and then investigated the mechanical properties of the mineral. First, in order to gain information on the compressional behaviour of a pure pyrophyllite model, we analyzed the talc structure from 0 GPa to about 10 GPa. A small range of negative pressures were

also considered to explore the mineral behavior under the effect of an hydrostatic tensile stress. These data were used to predict the equation of state, lattice and internal structural parameters of pyrophyllite at different temperatures and were compared with previous theoretical and experimental results.

Three-dimensional plots of thermochemical results will be provided, which can be useful to both understand the metamorphic and igneous equilibriums and industrial applications. Thermochemical results will be compared to experimental investigations (Hemingway, 1991; Krupka et al., 1985) obtained by differential scanning calorimetry.

5.2 Computational details

The calculations presented in this work have been performed with the *ab initio* CRYSTAL09 code (Dovesi et al., 2009), which implements the Hartree–Fock and Kohn–Sham self-consistent field method for the study of periodic systems. The graphical drawings have been carried out with the molecular graphics software VESTA (Momma and Izumi, 2008).

Model structures

We modelled the pyrophyllite structure starting from XRD refinement data reported in literature (Lee and Guggenheim, 1981). The unit cell belongs to $C\bar{1}$ space group. Since hydrogen atoms location has not been characterized by crystallographic studies, we oriented the O-H bond parallel to the [001] direction. Oxygen atoms are subdivided in three groups: apical [O^a or O(a)] shared between Si and Al; hydroxyl [O^h or O(h)]; basal [O^b or O(b)] shared between silica tetrahedrons. See the stick and ball model in Figure 5.1 for a graphical representation.

Theoretical Details

We employed for the simulations the hybrid exchange functional B3LYP, which is the combination of the Becke three-parameter functional (Becke, 1993) and the gradient-corrected correlation functional of Lee, Yang, and Parr (Lee et al., 1988). The exchange–correlation contribution was calculated over a grid of 75 points and 974 angular points, obtained from the Gauss–Legendre quadrature and Lebedev schemes (Prencipe et al., 2004). This represents a good compromise between accuracy and cost of calculation for geometry optimization and vibrational frequencies. The values of the tolerances

that control the Coulomb and exchange series are the default provided by CRYSTAL09, but we increased the pseudo-overlap parameter from 12 to 14 (Dovesi et al., 2009) to stabilize the self-consistent behaviour during unit-cell deformations. The Hamiltonian matrix has been diagonalized (Monkhorst and Pack, 1976) using a 4×4×4 k-mesh that leads to 36 k-points.

Multi-electron wave functions are described by linear combination of crystalline orbitals (CO), expanded in terms of Gaussian-type orbital (GTO) basis sets. We chose basis sets from those used by other authors, optimized for their investigations on similar structures. For all the calculations, aluminium and oxygen have been described by a 8-511d1G (Catti et al., 1994) and a 8-411d11G basis sets, respectively, silicon by a 88-31G* (Nada et al., 1996) and hydrogen by a 3-1p1G basis set (Gatti et al., 1994).

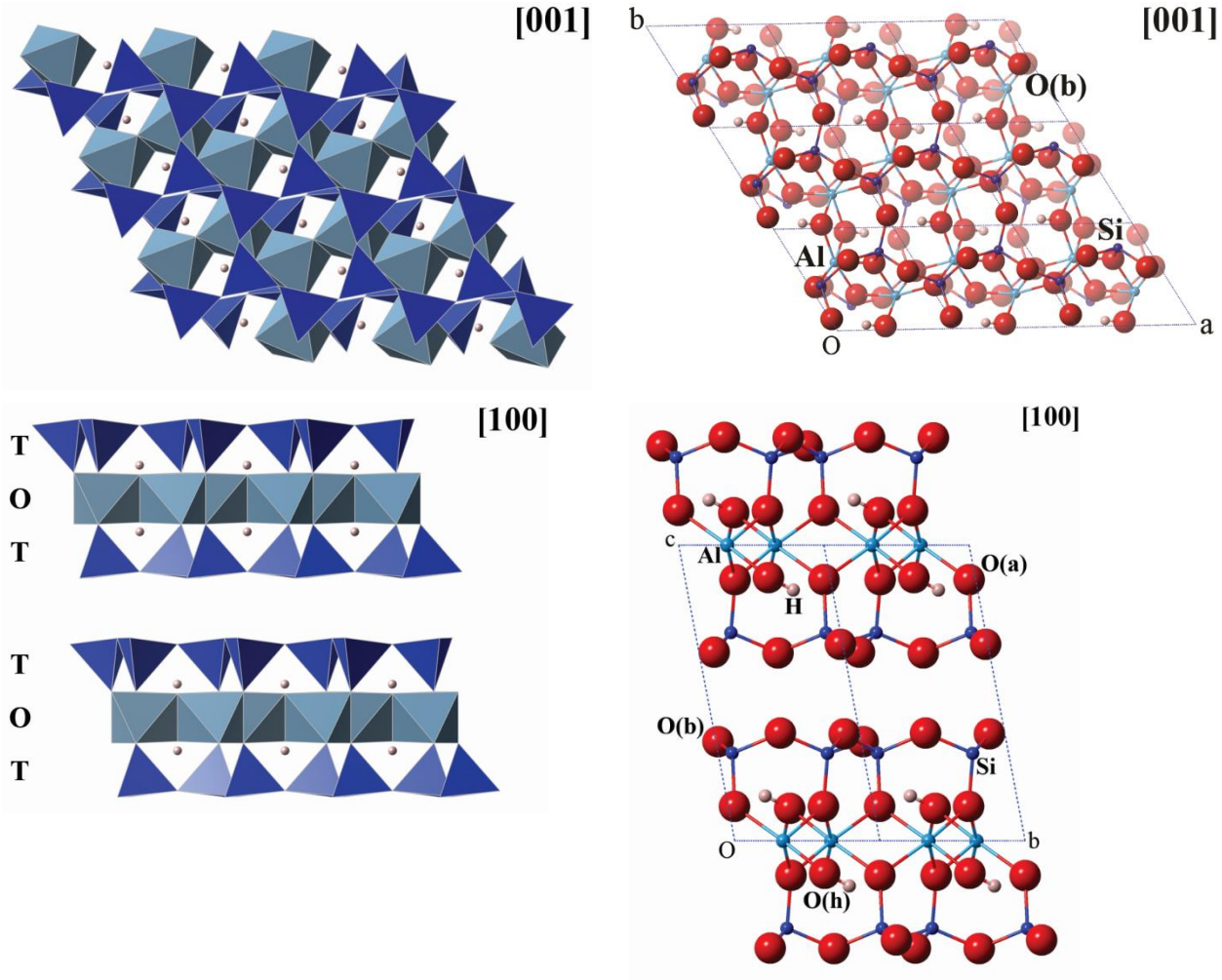

Figure 5.1. Polyhedral models of the primitive cell of pyrophyllite as seen from the [010] and [001] directions. Stick and ball representation along the [100] direction was reported to clearly show the atomic arrangement within the mineral.

We optimized within the same run the lattice constants and internal coordinates using the analytical gradient method for the atomic positions and a numerical gradient for the unit-cell parameters. The

Hessian matrix is upgraded with the Broyden–Fletcher–Goldfarb–Shanno algorithm (Broyden, 1970a; Broyden, 1970b; Fletcher, 1970; Goldfarb, 1970; Shanno, 1970). The tolerances for the maximum allowed gradient and the maximum atomic displacement for considering the geometry as converged have been set to 0.00006 hartree bohr^{-1} and 0.00012 bohr, respectively.

Within Density Functional Theory, both GGA and LDA functionals often fail to adequately describe long-range dispersive interactions. To overcome this problem, dispersive forces are evaluated according to the semiempirical approach (DFT+D) of Grimme (2006), which adds the following contribution to the calculated DFT energy:

$$E_{DISP} = -s_6 \sum_{\mathbf{g}} \sum_{i \neq j} f_{dump}\left(R_{ij,\mathbf{g}}^6\right) \frac{C_6^i C_6^j}{R_{ij,\mathbf{g}}^6} \qquad (5.1)$$

$$f_{dump} = \frac{1}{1 + e^{-d\left(R_{ij,\mathbf{g}}/R_{vdw} - 1\right)}}$$

The summation over all atom pairs *ij* and **g** lattice vectors excludes the self- interaction contribution ($i = j$) for every **g**. The parameters C_6^i represent the dispersion coefficient for the atom *i*, $R_{ij,\mathbf{g}}$ is the interatomic distance between atom *i* in the reference cell and atom *j* in the neighbouring cells at distance |**g**| and s_6 is a functional-dependent scaling factor. We employed the C_6^i parameters reported in the work of Grimme (2006), which were obtained from atomic ionization potentials (I_p) and static dipole polarizabilities (α) according to the formula $C_6^i = 0.05 N I_p^i \alpha^i$, where *N* depends on atom row in the periodic table. The function f_{dump} is used to dump the energy correction to avoid double counting of short-range contributions and depends on the sum of atomic van der Waals radii (R_{vdw}) and on a steepness parameter (d = 20). According to results previously reported in literature for urea crystals (Civalleri et al., 2008), showing that the E_{DISP} correction tends to overestimate cohesive energy in solid crystals, the original B3LYP-D parameters where modified setting s_6 to 1, the hydrogen atom van der Waals radius, R_{vdw}(H), to 1.30 and the heavier atom van der Waals radii were scaled by a factor 1.05. This modified method, called B3LYP-D*, has been adopted with good results in our previous works on talc (Ulian et al., 2013a; Ulian et al., 2013b).

Vibrational features

In periodic systems and within the harmonic approximation, the phonon frequencies at Γ point are evaluated diagonalising the central zone (k = 0) mass-weighted Hessian matrix:

$$W_{ij}(k=0)=\sum_{G}\frac{H_{ij}^{0G}}{\sqrt{M_i M_j}} \tag{5.2}$$

H_{ij}^{0G} represents the second derivative of the electronic and nuclear repulsion energy E evaluated at equilibrium **u=0** with respect to the displacement of atom A in cell 0 ($u_i = x_i - x_i^*$) and displacement of atom B in cell G ($u_j = x_j - x_j^*$) from their equilibrium position x_i^*, x_j^*:

$$\sum_{G} H_{ij}^{0G} = \sum_{G}\left[\frac{\partial^2 E}{\partial u_i^0 \partial u_j^G}\right]_0 \qquad i=1,...,3N; \quad j=1,...,3N \tag{5.3}$$

The calculation of the Hessian at equilibrium is made by the analytical evaluation of the energy first derivatives, Φ_j of E with respect to the atomic displacements:

$$\Phi_j = \sum_{G} v_j^G = \sum_{G}\frac{\partial E}{\partial u_j^G} \qquad j=1,...,3N \tag{5.4}$$

while second derivatives at **u = 0** (where all first derivatives are zero) are calculated numerically using a "two-point" formula:

$$\left[\frac{\partial \Phi_j}{\partial u_i^0}\right]_0 \approx \frac{\Phi_j(0,...,u_i^0,...,0)-\Phi_j(0,...,u_i^0,...,0)}{u_i^0} \qquad i=1,...,3N; \quad j=1,...,3N \tag{5.5}$$

More details on the vibrational calculation made by CRYSTAL can be found in literature.(Pascale et al., 2004; Tosoni et al., 2005) The Hessian matrix eigenvalues provide the normal harmonic frequencies ω_h and it is obtained with 3N+1 SCF and gradient calculation. This method can be quite demanding for large unit cells, but point symmetry facilitates a remarkable time saving, because only the lines of the Hessian matrix referring to irreducible atoms need to be generated. The tolerances were increased to obtain better results (TOLDEE = 10).

5.3 Results

Geometry optimization

The optimization of the pyrophyllite was made on the primitive cell ($P\bar{1}$) to reduce the computational costs of the procedure, then the results were reported in terms of the crystallographic cell. A detailed description of the data obtained by GTO/B3LYP-D* approach is presented in Table 5.1 alongside XRD structural refinement (Lee and Guggenheim, 1981; Wardle and Brindley, 1972) and very recent theoretical results (Tunega et al., 2012) reported in literature.

The adoption of the modified Grimme's dispersion parameters (B3LYP-D*) provided lattice parameters and bond lengths in very good agreement with experimental data, with only a small underestimation of the cell volume (0.4%). In particular, the description of the **c**-axis is adequately accurate. As observed in a previous work on talc (Ulian et al., 2013a), the use of original B3LYP-D parameterization (Grimme, 2006) method gives larger cell contractions than B3LYP-D* ones, because it was intended for molecules rather than solids. Compared to the planewaves/PBE-D approach, we provide a slight improvement in the description of the lattice axis *a*, *b* and in particular *c*, but there are some differences in the unit-cell angles, especially β. The volume contraction is also very similar.

Table 5.1. Experimental and theoretical lattice parameters and internal geometry of pyrophyllite

PYROPHYLLITE	**Single-crystal XRD**		**Theoretical**	
	(1)	**(2)**	**B3LYP-D*(3)**	**PBE-D(4)**
Lattice				
a (Å)	5.160	5.1614	5.183	5.167
b (Å)	8.966	8.9576	8.956	8.978
c (Å)	9.347	9.3511	9.317	9.300
α (°)	91.18	91.03	90.43	90.97
β (°)	100.46	100.37	96.68	100.91
γ (°)	89.64	89.75	89.84	89.73
Basal *d* spacing (Å)	9.192	9.198	9.254	9.132
Vcc (Å^3)	425.157	425.206	423.316	423.610
	Mean bond lengths (Å)			
Si–O^b	1.6117	-	1.6236	1.6280
Si–O^a	1.632	-	1.6461	1.6480
Al-O	1.924	-	1.9290	1.9230
Al-O^h	1.8885	-	1.8938	1.8940
O–H	-	-	0.9582	0.9710

(1) (Lee and Guggenheim, 1981)
(2) (Wardle and Brindley, 1972)
(3) Present study
(4) (Tunega et al., 2012)

The internal geometry, namely the mean bond lengths, is very similar to the one obtained by previous theoretical study. Both results are slightly larger than experimental values of about 0.7%. Pyrophyllite, as other phyllosilicates, have a distorted hexagonal tetrahedral layer due to the non-ideal SiO_4^{3-} tetrahedrons. The same observation can be extended to the octahedral layer. In our simulation, the tetrahedral rotation angle, defined as

$$\alpha = 1/2\left(\sum_{i=1}^{6} |\phi_i - 120°| \Big/ 6 \right) \tag{5.6}$$

where ϕ_i is the angle described by triples of basal oxygen atoms (Bailey, 1988), is 23.82°, in good agreement with the reported experimental value (20.4°) (Lee and Guggenheim, 1981).

The octahedral rotation angle is given by

$$\cos\psi = \Phi_0 / 2\langle M - O, OH \rangle \tag{5.7}$$

with Φ_0 the thickness of the O-layer (Å) and $\langle M - O, OH \rangle$ the mean bond lengths in the octahedrons. The obtained ψ value is 41.12°, in good agreement with previous data (Lee and Guggenheim, 1981). According to Lee and Guggenheim (Lee and Guggenheim, 1981) the tetrahedral rotation reduces the lateral dimensions of the tetrahedral sheet. Since tetrahedral faces may be approximately described as equilateral triangles, the resulting distance between apical oxygens, AO_a, may be calculated as

$$AO_a = \left[e_{th} \cos(\alpha/2) \right] / \sqrt{3} \tag{5.8}$$

where e_{th} is the mean tetrahedral edge length. In the B3LYP-D* simulated structure, the AO_a value is 3.01 Å, in very good agreement with the observed 3.00 Å obtained from XRD refinement (Lee and Guggenheim, 1981).

Phonon calculations

The vibrational features of pyrophyllite were simulated in the primitive cell, which has 20 atoms. The number of normal modes are given by 20 x 3 = 60, three of them are related to translation of the whole unit-cell. The remnant 57 modes are vibrational and subdivided as:

$$\Gamma_{tot} = 30A_g + 27A_u$$

Modes with A_g symmetry are Raman-active, while A_u ones are IR-active. None of them exhibits symmetry-related degeneracies, thus the IR and Raman spectra have 27 and 30 signals, respectively. We report in Table 5.2 the results obtained from our simulated IR/Raman analysis and the calculated IR

spectrum in Figure 5.2. The analysis of the vibrational modes has been conducted with the aid of the visualization software MOLDRAW (Ugliengo et al., 1993) and the potential energy distribution (PED) computed by CRYSTAL09.

Table 5.2. Calculated pyrophyllite harmonic phonon frequencies.

Mode	IRREP	Active	Frequency (cm^{-1})	IR Intensity	Exp[1]	Exp[2]
O^a – H --- O^b	A_u	IR	411	220		
O^a – H --- O^b	A_u	IR	424	49		420
O^a – H --- O^b	A_u	IR	427	28		
	A_g	R	436	0		
	A_g	R	454	0		
Al – O^a – Al	A_u	IR	474	1318		
	A_g	R	477	0		
Si – O^a – Al + OH libration	A_u	IR	488	1532		
	A_g	R	502	0		
	A_g	R	531	0		
Si – O^a – Al	A_u	IR	533	352		
	A_g	R	546	0		
Si – O^a – Al	A_u	IR	549	640		537
Si – O^a – Al + OH libration	A_u	IR	556	937		579
	A_g	R	613	0		
O^a – Si – O^b bending	A_u	IR	643	2		625
	A_g	R	656	0		
	A_g	R	718	0		
O^a – Si – O^b “umbrella”	A_u	IR	749	49		
	A_g	R	819	0		
Si – O^b symm	A_u	IR	819	165		814
Si – O^b symm	A_u	IR	842	183		835
	A_g	R	849	0		
Si – O^a in phase	A_u	IR	849	13		853
Si – O^a out of phase / Al-(OH)	A_u	IR	908	2399	950	949
	A_g	R	927	0		
OH libration	A_u	IR	1016	616		
	A_g	R	1021	0		
Si – O^b symm	A_u	IR	1048	2570	1046	1048
	A_g	R	1049	0		
Si – O^b symm	A_u	IR	1063	2204		1067
	A_g	R	1065	0		
	A_g	R	1078	0		
Si – O^b symm / Al-(OH)	A_u	IR	1107	244	1120	1119
	A_g	R	1110	0		
	A_g	R	3884	0		
OH stretching (harmonic)	A_u	IR	3886	551		
OH stretching (anharmonic)	A_u	IR	3709	-	3669	

[1] (Mukhopadhyay et al., 2010)
[2] (Ogorodova et al., 2011)

The region between 0 – 400 cm^{-1}, which is not completely shown in the spectrum of Figure 5.2, is characterized by 8 low-intensity phonon modes. The first intense peak is composed by two Al–O^a–Al modes which fall at 474 and 488 cm^{-1}, respectively. From the PED analysis it was found an OH libration component in the signal at 488 cm^{-1}. The peak between 500 – 600 cm^{-1} is formed by three signals at 533, 549 and 556 cm^{-1}, related to Si – O^a – Al bending modes. The mode at 556 cm^{-1} exhibits an OH libration component. Two modes related to O^a – Si – O^b modes have been identified.

The first one is at 643 cm^{-1}, but is not visible in the spectrum because of its low intensity. The second is associated to an "umbrella" bending mode at 749 cm^{-1}, faintly visible.

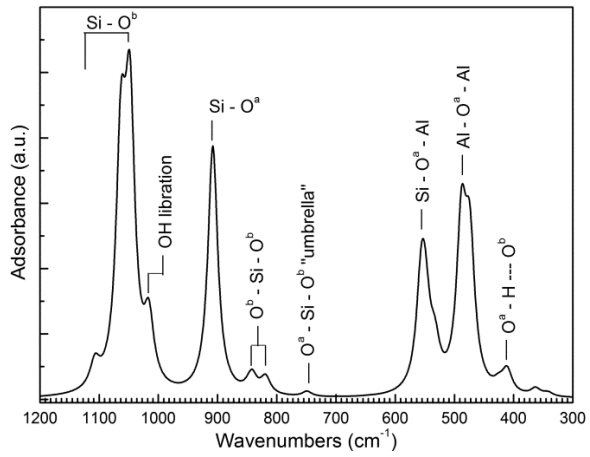

Figure 5.2. Simulated infrared spectrum of pyrophyllite.

In the spectral region above 800 cm^{-1} there are the Si – O stretching modes. There are two low intensity signals at 819 and 842 cm^{-1}, which have been assigned to symmetric Si – O^b stretching vibrations. Two modes have been identified as Si – O^a stretching: one at 849 cm^{-1}, but it is very faint and overlapped to the one at 842 cm^{-1}; the other is at 908 cm^{-1}, with high intensity. Finally three signals are related to the asymmetric Si – O^b stretching modes, at 1048 (very intense), 1063 (very intense) and 1107 cm^{-1} (low intensity).

Regarding OH phonon modes, there is a medium-intensity signal with at 1016 cm^{-1}, related to a pure OH libration mode and the OH stretching mode at 3886 cm^{-1}. When anharmonicity was taken into account, the latter fell at 3709 cm^{-1}, with an anharmonic constant of 82 cm^{-1}. Unfortunately, the CRYSTAL09 code do not extend the anharmonic calculation to other modes but the stretching one, preventing the calculation of the anharmonicity of libration modes.

The simulated infrared spectrum is in reasonable agreement with the one reported in an experimental work (Mukhopadhyay et al., 2010). The differences are imputable both to the approximations adopted and the considered model, which is an end-member of the pyrophyllite mineral.

Equation of state of pyrophyllite

The *P-T* behaviour of any solid insulator can be derived from the Helmholtz energy (Anderson, 1995)

$$F = E_{ST}(V) + F_{VIB}(V,T) \tag{5.9}$$

where E_{ST} is the potential of a static lattice at absolute zero (athermal limit), F_{VIB} is the vibrational energy related to the thermal motion of the atoms. The pressure can be obtained by the first derivative of Eq.(5.9)

$$P = -\left(\frac{\partial F}{\partial V}\right)_T = -\left(\frac{\partial E_{ST}}{\partial V}\right)_{T=0} + \left(\frac{\partial F_{VIB}}{\partial V}\right)_T \tag{5.10}$$

In the present work, the evaluation of the pyrophyllite equation of state is subdivided in two subsections. In the first one, only the static lattice values of the mineral are obtained and an atomic description of the pressure-induced variations to the structure is provided. In the second one, the thermal contribution are included to evaluate the thermomechanical properties of the mineral at different temperatures.

Static calculations

The description of the compressional behaviour of a solid phase within the periodic boundary conditions has been conducted with the EOS algorithm present in the CRYSTAL09 code (Ottonello et al., 2009a). With this method, starting from the optimized pyrophyllite primitive cell presented above, a cell optimization is carried out with a symmetry-preserving relaxation procedure by exploring, at selected values of V, the minimum energy *a/b* and *c/b* ratios and internal coordinates. We considered twenty volumes between 0.90*V_{init} and 1.10 V_{init}, where V_{init} is the volume of the original cell. The relaxed lattice parameters at the athermal limit are reported in Table 5.3. The partial derivation of a third-order polynomial fit on the computed E-V couples (Figure 5.3a) reproduced the local values of the *ab initio* pressure, allowing the analysis of the functional dependence of the structural details on *P* at *T* = 0 K:

$$P_{st} = -\left(\frac{\partial E}{\partial V}\right)_{T=0} = 3p_1V^2 + 2p_2V + p_3 \qquad (5.11)$$

with p_1 = -5.27514·10^{-7}, p_2 = 3.63107·10^{-4} and p_3 = -0.0828 the fitting parameters (R = 0.99994), 1 Ha/Å^3 = 4357.743335 GPa. A graphical representation of P_{st}/V trend is shown in Figure 5.3b.

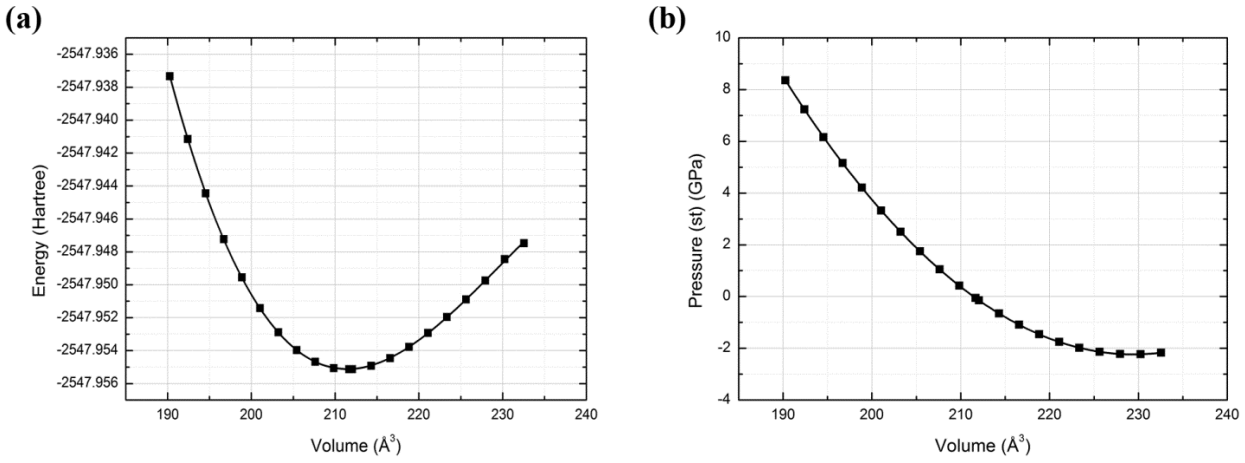

Figure 5.3. Calculated Energy/Volume (a) and related Pressure/Volume (b) diagrams for the pyrophyllite unit-cell.

Pyrophyllite volume *vs*. P_{st} data were fitted using a third-order finite strain isothermal Birch-Murnaghan Equation of State (III-BM EOS) (Birch, 1947):

$$P_{st} = -\left(\frac{\partial E}{\partial V}\right)_{T=0} = \frac{3}{2}K_0\left[\eta^{-7/3} - \eta^{-5/3}\right]\left\{1 - \frac{3}{4}(4 - K')\left(\eta^{-2/3} - 1\right)\right\} + P_0 \qquad (5.12)$$

where $\eta = V/V_0$ is a dimensionless parameter and V_0 is the volume at reference pressure P_0. The best fitting procedure was made by least-square method, using the EOS-FIT5.2 software (Angel, 2001). We obtained the refined elastic parameters: V_0 = 211.634 Å^3, K_0 = 46.90 GPa and K_0' = 11.14.

Table 5.3. Simulated unit-cell constants of pyrophyllite at different volumes

Volume (Å^3)	a (Å)	b (Å)	c (Å)	α (°)	β (°)	γ (°)	P_{st} (GPa)	V/V_0
190.258445	5.033160	5.051135	8.824885	84.363006	95.917132	59.969962	8.3590	0.8990
192.398826	5.050671	5.067158	8.866686	84.429182	95.963983	59.947113	7.2332	0.9091
194.549270	5.067750	5.082592	8.909848	84.500862	96.014848	59.925877	6.1658	0.9193
196.707019	5.084378	5.097450	8.954283	84.573699	96.067045	59.906569	5.1589	0.9295
198.881057	5.100584	5.111713	9.000493	84.647029	96.123094	59.889268	4.2094	0.9397
201.045976	5.116131	5.125187	9.048243	84.715623	96.183915	59.874635	3.3286	0.9500
203.223276	5.131134	5.137965	9.098297	84.778425	96.252092	59.862467	2.5081	0.9603
205.416561	5.145540	5.149986	9.151203	84.836770	96.332732	59.852470	1.7477	0.9706
207.621754	5.159336	5.161291	9.206906	84.888329	96.428422	59.844936	1.0501	0.9811
209.836434	5.172398	5.171888	9.265655	84.927212	96.535527	59.839466	0.4170	0.9915
211.658081	*5.182925*	*5.180296*	*9.317256*	*84.983157*	*96.684910*	*59.821935*	*-0.0530*	*1.0001*
212.048948	5.184471	5.181516	9.327546	84.955858	96.646898	59.836459	-0.1479	1.0020
214.306448	5.195819	5.190379	9.393269	84.980722	96.749531	59.834974	-0.6547	1.0126
216.556663	5.206030	5.198345	9.461737	84.996412	96.841423	59.834115	-1.0898	1.0233
218.814921	5.214549	5.204738	9.535033	84.983821	96.888671	59.836475	-1.4563	1.0339
221.080194	5.221265	5.209750	9.614075	84.957898	96.920582	59.837812	-1.7531	1.0446
223.350435	5.225938	5.213228	9.700864	84.886180	96.941950	59.839072	-1.9796	1.0554
225.623173	5.228108	5.214615	9.799609	84.726255	96.971729	59.841425	-2.1351	1.0661
227.929586	5.228052	5.214306	9.917720	84.387466	97.088552	59.844723	-2.2201	1.0770
230.243840	5.224255	5.211169	10.091980	83.331826	97.464767	59.853646	-2.2315	1.0879
232.553445	5.222510	5.209808	10.214643	82.984028	97.450138	59.854612	-2.1693	1.0989

In Figure 5.4 we report (a) the evolution of volume and (b) lattice parameters at different pressure. Regarding the compressive regime (P > 0 GPa), the calculated trend is monotonic. It is graphically clear that pyrophillite deformation exhibits a strongly anisotropic behaviour, with smaller variations for *a* and *b* cell parameters than for the *c* one. It is possible to describe the observed anisotropy calculating the axial bulk moduli with a III-BM EOS fit on the lattice parameters values at different pressures. The obtained refined data for the *a*, *b* and *c* axis were, respectively: : a_0 = 5.181 Å, $K_{T0}(a)$ = 83.63 GPa and $K'(a)$ = 3.25; b_0 = 5.178 Å, $K_{T0}(b)$ = 101.94 GPa and $K'(b)$ = 3.17; c_0 = 9.311 Å, $K_{T0}(c)$ = 27.74 GPa and $K'(c)$ = 8.16. The axial compressibilities, described as $\beta = 1/3K_{T0}$, are in

ratio β(a): β(b): β(c) = 1.219 : 1.000 : 3.674. The obtained axial values are very close to those reported in a previous work on talc (Ulian et al., 2013b). This is not surprising because the covalent bonds in the dioctahedral TOT layers are less compressible than the interlayer dominated by Columbian and van der Waals forces (*c* direction).

In the explored volume range we observed a negligible variation of the TOT layer thickness. The $\langle$Si-O$\rangle$ and $\langle$Al-O$\rangle$ bond lengths span from 1.631 Å and 1.926 Å (lower limit) to 1.620 Å and 1.886 Å (upper limit), respectively. More in detail, in the SiO_4 tetrahedrons the Si – O^a distances are slightly more influenced than the Si – O^b ones, but in AlO_6 octahedrons we did not find the same trend.

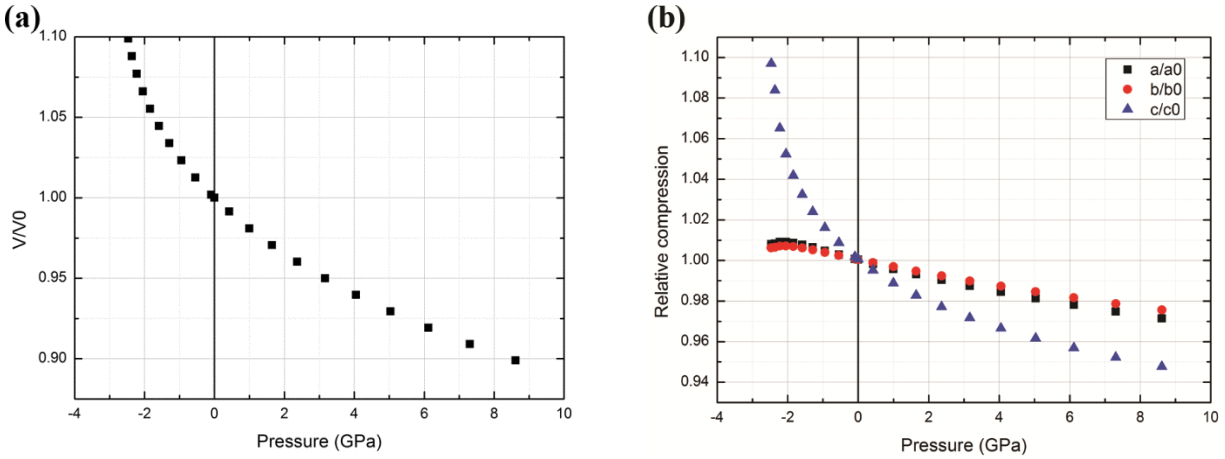

Figure 5.4. (a) Volume and (b) lattice parameters compressional behaviour of pyrophyllite under compression and expansion.

Furthermore, we noticed that the expansion of the unit cell causes an increase of the distortion index both tetrahedrons and octahedrons, while the compression leads to the opposite behaviour. Similarly to talc structure (Ulian et al., 2013b), the increase of pressure is followed by higher rotation angle ρ (34.88° at 8 GPa) than that of the uncompressed pyrophyllite structure. Expanding the unit-cell, ρ diminishes to 20.06° at -2 GPa.

Negligible O-H bond length and Al – O – H angle variations in the pressure range investigated have been observed.

Thermal contribution and thermomechanical properties

In statistical thermodynamics, the vibrational energy is given by

$$F_{VIB} = -kT \ln Z \tag{5.13}$$

with Z the partition function found by taking the sum of all quantum energy levels for each independent oscillators in the solid lattice

$$Z = \sum_i e^{-\varepsilon_i / kT} \tag{5.14}$$

The ε_i values are the eigenvalues of the energy operator, which can be used to define the partition function for each vibrational mode, Z_i.

$$\varepsilon_i = \frac{1}{2}\hbar\varpi_i, \frac{3}{2}\hbar\varpi_i \frac{5}{2}\hbar\varpi_i, etc... \tag{5.15}$$

$$Z_i = e^{-\hbar\varpi_i/2kT} \sum_{i=0}^{\infty} e^{-3\hbar\varpi_i/2kT} = \frac{e^{-\hbar\varpi_i/2kT}}{\left(1 - e^{-\hbar\varpi_i/kT}\right)} \tag{5.16}$$

It is then possible to define the vibrational contribution to the Helmholtz given by each mode as:

$$F_{VIB_i} = -kT \ln Z_i = \frac{\hbar\varpi_i}{2kT} \ln\left(1 - e^{\hbar\varpi_i/kT}\right) \tag{5.17}$$

which can then be summed over the *3n-3* oscillators (*n* the number of atoms in the unit-cell) in the considered lattice to obtain the whole thermal contribution to the free energy

$$F_{VIB} = \frac{1}{2}\sum_{i=1}^{3n-3} \hbar\varpi_i + kT \sum_{i=1}^{3n-3} \ln\left(1 - e^{-\hbar\varpi_i/kT}\right) \tag{5.18}$$

where the first addendum represents the zero point energy (E_{ZP}) of the solid, unaffected by the temperature and the second term is the energy arising from excitation due to temperature (F_{TH}). The term $\hbar\varpi_i/kT$ can be substituted with X_i to simplify the expression

$$F_{VIB} = \frac{kT}{2}\sum_{i=1}^{3n-3} X_i + kT \sum_{i=1}^{3n-3} \ln\left(1 - e^{-X_i}\right) \tag{5.19}$$

Applying Eq. (19) to Eq. (10) allows to find the pressure related to each volume transformation

$$P = -\left(\frac{\partial E_{ST}}{\partial V}\right)_{T=0} + \frac{kT}{2V}\sum_{i=1}^{3n-3} \gamma_i X_i + \frac{kT}{V}\sum_{i=1}^{3n-3} \gamma_i \frac{X_i}{e^{X_i} - 1} \tag{5.20}$$

where γ_i is the mode-gamma of each vibrational frequency, given by

$$\gamma_i = -\frac{\partial \ln \varpi_i}{\partial \ln V} = -\frac{V}{\varpi_i}\frac{\partial \varpi_i}{\partial V} \tag{5.21}$$

The mode-gammas for pyrophyllite are summarized in Table 5.4.

In the quasiharmonic treatment the vibrational modes are dependent only on volume variations, but the thermodynamic properties are dependent on temperature by the second term of Eq. (5.18) (Anderson, 1995; Ottonello et al., 2009a; Ottonello et al., 2009b). Rewriting Eq. (5.20)

$$P = P_{ST} + P_{ZP} + P_{TH} = P_{T=0} + P_{TH} \qquad (5.22)$$

the pressure evaluated in the previous section is corrected by the zero point energy (P_{ZP}) and by the thermal contribution (P_{TH}). In Table 5.5 the corrected pressure values for Eq. (5.20) are reported for different in the range of temperatures 298.15 – 1000 K.

Table 5.4. Vibrational frequencies for pyrophyllite and related mode-gamma.

N	ν (cm^{-1})	Mode	IR,Raman	γi	N	ν (cm^{-1})	Mode	IR,Raman	γi
1	111.3	Acoustic	A,I	-	30	476.9	A_g	I,A	0.2
2	111.3	Acoustic	A,I	-	31	487.6	A_u	A,I	0.2
3	186.5	Acoustic	A,I	-	32	501.8	A_g	I,A	0.2
4	105.4	A_g	I,A	1.2	33	531.2	A_g	I,A	0.5
5	118.1	A_g	I,A	1.2	34	532.9	A_u	A,I	0.5
6	152.3	A_u	A,I	-0.1	35	545.5	A_g	I,A	0.4
7	188.2	A_g	I,A	0.9	36	549.0	A_u	A,I	0.4
8	188.3	A_u	A,I	0.3	37	555.6	A_u	A,I	0.3
9	189.2	A_u	A,I	0.3	38	613.4	A_g	I,A	0.4
10	208.8	A_u	A,I	1.0	39	642.5	A_u	A,I	0.3
11	209.4	A_g	I,A	1.3	40	656.1	A_g	I,A	0.2
12	219.2	A_g	I,A	1.3	41	717.7	A_g	I,A	0.3
13	263.5	A_u	A,I	0.5	42	749.1	A_u	A,I	0.2
14	267.3	A_g	I,A	0.7	43	818.8	A_g	I,A	0.2
15	301.9	A_g	I,A	0.2	44	818.9	A_u	A,I	0.2
16	320.8	A_g	I,A	0.1	45	841.9	A_u	A,I	0.2
17	340.6	A_u	A,I	0.2	46	848.9	A_g	I,A	0.3
18	345.4	A_g	I,A	0.3	47	849.0	A_u	A,I	0.3
19	346.2	A_u	A,I	0.5	48	907.5	A_u	A,I	0.2
20	362.7	A_u	A,I	0.1	49	926.7	A_g	I,A	0.3
21	380.4	A_g	I,A	0.2	50	1015.5	A_u	A,I	0.2
22	384.0	A_g	I,A	0.3	51	1021.0	A_g	I,A	0.2
23	398.5	A_g	I,A	0.4	52	1048.5	A_u	A,I	0.1
24	410.8	A_u	A,I	0.1	53	1049.3	A_g	I,A	0.1
25	424.0	A_u	A,I	0.2	54	1063.3	A_u	A,I	0.1
26	426.9	A_u	A,I	0.4	55	1065.1	A_g	I,A	0.1
27	436.4	A_g	I,A	0.2	56	1078.0	A_g	I,A	0.2
28	453.8	A_g	I,A	0.3	57	1107.2	A_u	A,I	0.0
29	473.5	A_u	A,I	0.2	58	1110.3	A_g	I,A	0.0
30	476.9	A_g	I,A	0.2	59	3883.9	A_g	I,A	0.0
31	487.6	A_u	A,I	0.2	60	3886.5	A_u	A,I	0.0

The bulk modulus (K_T) at a given cell volume (pressure) and temperature has been calculated by the 3rd-order BM3 EOS. Using isothermal curves, at different T, we can obtain at each temperature value the bulk modulus (K), its first derivative (K') and reference volume (V_0), at any fixed reference pressure. The values for T = 300 K are very close to those obtained with the experimental procedure

described by Pawley et al. (2002). Also, the calculated relative compression of pyrophyllite *vs* pressure at 300 K is in good agreement with the experimental data (see Figure 5.5). Pyrophyllite volume as a function of both temperature and pressure is reported in the three-dimensional plot of Figure 5.6.

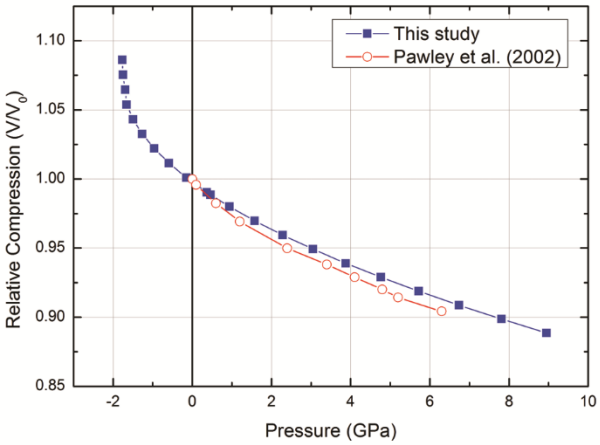

Figure 5.5. Comparison between theoretical (blu line) and experimental (red line) relative compression (V/V0) of pyrophyllite at 300 K.

Regarding the axial compressibility at room temperature, we fitted by the 3rd-order Birch Murnaghan equation the *a*, *b* and *c* axis data, obtaining, respectively: a_0 = 5.189 Å, $K_{T0}(a)$ = 89.46 GPa and $K'(a)$ = 3.00; b_0 = 5.184 Å, $K_{T0}(b)$ = 109.01 GPa and $K'(b)$ = 3.00; c_0 = 9.368 Å, $K_{T0}(c)$ = 26.03 GPa and $K'(c)$ = 8.12. The related axial compressibilities are β(a) = $3.73 \cdot 10^{-3}$, β(b) = $3.06 \cdot 10^{-3}$ and β(c) = $12.8 \cdot 10^{-3}$ GPa^{-1}, in ratio β(a): β(b): β(c) = 1.218 : 1.000 : 4.188.

From the quasi-harmonic mode gamma analysis of the 3*n* – 3 optic modes we obtained the $\alpha_T K_T$ product, by using the formula (Anderson, 1995; Ottonello et al., 2010)

$$\alpha_T K_T = \frac{R}{ZV} \sum_{i=4}^{3n} \gamma_i e^{X_i} \left(\frac{X_i}{e^{X_i} - 1} \right)^2 \tag{5.23}$$

As shown in Figure 5.7a, this product asymptotically attains a constant value at high temperatures, depending of the considered pressure. For example, at 0 GPa $\alpha_T K_T$ reaches a constant value of 1.2×10^{-3} GPa/K above the Debye temperature of the mineral (computed $\Theta = 927.17$ K at 0 GPa) (Figure 5.7a,b). To our knowledge, no experimental or theoretical data are available for pyrophyllite for a proper comparison at the moment. However, we reported a three-dimensional plot of the $\alpha_T K_T$ product to help the interpretation of the results from eventual future researches.

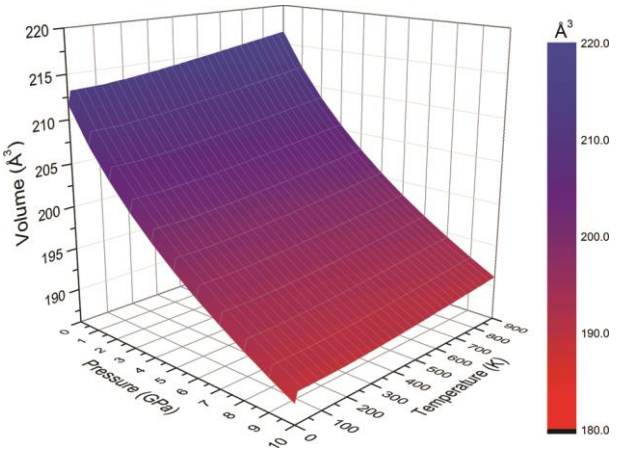

Figure 5.6. Compressional behaviour of talc between 0 – 10 GPa and 0 – 1000 K.

Table 5. Pressure values at different temperatures and volumes for pyrophyllite mineral and fit parameters of the third-order Birch-Murnaghan EoS.

Volume (Å^3)	**Temperature (K)**															
	0	*10*	*50*	*100*	*150*	*200*	*250*	*300*	*350*	*400*	*450*	*500*	*600*	*700*	*800*	*900*
232.553	-2.17	-2.21	-2.21	-2.20	-2.18	-2.16	-2.14	-2.12	-2.11	-2.09	-2.07	-2.05	-2.02	-1.99	-1.96	-1.92
230.244	-2.23	-2.23	-2.22	-2.21	-2.20	-2.18	-2.15	-2.13	-2.11	-2.09	-2.07	-2.05	-2.01	-1.96	-1.92	-1.88
227.930	-2.22	-2.17	-2.17	-2.16	-2.14	-2.12	-2.09	-2.07	-2.04	-2.02	-1.99	-1.97	-1.92	-1.87	-1.82	-1.76
225.623	-2.14	-2.04	-2.04	-2.03	-2.01	-1.98	-1.96	-1.93	-1.90	-1.88	-1.85	-1.82	-1.76	-1.70	-1.64	-1.57
223.350	-1.98	-1.84	-1.84	-1.83	-1.81	-1.78	-1.75	-1.73	-1.69	-1.66	-1.63	-1.60	-1.53	-1.46	-1.39	-1.32
221.080	-1.75	-1.57	-1.57	-1.56	-1.54	-1.51	-1.48	-1.45	-1.41	-1.38	-1.34	-1.31	-1.23	-1.15	-1.07	-0.99
218.815	-1.46	-1.23	-1.23	-1.22	-1.19	-1.17	-1.14	-1.10	-1.06	-1.03	-0.99	-0.94	-0.86	-0.77	-0.68	-0.60
216.557	-1.09	-0.82	-0.82	-0.81	-0.78	-0.76	-0.72	-0.68	-0.64	-0.60	-0.56	-0.51	-0.42	-0.33	-0.23	-0.13
214.306	-0.65	-0.34	-0.34	-0.33	-0.30	-0.27	-0.24	-0.20	-0.16	-0.11	-0.06	-0.02	0.08	0.19	0.29	0.40
212.049	-0.15	0.21	0.21	0.22	0.25	0.28	0.31	0.36	0.40	0.45	0.50	0.55	0.66	0.77	0.89	1.00
211.658	-0.05	0.31	0.31	0.33	0.35	0.38	0.42	0.46	0.51	0.56	0.61	0.66	0.77	0.88	1.00	1.11
209.836	0.42	0.82	0.82	0.83	0.85	0.89	0.93	0.97	1.02	1.07	1.12	1.18	1.29	1.41	1.54	1.66
207.622	1.05	1.49	1.50	1.51	1.53	1.56	1.60	1.65	1.70	1.76	1.81	1.87	1.99	2.12	2.25	2.38
205.417	1.75	2.24	2.24	2.25	2.27	2.30	2.35	2.40	2.45	2.51	2.57	2.63	2.76	2.89	3.03	3.17
203.223	2.51	3.04	3.04	3.05	3.07	3.11	3.15	3.20	3.26	3.32	3.38	3.45	3.58	3.72	3.87	4.02
201.046	3.33	3.90	3.90	3.91	3.94	3.97	4.02	4.07	4.13	4.19	4.25	4.32	4.46	4.61	4.77	4.92
198.881	4.21	4.82	4.83	4.83	4.86	4.89	4.94	4.99	5.05	5.12	5.19	5.26	5.41	5.56	5.72	5.88
196.707	5.16	5.82	5.82	5.83	5.85	5.89	5.93	5.99	6.05	6.12	6.19	6.26	6.41	6.58	6.74	6.91
194.549	6.17	6.87	6.87	6.87	6.90	6.93	6.98	7.04	7.10	7.17	7.24	7.32	7.48	7.65	7.82	8.00
192.399	7.23	7.97	7.97	7.98	8.01	8.04	8.09	8.15	8.22	8.29	8.36	8.44	8.61	8.78	8.96	9.15
190.258	8.36	9.14	9.14	9.15	9.17	9.21	9.26	9.32	9.39	9.46	9.54	9.62	9.79	9.97	10.16	10.35
V_0	211.63	213.21	213.22	213.27	213.37	213.51	213.67	213.86	214.06	214.27	214.48	214.71	215.17	215.64	216.11	216.58
K_T	48.63	47.33	47.30	47.17	46.97	46.77	46.56	46.37	46.19	46.03	45.87	45.73	45.48	45.28	45.12	45.01
K_T'	11.14	10.54	10.54	10.55	10.56	10.55	10.54	10.51	10.48	10.45	10.41	10.36	10.26	10.15	10.04	9.91

We calculated the isobaric temperature derivative of bulk modulus for pyrophyllite by linear regression of the K_T data as a function of temperature in the 100 – 900 K range. We reported the results in Table 5.6. It can be observed that the $(\partial K_T/\partial T)_P$ values decreases by incrementing pressure, with a ratio $(\partial K_T/\partial T \partial P)$ = -4.95. Worth to note that the quasi-harmonic treatment does not consider the fact that K_T would not vary linearly with T.

Table 5.6. Pyrophyllite bulk modulus K_T (GPa) at different *PT* conditions.

T (K)	**Pressure (GPa)**										
	0	*1*	*2*	*3*	*4*	*5*	*6*	*7*	*8*	*9*	*10*
0	48.6	57.5	67.2	76.4	85.1	93.5	101.6	109.5	117.2	124.7	132.1
10	47.3	57.4	66.7	75.5	83.9	92.0	99.9	107.6	115.0	122.3	129.5
20	47.3	57.4	66.7	75.5	83.9	92.0	99.9	107.6	115.0	122.3	129.5
30	47.3	57.4	66.7	75.5	83.9	92.0	99.9	107.6	115.0	122.3	129.5
40	47.3	57.4	66.7	75.5	83.9	92.0	99.9	107.5	115.0	122.3	129.5
50	47.3	57.4	66.7	75.5	83.9	92.0	99.9	107.5	115.0	122.3	129.5
60	47.3	57.3	66.7	75.5	83.9	92.0	99.9	107.5	115.0	122.3	129.5
70	47.3	57.3	66.7	75.5	83.9	92.0	99.9	107.5	115.0	122.3	129.5
80	47.2	57.3	66.6	75.4	83.9	92.0	99.8	107.5	115.0	122.3	129.4
90	47.2	57.3	66.6	75.4	83.8	91.9	99.8	107.5	114.9	122.2	129.4
100	47.2	57.2	66.6	75.4	83.8	91.9	99.8	107.4	114.9	122.2	129.4
150	47.0	57.0	66.4	75.2	83.6	91.7	99.6	107.2	114.7	122.0	129.2
200	46.8	56.8	66.2	75.0	83.4	91.5	99.3	107.0	114.4	121.7	128.9
250	46.6	56.6	65.9	74.7	83.1	91.2	99.0	106.7	114.1	121.4	128.6
300	46.4	56.4	65.7	74.5	82.8	90.9	98.7	106.4	113.8	121.1	128.2
350	46.2	56.2	65.5	74.2	82.6	90.6	98.4	106.0	113.4	120.7	127.8
400	46.0	56.0	65.2	74.0	82.3	90.3	98.1	105.7	113.1	120.3	127.4
450	45.9	55.8	65.0	73.7	82.0	90.0	97.8	105.3	112.7	119.9	127.0
500	45.7	55.6	64.8	73.4	81.7	89.7	97.4	105.0	112.3	119.5	126.6
600	45.5	55.3	64.4	73.0	81.2	89.1	96.8	104.3	111.6	118.7	125.8
700	45.3	55.0	64.0	72.5	80.7	88.5	96.2	103.6	110.8	118.0	124.9
800	45.1	54.7	63.6	72.1	80.2	88.0	95.5	102.9	110.1	117.2	124.1
900	45.0	54.5	63.3	71.7	79.7	87.4	94.9	102.3	109.4	116.4	123.3
$(\partial K_T/\partial T)_P$	-27.6	-35.1	-41.6	-47.3	-52.6	-57.5	-62.1	-66.4	-70.5	-74.4	-78.2

Notes: $(\partial K_T/\partial T)_P$ values are reported in bar K^{-1}.

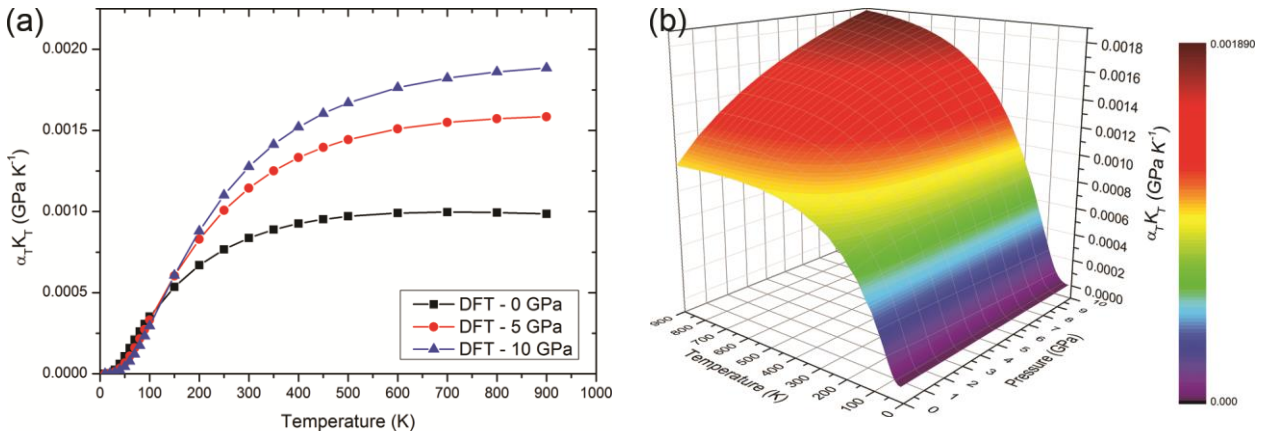

Figure 5.7. (a) Isobaric *ab initio* αK product at three different pressures and (b) three-dimensional plot of the αK product in different *PT* conditions.

With the knowledge of the bulk moduli at each *P-T* condition, obtained from the BM3 EOS fitting, we can directly calculate the thermal expansion coefficient (α_T) of pyrophyllite. We calculated α_T in the *P* range 0 – 10 GPa from 10 to 900 K and the results are reported in Table 5.7. As it can be observed from the plot in Figure 5.8a, the thermal expansion coefficient increases with *T*, but it is reduced by augmenting the pressure.

Table 7. Thermal expansion coefficient (α_T, 10^{-5} K^{-1}) in the pressure range 0-10 GPa at different temperatures.

T (K)	Pressure (GPa)										
	0	*1*	*2*	*3*	*4*	*5*	*6*	*7*	*8*	*9*	*10*
20	0.008	0.005	0.004	0.003	0.002	0.002	0.002	0.001	0.001	0.001	0.001
30	0.052	0.037	0.028	0.021	0.017	0.014	0.012	0.010	0.009	0.007	0.007
40	0.130	0.094	0.072	0.057	0.046	0.038	0.031	0.027	0.023	0.020	0.017
50	0.228	0.170	0.133	0.107	0.088	0.073	0.062	0.053	0.045	0.039	0.034
60	0.336	0.257	0.205	0.168	0.141	0.120	0.103	0.089	0.078	0.068	0.060
70	0.445	0.348	0.284	0.237	0.202	0.175	0.152	0.134	0.118	0.105	0.094
80	0.551	0.440	0.365	0.310	0.268	0.235	0.208	0.185	0.166	0.149	0.135
90	0.652	0.529	0.445	0.383	0.336	0.297	0.266	0.239	0.217	0.197	0.180
100	0.747	0.614	0.523	0.456	0.403	0.360	0.325	0.295	0.270	0.247	0.228
150	1.141	0.984	0.872	0.786	0.716	0.659	0.610	0.568	0.532	0.499	0.470
200	1.431	1.268	1.147	1.051	0.973	0.907	0.850	0.801	0.757	0.718	0.683
250	1.646	1.483	1.359	1.259	1.176	1.104	1.043	0.988	0.940	0.896	0.857
300	1.806	1.647	1.523	1.420	1.334	1.259	1.194	1.137	1.085	1.038	0.996
350	1.924	1.771	1.648	1.545	1.457	1.381	1.313	1.253	1.200	1.151	1.106
400	2.012	1.866	1.744	1.642	1.553	1.476	1.407	1.346	1.290	1.240	1.194
450	2.076	1.937	1.818	1.717	1.628	1.550	1.481	1.419	1.362	1.311	1.263
500	2.123	1.991	1.876	1.775	1.688	1.610	1.540	1.477	1.420	1.367	1.319
600	2.179	2.061	1.954	1.858	1.772	1.695	1.625	1.562	1.504	1.451	1.402
700	2.201	2.099	2.000	1.909	1.826	1.750	1.682	1.619	1.561	1.508	1.459
800	2.203	2.117	2.026	1.940	1.861	1.787	1.720	1.658	1.601	1.548	1.499
900	2.191	2.120	2.039	1.959	1.883	1.812	1.747	1.686	1.630	1.578	1.529

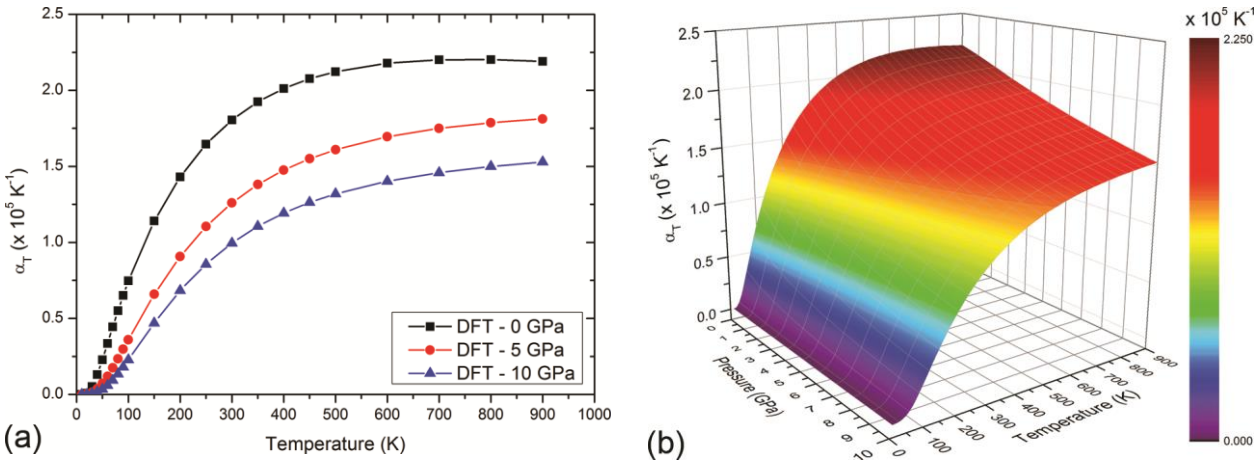

Figure 5.8. (a) Isobaric *ab initio* αK product at three different pressures and (b) three-dimensional plot of the αK product in different *PT* conditions.

The calculation of thermodynamic properties relies on the Einstein model for optic modes. Differently from the work of Ottonello et al. (2009a), the acoustic modes contribution described by Kieffer's

approach (Kieffer, 1979a; Kieffer, 1979b; Kieffer, 1979c) was not considered. Within the harmonic approximation, the isochoric heat capacity of a solid insulator can be expressed as (Anderson, 1995):

$$C_V = \frac{3R}{Z}\left(\frac{2}{\pi}\right)^3 \sum_{i=1}^{3}\int_0^{X_i} \frac{\left[\arcsin\left(X/X_i\right)\right]^2 X^2 e^X dX}{\left(X_i^2 - X^2\right)^{1/2}\left(e^X - 1\right)^2} + \frac{R}{Z}\sum_{i=4}^{3n} e^{X_i}\left(\frac{X_i}{e^{X_i}-1}\right)^2 \quad (5.24)$$

The relationship

$$C_P = C_V + T\alpha_T^2 K_{T,P} V_{P,T} \quad (5.25)$$

allows to obtain the isobaric heat capacity. The first term of Eq. (24) is the acoustic modes contribution described by Kieffer's approach (Kieffer, 1979a; Kieffer, 1979b; Kieffer, 1979c), while the second one is related to the optical modes. The complete calculation of the maximum frequency of each acoustic branch requires the knowledge of the averaged shear and longitudinal wave velocities at each volume (pressure) and these quantities can be obtained by the elastic constants at each compressional state (Perger et al., 2009; Ulian et al., 2013b). Due to computational costs, we considered the acoustic mode contribution to the thermochemical properties only at 0 GPa. However, as shown in our previous work on talc (Ulian and Valdrè, 2014), the acoustic contribution to the whole property is very low (< 4%) at room temperature and above. Then, the optical part of Eq.(24) represents an adequate approximation of the heat capacity fot T > 300 K.

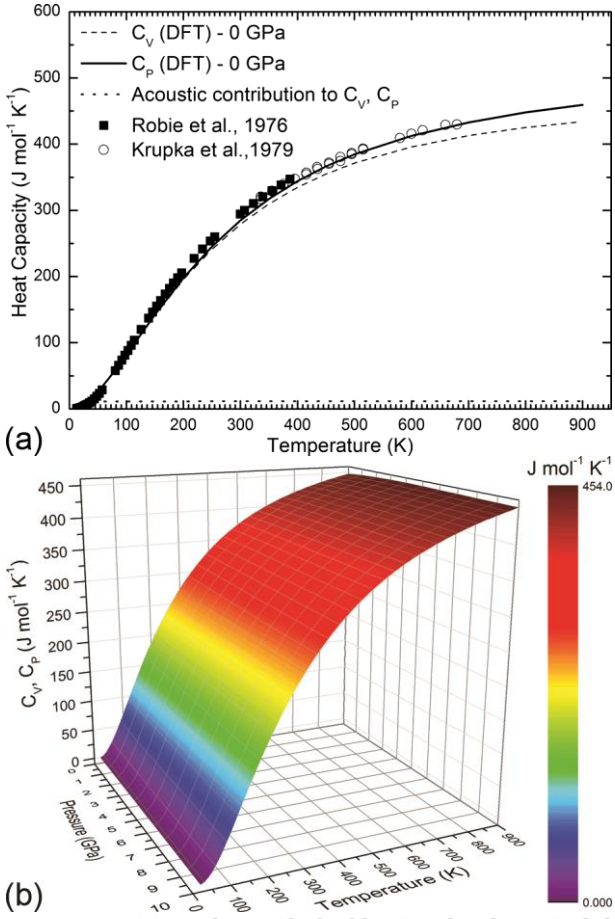

Figure 5.9. (a) Isochoric (dashed line) and isobaric (solid line) *ab initio* heat capacity at 0 GPa. Acoustic modes contribution has been reported as dotted gray line. (b) Three-dimensional plot of isobaric heat capacity at different *PT* conditions.

The C_V and C_P values obtained at 0 GPa are plotted in Figure 5.9a, alongside previous experimental isobaric heat capacity data of pyrophyllite (Krupka et al., 1979; Robie et al., 1976). There is a very good agreement between theoretical and experimental results above 400K, but the *ab initio* results are slightly underestimated in the range between 10 – 400 K. The isobaric heat capacity calculated with Eq. 28 has been fitted in the range 300 – 900 K by the Haas-Fisher polynomial expression (Haas and Fisher, 1976)

$$C_p = a + bT + cT^{-2} + dT^2 + eT^{-1/2} \quad (5.26)$$

with regression coefficients $a = 7.2864 \cdot 10^2$, $b = 2.9561 \cdot 10^{-2}$, $c = -3.5316 \cdot 10^{-5}$, $d = -4.5722 \cdot 10^{-5}$ and $e = -7.7738 \cdot 10^3$. The polynomial regression in the chosen temperature range is very accurate, with a mean error of 0.1 J/(mol K). We reported also a three-dimensional plot of the C_P data from 0 to 10 GPa (Figure 9b) to show how the pressure affects this thermochemical property. It can be observed that, for $T < 500$ K, the isobaric heat capacity decrease upon pressure raising, while for $T > 500$ K C_P increases.

5.4 Discussion and Conclusions

The DFT/B3LYP-D* together with an all-electron GTO basis set proposed in this study proved to be adequately accurate in the description of the pyrophyllite mineral. We have shown in previous works that it is also a good modelling approach for talc mineral (Ulian et al., 2013a; Ulian et al., 2013b; Ulian and Valdrè, 2014), and for sheet silicates in general. The correct evaluation of the weak interaction forces is crucial for both the energy and geometry of the mineral phase, which also affects other physical-chemical properties. In particular, while *a* and *b* lattice parameters have been accurately simulated in the past by DFT, because they are dominated by strong covalent bonding, the **c**-axis length is the most affected by dispersive forces and, prior to the semi-empirical correction for van der Waals forces in quantum-mechanics codes, it was generally overestimated in the range 10 – 12 Å (Refson et al., 2003; Sainz-Diaz et al., 2001).

Regarding the vibrational spectrum, we observed that the inclusion of dispersive forces increased anharmonicity of hydroxyl group vibrations and a general blue shift of the other modes. This effects can be explained by the reduction of the *c* parameter due to the B3LYP-D* approach. The same conclusion has been drawn in a previous theoretical study on kaolinite, conducted with similar computational approach (Ugliengo et al., 2009). However, the results obtained in the present work on pyrophyllite are encouraging because the most intense signals, even the anharmonic-corrected OH stretching, are in reasonable agreement with FTIR data on the raw mineral reported in literature (Mukhopadhyay et al., 2010; Ogorodova et al., 2011). Unfortunately, the CRYSTAL09 code do not allow to apply the anharmonic correction to other OH vibrational modes, such as librations, thus a proper comparison with experimental data on these signals is limited.

Accordingly to our data, pyrophyllite exhibits a strong anisotropic behaviour, with *a* and *b* lattice parameters less compressible than the *c* one. This is a general observation obtained for almost all

phyllosilicates, where the TOT layers are made by covalent bonds and held together by weak interactions. This is in good agreement with previous study conducted on this mineral class (Gatta et al., 2013; Pawley et al., 2002; Ulian et al., 2013b).

The bulk modulus and its pressure derivative obtained at the athermal limit (K_{T0} = 48.67 GPa, K'_{T0} = 11.14) are in quite good agreement with previous theoretical data (Voora et al., 2011), expressing a stiffer structure than the one observed by plane-wave simulations ($K_{T0\text{-}DFT\text{-}D2}$ = 38 GPa, $K'_{T0\text{-}DFT\text{-}D2}$ = 11; $K_{T0\text{-}vdW\text{-}TS}$ = 41 GPa; $K'_{T0\text{-}vdW\text{-}TS}$ = 12) . However, it is worth to note that the reported results from the previous simulations are related to the uniaxial compression of pyrophyllite along the **c**-axis. The authors considered a series of different *c* lattice vectors (in the range *c* ± 1.5Å) around the equilibrium geometry and then relaxed the atomic positions at constant unit-cell volumes. Thus, the calculated bulk modulus reported by Voora et al. (2011) is an approximation, because the authors neglected the contribution of the **a-** and **b-**axis axial moduli to the bulk one. Considered the chemical nature of pyrophyllite (covalent bonds in the *a* and *b* directions and weak forces dominating along the *c* one), this can be assumed as a fair approximation. Then, a proper comparison with our results have to be on the **c**-axis modulus, for which we obtained $K_{T0}(c)$ = 27.74 GPa and $K'(c)$ = 8.16. In this sense, our results show a softer behaviour of pyrophyllite than that obtained by PBE functional corrected for dispersive forces (DFT-D2). This could be due to both the different basis set and the *k*-sampling along the *c* lattice direction (2 points in plane-wave simulation, 4 points in our GTO one) adopted. The study of Voora et al. (2011), like ours, shows the importance of the role of dispersive forces in the calculation of mechanical properties. Indeed, when using standard DFT functionals, the bulk modulus is highly underestimated ($K_{T0\text{-}PBE}$ = 6 GPa) and the adoption of correction improved the results, depending on both the functional and the basis set quality.

We made a comparison between our theoretical results with experimental ones by considering the thermal equation of state and related quantities. We included the thermal effects on the physical-chemical properties of pyrophyllite with the quasi-harmonic approximation, which we successfully introduced in our previous work on talc (Ulian and Valdrè, 2014). Our theoretical results at room temperature are in quite good agreement with the ones of Pawley et al. (2002), where the authors experimentally obtained K_{298} = 37 GPa and K_{298}' = 10. However, we have a very good agreement of the axial compressibility data from our simulations ($\beta(a)$ = $3.73 \cdot 10^{-3}$, $\beta(b)$ = $3.06 \cdot 10^{-3}$ and $\beta(c)$ = $12.8 \cdot 10^{-3}$ GPa^{-1}) with that obtained by experimental means $\beta(a)$ = $3.7 \cdot 10^{-3}$, $\beta(b)$ = $3.3 \cdot 10^{-3}$ and $\beta(c)$ = $13.6 \cdot 10^{-3}$ GPa^{-1}). We noted a deviation between our thermal dependency of the bulk modulus and that obtained by Pawley et al. (2002). At 0 GPa, in the *T* range 100 – 900 K, it seems that our model softens more slowly than experimentally observed (-27.6 bar K^{-1} and -55 bar K^{-1}, respectively). This

could be to two reasons. On one hand, the thermal behaviour reported by Pawley at a. (2002) is an estimation from several points on a *P-T* path, while with our approach we obtained a series of compressional isotherms, $V(P)_T$. On the other hand, our model is a single-crystal pyrophyllite end-member, while the experimental sample is a powder that presents some substitutional defects (mainly Fe). As previously discussed (Ulian et al., 2013b), the quantum-mechanical approach based on periodic boundary conditions produces results more similar to single-crystal XRD experiments than X-Ray Powder diffraction ones.

To our knowledge, no other equation of state of pyrophyllite has been formulated by experimental procedure at the moment, so the comparison is somewhat limited, but still encouraging.

REFERENCES CITED

Alimdzhanova, D.I., Ismatov, A.A., and Ganieva, M.M. (1999) The effect of quartz-pyrophyllite raw material on porcelain structure formation. Glass and Ceramics, 56(1-2), 61-63.

Anderson, O.L. (1995) Equation of state of solids for geophysics and ceramic science. 405 p. Oxford University Press, New York, US.

Angel, R.J. (2001) EOS-FIT6.0. Computer Program (http://www.rossangel.com).

Bailey, S.W. (1988) Introduction, Hydrous Phyllosilicates. Reviews in Mineralogy & Geochemistry, 19, 1-8.

Becke, A.D. (1993) Density-Functional Thermochemistry .3. The Role of Exact Exchange. Journal of Chemical Physics, 98(7), 5648-5652.

Bhasin, S., Amritphale, S.S., and Chandra, N. (2003) Effect of pyrophyllite additions on sintering characteristics of fly ash based ceramic wall tiles. British Ceramic Transactions, 102(2), 83-86.

Birch, F. (1947) Finite elastic strain of cubic crystal. Physical Review, 71, 809-824.

Broyden, C.G. (1970a) The convergence of a class of double-rank minimization algorithms 1. General considerations. IMA Journal of Applied Mathematics (Institute of Mathematics and Its Applications), 6(1), 76-90.

-. (1970b) The convergence of a class of double-rank minimization algorithms: 2. The new algorithm. IMA Journal of Applied Mathematics (Institute of Mathematics and Its Applications), 6(3), 222-231.

Bruno, M., Prencipe, M., and Valdre, G. (2006) Ab initio quantum-mechanical modeling of pyrophyllite Al2Si4O10(OH)(2) and talc Mg3Si4O10(OH)(2) surfaces. Physics and Chemistry of Minerals, 33(1), 63-71.

Catti, M., Valerio, G., Dovesi, R., and Causa, M. (1994) Quantum-mechanical calculation of the solid-state equilibrium MgO + alpha-Al_2O_3 $MgAl_2O_4$ (spinel) versus pressure. Physical Review B, 49(20), 14179-14187.

Civalleri, B., Zicovich-Wilson, C.M., Valenzano, L., and Ugliengo, P. (2008) B3LYP augmented with an empirical dispersion term (B3LYP-D*) as applied to molecular crystals. Crystengcomm, 10(4), 405-410.

Dovesi, R., Saunders, V.R., Roetti, C., Orlando, R., Zicovich-Wilson, C.M., Pascale, F., Civalleri, B., Doll, K., Harrison, N.M., Bush, I.J., D'Arco, P., and Llunell, M. (2009) CRYSTAL09 User's Manual. University of Torino, Torino.

Evans, B.W., and Guggenheim, S. (1988) Talc, Pyrophyllite, and Related Minerals. Reviews in Mineralogy, 19, 225-294.

Fletcher, R. (1970) A new approach to variable metric algorithms. The Computer Journal, 13(3), 317-322.

Gatta, G.D., Merlini, M., Valdre, G., Liermann, H.-P., Nenert, G., Rothkirch, A., Kahlenberg, V., and Pavese, A. (2013) On the crystal structure and compressional behavior of talc: a mineral of interest in petrology and material science. Physics and Chemistry of Minerals, 40(2), 145-156.

Gatti, C., Saunders, V.R., and Roetti, C. (1994) Crystal-field effects on the topological properties of the electron-density in molecular-crystals - the case of urea. Journal of Chemical Physics, 101(12), 10686-10696.

Ghanaati, S.M., Thimm, B.W., Unger, R.E., Orth, C., Kohler, T., Barbeck, M., Muller, R., and Kirkpatrick, C.J. (2010) Collagen-embedded hydroxylapatite-beta-tricalcium phosphate-silicon dioxide bone substitute granules assist rapid vascularization and promote cell growth. Biomedical Materials, 5(2).

Goldfarb, D. (1970) A family of variable-metric methods derived by variational means. Mathematics of Computation, 24, 23-26.

Grimme, S. (2006) Semiempirical GGA-type density functional constructed with a long-range dispersion correction. Journal of Computational Chemistry, 27(15), 1787-1799.

Haas, J.L., and Fisher, J.R. (1976) Simultaneous evaluation and correlation of thermodynamic data. American Journal of Science, 276, 525-545.

Hemingway, B.S. (1991) Thermodynamic properties of anthophyllite and talc: Corrections and discussion of calorimetrlc data. American Mineralogist, 76(9-10), 1589-1596.

Holland, T.J.B., and Powell, R. (1998) An internally consistent thermodynamic data set for phases of petrological interest. Journal of Metamorphic Geology, 16(3), 309-343.

Kieffer, S.W. (1979a) Thermodynamics and lattice vibrations of minerals - 1. mineral heat capacities and their relationships to simple lattice vibrational models. Reviews of Geophysics and Space Physics, 17(1), 1-19.

-. (1979b) Thermodynamics and lattice vibrations of minerals - 2. vibrational characteristics of silicates. Reviews of Geophysics and Space Physics, 17(1), 20-34.

Kieffer, S.W. (1979c) Thermodynamics and lattice vibrations of minerals - 3. lattice dynamics and an approximation for minerals with application to simple substances and framework of silicates. Reviews of Geophysics and Space Physics, 17(1), 35-59.

Krupka, K.M., Hemingway, B.S., Borie, R.A., and Kerrick, D.M. (1985) High-temperature heat capacities and derived thermodynamic properties of anthophyllite, diopside, dolomite, enstatite, bronzite, talc, tremolite and wollastonite. American Mineralogist, 70(3-4), 261-271.

Krupka, K.M., Robie, R.A., and Hemingway, B.S. (1979) High-temperature heat capacities of corundum, periclase, anorthite, $CaAl_2Si_2O_8$ glass, muscovite, pyrophyllite, $KAISi_3O_8$ glass, grossular, and $NaAlSi_3O_8$ glass. American Mineralogist, 64, 86-101.

Lee, C.T., Yang, W.T., and Parr, R.G. (1988) Development of the Colle-Salvetti Correlation-Energy Formula into a Functional of the Electron-Density. Physical Review B, 37(2), 785-789.

Lee, J.H., and Guggenheim, S. (1981) Single-crystal X-Ray refinement of pyrophyllite-1Tc. American Mineralogist, 66(3-4), 350-357.

Lintz, E.H. (1938) Use of talc and pyrophyllite in semi-vitreous dinnerware bodies. Journal of the American Ceramic Society, 21(6), 229-237.

Mazo, M.A., Manevitch, L.I., Gusarova, E.B., Berlin, A.A., Balabaev, N.K., and Rutledge, G.C. (2008) Molecular Dynamics Simulation of Thermomechanical Properties of Montmorillonite Crystal. II. Hydrated Montmorillonite Crystal. Journal of Physical Chemistry C, 112(44), 17056-17062.

Momma, K., and Izumi, F. (2008) VESTA: a three-dimensional visualization system for electronic and structural analysis. Journal of Applied Crystallography, 41, 653-658.

Mukhopadhyay, T.K., Dana, K., and Ghatak, S. (2011) Pyrophyllite - a potential material for application in tri-axial porcelain systems. Industrial Ceramics, 31(3), 165-173.

Mukhopadhyay, T.K., Ghatak, S., and Maiti, H.S. (2010) Pyrophyllite as raw material for ceramic applications in the perspective of its pyro-chemical properties. Ceramics International, 36(3), 909-916.

Murnaghan, F.D. (1937) Finite deformations of an elastic solid. American Journal of Mathematics, 49, 235-260.

Nada, R., Nicholas, J.B., McCarthy, M.I., and Hess, A.C. (1996) Basis sets for ab initio periodic Hartree-Fock studies of zeolite/adsorbate interactions: He, Ne, and Ar in silica sodalite. International Journal of Quantum Chemistry, 60(4), 809-820.

Ogorodova, L.P., Kiseleva, I.A., Mel'chakova, L.V., Vigasina, M.F., and Spiridonov, E.M. (2011) Calorimetric determination of the enthalpy of formation for pyrophyllite. Russian Journal of Physical Chemistry A, 85(9), 1492-1494.

Ottonello, G., Civalleri, B., Ganguly, J., Perger, W.F., Belmonte, D., and Zuccolini, M.V. (2010) Thermo-chemical and thermo-physical properties of the high-pressure phase anhydrous B ($Mg_{14}Si_5O_{24}$): An ab-initio all-electron investigation. American Mineralogist, 95(4), 563-573.

Ottonello, G., Civalleri, B., Ganguly, J., Zuccolini, M.V., and Noel, Y. (2009a) Thermophysical properties of the α–β–γ polymorphs of Mg2SiO4: a computational study. Physics and Chemistry of Minerals, 36(2), 87-106.

Ottonello, G., Zuccolini, M.V., and Civalleri, B. (2009b) Thermo-chemical and thermo-physical properties of stishovite: An ab-initio all-electron investigation. CALPHAD: Computer Coupling of Phase Diagrams and Thermochemistry, 33(3), 457-468.

Pascale, F., Zicovich-Wilson, C.M., Gejo, F.L., Civalleri, B., Orlando, R., and Dovesi, R. (2004) The calculation of the vibrational frequencies of crystalline compounds and its implementation in the CRYSTAL code. Journal of Computational Chemistry, 25(6), 888-897.

Pawley, A.R., Clark, S.M., and Chinnery, N.J. (2002) Equation of state measurements of chlorite, pyrophyllite, and talc. American Mineralogist, 87(8-9), 1172-1182.

Perger, W.F., Criswell, J., Civalleri, B., and Dovesi, R. (2009) Ab-initio calculation of elastic constants of crystalline systems with the CRYSTAL code. Computer Physics Communications, 180(10), 1753-1759.

Prencipe, M., Pascale, F., Zicovich-Wilson, C.M., Saunders, V.R., Orlando, R., and Dovesi, R. (2004) The vibrational spectrum of calcite (CaCO3): an ab initio quantum-mechanical calculation. Physics and Chemistry of Minerals, 31(8), 559-564.

Refson, K., Park, S.H., and Sposito, G. (2003) Ab initio computational crystallography of 2 : 1 clay minerals: 1. Pyrophyllite-1Tc. Journal of Physical Chemistry B, 107(48), 13376-13383.

Robie, R.A., Hemingway, B.S., and Wilson, W.H. (1976) Heat capacities of calorimetry conference copper and of muscovile $KAl_2(AlSi_3)O_{10}(OH)_2$, pyrophyllite $Al_2Si_4O_{10}(OH)_2$, and illite $K_3(Al_7Mg)(Si_{14}Al_2)O_{40}(OH)_8$ between 15 and 375 K and their standard entropies at 298.15K. Journal of Research of the U.S. Geological Survey, 4(6), 631-644.

Sainz-Diaz, C.I., Hernandez-Laguna, A., and Dove, M.T. (2001) Modeling of dioctahedral 2 : 1 phyllosilicates by means of transferable empirical potentials. Physics and Chemistry of Minerals, 28(2), 130-141.

Shanno, D.F. (1970) Conditioning of quasi-Newton methods for function minimization. Mathematics of Computation, 24, 647-656.

Sima, L.E., Stan, G.E., Morosanu, C.O., Melinescu, A., Ianculescu, A., Melinte, R., Neamtu, J., and Petrescu, S.M. (2010) Differentiation of mesenchymal stem cells onto highly adherent radio frequency-sputtered carbonated hydroxylapatite thin films. Journal of Biomedical Materials Research Part A, 95A(4), 1203-1214.

Tosoni, S., Pascale, F., Ugliengo, P., Orlando, R., Saunders, V.R., and Dovesi, R. (2005) Quantum mechanical calculation of the OH vibrational frequency in crystalline solids. Molecular Physics, 103(18), 2549-2558.

Tunega, D., Bucko, T., and Zaoui, A. (2012) Assessment of ten DFT methods in predicting structures of sheet silicates: Importance of dispersion corrections. Journal of Chemical Physics, 137(11).

Ugliengo, P., Viterbo, D., and Chiari, G. (1993) MOLDRAW: molecular graphic on a personal computer. Zeitschrift Fur Kristallographie, 207, 9-23.

Ugliengo, P., Zicovich-Wilson, C.M., Tosoni, S., and Civalleri, B. (2009) Role of dispersive interactions in layered materials: a periodic B3LYP and B3LYP-D* study of Mg(OH)(2), Ca(OH)(2) and kaolinite. Journal of Materials Chemistry, 19(17), 2564-2572.

Ulian, G., Tosoni, S., and Valdrè, G. (2013a) Comparison between Gaussian-type Orbitals and Plane Wave *ab initio* DFT modeling of layered silicates: Talc mineral as model system. Journal of Chemical Physics, 139(20), 204101.

-. (2013b) The compressional behaviour and the mechanical properties of talc $[Mg_3Si_4O_{10}(OH)_2]$: a density functional theory investigation. Physics and Chemistry of Minerals, Submitted.

Ulian, G., and Valdrè, G. (2014) Thermo-physical and thermo-chemical properties of Talc $[Mg_3Si_4O_{10}(OH)_2]$: a first principle investigation. Journal of Geophysical Research, in preparation.

Voora, V.K., Al-Saidi, W.A., and Jordan, K.D. (2011) Density Functional Theory Study of Pyrophyllite and M-Montmorillonites (M = Li, Na, K, Mg, and Ca): Role of Dispersion Interactions. Journal of Physical Chemistry A, 115(34), 9695-9703.

Wardle, R., and Brindley, G.W. (1972) The crystal structure of pyrophyllite, 1Tc, and of its dehydroxylate. American Mineralogist, 57, 732-750.

CHAPTER 6 – Thermo-physical and thermo-chemical properties of Muscovite [$KAl_2(AlSi_3)O_{10}(OH)_2$] as revealed by DFT investigation.[5]

Abstract

Thermo-chemical and thermo-physical properties of the $2M_1$ polytype of muscovite (Ms) were computed with the hybrid DFT/B3LYP-D* density functional method and quasi-harmonic treatment. The bulk modulus of muscovite and its first derivative at 298.15 K, calculated using a third-order Birch-Murnaghan equation of state were K_{T0} = 59.93 GPa, K' = 7.84 and V_0 = 940.6 Å^3. The values of $\partial K_T/\partial T$ and α_T were -158.0 bar/K and $3.34 \cdot 10^{-5}$ K^{-1}, respectively. Calculated data have been compared to previous experimental results, finding a good agreement. The results of this kind of analysis can be used in the study of the thermodynamic properties of solid phases at physical conditions that are difficult to obtain during experimental procedures, especially controlled high pressures and temperatures. A set of thermodynamic properties (*e.g.*, K_T, α_T, C_V, C_P) of Ms at different *P*-*T*-*V* is provided, which could be useful in both geophysical and technological applications.

6.1 Introduction

White dioctahedral micas (2:1 phyllosilicates) play a crucial role in most petrogenetic processes, in both magmatic and low- and medium-pressure metamorphic environments. For example, muscovite [$KAl_2(AlSi_3)O_{10}(OH)_2$, Ms] commonly occurs in metamorphic rocks and has been used as marker to estimate the *P*-*T* conditions of crystallization. Among the physical properties of interest, one of the most important parameters is the equation of state (EOS), which is the pressure- and temperature-dependence of the mineral unit-cell volume. Such equation is necessary for calculating the *P*-*T* conditions of mineral reactions. Understanding the mineral thermoelastic behaviour is important to provide a reliable basis for interpretation and prediction of phase equilibria, as they are used as geothermometers and geobarometers.

Nonetheless, only few experimental studies by in situ high-pressure and high-temperature experiments on muscovite (Ms), paragonite (Pg) and phengites are available in literature. The only *P*–*V*–*T* equation of state (EoS) is referred to be on phengite-3T (Pavese et al. 1999). In a first approximation,

[5] This chapter consists of a paper by Gianfranco Ulian and Giovanni Valdrè, "Thermo-physical and thermo-chemical properties of Muscovite [$KAl_2(AlSi_3)O_{10}(OH)_2$] as revealed by DFT investigation", in preparation for *American Mineralogist*.

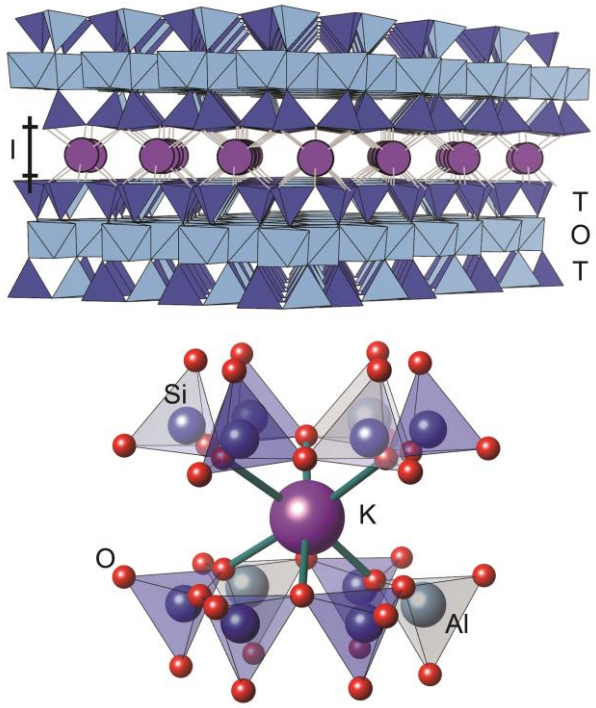

Figure 6.1. (Top panel) Schematic structure of ideal muscovite: embedding of one interlayer I in between two TOT layers, each one of which consists of one octahedral sheet O sandwiched by two tetrahedral sheets T. (Bottom panel) The local structure of the interlayer potassium ions, where 12 oxygen atoms in the first shell are interlayer atom, while Si and Al atoms locate in the centres of O tetrahedrons.

the rock-forming white micas can be described as crystalline solutions among the three end members muscovite, paragonite and margarite. In the past, researchers attempted to use the partitioning of Na and K between coexisting Ms and paragonite (Pg) as a geothermometer (Guidotti and Sassi 1976). Difficulties arise from using solvus curves that are not accurate enough to model the thermodynamic properties of these two micas. Inasmuch as the exact shape of the solvus and how it changes in function of pressure and temperature are not well known, thermometric estimates are often inconsistent. The molar volumes of the terms along the Ms–Pg join and how they change with pressure and temperature must be exactly known before a more accurate phase diagram can be drawn. Studies by Comodi and Zanazzi (1995, 1997) contributed to the knowledge of the molar volumes of muscovite and paragonite-2*M*1 polytypes and of their variation with P through compressibility measurements on single crystals in a diamond-anvil cell at room temperature. These data, together with thermal expansion coefficients measured at room pressure for Ms (Symmes 1986; Guggenheim et al. 1987; Catti et al. 1989) and Pg (Comodi and Zanazzi 2000) allowed a definition of an approximate *P–V–T* equation of state for K- and Na-dioctahedral micas. However, these are only an indication of volumetric behaviour at the boundaries of the P–T conditions achieved in rocks in the Earth's crust. To determine more accurately the behaviour of Ms–Pg micas it is essential to verify if there are any ''non-linear effects'' when both *P* and *T* are high. If the effects of *P* and *T* on the volumetric properties of Ms–Pg micas were precisely known for the full range of P–T conditions of geologic interest, it would be possible to accurately calculate effects on the Ms–Pg solvus. Relatively small changes in excess molar volume could have significant effects on solvus limb positions, particularly in the 600 to 700 °C range. Comodi et al. (2002) tried to fill this gap calculating the thermal equation of state of the muscovite-paragonite series at different temperatures (298, 573, 723 and 873 K) and pressures (range of 0 – 5 GPa) by experimental X-Ray Powder Diffraction technique. The authors fitted the data with a third-order Birch-Murnaghan equation

(Birch, 1947), obtaining the bulk moduli at specific temperatures (K_T) and their pressure-first derivative (K').

However, it is often difficult to obtain the equation of state, especially in natural mineral samples, because they present a series of internal heterogeneities (cation order/disorder, morphological, crystal-chemical, and crystal-physical variations) which hinders a well-constrained evaluation of the physical properties (Mondol et al., 2008). Furthermore, obtaining experimentally and simultaneously both the pressure and thermal behavior of a mineral is still a difficult task, which requires complex and expensive apparatuses.

In recent years, the adoption of accurate computational approaches was used to increase the knowledge about these minerals. These computational methods can provide reliable crystal structures, subsequently used to yield both the elastic and thermal properties by varying the mineral unit-cell and using quasi harmonic approximations, respectively (Militzer et al., 2011; Ortega-Castro et al., 2010; Ottonello et al., 2010; Ottonello et al., 2009b; Prencipe et al., 2011; Stixrude, 2002). Such methods provide results that can help to explain the thermo-chemical and thermo-physical behavior of minerals and aid interpretations of the seismologic data.

Muscovite and paragonite present an interesting challenge to computational mineralogists, because their structure is composed by tetrahedral-octahedral-tetrahedral (T-O-T) layers with potassium (in end-member Ms) or sodium ions (in end-member Pg) in the interlayer. As an example, Figure 6.1 reports the structure of muscovite. The simulation parameters should be chosen carefully when dealing with micas, because two directions of the mineral are dominated by covalent bonds (within the TOT layers), while the third dimension exhibits an interplay of both weak van der Waals forces (between the layers) and strong ionic interactions due to the interlayer cations. The description of these forces should not be as simple as in TOT minerals without interlayer ions, such as talc (Ulian et al., 2013a).

Very recently, Hernandez-Haro and co-workers (2013) presented a Density Functional Theory (DFT) investigation on the elastic constants of the Ms-Pg mineral series, employing the GGA-PBE functional and numeric atomic orbitals. The authors studied the effect of the K and Na content in the crystal lattice on the second order elastic constant tensor. However, the equation of state of the different structures and the thermal effects were not calculated. Furthermore, the authors did not considered in their simulation the contribution of the weak dispersive forces acting between the TOT layers.

The aim of this paper is a detailed thermo-physical and thermo-chemical analysis of the $2M_1$ polytype of muscovite (Ms), which ideal chemical formula is $KAl_2(AlSi_3)O_{10}(OH)_2$. First, a structural investi-

gation of the end-member muscovite mineral is provided using DFT/B3LYP-D* functional (dispersive forces corrected) and an all-electron localized Gaussian-type orbital basis set. The optimized structure is then compared to experimental and theoretical data presented in literature. Secondly, the muscovite athermal equation of state will be obtained by varying the unit-cell volume, as done in a previous work on talc (Ulian et al., 2013b). Finally, using the quasi-harmonic treatment described by Anderson (1995) we investigated the thermo-mechanical and thermo-chemical behavior of muscovite with the same approach adopted in a previous work (Ulian and Valdrè, 2014). The results of this kind of analysis can be adopted in the study of the thermodynamic properties of solid phases at physical conditions that are difficult to obtain in experimental procedures, especially controlled high pressures and temperatures. A set of thermodynamic properties, such as K_T, α_T, C_V and C_P, of muscovite at different P-T-V are provided, which could be useful in both geophysical and technological applications. Thermochemistry results will be compared to previous data obtained by differential scanning calorimetry (Robie et al., 1976).

6.2 Computational details

All calculations have been performed on a Debian (Linux) Cluster with the CRYSTAL09 code (Dovesi et al., 2009), which implements the Hartree–Fock and Kohn–Sham self-consistent field method for the study of periodic systems. The graphical drawings have been carried out with the molecular graphics software MOLDRAW (Ugliengo et al., 1993) and VESTA (Momma and Izumi, 2008).

Hamiltonian and computational parameters

The Becke three-parameter hybrid exchange functional (Becke, 1993) in combination with the gradient-corrected correlation functional of Lee, Yang, and Parr (Lee et al., 1988) have been adopted for all calculations (B3LYP). The exchange–correlation contribution is calculated over a grid of points and is the result of a numerical integration of the electron density and its gradient. The adopted pruned grid is given by 75 points and 974 angular points and obtained from the Gauss–Legendre quadrature and Lebedev schemes (Prencipe et al., 2004). This is a good compromise between accuracy and cost of calculation for geometry optimization and vibrational frequencies. The values of the tolerances that control the Coulomb and exchange series are the default provided by CRYSTAL09, but we increased the pseudo-overlap parameter to stabilize the self-consistent behaviour during unit-cell deformations. The Hamiltonian matrix has been diagonalized (Monkhorst and Pack, 1976) using a 4×4×4 k-mesh, which leads to 36 reciprocal lattice points.

Within the CRYSTAL code, multi-electron wave functions are described by linear combination of crystalline orbitals (CO), expanded in terms of Gaussian-type orbital (GTO) basis sets. The basis sets have been previously optimized ones used by other authors for their investigations similar structures. For all the calculations, aluminium and oxygen have been described by a 8-511d1G (Catti et al., 1994b) and a 8-411d11G basis sets, silicon by a 88-31G* (Nada et al., 1996) and hydrogen by a 3-1p1G basis set (Gatti et al., 1994).

Lattice constants and internal coordinates have been optimized within the same run using the analytical gradient method for the atomic positions and a numerical gradient for the unit-cell parameters. The Hessian matrix is upgraded with the Broyden–Fletcher–Goldfarb–Shanno algorithm (Broyden, 1970a; Broyden, 1970b; Fletcher, 1970; Goldfarb, 1970; Shanno, 1970). The tolerances for the maximum allowed gradient and the maximum atomic displacement for considering the geometry as converged have been set to 6 10^{-5} hartree bohr^{-1} and 1.2 10^{-5} bohr, respectively.

In periodic systems and within the harmonic approximation, the phonon frequencies at Γ-point are evaluated diagonalising the central zone (k = 0) mass-weighted Hessian matrix:

$$W_{ij}(k=0) = \sum_G \frac{H_{ij}^{0G}}{\sqrt{M_i M_j}} \tag{6.1}$$

H_{ij}^{0G} represents the second derivative of the electronic and nuclear repulsion energy E evaluated at equilibrium **u=0** with respect to the displacement of atom A in cell 0 ($u_i = x_i - x_i^*$) and displacement of atom B in neighbouring cells G ($u_j = x_j - x_j^*$) from their equilibrium position x_i^*, x_j^*:

$$\sum_G H_{ij}^{0G} = \sum_G \left[\frac{\partial^2 E}{\partial u_i^0 \partial u_j^G} \right]_0 \qquad i = 1,...,3N; \quad j = 1,...,3N \tag{6.2}$$

The calculation of the Hessian at equilibrium is made by the analytical evaluation of the energy first derivatives, Φ_j of E with respect to the atomic displacements:

$$\Phi_j = \sum_G v_j^G = \sum_G \frac{\partial E}{\partial u_j^G} \qquad j = 1,...,3N \tag{6.3}$$

while second derivatives at **u = 0** (where all first derivatives are zero) are calculated numerically using a "two-point" formula:

$$\left[\frac{\partial \Phi_j}{\partial u_i^0}\right]_0 \approx \frac{\Phi_j\left(0,...,u_i^0,...,0\right)-\Phi_j\left(0,...,u_i^0,...,0\right)}{u_i^0} \qquad (6.4)$$
$$i=1,...,3N; \quad j=1,...,3N$$

More details on the vibrational calculation made by CRYSTAL is beyond the scope of the present paper and can be found in specific literature (Pascale et al., 2004; Tosoni et al., 2005). The Hessian matrix eigenvalues provide the normal harmonic frequencies ω_h and it is obtained with 3N+1 SCF and gradient calculations. This method can be quite demanding for large unit cells, but point symmetry facilitates a remarkable time saving, because only the lines of the Hessian matrix referring to irreducible atoms need to be generated. The tolerances were increased to obtain better results, TOLDEE = 10.

Density Functional Theory often fails to adequately describe long-range dispersive interactions. To overcome this problem, dispersive forces have been evaluated according to the semiempirical approach (DFT+D) suggested by Grimme (2006), which adds the following contribution to the calculated DFT energy:

$$E_{DISP} = -s_6 \sum_{\mathbf{g}} \sum_{i \neq j} f_{dump}\left(R_{ij,\mathbf{g}}^6\right) \frac{C_6^i C_6^j}{R_{ij,\mathbf{g}}^6}$$
$$f_{dump} = \frac{1}{1+e^{-d\left(R_{ij,\mathbf{g}}/R_{vdw}-1\right)}} \qquad (6.5)$$

The summation over all atom pairs *ij* and **g** lattice vectors excludes the self- interaction contribution ($i = j$) for every $\mathbf{g}$. The parameters C_6^i represent the dispersion coefficient for the atom *i*, $R_{ij,\mathbf{g}}$ is the interatomic distance between atom *i* in the reference cell and atom *j* in the neighbouring cells at distance |**g**| and s_6 is a functional-dependent scaling factor. The function f_{dump} is used to dump the energy correction to avoid double counting of short-range contributions to the energy and depends on the sum of atomic van der Waals radii (R_{vdW}) and on a steepness parameter (d = 20). According to results previously reported in literature, showing that the E_{DISP} correction tends to overestimate cohesive energy in solid crystals, the original B3LYP+D parameters where modified according to a previous study (Civalleri et al., 2008), setting s_6 to 1, the hydrogen atom van der Waals radius R_{vdw}(H) to 1.30 and the heavier atom van der Waals radii were scaled by a factor 1.05. The same approach has been adopted with good results in a previous work on talc (Ulian et al., 2013a). Among the Gaussian-type orbitals-based methods proposed in the cited paper, it was the most accurate in both structural and energy prediction.

Thermomechanical and thermochemical properties

We calculated the total pressures, bulk moduli, thermal expansion coefficients and heat capacity in the limit of the quasi-harmonic approximation described by Anderson (1995). The approach is based on the Grüneisen's mode-γ parameters, namely the evaluation of unit cell volume dependence of the vibrational normal mode frequencies, calculated at Γ point. Due to the limited computational resources, we did not take into account dispersion effects in the muscovite phonon spectra at different pressures. However, the number of atoms in the unit cell, and the corresponding number of vibrational frequencies at Γ point, are sufficiently large and the corresponding Grüneisen's parameters can be considered representative of the whole set of parameters. In previous works (Ottonello et al., 2010; Ottonello et al., 2009a; Ottonello et al., 2009b; Prencipe et al., 2011; Ulian and Valdrè, 2014) the dispersion effects were neglected, but the thermomechanical and thermochemical properties were correctly estimated for minerals with smaller unit cell than muscovite. Indeed, thermodynamic properties, which are obtained as averages over the relevant quantities at the atomic level, can reliably be derived even without a detailed knowledge of the phonon density of state (Kieffer, 1979).

The pressure at each unit cell volume and temperature is related to the Helmholtz energy F of a solid insulator (Anderson, 1995)

$$F = E_{ST}(V) + F_{VIB}(V,T) \tag{6.6}$$

where E_{ST} is the potential of a static lattice at absolute zero (athermal limit), F_{VIB} is the vibrational energy related to the thermal motion of the atoms and E_{el} is the potential due to free electrons.

The pressure can be obtained by the first derivative of Eq.(6.6)

$$P = -\left(\frac{\partial F}{\partial V}\right)_T = -\left(\frac{\partial E_{ST}}{\partial V}\right)_{T=0} + \left(\frac{\partial F_{VIB}}{\partial V}\right)_T \tag{6.7}$$

Using the energy partition principle, the expression that relates the pressure at each volume and temperature is given by,

$$P = -\left(\frac{\partial E_{ST}}{\partial V}\right)_{T=0} + \frac{kT}{2V}\sum_{i=1}^{3n-3}\gamma_i X_i + \frac{kT}{V}\sum_{i=1}^{3n-3} n_i(\nu_i, Y)\gamma_i X_i \tag{6.8}$$

$$n_i(\nu_i, T) = \frac{1}{e^{X_i} - 1} \tag{6.9}$$

where $X_i = h\nu_i/kT$, h and k are the Planck's and Boltzmann's constants, respectively, ν_i is the vibrational frequency of the ith normal mode and n_i is the Bose-Einstein distribution applied to the phonon gas. The Grüneisen's mode-γ parameter is defined as

$$\gamma_i = -\frac{\partial \ln \nu_i}{\partial \ln V} = -\frac{V}{\nu_i}\frac{\partial \nu_i}{\partial V} \tag{6.10}$$

and where estimated by the analytical derivatives with respect to *V* of quadratic polynomials fitting the numerically determined $\gamma_i(V)$ curves. The total pressure given by Eq.(6.8) is the sum of three contributions: in order, the first one is the *static* pressure $P_{st}(V)$; the second one is the *zero point* pressure $P_{zp}(V)$ and the third one is the *thermal* pressure $P_{th}(V,T)$. It can be observed that the first two terms of Eq.(6.8) depend only on the volume of the unit cell and their sum is called *athermal* pressure, $P_{ath}(V) = P_{st}(V) + P_{zp}(V)$.

We calculated the static pressure values by interpolation of the $E_{st}(V)$ curve by Legendre's polynomials up the third order and getting the static pressures as derivatives of the resulting analytical curves. The *vibrational* pressure, namely $P_{vib}(V,T) = P_{zp}(V) + P_{th}(V,T)$, was obtained directly from Eqs. (6.8) and (6.9). As observed by Prencipe et al. (2011) this method would implicitly assumes the constancy of the Grüneisen's parameters as the cell volume is reduced in a finite interval. However we calculated the volume dependence of the mode-γ parameters.

With the set of *P(V,T)* data obtained as described above, we derived the volume at zero pressure (V_0), the bulk modulus (K_T) and its first derivative with respect to *P* (K_T') using a third order Birch-Murnaghan equation of state (BM3) (Birch, 1947):

$$P_{BM3} = \frac{3}{2}K_T\left[\eta^{-7/3} - \eta^{-5/3}\right]\left\{1 - \frac{3}{4}\left(4 - K'\right)\left(\eta^{-2/3} - 1\right)\right\} + P_0 \tag{6.11}$$

with $\eta = V/V_0$ a dimensionless parameter called "dilaton" and V_0 the volume at reference pressure P_0 (P_0 = 0.0 GPa). We made the root mean square fitting of *P* as a function of *V* at each temperature with the EOS-FIT5.2 software (Angel, 2001).

The thermal expansion coefficient at any given cell volume (pressure), as a function of *T*, has been obtained by direct evaluation of the $\alpha_T K_T$ product (Anderson, 1995):

$$\alpha_T K_T = \frac{R}{ZV}\sum_{i=4}^{3n}\gamma_i e^{X_i}\left(\frac{X_i}{e^{X_i} - 1}\right)^2 \tag{6.12}$$

by knowing the bulk modulus at each *P*-*T* condition, obtained from Eq.(6.11).

Within the harmonic approximation, the isochoric heat capacity as a function of *T* of a solid insulator can be expressed as (Anderson, 1995)

$$C_V = \frac{R}{Z}\sum_{i=4}^{3n}\frac{X_i^2 e^{X_i}}{\left(e^{X_i} - 1\right)^2} \tag{6.13}$$

The specific heat at constant pressure (C_P) can be obtained from the relationship

$$C_P = C_V + T\alpha_T^2 K_{T,P} V_{P,T} \quad (6.14)$$

where $V_{P,T}$ is the cell volume at pressure P and temperature T, respectively. Worth noting that the isochoric specific heat expression in Eq. (6.13) does not include the acoustic mode contribution described by the Kieffer's sinusoidal dispersion (Kieffer, 1979). This contribution is calculated from the acoustic (seismic) wave velocities within the mineral, which are in turn derived from the second order elastic constants (SOEC). Due to computational costs, we did not obtained the muscovite SOEC, but, as observed in our previous work on talc (Ulian and Valdrè, 2014), the contribution from the acoustic branch is very small at T > 300 K and the description of the thermochemical properties is adequately described by the sole optical modes.

6.3 Results and discussion

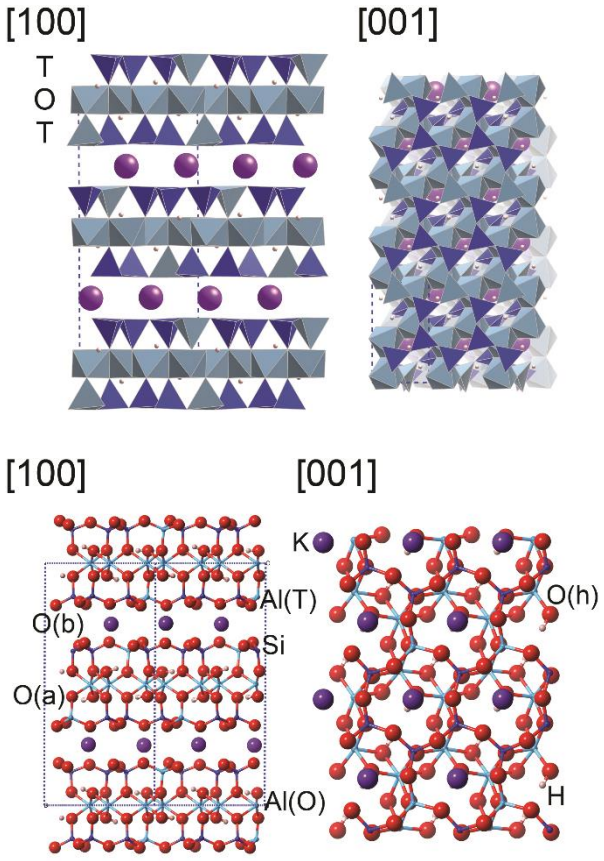

Figure 6.2. Views along [100] and [001] directions of the DFT optimized Ms model.

Geometry

The starting muscovite structure was taken from XRD refinement data (Guggenheim et al., 1987). The unit cell adopted in the simulations belongs to the $P\bar{1}$ space group. Hydrogen atoms location is similar to the one of pyrophyllite structure, with O-H bond direction canted by about 30° on the [001] direction. Oxygen atoms are subdivided in three groups: apical [O^a or O(a)] shared between Si and Al; hydroxyl [O^h or O(h)]; basal [O^b or O(b)] shared between silica tetrahedrons. Aluminium atoms substituted silicon ones in the tetrahedral layer so as to maintain the unit-cell symmetry. Albeit this choice do not consider all possible variety of defect distribution in the real mineral, it is sufficiently accurate with experimental observations and allows speeding up calculations. See the stick and ball model in Figure 6.2 for a graphical representation.

The optimization results of Ms obtained by GTO/B3LYP-D* approach are described in details in Table 6.1, in comparison with a series of X-Ray and Neutron Diffraction refinements (Brigatti et al., 1998; Gatta et al., 2011; Guggenheim et al., 1987) and very recent theoretical results reported in literature (Hernandez-Haro et al., 2013). The adoption of the modified Grimme's dispersion parameters (B3LYP-D*) provided accurate lattice parameters and bond lengths in comparison with experimental data, with only a small over-estimation of the cell volume (+0.6%). In particular, the description of the **c**-axis is quite accurate, although with a small underestimation of about 0.7%.

Table 6.1. Calculated and experimental unit-cell and internal geometry of Muscovite.

	This study	Experimental[1]	Experimental[2]	Neutron Diffraction[3]	DFT[4]
Lattice parameters					
a (Å)	5.1974	5.1579	5.174-5.226	5.1999	5.187
b (Å)	9.0389	8.9505	8.976-9.074	9.0198	9.006
c (Å)	19.8444	20.071	19.875-20.097	19.945	20.148
α (°)	90.27	90.00	90.00	90.00	90.00
β (°)	96.23	95.75	95.59-95.84	95.81	95.44
γ (°)	89.88	90.00	90.00	90.00	90.00
½csinβ	9.366	9.985	9.890-9.996	9.9213	10.029
Volume (Å^3)	926.74	921	926-945.4	930.66	936.999
Mean bond lengths (Å)					
O-H	0.961	-	0.95	-	0.974
Si-O	1.634	1.647	1.64	1.642	1.651
Al(T)-O	1.741	-	-	-	1.757
Al(Oc)-O(a)	1.937	1.921	1.927-1.94	1.939	1.934
Al(Oc)-O(h)	1.919	1.935	1.911	1.939	1.918
K-O_{outer}	3.380	3.368	3.272-3.373	3.329	3.427
K-O_{inner}	2.798	2.848	2.832-2.934	2.863	2.759
ΔK	0.582	0.520	0.426-0.509	0.466	0.6680
TOT structure					
Tetrahedral rotation (°)	12.2	11.8	10.3-11.3	10.39	14.6
Volume (T) Si,Al (Å^3)	2.222, 2.697	2.25	-	2.265	2.273, 2.774
Volume (Oc) (Å^3)	9.345	9.15	-	9.518	9.386
T thickness (Å)	2.248	2.234	2.262	2.224	2.277
Oc thickness (Å)	2.086	2.081	2.083	2.102	2.093
I thickness (Å)	3.260	3.436	3.375	3.125	3.361

[1] data from (Guggenheim et al., 1987) $K_{1.00}Na_{0.03}Ca_{0.01}(Al_{1.93}Fe_{0.01}Mn_{0.01})(Al_{0.91}Si_{3.09})O_{10}(OH)_{1.88}F_{0.12}$

[2] data collected from different sources (Burnham and Radoslovich, 1964): $K_{0.66}Na_{0.34}Al_2(AlSi_3)O_{10}(OH)_2$; (Rothbauer, 1971): $K_{0.85}Na_{0.1}(Al_{1.81}Fe^{2+}_{0.14}Mg_{0.12})(Al_{0.9}Si_{3.1})O_{9.8}(OH)_2$; (Catti et al., 1989): $K_{0.86}Na_{0.11}(Al_{1.93}Fe_{0.07}Mg_{0.02})(Al_{0.92}Si_{3.08})O_{10}(OH)_2$; (Catti et al., 1994a): $K_{0.90}Na_{0.07}(Al_{1.63}Fe_{0.23}Mg_{0.16}Ti_{0.03})(Al_{0.80}Si_{3.20})O_{10}(OH)_2$; (Brigatti et al., 1998): different compositions; (Mookherjee and Redfern, 2002): $K_{0.95}Na_{0.05}(Al_{0.76}Fe_{0.14}Mg_{0.10})_2(Al_{0.75}Si_{3.25})O_{10}(OH_{1.96}F_{0.04})$.

3 data from neutron diffraction experiments at 20K (Gatta et al., 2011).

[4] theoretical data from (Hernandez-Haro et al., 2013)

The internal geometry, namely the mean bond lengths, is very similar to the one obtained by previous theoretical study (Hernandez-Haro et al., 2013). Both results are slightly larger than experimental

values of about 0.7%. Two types of distances could be defined from the potassium interlayer cation to the O(b) atoms, according to the work of Hernandez-Haro et al. (2013): (1) the nearest O atoms distance ($K\cdots O_{inner}$) and (2) the farthest O atoms distance ($K\cdots O_{outer}$), which in our calculations were overestimated (0.4%) and underestimated (1.8%), respectively, in comparison with experimental data. This result is in good agreement with previous DFT-GGA observations (Hernandez-Haro et al., 2013). Mean O-H bond length falls between the theoretical and experimental data reported in literature.

In the case of polyhedron volumes, Si and Al^{3+} tetrahedrons were close to the Ms experimental values, but the Al^{3+} octahedrons showed a slight overestimation (2.1%). The different layer thicknesses (Oc-, T-sheet and interlayer, I) are close to the reported experimental values. In particular, the interlayer thickness is in very good agreement with experimental ones, despite a small underestimation. These results results suggests the Grimme's semi-empirical correction for dispersive forces provides an adequate description of the energy, and thus the geometry, of the muscovite mineral.

Athermal equation of state

We report in Table 6.2 the Ms relaxed lattice parameters at the athermal limit. We found that the relationship between the muscovite energy E_{st} at different volumes V, i.e. $E_{st}(V)$ curve, is well described by a 3rd-order polynomial equation with parameters $p_1 = -3.509124\cdot10^{-8}$, $p_2 = 1.052001\cdot10^{-4}$, $p_3 = -1.045679\cdot10^{-1}$ and $p_4 = 3.448660\cdot10^{+1}$ ($R^2 = 0.999995$). We were able to obtain the static pressure related to each volume by derivation of the $E_{st}(V)$ curve, according to Eq.(6.7). A graphical representation of the $\Delta E_{st}/V$ and P_{st}/V trends are shown in Figure 6.3a,b, respectively. We plotted $\Delta E_{st} = E_{st}(V) - E_{st}(V_{eq})$, where $E_{st}(V_{eq})$ is the energy at equilibrium volume, to ease the comparison.

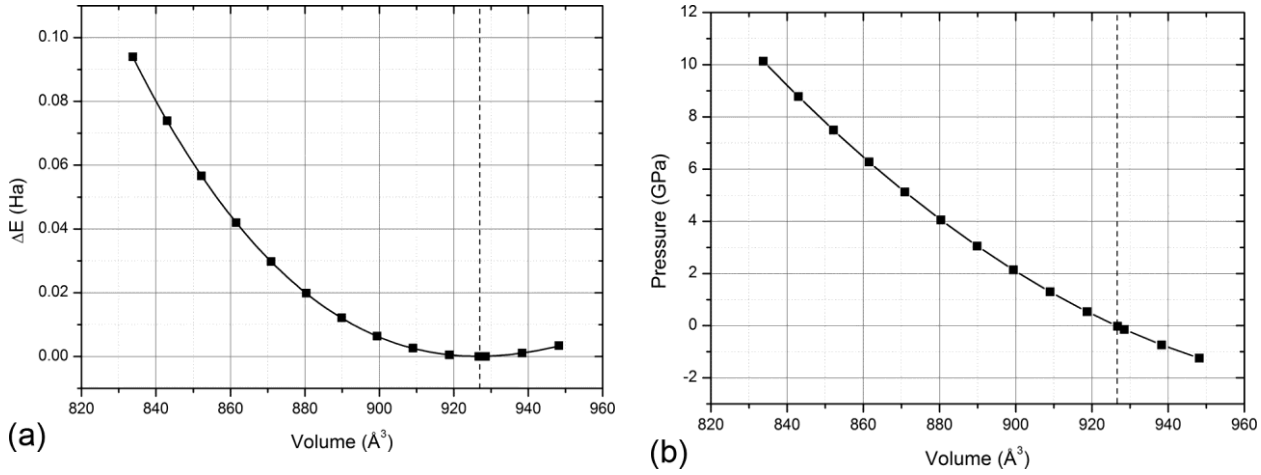

Figure 6.3 (a) $\Delta E(V)$ and (b) $P(V)$ plots of muscovite obtained from ab initio calculations. The dashed lines helps in distinguishing compression regime (on the left) and expansion (on the right).

Table 6.2. Simulated Muscovite unit-cell parameters at different volumes.

P_{st} (GPa)	$P_{BM\text{-}III}$ (GPa)	Volume (Å^3)	a (Å)	b (Å)	c (Å)	α (°)	β (°)	γ (°)
-1.24	-1.33	948.2	5.2149	9.0745	20.1613	90.24	96.36	89.89
-0.74	-0.75	938.3	5.2072	9.0587	20.0138	90.26	96.30	89.89
-0.14	-0.11	928.5	5.1990	9.0421	19.8699	90.27	96.25	89.88
-0.03	0.01	926.7	5.1974	9.0389	19.8444	90.27	96.23	89.88
0.53	0.58	918.8	5.1903	9.0246	19.7305	90.28	96.20	89.88
1.29	1.34	909.1	5.1811	9.0061	19.5953	90.29	96.15	89.88
2.13	2.16	899.4	5.1713	8.9866	19.4646	90.29	96.10	89.87
3.05	3.06	889.9	5.1610	8.9661	19.3384	90.30	96.05	89.87
4.05	4.03	880.4	5.1502	8.9446	19.2164	90.30	96.01	89.87
5.12	5.08	870.9	5.1389	8.9220	19.0987	90.30	95.96	89.86
6.27	6.22	861.5	5.1270	8.8987	18.9844	90.30	95.92	89.86
7.49	7.45	852.2	5.1148	8.8746	18.8734	90.31	95.87	89.85
8.77	8.77	843.0	5.1023	8.8499	18.7659	90.31	95.83	89.85
10.13	10.20	833.8	5.0893	8.8245	18.6604	90.31	95.78	89.84

Note: P_{st} values were obtained from both 3-order polynomial fitting (p-fit) and $P_{BM\text{-}III}$ data from 3-order Birch-Murnaghan fitting (BM-III).

Next step is the calculation of muscovite bulk modulus at 0 K (K_{T0}), its pressure first derivative (K') and the volume at zero pressure (V_0) by fitting the volume *vs*. P_{st} data using BM3 equation of state. The refined elastic parameters are V_0 = 926.86 Å^3, K_{T0} = 64.2 GPa and K' = 7.98.

In Figure 4a,b we report the evolution of volume and lattice parameters at different pressure, respectively. Regarding the compressive regime (P > 0 GPa), the calculated trend is monotonic (Figure 4a). It is graphically clear that muscovite deformation exhibits a strongly anisotropic behaviour, with smaller variations for *a* and *b* cell parameters than for the *c* one. It is possible to describe the observed anisotropy calculating the axial bulk moduli with a III-BM EOS fit on the lattice parameters values at different pressures. The obtained refined data for the *a*, *b* and *c* axis were, respectively: a_0 = 5.1975 Å, $K_{T0}(a)$ = 136.95 GPa and $K'(a)$ = 5.27; b_0 = 9.0392 Å, $K_{T0}(b)$ = 118.25 GPa and $K'(b)$ = 5.01; c_0 = 19.8495 Å, $K_{T0}(c)$ = 30.27 GPa and $K'(c)$ = 6.60. The axial compressibilities, described as $\beta = 1/3K_{T0}$, are in ratio β(a): β(b): β(c) = 1.000 : 1.158 : 4.525. This result suggests that the covalent bonds in the dioctahedral TOT layers are less compressible than the interlayer dominated by electrostatic and van der Waals forces (*c* direction).

There is a good agreement with previous theoretical results reported in literature at athermal conditions (Ortega-Castro et al., 2010), obtained with generalized gradient approximation (GGA) and the Perdew-Burke-Ernzerhof (PBE) functional. The BM3 fit on $V(P)$ data in the cited work resulted is very similar to ours, albeit with small underestimations (K_{T0} = 60.1 GPa and K' = 7.3). Hernández-

Haro et al. (2013) derived with DFT simulations at T = 0 K the bulk modulus of end-member muscovite from the elastic constants, obtaining K_{T0} = 68.4 GPa. The difference between our results and the previous ones is imputable to several reasons. First, in our simulations we adopted an all-electron GTO basis set with hybrid B3LYP functional, including a correction for dispersive forces, while in both previous works (Hernandez-Haro et al., 2013; Ortega-Castro et al., 2010) the authors used a GGA functional (PBE) with norm conserving pseudopotentials. The generalized gradient approximation tends to soften bonds and consequently the bulk modulus, which explain the lower K_{T0} value of Ortega-Castro et al. (2010). Secondly, we observed in a previous work on talc (Ulian et al., 2013b) that the bulk modulus obtained from the elastic stiffness is very sensitive on both its expression (Reuss bound, Voigth bound, etc.) and anisotropic behaviour of the mineral.

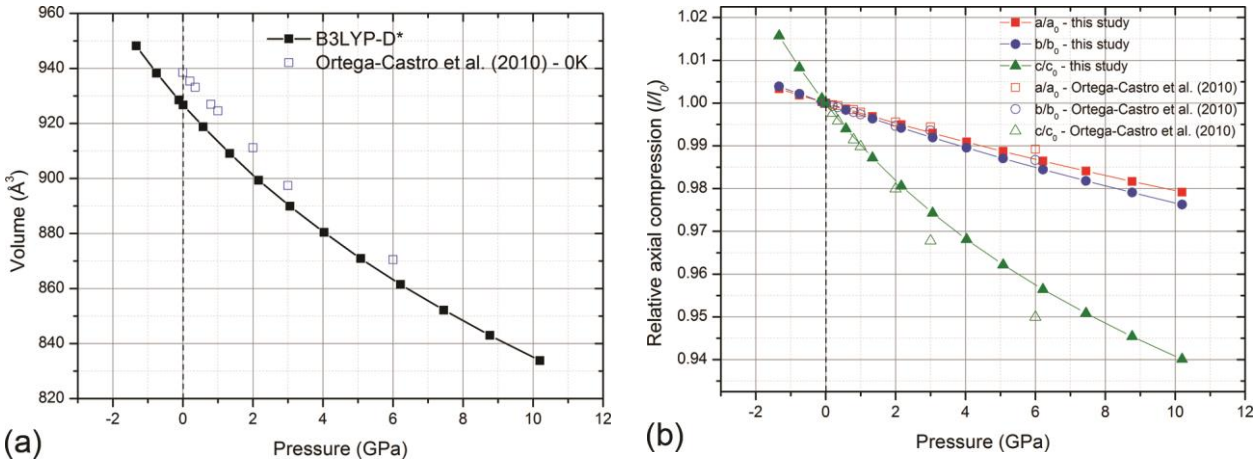

Figure 6.4 *Ab initio* pressure effects on muscovite unit-cell volume and axis lengths. The theoretical athermal results has been compared to previous ones (Ortega-Castro et al., 2010).

Regarding the internal geometry of muscovite, the volume variation (pressure) affects the size, shape and orientation of the coordination polyhedrons. While the thickness of the TOT layers is almost non-affected by pressure (-2.0%), but the interlayer thickness shrinks of about 15% at ca. 9 GPa (Figure 6.5), in agreement with the axial moduli. The pressure increase produces a volume reduction in both SiO_4/AlO_4 tetrahedra and AlO_6 octahedra of about 3-4%. Mean Si – O and Al – O bond lengths are contracted by 0.9% and 1.3%, respectively, from 0 to 10 GPa. In the case of Si tetrahedron, the reduction is more evident for the apical oxygen than for the basal ones. In both cases, the bond length contraction removes some distortion in the tetrahedra and in the octahedra.

Another structural response to the compression is the increase of the tetrahedral rotation angle (Figure 6.6), which is defined as $\alpha = 1/2\left(\sum_{i=1}^{6}|\phi_i - 120°|\Big/6\right)$, where ϕ_i is the angle described by triples of basal oxygen atoms (Bailey, 1988; Ulian et al., 2013b). The predicted value of α increases from 13.2° at 0 GPa to 14.6° at 9 GPa.

We did not observe any significant variation in O-H bond lengths in the pressure range investigated (0.962 Å at 0 GPa and 0.963 Å at 9 GPa), nor in their directions.

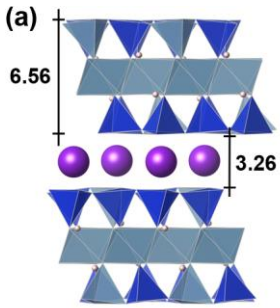

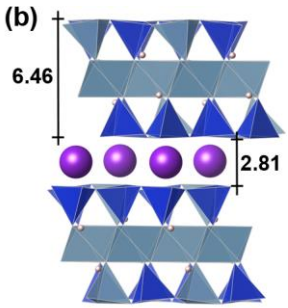

Figure 6.5 Structural deformations of Muscovite from (a) 0 GPa to (b) 9 GPa. Values are reported in Å.

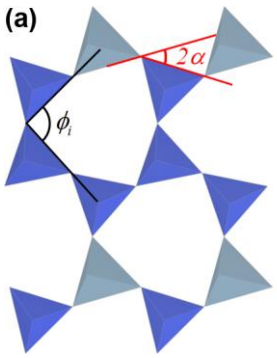

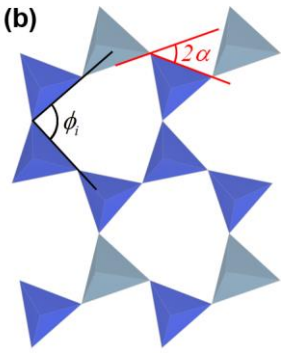

Figure 6.6 Variations of tetrahedral rotation angle of Muscovite from (a) 0 GPa to (b) 9 GPa.

Thermo-mechanical and thermochemical properties

There are 84 atoms in the Ms unit-cell, which result in 84 x 3 = 252 normal modes, three of them related to translation of the whole unit-cell. The remaining 249 optic modes are subdivided in the following irreducible representations:

$$\Gamma_{tot} = 126A_g + 123A_u$$

Modes with A_g symmetry are Raman-active, while A_u ones are IR-active, but both do not exhibit degeneracies. For each optic normal mode ($3n - 3$) we determined the mode-γ parameters. Between 30 and 1200 cm^{-1} (see Figure 6.7a), all parameters are positive and, according to Eq.(6.8), they contribute positively to the total pressure. In this frequency range, only one vibrational mode is associated with a small negative γ. Above 1200 cm^{-1} the mode-g are negative ($\gamma \approx$ -0.1) and give negative contribution to the pressure values. The mean Grüneisen's parameter ($\bar{\gamma}$) is equal to 0.67. We reported the results and the mode-gammas for each frequency at zero pressure in Table 6.3.

Using Eq.(6.11) we calculated the thermal contribution to athermal pressure values in the range 10 – 900 K. To help the interested readers in better understanding how the quasi-harmonic approximation works, we plotted in Figure 6.7b the static, zero point and thermal pressure contribution to P = 0 GPa total pressure as a function of temperature. The zero point pressure is almost constant, as it is a function of the sole volume. The thermal pressure increases, as the Grüneisen's parameters are almost all positive. Since there is an external pressure constrain (0 GPa), to maintain the equilibrium the static pressure mirrors the thermal pressure behaviour, with a shift in pressure due to P_{zp}.

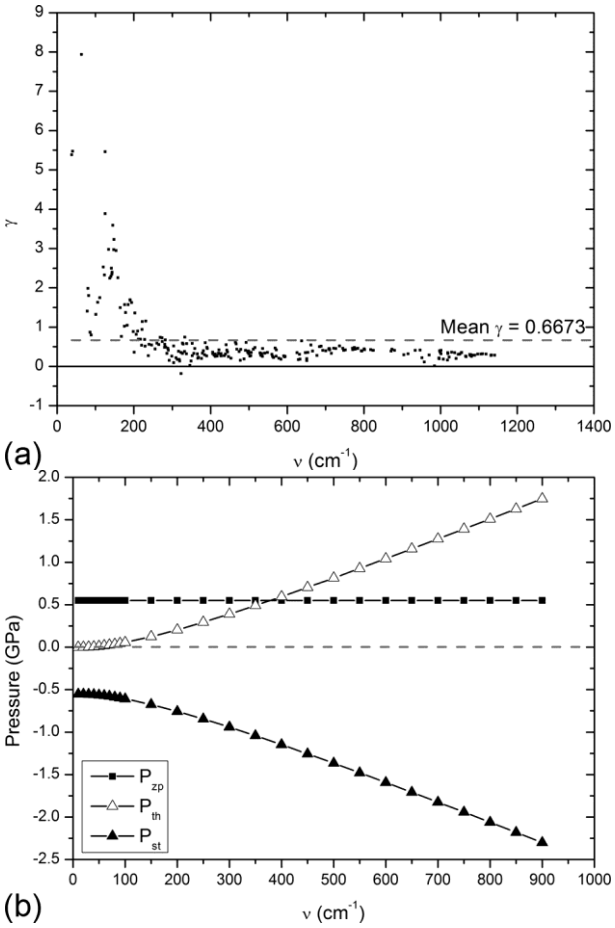

Figure 6.7 (a) Grüneisen's parameters (γ) at P = 0 GPa as a function of frequency (ν). The dashed line represents the mean of the mode-γ. (b) Contributions to the zero total pressure of the static, zero point and thermal pressures.

In Figure 6.8a the *V(P)* values obtained at 298K, alongside experimental data from powder XRD (Comodi et al., 2002; Curetti et al., 2006). There is a good agreement with the volumetric behaviour of Ms in the range 0 – 10 GPa. We noticed also that the comparison is more favourable with the data of Curetti and co-workers (2006) than with that of Comodi et al. (2002), despite the small difference observed with the B3LYP-D* approach. In fact, the trend of our theoretical *V(P)* curve at 298 K is almost the same of the one obtained by Curetti et al. (2006) at the same temperature. The difference between the two experimental results and our set of data resides in the chemical composition of the mineral. While both powdered samples exhibit a wide presence of substitutional defects, such as Mg and Fe^{3+} in the octahedral sheet, our model represents an "ideally" pure muscovite mineral. Furthermore, the volumetric difference may also be ascribed to the investigation approaches. As discussed in our previous work (Ulian at al., 2013b), the theoretical approach is more similar to single-crystal XRD experimental setting than powder XRD one. In Figure 6.8b we reported a three-dimensional plot of the *V(P,T)* data in the range 100 – 900 K.

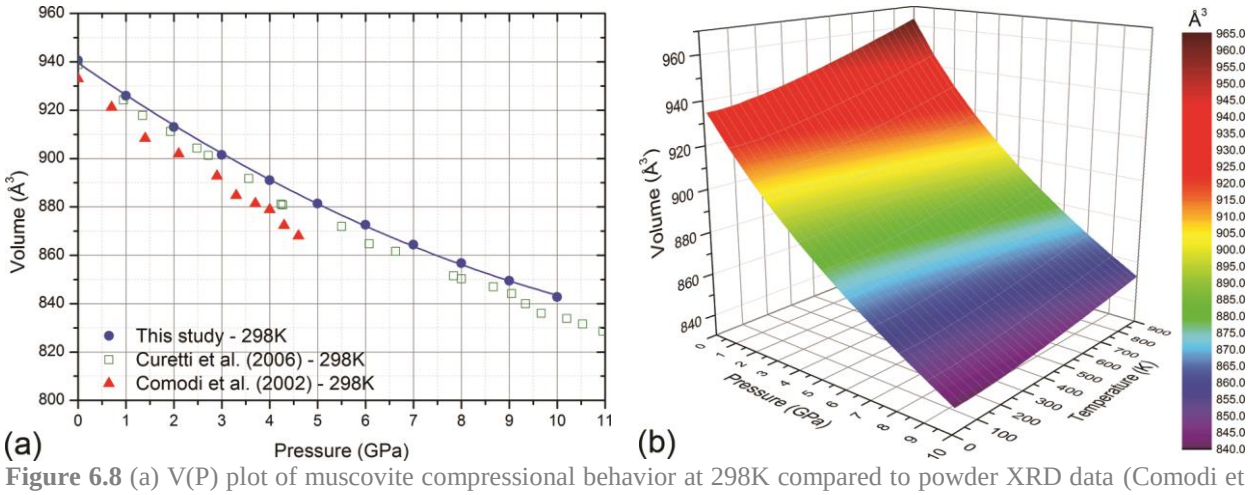

Figure 6.8 (a) V(P) plot of muscovite compressional behavior at 298K compared to powder XRD data (Comodi et al., 2002; Curetti et al., 2006) and (b) V(P,T) three-dimensional plot obtained with DFT/B3LYP-D*.

Table 6.3. Ms frequencies (cm^{-1}) and mode-gamma analysis at 0 Gpa

Mode	IRREP	Frequency	γ	Mode	IRREP	Frequency	γ
1	A_u	Acoustic	-	64	A_u	281.91	0.7
2	A_u	Acoustic	-	65	A_g	283.11	0.5
3	A_u	Acoustic	-	66	A_g	286.44	0.3
4	A_u	37.78	5.4	67	A_g	288.60	0.5
5	A_u	40.68	5.5	68	A_u	289.84	0.4
6	A_u	63.36	7.9	69	A_g	292.40	0.2
7	A_g	78.84	1.4	70	A_u	299.10	0.3
8	A_u	80.37	2.0	71	A_g	303.97	0.1
9	A_u	82.19	1.8	72	A_u	304.08	0.5
10	A_g	85.78	0.9	73	A_g	310.18	0.2
11	A_g	88.98	0.8	74	A_g	313.33	0.2
12	A_g	101.27	1.3	75	A_u	316.54	0.4
13	A_g	105.84	1.6	76	A_g	318.58	0.2
14	A_g	111.23	1.7	77	A_u	319.53	0.1
15	A_u	120.38	2.5	78	A_u	323.44	-0.2
16	A_u	123.44	2.3	79	A_g	323.52	0.4
17	A_u	125.13	3.9	80	A_g	326.73	0.3
18	A_g	125.17	5.5	81	A_u	327.11	0.6
19	A_u	134.59	3.0	82	A_g	328.56	0.6
20	A_u	137.59	2.2	83	A_u	332.16	0.4
21	A_g	140.49	2.3	84	A_g	332.80	0.7
22	A_g	141.82	2.5	85	A_g	337.20	0.3
23	A_u	142.53	2.3	86	A_u	337.52	0.6
24	A_u	143.56	2.4	87	A_u	346.04	0.0
25	A_g	144.99	3.6	88	A_g	349.61	0.1
26	A_g	147.83	3.0	89	A_g	352.07	0.3
27	A_u	148.05	3.2	90	A_u	352.17	0.6
28	A_g	153.61	2.9	91	A_u	356.37	0.3
29	A_u	158.48	2.3	92	A_u	359.02	0.5
30	A_u	164.51	1.5	93	A_u	365.38	0.3
31	A_u	167.58	0.8	94	A_g	365.60	0.3
32	A_u	175.62	1.0	95	A_g	367.16	0.2
33	A_g	176.17	1.6	96	A_u	368.82	0.2
34	A_u	178.70	1.4	97	A_g	376.85	0.2
35	A_u	182.73	1.0	98	A_g	379.10	0.3
36	A_g	185.21	1.6	99	A_u	381.69	0.4
37	A_g	190.07	1.7	100	A_g	384.65	0.3
38	A_u	190.83	1.7	101	A_g	386.39	0.6
39	A_u	194.06	1.6	102	A_u	389.67	0.3
40	A_g	198.28	0.9	103	A_g	390.64	0.5
41	A_g	201.02	0.4	104	A_g	391.98	0.5
42	A_g	202.69	1.4	105	A_g	405.45	0.3
43	A_u	206.50	0.8	106	A_u	405.75	0.4
44	A_u	209.94	0.9	107	A_u	409.07	0.3
45	A_g	212.00	0.7	108	A_g	412.10	0.3
46	A_g	216.98	0.7	109	A_u	412.42	0.3
47	A_u	220.32	0.5	110	A_g	416.76	0.3
48	A_g	221.39	0.9	111	A_u	417.38	0.3
49	A_g	222.41	1.1	112	A_u	421.02	0.3
50	A_u	228.15	0.7	113	A_g	421.98	0.4
51	A_g	229.35	0.5	114	A_u	423.96	0.3
52	A_u	231.25	1.2	115	A_g	427.09	0.3
53	A_g	237.88	0.3	116	A_g	427.64	0.3
54	A_u	239.80	0.6	117	A_u	428.21	0.3
55	A_g	246.36	0.5	118	A_u	435.94	0.3
56	A_u	255.47	0.4	119	A_g	439.15	0.3
57	A_g	259.99	0.6	120	A_u	440.62	0.6
58	A_u	264.86	0.6	121	A_u	442.59	0.4
59	A_g	269.00	0.7	122	A_g	444.38	0.4
60	A_g	273.88	0.7	123	A_g	446.55	0.2
61	A_u	274.09	0.6	124	A_g	453.58	0.2
62	A_u	280.36	0.5	125	A_g	465.07	0.6
63	A_g	281.12	0.6	126	A_u	466.90	0.6

Table 6.3. (continued) Ms frequencies (cm^{-1}) and mode-gamma analysis at 0 Gpa

Mode	IRREP	Frequency	γ	Mode	IRREP	Frequency	γ
127	A_g	468.49	0.4	190	A_g	777.30	0.4
128	A_u	474.47	0.4	191	A_g	783.38	0.5
129	A_g	477.75	0.2	192	A_u	784.59	0.5
130	A_g	478.90	0.4	193	A_u	793.63	0.4
131	A_u	487.67	0.2	194	A_g	794.54	0.4
132	A_u	491.12	0.4	195	A_u	801.03	0.4
133	A_u	493.11	0.6	196	A_g	802.17	0.4
134	A_g	496.95	0.4	197	A_u	817.70	0.4
135	A_u	498.23	0.4	198	A_u	823.97	0.4
136	A_g	499.48	0.3	199	A_g	825.05	0.4
137	A_u	499.68	0.4	200	A_u	871.27	0.4
138	A_u	502.70	0.3	201	A_g	873.50	0.4
139	A_g	505.23	0.3	202	A_u	880.22	0.4
140	A_g	506.33	0.4	203	A_u	904.33	0.3
141	A_u	511.35	0.4	204	A_g	915.47	0.3
142	A_u	515.77	0.5	205	A_g	933.97	0.4
143	A_u	529.39	0.3	206	A_g	946.68	0.4
144	A_g	531.04	0.3	207	A_g	951.65	0.2
145	A_g	533.28	0.3	208	A_u	957.55	0.1
146	A_g	535.17	0.3	209	A_u	970.43	0.3
147	A_g	536.01	0.5	210	A_u	984.56	0.0
148	A_u	541.33	0.3	211	A_u	995.96	0.2
149	A_u	548.29	0.4	212	A_g	996.56	0.2
150	A_g	559.93	0.3	213	A_u	997.82	0.4
151	A_g	562.13	0.3	214	A_g	999.44	0.4
152	A_u	564.56	0.2	215	A_g	1001.06	0.3
153	A_g	568.28	0.5	216	A_u	1001.12	0.4
154	A_u	571.23	0.3	217	A_g	1007.43	0.2
155	A_g	571.46	0.4	218	A_g	1018.43	0.2
156	A_u	578.47	0.2	219	A_u	1018.75	0.3
157	A_u	583.94	0.2	220	A_u	1019.53	0.3
158	A_u	590.70	0.3	221	A_g	1022.35	0.2
159	A_g	593.57	0.2	222	A_u	1029.27	0.4
160	A_g	594.34	0.3	223	A_u	1037.26	0.3
161	A_u	625.21	0.4	224	A_g	1040.86	0.2
162	A_g	628.85	0.2	225	A_u	1046.33	0.3
163	A_u	631.91	0.3	226	A_g	1046.54	0.3
164	A_u	633.63	0.2	227	A_g	1050.66	0.3
165	A_u	637.75	0.6	228	A_u	1054.44	0.3
166	A_u	647.25	0.3	229	A_g	1055.06	0.4
167	A_u	650.66	0.2	230	A_g	1065.52	0.3
168	A_g	651.17	0.1	231	A_u	1066.45	0.2
169	A_g	653.98	0.4	232	A_u	1076.34	0.3
170	A_u	661.70	0.5	233	A_g	1077.04	0.3
171	A_g	665.90	0.4	234	A_u	1079.19	0.3
172	A_g	677.55	0.3	235	A_g	1080.41	0.3
173	A_g	684.05	0.5	236	A_g	1084.57	0.3
174	A_g	688.20	0.5	237	A_u	1089.07	0.3
175	A_u	693.01	0.4	238	A_g	1096.95	0.3
176	A_g	700.85	0.4	239	A_u	1105.44	0.3
177	A_u	708.64	0.4	240	A_g	1110.01	0.3
178	A_u	709.56	0.5	241	A_u	1118.85	0.3
179	A_g	710.65	0.4	242	A_g	1131.58	0.3
180	A_g	714.88	0.3	243	A_u	1133.04	0.3
181	A_u	720.96	0.5	244	A_g	1141.36	0.3
182	A_g	727.15	0.5	245	A_u	3804.94	-0.1
183	A_u	736.79	0.5	246	A_g	3804.98	-0.1
184	A_u	745.27	0.5	247	A_g	3817.67	-0.1
185	A_g	747.72	0.4	248	A_u	3818.90	-0.1
186	A_u	751.77	0.4	249	A_u	3820.09	0.0
187	A_u	770.53	0.5	250	A_g	3821.56	0.0
188	A_g	771.01	0.4	251	A_u	3825.84	-0.1
189	A_u	775.28	0.5	252	A_g	3826.48	-0.1

With the set of pressure and temperature data, we fitted the results by the third-order Birch-Murnaghan equation of state for each *P-T* condition. The results, K_{T0}, K_T' and V_T obtained in the pressure range 0 – 10 GPa and between 10 – 900 K are reported in Tables S2, S3 and S4 (Supplementary Materials), respectively. At ambient *T* the refined equation of state parameters are K_{T0} = 59.93 GPa, K' = 7.84 and V_0 = 940.6 Å^3. These data well match those obtained in previous powder XRD experiments, K_{T0} = 57.3 GPa, K' = 6.97 and V_0 = 938.9 Å^3 in the work of Curetti et al. (2002) and K_{T0} = 57.0 GPa and V_0 = 933.0 Å^3 in the investigation of Comodi et al. (2002). We also compared our theoretical BM3 results at 573, 723 and 873 K with the corresponding experimental values at the same temperatures from the work of Comodi et al. (2002) (see Table 6.4). The theoretical BM3 fitting for each isotherm is in reasonable agreement with experimental data, with a slight overestimation of both bulk moduli (+3.8%) and unit cell volume at zero pressure (+1.3%). This systematic shift suggests that the quasi-harmonic approximation describes well the thermalmechanical behaviour of muscovite at high temperature and the deviations could be imputable to the different composition in the experimental sample, as explained above.

Table 6.4. Comparison on theoretical and experimental BM3 results

	Present work	Experimental
T = 573 K		
K_{T0} (GPa)	55.52	55.1
K_T'	8.07	-
V_0 (Å^3)	950.2	938.0
T = 723 K		
K_{T0} (GPa)	53.08	51.1
K_T'	8.20	-
V_0 (Å^3)	956.1	944.1
T = 873 K		
K_{T0} (GPa)	50.62	48.9
K_T'	8.33	-
V_0 (Å^3)	962.4	952.5

Notes: experimental values are taken from the work of Comodi et al. (2002).

From the calculated bulk modulus at different temperatures, we obtained its thermal dependency, $(\partial K_T/\partial_T)_P$ = -0.0158 GPa K^{-1}, which is close to the experimental result of Comodi et al. (2002) (–0.0146 GPa K^{-1}).

The $\alpha_T K_T$ product attains the value of 2.39·10^{-3} GPa/K in the 100 – 900 K range and reach a constant value of 2.48·10^{-3} GPa/K at very high temperatures (see Figure 6.9a,b). To our knowledge, no experimental or theoretical data are available for muscovite at the moment for a proper comparison.

We calculated the thermal expansion coefficient (α_T) from the $\alpha_T K_T$ product by the thermal bulk modulus previously obtained. We plotted the $\alpha(T)_P$ values at pressures 0, 5 and 10 GPa in Figure 6.9c. It is possible to observe that the thermal expansion coefficient decreases with pressure increase. There is a good agreement between the theoretical value at standard *P* and *T* (α_T = 3.34 · 10^{-5} K^{-1}) and different experimental results obtained in the same conditions: α_T = 3.57 · 10^{-5} K^{-1} (Comodi et al., 2002) and α_T = 3.54 · 10^{-5} K^{-1} (Guggenheim et al., 1987). A three-dimensional plot in the range 0 – 10 GPa and 10 – 900 K is reported in Figure 6.9d.

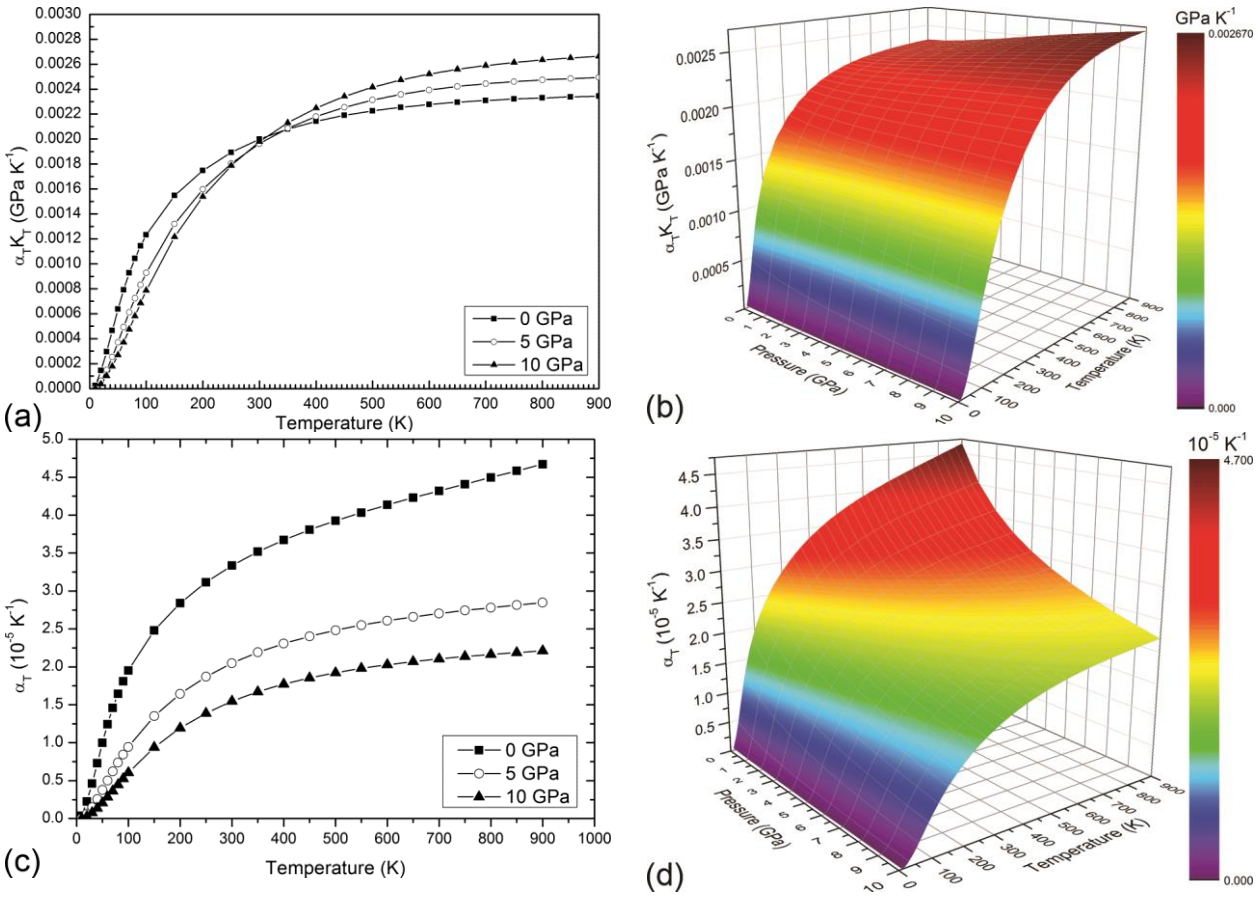

Figure 6.9 *Ab initio* $\alpha_T K_T$ product (a) and α_T (c) calculated for muscovite at selected pressures. 3D plots of TKT product (b) and thermal expansion coefficients (d) in the temperature range 100 – 900 K.

The isochoric and isobaric heat capacities were calculated with Eqs. (6.13) and (6.14), respectively (see Figures 6.10a,b). It was observed that C_V attains the Dulong-Petit limit at high temperatures. For both isochoric and isobaric specific heat, it can be observed a decrease of their values by increasing pressure. The C_P vs. T data are fitted between in the range 298.15–900K according to the form of a Haas–Fisher polynomial expression (Haas and Fisher, 1976), which is:

$$C_p = a + b \cdot T + c \cdot T^{-2} + d \cdot T^2 + e \cdot T^{-1/2} \qquad (6.14)$$

The retrieved regression coefficients, listed in Table 6.5, reproduce computed heat capacities with a mean error of about ±0.26 J mol^{-1} K^{-1} and the summation of squared residuals over 13 values is 1.1.

Table 6.5 Haas–Fisher polynomial regression coefficients for C_P at 298.15K and 0.0GPa

Phase	**a**	**b**	**c**	**d**	**e**
Muscovite	$8.2044 \cdot 10^{2}$	$-3.5759 \cdot 10^{-2}$	0.8976	$5.4382 \cdot 10^{-5}$	$-8.5978 \cdot 10^{3}$

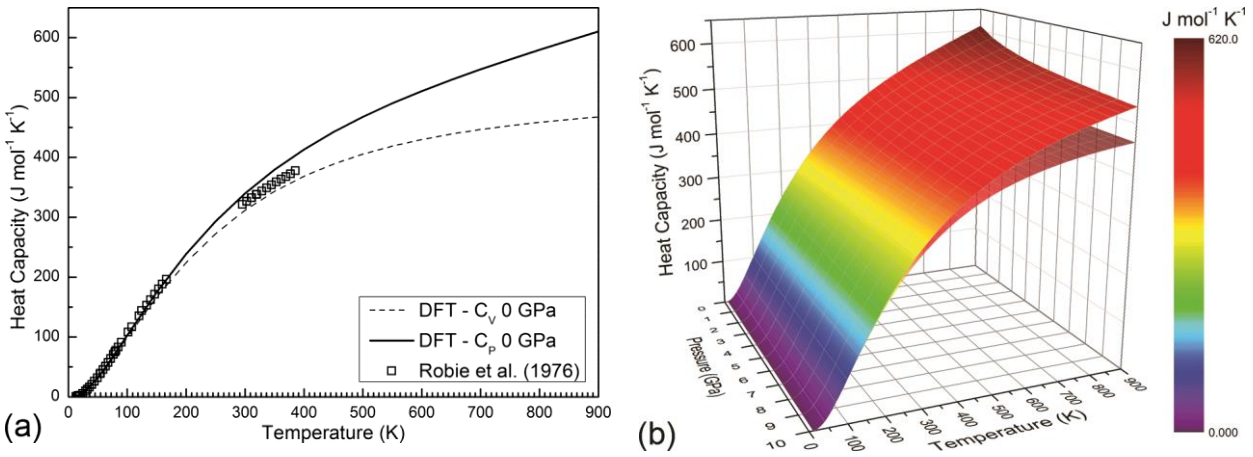

Figure 6.10 (a) Muscovite *ab initio* isochoric (dashed lines) and isobaric (solid lines) heat capacities, compared to experimental calorimetric data (Robie et al., 1976). (b) Three-dimensional plot of heat capacities at different volumes and in the temperature range 10 – 900 K.

Compared to previous scanning calorimetric data (Robie et al., 1976), the *ab initio* isobaric heat capacity in the range 10 – 380 K nicely fit the experimental results, albeit with a small deviation above room temperature.

In general, muscovite thermo-mechanical properties, obtained with a DFT/B3LYP-D* quantum mechanics modelling of the structure and quasi harmonic treatment to include the thermal effects, are in adequate if not very good agreement with experimental results reported in literature. The proposed theoretical approach, which was also successfully adopted by other authors (Ottonello et al., 2010; Ottonello et al., 2009b; Prencipe et al., 2011), is promising for detailed thermo-mechanical and thermo-chemical analysis of phyllosilicates. Regarding the compressional behavior, we obtained theoretical data in good agreement with experimental ones, with *V(P)* trend very close to the one observed by both Curetti et al. (2006) and Comodi et al. (2002), which studied Ms powdered sample by XRD. These results could be helpful to researchers that would eventually study this mineral by single-crystal XRD in P-T conditions similar to ours.

REFERENCES CITED

Anderson, O.L. (1995) Equation of state of solids for geophysics and ceramic science. 405 p. Oxford University Press, New York, US.

Angel, R.J. (2001) EOS-FIT6.0. Computer Program (http://www.rossangel.com).

Becke, A.D. (1993) Density-Functional Thermochemistry .3. The Role of Exact Exchange. Journal of Chemical Physics, 98(7), 5648-5652.

Birch, F. (1947) Finite elastic strain of cubic crystal. Physical Review, 71, 809-824.

Brigatti, M.F., Frigieri, P., and Poppi, L. (1998) Crystal chemistry of Mg-, Fe-bearing muscovites-2M(1). American Mineralogist, 83(7-8), 775-785.

Broyden, C.G. (1970a) The convergence of a class of double-rank minimization algorithms 1. General considerations. IMA Journal of Applied Mathematics (Institute of Mathematics and Its Applications), 6(1), 76-90.

-. (1970b) The convergence of a class of double-rank minimization algorithms: 2. The new algorithm. IMA Journal of Applied Mathematics (Institute of Mathematics and Its Applications), 6(3), 222-231.

Burnham, C.W., and Radoslovich, E.W. (1964) Crystal structure of coexisting muscovite and paragonite. Carnegie Institute of Washington Year Book, 63, 232-236.

Catti, M., Ferraris, G., Hull, S., and Pavese, A. (1994a) Powder Neutron-Diffraction Study of 2m1 Muscovite at Room Pressure and at 2 Gpa. European Journal of Mineralogy, 6(2), 171-178.

Catti, M., Ferraris, G., and Ivaldi, G. (1989) Thermal Strain Analysis in the Crystal-Structure of Muscovite at 700-Degrees-C. European Journal of Mineralogy, 1(5), 625-632.

Catti, M., Valerio, G., Dovesi, R., and Causa, M. (1994b) Quantum-mechanical calculation of the solid-state equilibrium MgO + alpha-Al_2O_3 $MgAl_2O_4$ (spinel) versus pressure. Physical Review B, 49(20), 14179-14187.

Civalleri, B., Zicovich-Wilson, C.M., Valenzano, L., and Ugliengo, P. (2008) B3LYP augmented with an empirical dispersion term (B3LYP-D*) as applied to molecular crystals. Crystengcomm, 10(4), 405-410.

Comodi, P., Gatta, G.D., Zanazzi, P.F., Levy, D., and Crichton, W. (2002) Thermal equations of state of dioctahedral micas on the join muscovite-paragonite. Physics and Chemistry of Minerals, 29(8), 538-544.

Comodi, P., and Zanazzi, P.F. (1995) High-Pressure Structural Study of Muscovite. Physics and Chemistry of Minerals, 22(3), 170-177.

Dovesi, R., Saunders, V.R., Roetti, C., Orlando, R., Zicovich-Wilson, C.M., Pascale, F., Civalleri, B., Doll, K., Harrison, N.M., Bush, I.J., D'Arco, P., and Llunell, M. (2009) CRYSTAL09 User's Manual. University of Torino, Torino.

Fletcher, R. (1970) A new approach to variable metric algorithms. The Computer Journal, 13(3), 317-322.

Gatti, C., Saunders, V.R., and Roetti, C. (1994) Crystal-field effects on the topological properties of the electron-density in molecular-crystals - the case of urea. Journal of Chemical Physics, 101(12), 10686-10696.

Goldfarb, D. (1970) A family of variable-metric methods derived by variational means. Mathematics of Computation, 24, 23-26.

Grimme, S. (2006) Semiempirical GGA-type density functional constructed with a long-range dispersion correction. Journal of Computational Chemistry, 27(15), 1787-1799.

Guggenheim, S., Chang, Y.H., and Koster Van Groos, A.F. (1987) Muscovite dehydroxylation: high-temperature studies. American Mineralogist, 72(5-6), 537-550.

Guidotti, C.V., and Sassi, F.P. (1976) Muscovite as a petrogenetic indicator mineral in pelitic schists. Neues Jahrbuch fuer Mineralogie, Abhandlungen, 123, 97-142.

Haas, J.L., and Fisher, J.R. (1976) Simultaneous evaluation and correlation of thermodynamic data. American Journal of Science, 276, 525-545.

Hernandez-Haro, N., Ortega-Castro, J., Del Valle, C.P., Munoz-Santiburcio, D., Sainz-Diaz, C.I., and Hernandez-Laguna, A. (2013) Computational study of the elastic behavior of the 2M(1) muscovite-paragonite series. American Mineralogist, 98(4), 651-664.

Lee, C.T., Yang, W.T., and Parr, R.G. (1988) Development of the Colle-Salvetti Correlation-Energy Formula into a Functional of the Electron-Density. Physical Review B, 37(2), 785-789.

Militzer, B., Wenk, H.R., Stackhouse, S., and Stixrude, L. (2011) First-principles calculation of the elastic moduli of sheet silicates and their application to shale anisotropy. American Mineralogist, 96(1), 125-137.

Momma, K., and Izumi, F. (2008) VESTA: a three-dimensional visualization system for electronic and structural analysis. Journal of Applied Crystallography, 41, 653-658.

Mondol, N.H., Jahren, J., and Bjørlykke, K. (2008) Elastic properties of clay minerals. Leading Edge (Tulsa, OK), 27(6), 758-770.

Monkhorst, H.J., and Pack, J.D. (1976) Special points for Brillouin-zone integrations. Physical Review B, 8, 5188-5192.

Mookherjee, M., and Redfern, S.A.T. (2002) A high-temperature Fourier transform infrared study of the interlayer and Si-O-stretching region in phengite-2M(1). Clay Minerals, 37(2), 323-336.

Nada, R., Nicholas, J.B., McCarthy, M.I., and Hess, A.C. (1996) Basis sets for ab initio periodic Hartree-Fock studies of zeolite/adsorbate interactions: He, Ne, and Ar in silica sodalite. International Journal of Quantum Chemistry, 60(4), 809-820.

Ortega-Castro, J., Hernandez-Haro, N., Timon, V., Sainz-Diaz, C.I., and Hernandez-Laguna, A. (2010) High-pressure behavior of 2M(1) muscovite. American Mineralogist, 95(2-3), 249-259.

Ottonello, G., Civalleri, B., Ganguly, J., Perger, W.F., Belmonte, D., and Zuccolini, M.V. (2010) Thermo-chemical and thermo-physical properties of the high-pressure phase anhydrous B ($Mg_{14}Si_5O_{24}$): An ab-initio all-electron investigation. American Mineralogist, 95(4), 563-573.

Ottonello, G., Civalleri, B., Ganguly, J., Zuccolini, M.V., and Noel, Y. (2009a) Thermophysical properties of the alpha-beta-gamma polymorphs of Mg2SiO4: a computational study. Physics and Chemistry of Minerals, 36(2), 87-106.

Ottonello, G., Zuccolini, M.V., and Civalleri, B. (2009b) Thermo-chemical and thermo-physical properties of stishovite: An ab-initio all-electron investigation. CALPHAD: Computer Coupling of Phase Diagrams and Thermochemistry, 33(3), 457-468.

Pavese, A., Ferraris, G., Pischedda, V., and Mezouar, M. (1999) Synchrotron powder diffraction study of phengite 3T from the Dora-Maira massif: P-V-T equation of state and petrological consequences. Physics and Chemistry of Minerals, 26(6), 460-467.

Prencipe, M., Pascale, F., Zicovich-Wilson, C.M., Saunders, V.R., Orlando, R., and Dovesi, R. (2004) The vibrational spectrum of calcite (CaCO3): an ab initio quantum-mechanical calculation. Physics and Chemistry of Minerals, 31(8), 559-564.

Prencipe, M., Scanavino, I., Nestola, F., Merlini, M., Civalleri, B., Bruno, M., and Dovesi, R. (2011) High-pressure thermo-elastic properties of beryl (Al4Be6Si12O36) from ab initio calculations, and observations about the source of thermal expansion. Physics and Chemistry of Minerals, 38(3), 223-239.

Robie, R.A., Hemingway, B.S., and Wilson, W.H. (1976) Heat capacities of calorimetry conference copper and of muscovile $KAl_2(AlSi_3)O_{10}(OH)_2$, pyrophyllite $Al_2Si_4O_{10}(OH)_2$, and illite $K_3(Al_7Mg)(Si_{14}Al_2)O_{40}(OH)_8$ between 15 and 375 K and their standard entropies at 298.15K. Journal of Research of the U.S. Geological Survey, 4(6), 631-644.

Rothbauer, R. (1971) Untersuchung eines $2M_1$-muskovits mit neutronenstrahlen. Neues Jahrbuch fuer Mineralogie, Monatshefte, 143-154.

Shanno, D.F. (1970) Conditioning of quasi-Newton methods for function minimization. Mathematics of Computation, 24, 647-656.

Stixrude, L. (2002) Talc under tension and compression: Spinodal instability, elasticity, and structure. Journal of Geophysical Research-Solid Earth, 107(B12).

Ugliengo, P., Viterbo, D., and Chiari, G. (1993) MOLDRAW: molecular graphic on a personal computer. Zeitschrift Fur Kristallographie, 207, 9-23.

Ulian, G., Tosoni, S., and Valdrè, G. (2013a) Comparison between Gaussian-type Orbitals and Plane Wave *ab initio* DFT modeling of layered silicates: Talc mineral as model system. Journal of Chemical Physics, Submitted.

-. (2013b) The mechanical properties of talc $[Mg_3Si_4O_{10}(OH)_2]$: a density functional theory contribution. Physics and Chemistry of Minerals, Submitted.

CHAPTER 7 – Periodic a*b initio* bulk investigation of hydroxylapatite and type A carbonated apatite with both pseudopotential and all-electron basis sets for calcium atoms.[6]

Abstract

Apatite minerals draw the attention of many researchers not only in mineralogy, but also in biology, biochemistry, and medicine because hydroxylapatite [$Ca_{10}(PO_4)_6(OH)_2$] is the main component of the mineral phase of mammalian bones. However, in nature this mineral is mostly present with various stoichiometric defects. The carbonate ion is found commonly in its structure where it can occupy different crystallographic sites; however, its configurational energy and relative orientation in the apatite lattice is still debated.

In this work, bulk structural features of hexagonal hydroxylapatite (space group $P6_3$) and type A carbonated apatite [$Ca_{10}(PO_4)_6(CO_3)$, space group $P1$] have been modeled by density function method using the hybrid B3LYP functional and an all-electron polarized double-ζ quality Gaussian-type basis set using the CRYSTAL09 computer program. The effect on the structural parameters due to the adoption of the present all-electron basis set for the Ca ion compared to the pseuodpotential adopted in previous work has also been discussed. Different orientations of the carbonate ion in the apatite unit cell have been considered. The B3LYP functional and Gaussian-type basis set with polarization have been adopted. The geometry of the model (lattice parameters and internal coordinates) has been fully optimized and resulted in very good agreement with XRD data reported in literature that suggest a "close" configuration (type A1) of the carbonate ion, i.e., with a C-O bond perpendicular to the **c**-axis of the apatite cell.

7.1 Introduction

Apatite minerals are found in almost all igneous rocks and also in some metamorphic and sedimentary ones. The most important member of the apatite family, both as naturally occurring mineral and as synthetic compound, is hydroxylapatite OHAp [$Ca_{10}(PO_4)_6(OH)_2$]. As shown by X-ray diffraction (XRD) analysis performed by Suda and co-workers (1995), OHAp can be found in nature as two

[6] This chapter consists of a paper by Gianfranco Ulian, Giovanni Valdrè, Marta Corno and Piero Ugliengo, "Periodic ab initio bulk investigation of hydroxylapatite and type A carbonated apatite with both pseudopotential and all-electron basis sets for calcium atoms", published in *American Mineralogist*, 98(2-3), p. 410-416.

polymorphs: monoclinic [$P2_1/b$] or hexagonal [$P6_3/m$]. The monoclinic cell is obtained from the hexagonal one by doubling the **b** parameter and presents hydroxyl columns with different OH orientations along the **c**-axis (Rabone and de Leeuw, 2005). The hexagonal cell ($a = b$) is related to the monoclinic structure when the glide plane b is a mirror plane m and the twofold axis is a 6_3 axis (Corno et al., 2006). Suda and co-workers (1995) observed also that at low temperature, the monoclinic cell is more stable than the hexagonal one; the phase transition between the two polymorphs (order/disorder) takes place at 200 °C. The hexagonal OHAp is an extremely important phase, because it is the inorganic component of mammalian bone tissues. OHAp may contain a certain amount of compositional defects, the most abundant is the carbonate ion (CO_3^{2-}, ~6% in weight). The presence of CO_3^{2-} in the mammalian OHAp is necessary to stabilize the hexagonal structure at room temperature (Suda et al., 1995).

Since the first half of the 20th century, researchers were interested in the role of OHAp as a biomaterial for bone and tooth repair, reconstruction and replacement (Albee, 1920). However, to improve biocompatibility, the biomaterial should be similar to the bone tissue mineral phase, rather than to pure hydroxylapatite.

The structure of hexagonal OHAp allows extensive atomic substitution and non-stoichiometry in Ca, P, and OH channel sites. For example, anions such as fluoride, chloride and carbonate can easily enter in the channel parallel to the **c**-axis, leading to fluoro-, chloro- and carbonate apatites, both as end-members and in mutual solid solutions (Elliott, 1998; Hughes and Rakovan, 2002). Many experimental works (Antonakos et al., 2007; Fleet, 2009; Fleet and Liu, 2007; Fleet and Liu, 2003; Fleet and Liu, 2004; Fleet et al., 2011; Sturgeon and Brown, 2009; Suetsugu et al., 1998) and theoretical studies (Astala and Stott, 2005; Peroos et al., 2006; Rabone and de Leeuw, 2007; Stott and Yin, 2003; Zahn and Hochrein, 2008) have been done to better understand the role and the positions of CO_3^{2-} in the hydroxylapatite lattice. It appears that the carbonate ion can substitute both OH^- in the **c**-axis channel of apatite (type A) and the phosphate group (type B). This is suggested by Fourier transform infrared (FTIR) analysis showing that the normal modes of the carbonate group fall at different frequencies according to the site occupied by the anion (Fleet and Liu 2003; Fleet and Liu 2004; Fleet and Liu 2007).

Despite many results provided by experimental and theoretical investigations, carbonated hydroxylapatite presents some unclear features and it is still debated. There is not a full agreement on the

entity of the crystallographic lattice variations due to the carbonate ion substitutions and on the preferred geometrical orientation of the CO_3^{2-}, especially relative to the calcium channel ion of type A carbonated hydroxylapatite.

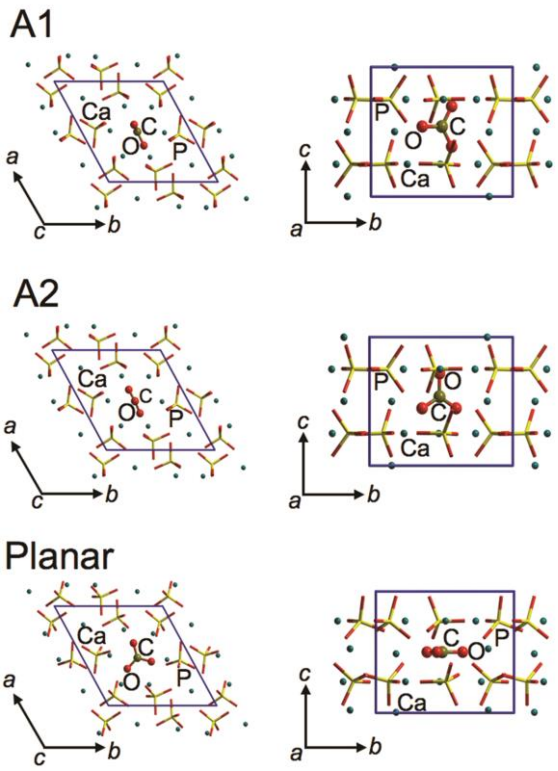

Figure 7.1. Views along [001] (left) and [100] (right) of type A CAp with three different configurations of CO_3^{2-}. (A1) "close" configuration, (A2) "open" configuration and "planar" configuration.

The carbonate ion in OHAp may constitute both a negatively and a positively charged defect if it substitutes an OH^- or a PO_4^{3-}, respectively. While for type A the charge compensation usually takes place by OH vacancies, in type B carbonated hydroxylapatite there are many possible ways to restore the neutrality, for example by combinations of hydroxyl group and calcium ion vacancies, which can produce different effects on the geometry of the structure (Astala and Stott 2005). In the present work, we deal with only type A carbonate substitution. The modeling of type B carbonated hydroxylapatite will be the subject of a future work.

There are three proposed CO_3^{2-} configurations in the type A apatite cell (see Figure 7.1). Interpretation of experimental FTIR spectra suggested two possible configurations for the CO_3^{2-} in the Ca^{2+} channel. The first one is a "close" configuration (type A1) in which a C-O bond is perpendicular to the **c**-axis (space group $P\bar{3}$) (Fleet and Liu 2003; Fleet et al. 2011). This configuration was also investigated by two different theoretical approaches. A static-lattice cluster of a type A carbonated apatite supermolecule (SM) evaluated by Hartree-Fock methods (Peeters et al., 1997) and a periodic lattice calculated using the density functional theory (DFT) with a generalized gradient approximation (GGA) and pseudopotentials on all the atoms of the structure (Astala and Stott 2005).

The second one is an "open" configuration (type A2), where a C-O bond is parallel to the **c**-axis (space group $P\bar{6}$) (Suetsugu et al. 1998). Both the close and open configurations have the CO_3^{2-} molecular plane parallel to the apatite (100) crystallographic plane.

The third carbonate configuration (planar) was proposed and investigated by Peroos and co-workers using static and dynamic quantum mechanics (QM) methods adopting empirical interatomic potentials (Peroos et al. 2006). In this configuration, the CO_3^{2-} molecular plane is parallel to the (001) plane and all the C-O bonds are perpendicular to the **c**–axis. However, QM proved that this configuration is not energetically favorable. Also, there is no experimental evidence of this kind of orientation of the carbonate ion (Fleet et al. 2011).

The aim of the present research is to investigate in details type A carbonated apatite (CAp) by periodic ab initio quantum mechanics modeling using both the proposed modeling approach of Corno and co-workers (2006) with pseudopotential on calcium atoms and, for the first time, an all electron basis set for all the atoms of the carbonated apatite structure. The steps of the modeling with the CO_3^{2-} in different configurations were the following: first we simulated an OHAp bulk cell, then we removed the OH^- groups and placed the carbonate ion in one of the equivalent orientation within the selected configuration (open, close and planar). The crystallographic parameters of the optimized structures were compared with the data presented in literature.

7.2 Computational details

All calculations have been performed on a Debian (Linux) Cluster with the ab initio CRYSTAL09 code (Dovesi et al., 2009), which implements the Hartree–Fock and Kohn–Sham self consistent field method for the study of periodic systems. All graphical drawings have been carried out with the molecular graphics program MOLDRAW (Ugliengo et al., 1993).

Basis set

Multielectron wave functions are described by linear combination of crystalline orbitals (CO), expanded in terms of Gaussian-type basis sets. The basis sets have been chosen from optimized ones used by other authors for their investigations of OHAp, CAp or similar structures. Calcium has been described with two different basis sets. The first one is a Hay-Wadt Small Core Pseudopotential (HWSCP) (Hay and Wadt, 1985), proposed and modified by Corno and co-workers (2006) for their study on pure hydroxylapatite mineral. The second adopted basis set for calcium atoms is a 8-6511G(2d), used by other authors for calcite (Valenzano et al., 2006), with outer shell exponents α_{sp} = 0.453 $bohr^{-2}$, α_{d1} = 3.1910 and 0.8683 $bohr^{-2}$ and α_{d2} = 0.2891 $bohr^{-2}$. For all the calculations, the

phosphorus atom is described by the basis 85-21G(d), α_{sp} = 0.48105 and 0.135 bohr^{-2} and α_d = 0.74583 bohr^{-2}, respectively. Oxygen and hydrogen are both represented by a 6-31G* basis set with the outer shell exponents α_{sp} = 0.2742 bohr^{-2} and α_d = 0.538 bohr^{-2}; and α_{sp} = 0.1613 and α_p = 1.1 bohr^{-2}, respectively. P, O, and H basis sets have been tested and adopted in previous works on hydroxylapatite (Corno et al. 2006). Finally, the carbon atom is described by a 6-21G* basis set with α_{sp} = 0.26 bohr^{-2} and α_d = 0.8 bohr^{-2}, previously adopted for magnesite (Catti et al., 1993).

Hamiltonian and computational parameters

The Becke three-parameter (B3LYP) hybrid exchange functional (Becke, 1993) in combination with the gradient-corrected correlation functional of Lee, Yang, and Parr (Lee et al., 1988) has been adopted for all calculations. This functional has been already used for alkali oxides, α-quartz, calcite and hydroxylapatite (Corno et al., 2006; Dovesi et al., 1991; Pascale et al., 2004; Prencipe et al., 2004). The presence of some fraction of exact exchange increases the electronic localization, which in turn increases the ionic nature of the materials, causing a systematic decrease of the lattice parameters and an increase of the elastic constants and bulk moduli. Standard DFT (with local-density approximation and generalized gradient approximation) and Hartree-Fock methods yield systematic errors with opposite signs. The hybrid functionals provide more accurate results (Corà et al., 2004). The exchange–correlation contribution is performed over a grid of points and is the result of a numerical integration of the electron density and its gradient. The adopted pruned grid is given by 75 points and 974 angular points, subdivided into 5 sub-intervals of 86, 194, 350, 974, and 350 points (75, 97-XLGRID) and obtained from the Gauss–Legendre quadrature and Lebedev schemes (Prencipe et al. 2004). This is a good compromise between accuracy and cost of calculation for geometry optimization and vibrational frequencies. The values of the tolerances that control the Coulomb and exchange series are the default provided by CRYSTAL09 (*ITOL*1 to *ITOL*4 = 6) (Dovesi et al. 2009), but we increased the pseudo-overlap parameter (*ITOL*5) from 12 to 14. The Hamiltonian matrix has been diagonalized (Monkhorst and Pack, 1976) using a shrinking factor of *IS* = 4 (Dovesi et al. 2009) that leads to 12 and 36 reciprocal lattice points (k-points) for OHAp and CAp, respectively.

Geometry

Lattice constants and internal coordinates have been optimized within the same run using the analytical gradient method for the atomic positions and a numerical gradient for the unit-cell parameters.

The Hessian matrix is upgraded with the Broyden–Fletcher–Goldfarb–Shanno algorithm. The tolerances for the maximum allowed gradient and the maximum atomic displacement for considering the geometry as converged have been set to 0.00006 hartree $bohr^{-1}$ and 0.00012 bohr, respectively.

Vibrational features

Within the harmonic approximation and in periodic systems, the phonon frequencies at Γ point are evaluated by diagonalising the central zone ($k = 0$) mass-weighted Hessian matrix

$$W_{ij}(k=0) = \sum_G \frac{H_{ij}^{0G}}{\sqrt{M_i M_j}}$$

where H^{0G}_{ij} is the second derivative of the electronic + nuclear repulsion energy E evaluated at equilibrium **u = 0**. The Hessian at equilibrium was obtained by numerical differentiation of the analytical first derivative, calculated at geometries obtained by small increments, υ, in each of the 3N nuclear coordinates with respect to the equilibrium geometry. An extensive discussion of the computational conditions and other numerical aspects concerning the calculation of the vibrational frequencies at Γ point can be found in the literature (Pascale et al., 2004; Tosoni et al., 2005).

The use of the B3LYP hybrid functional and all-electron basis set provides a good accuracy to the quantum mechanics simulations of solid phases with respect to the experimental results. However this improvement is expensive in terms of computational resources. In particular, we compared the optimization of the OHAp structure using both a pseudopotential (Habas et al., 1998) and the all-electron basis set on the calcium ions. While the different methods did not affect the number of optimization steps, the time needed to reach convergence is increased roughly by a factor of 2 when all-electron basis sets are used. This imposes a severe limit when larger cell are required or when the number of heavy atoms increases. It will be shown in the next sections that the differences of the equilibrium geometries obtained by the different methods are about 2% on lattice parameters, as observed in the comparison with the result of Astala and Stott (2005) and Corno and co-workers (2006).

However, it was observed in an earlier work by Valenzano et al. (2006) that the effect of the use of different basis sets and geometries are important for vibrational calculations. Richer basis sets are required to obtain more accurate data.

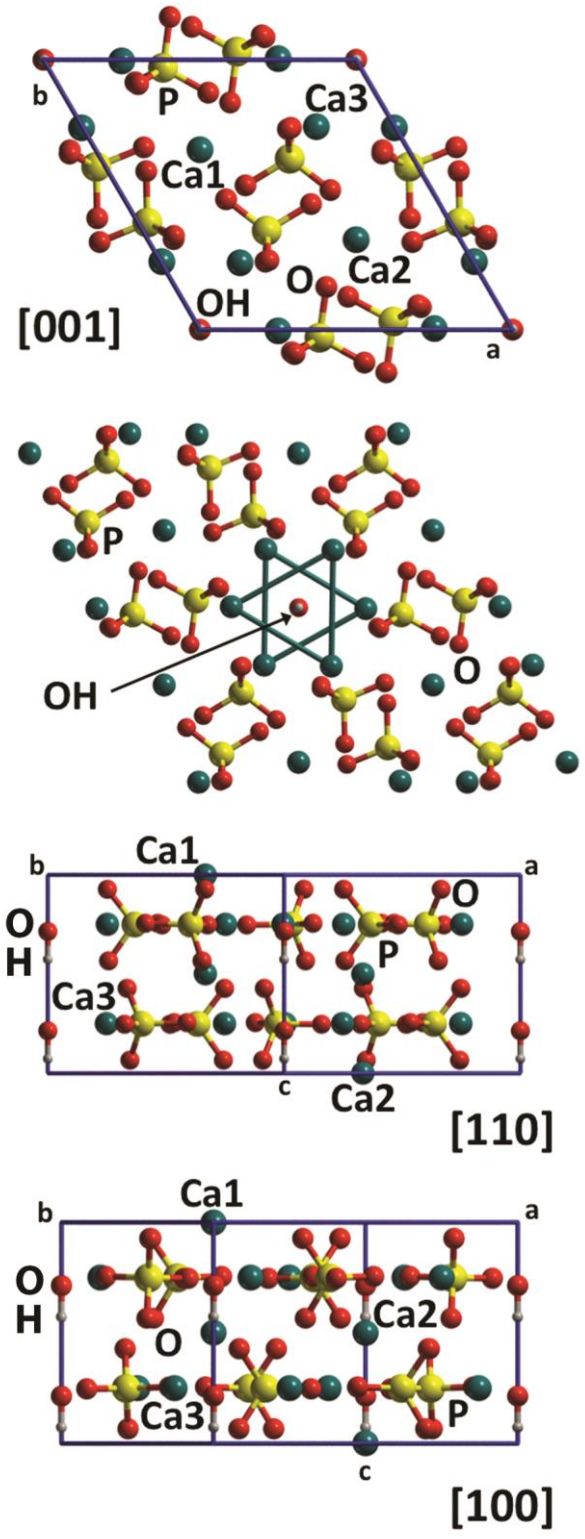

Figure 7.2. Optimization results and different views for the bulk structure of hydroxylapatite OHAp. Symmetrically different calcium ions are indicated.

7.3 Results and discussion

Quantum mechanics modeling of hydroxylapatite (OHAp)

Corno and co-workers (2006) have recently modeled the hydroxylapatite structure by ab initio quantum mechanics methods adopting an all electron basis set, except for the pseudopotentials for the calcium ions. The simulations referred to a structure of OHAp experimentally derived by XRD (Hughes et al. 1989). The unit-cell contains 44 atoms and two unit formula (Z = 2) of $Ca_5(PO_4)_3(OH)$. To take into account the half occupancy of the oxygen and hydrogen atoms of the hydroxyl group, Hughes and co-workers (1989) assigned a mirror plane *m* to the refined structure ($P6_3/m$ space group).

However, Corno and co-workers (2006) noted that within the experimentally observed $P6_3/m$ space group one cannot simulate the hexagonal OHAp because of the non-physical duplication of each OH group by the mirror plane. To avoid this situation, they reduced the symmetry to a $P6_3$ space group, in which all the OH groups maintain the same alignment in each column within the OHAp structure (see Figure 7.2). As a consequence of the symmetry reduction, the number of non-equivalent calcium atoms increases from two to three (Ca1, Ca2, and Ca3). The Ca1 atom has three O atoms as neighbors, Ca2 has six and Ca3 has four. The two hydroxyl groups are oriented in the same direction, along the **c** axis. Each hydroxyl group is placed in the center of an equilateral triangle described by three Ca3 atoms. The

results provided by their simulations were in agreement with the experimental results of Hughes and co-workers (1989) and of Saenger and Kuhs (1992) (see Table 7.1 for a comparison).

Table 7.1. Simulated and experimental results of hydroxylapatite OHAp

	B3LYP*	B3LYP†	XRD‡	Neutron§	Δ_{XRD}	$\Delta_{Neutron}$
Symmetry	$P6_3$	$P6_3$	$P6_3/m$	$P6_3/m$		
a (Å)	9.433	9.329	9.417	9.425	+0.016	+0.008
c (Å)	6.896	6.949	6.875	6.884	+0.021	+0.012
V (Å^3)	532	529	528	530	+4	+2
Bond length (Å)						
P-O1	1.547		1.529		+0.018	
P-O2	1.558		1.537		+0.021	
P-O3	1.551		1.537		+0.014	
P-O4	1.549		1.534		+0.015	
Mean	1.551	1.547	1.532	1.536	+0.019	+0.015
Ca3-Ca3	4.085		4.084		+0.001	
Ca3-O1	2.700		2.711		–0.011	
Ca3-O2	2.350		2.353		–0.003	
Ca3-O3	2.341		2.343		–0.002	
Ca3-O4	2.501		2.509		–0.008	
Ca3-O(H)	2.372		2.385		–0.013	
Mean Ca3-O	2.391	2.41	2.398	2.40	–0.007	–0.009
O-H	0.97	0.97	1.09	0.90	–0.12	+0.07

Notes: Mean Ca3-O distances have been evaluated with values <2.51 Å. Experimental data are referred to single-crystal analysis.
* Present work.
†(Corno et al., 2006).
‡ (Hughes et al., 1989).
§ (Saenger and Kuhs, 1992).

In the present work, we simulated the OHAp structure following the model of Corno and co-workers (2006), but we adopted a complete basis set for all atoms in the structure and the pseudopotential approximation on the Ca ion was completely removed. The optimization results are reported in Table 7.1 and graphically shown in Figure 7.2. In Table 7.1, the results were compared to those of the structure modeled by Corno et al. (2006) and to those experimentally obtained by single-crystal XRD (Hughes et al. 1989) and neutron diffraction (Saenger and Kuhs 1992). The structural features obtained from our simulation are slightly different with respect to those of Corno et al. (2006) because of the more complete basis set adopted. The cell parameters that we have obtained ($a = b$ = 9.433 Å, c = 6.896 Å) are very close to the experimental ones from XRD (Δa = +0.016 Å, Δc = +0.021 Å) and neutron diffraction (Δa = +0.008 Å, Δc = +0.012 Å). The mean bond lengths of P-O and Ca3-O interaction distances in our models are 1.551 Å and 2.391 Å, respectively. These results match very

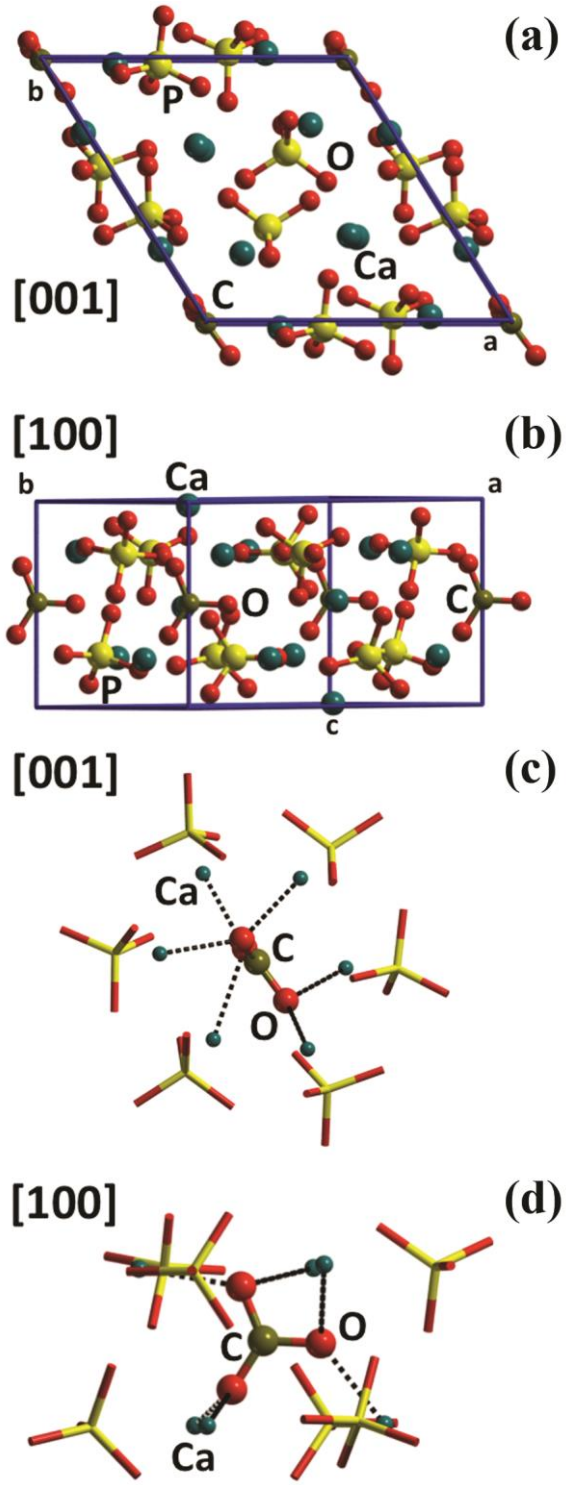

Figure 7.3. Simulation of CAp with carbonate ion in close configuration (type A1). The most stable structure was obtained from full geometry optimization. (a) [001] and (b) [100] projections. In **c** and **d**, the interactions between CO_3^{2-} and the channel calcium ions are showed along [001] and [100], respectively. Phosphorous, oxygen, and calcium radii were reduced for sake of clearness in **c** and **d**.

well with the ones from experimental analysis, with only a slight overestimation of the P-O bond lengths (Δ_{XRD} = +0.019 Å, $\Delta_{Neutron}$ = +0.015 Å) and a minimal underestimation of the Ca3-O interactions (Δ_{XRD} = –0.007 Å, $\Delta_{Neutron}$ = –0.009 Å). In particular, there is a very good agreement with the specific P-O and Ca-O bond/interaction lengths measured by Hughes et al. (1989), confirming the good choice of computational parameters, especially the rich basis set.

Quantum mechanics modeling of type A carbonated apatite (CAp)

The substitution of an OH ion by a CO_3 as in type-A carbonated apatite (independently of the sub type A1, A2, or planar) requires charge compensation. The simplest way to achieve this is the removal of the hydroxyl group remaining in the cell leading to the CAp cell with unit formula $Ca_{10}(PO_4)_6(CO_3)$. This method has also been adopted by Astala and Stott (2005) and by Peroos et al. (2006).

QM modeling involved initially the three configurations (A1, A2, and planar) described in the introduction and reported in Figure 7.1. In Table 7.2, all the details of the lattice parameters and bond lengths/angles for the three models optimized both the all-electron and pseudopotential on the Ca atom have been reported. In Table 7.3 the most stable carbonated apatite structures have been compared with the measured XRD data of Fleet and Liu (2003).

Table 7.2. Simulated results of type A CAp with all electron and pseudopotential basis sets on Ca atom

	Ca – All electron				Ca – Pseudopotential			
	A1	A2	Planar		A1	A2	Planar	
Symmetry	*P*1	*P*1	*P*1	*P*3	*P*1	*P*1	*P*1	*P*3
a (Å)	9.582	9.624	9.651	9.654	9.510	9.515	9.327	9.573
b (Å)	9.764	9.708	9.651	9.654	9.572	9.571	9.463	9.573
c (Å)	6.877	6.883	6.832	6.827	6.930	6.928	6.921	6.863
α (°)	89.3	89.5	90	90.0	89.5	89.5	90.2	90.0
β (°)	89.8	89.5	90	90.0	89.2	89.2	89.0	90.0
γ (°)	121.9	121.9	120	120.0	121.4	121.4	118.3	120.0
V_{cc} (Å^3)	546	546	551	551	538.1	538.3	537.6	544.7
Density (g/cm^3)	3.131	3.130	3.102	3.102	3.176	3.175	3.179	3.138
Mean bond length (Å)								
P-O	1.54	1.56	1.56	1.56	1.55	1.51	1.55	1.55
C-O	1.29	1.29	1.28	1.28	1.28	1.29	1.28	1.28
Ca-O_{CO3}	2.39	2.36	2.42	2.42	2.35	2.60	2.33	2.54
Mean bond angle (°)								
O-P-O	110.1	108.8	110.5	110.5	108.8	107.5	108.7	108.9
O-C-O	120.0	120.0	120.0	120.0	120.0	120.0	120.00	120.0

Type A1 configuration

The simulation was performed in absence of symmetry (space group *P*1) with two main advantages: no undesired atom is generated and the geometry optimization is unconstrained. This condition also allowed the carbonate ion to rotate and/or displace itself, passing through all the intermediate orientations until the minimum of energy was found.

The carbonate ion was placed with the central atom C at (x/*a*, y/*b*, z/*c*) = (0.0, 0.0, 0.5), in an intermediate position with respect to the two originally present hydroxyl ions that have been substituted by the CO_3^{2-} group in the OHAp cell. C-O bond lengths and OCO bond angles were set to 1.25Å and 120°, respectively.

The results from the geometry optimization of the models showed that the type A1 configuration was energetically favored with both the adopted basis sets, with a C-O bond (bisector of the CO_3^{2-} plane) perpendicular to the **c**-axis and the plane of the molecule slightly canted within the (100) plane by about 6° (Figs. 7.3a and 7.3b).

Table 7.3. Differences between experimental (XRD) and simulated results of type A CAp

	XRD*	A1-ae	A1-pp	SM-HF†	GGA-PBE‡
Symmetry	$P\bar{3}$	*P*1	*P*1	–	*P*1
a (Å)	9.521	+0.061	+0.011	9.544	9.88
b (Å)	9.521	+0.243	+0.051	9.544	9.69
c (Å)	6.873	+0.004	+0.057	6.859	7.14
α (°)	90	–0.7	-0.5	90.0	90.9
β (°)	90	–0.2	-0.8	90.0	89.6
γ (°)	120	+0.9	+1.4	120.0	118.7
Density (g/cm^3)	3.152	–0.021	+0.024	–	–
Mean bond length (Å)					
P-O	1.53	+0.01	+0.02	–	–
C-O	1.24	+0.05	+0.04	+0.03	+0.05
Ca-O_{CO3}	2.34	+0.05	+0.01	–	–
Mean bond angle (°)					
O-P-O	109.5	+0.6	-0.7	–	–
O-C-O	120.0	+0.0	+0.0	+0.0	+0.0

Notes: XRD data are referred to single-crystal analysis. A1-ae and A1-pp refers to the present results obtained with all electron and pseudopotential basis sets on Ca atoms, respectively. SM-HF and GGA-PBE results are related to earlier simulations conducted by static lattice/Hartree-Fock and periodic/DFT functionals, respectively. SM-HF lattice parameters have not been optimized.
* Fleet and Liu (2003).
† Peeters et al. (1997).
‡ Astala and Stott (2005).

Each oxygen of the carbonate ion interacts electrostatically with two Ca^{2+} of the apatite structure (Figs. 6.3c and 6.3d) with a mean interaction distance of 2.39 Å. The local geometry of CO_3^{2-} is very close to that of calcite, where the same O_{CO3} — Ca^{2+} interaction at 2.34 Å has been observed (Maslen et al., 1993).

Our simulation of CAp showed also that the two calcium ions in the channel placed on the (100) plane are shifted along the [010] direction with their relative distance increased from 5.84 Å (in OHAp) to 6.42 Å (in CAp). For the two Ca^{2+} along [100], their distance is slightly increased (+0.22 Å). The other remaining two calcium ions in the channel have not been significantly displaced (<0.001 Å) with respect to their position in OHAp. This general distortion from the ideal hexagonal channel allows the accommodation of the carbonate ion in the apatite structure.

The phosphate ions are slightly displaced to maintain a constant P-Ca^{2+} mean distance of 3.67 Å. The same value has been observed for pure OHAp. The internal bond lengths and angles of the PO_4^{3-}

tetrahedrons are slightly modified from the ideal ones to minimize the sterical encumbrance and optimize the electrostatic interaction with the surrounding ions. All the atomic positions of the modeled CAp can be found in the crystallographic information framework (CIF) data file.

In type A1 configuration, the main effect of the $CO_3^{2-}/2OH^-$ substitution is the increase of *a* and *b* cell parameters (*a* = 9.582 Å, *b* = 9.764) and a contraction of *c* (*c* = 6.877 Å). Despite the lack of symmetry, the unit-cell angles (α, β, γ) show only slight differences from the pure hydroxylapatite ones. Our structural observations are in good agreement with the results of the earlier theoretical works of Peeters et al. (1997) and Astala and Stott (2005). We observed an opposite effect on the *a*, *b*, α, and γ lattice parameters compared to those of type-A ordered CAp by Astala and Stott (2005), because of the different orientation of the carbonate ion in the unit cells.

Because the experimentally refined structures available in literature are not of pure carbonated apatite, the comparison of our model was made with the structure of the more carbonate-rich carbonated apatite (0.75CAp·0.25OHAp) that was characterized by single-crystal XRD and FTIR by Fleet and Liu (2003) and Fleet et al. (2011). The crystallographic parameters, bond lengths and angles of type A1 configuration modeled in our work are in very good agreement with those experimentally refined (see Table 7.2). The slight difference on the *b* lattice parameter may arise because the absence of symmetry constrains in the modeled CAp allowed a relaxation of the structure primarily along the **b**-axis. The carbonate ion plane is parallel to this direction and causes a stretch in the Ca^{2+} channel to minimize sterical encumbrance. Also, worth to be noted that our model refers to a pure carbonated apatite (CAp).

The results of our modeling are in agreement also with FTIR analysis. In Figure 7.4, we reported a comparison between the simulated vibrational spectra obtained by our model and those experimentally observed by Fleet and Liu (2003). In the figure, the asymmetrical stretching and the out-of-plane bending of the type A1 carbonate ion have been labeled as ν_3 and ν_2, respectively. ν_3 consists in a doublet in the 1600-1500 cm^{-1} region, with peaks centered at 1604 and 1518 cm^{-1}. These signals slightly shifted at higher wavenumbers than those observed by Fleet and Liu (2003) and Fleet et al.

(2011). However, the separation between the two peaks obtained by the simulation is very close to the experimental one, 86 and 83 cm^{-1}, respectively. For the out-of-plane (ν_2) vibrational mode, we obtained a band centered at 878 cm^{-1}, the same value observed by Fleet and Liu (2003) and Fleet et al. (2011).

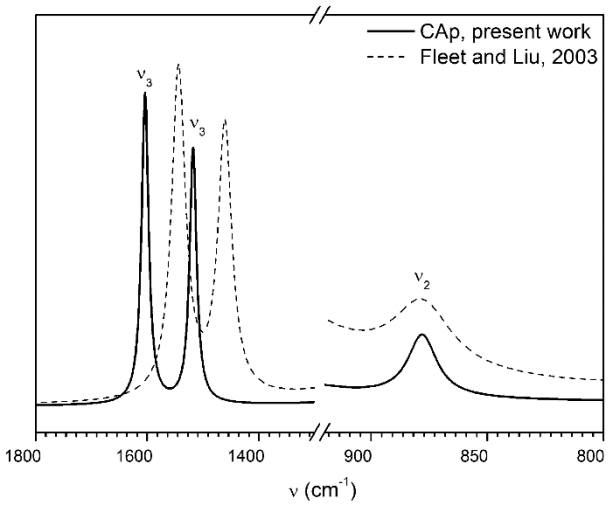

Figure 7.4. IR regions relative to type A1 CO_3^{2-} asymmetric stretching ν_3 and out-of-plane bending ν_2. Continuous line refers to our simulated data, whereas dashed line was extrapolated from the results of Fleet and Liu (2003).

Type A2 configuration

The unconstrained geometrical optimization of the CAp structure starting with the CO_3^{2-} in type A2 configuration brought the carbonate ion toward type A1 configuration through a molecular rotation of the CO_3^{2-} (see in Figure 1 the difference between the close and open configurations). This effect was also obtained adopting the pseudopotential on Ca atoms. The observed angle of rotation (30°) was the minimum angular value needed to pass from the open to the close configuration. The A2/A1 transition is in agreement with the results of Fleet et al. (2011), where they observed that type A1 is the preferred configuration.

Planar configuration

The planar configuration model was created with the CO_3^{2-} molecular plane parallel to the (001) cell plane. It was geometrically optimized with *P*3 and *P*1 space group symmetry. We observed two different results when adopting the proposed basis sets. Using the pseudopotential on calcium atoms, the carbonate ion was displaced and brought in the A1 configuration removing the symmetry constrains. Instead, with the all electron basis the planar configuration was maintained both with and without symmetry, although the difference in the crystal intrinsic electronic energy is very high if compared with the close configuration, resulting +165.78 kJ/mol for the *P*3 structure and +164.78 kJ/mol for the unconstrained one (*P*1). To better understand the nature of this difference, we calculated the vibrational features and we found that the planar configuration represents a saddle point on the potential energy surface. However the details of this investigation are beyond the scope of the present paper and will be the subject of a forthcoming work dedicated to the vibrational properties of carbonated apatite.

REFERENCES CITED

Albee, F.H. (1920) Studies in bone growth – triple calcium phosphate as stimulus to osteogenesis. Ann. Surg., 71, 32-39.

Antonakos, A., Liarokapis, E., and Leventouri, T. (2007) Micro-Raman and FTIR studies of synthetic and natural apatites. Biomaterials, 28, 3043-3054.

Astala, R., and Stott, M.J. (2005) First principles investigation of mineral component of bone: CO3 substitutions in hydroxyapatite. Chemistry of Materials, 17(16), 4125-4133.

Becke, A.D. (1993) A New Mixing of Hartree-Fock and Local Density-Functional Theories. Journal of Chemical Physics, 98(2), 1372-1377.

Catti, M., Pavese, A., Dovesi, R., and Saunders, V.R. (1993) Static lattice and electron properties of MgCO3 (Magnesite) calculated by ab-initio periodic Hartree-Fock methods. Physical Review B, 47, 9189-9198.

Corà, F., Alfredsson, M., Mallia, G., Middlemiss, D.S., Mackrodt, W.C., Dovesi, R., and Orlando, R. (2004) The performance of hybrid density functionals in solid state chemistry. In N.M.J.E. Kaltsoyannis, Ed. Principles and Applications of Density in Inorganic Chemistry Ii, 113, p. 171-232.

Corno, M., Busco, C., Civalleri, B., and Ugliengo, P. (2006) Periodic ab initio study of structural and vibrational features of hexagonal hydroxyapatite Ca10(PO4)6(OH)2. Physical Chemistry Chemical Physics, 8, 2464-2472.

Dovesi, R., Roetti, C., Freyria Fava, C., Prencipe, M., and Saunders, V.R. (1991) On the elastic properties of lithium, sodium an potassium oxide. An ab initio study. Chemical Physics, 156, 11-19.

Dovesi, R., Saunders, V.R., Roetti, C., Orlando, R., Zicovich-Wilson, C.M., Pascale, F., Civalleri, B., Doll, K., Harrison, N.M., Bush, I.J., D'Arco, P., and Llunell, M. (2009) CRYSTAL09 User's Manual. University of Torino, Torino.

Elliott, J.C. (1998) Recent studies of apatites and other calcium orthophosphates. In E. Brès, and P. Hardouin, Eds. Les matériaux en phosphate de calcium. Aspects fondamentaux, p. 25-66. Sauramps Medical, Montpellier.

Fleet, M.E. (2009) Infrared spectra of carbonate apatites: n2-Region bands. Biomaterials, 30, 1473-1481.

Fleet, M.E., and Liu, X. (2007) Coupled substitution of type A and B carbonate in sodium-bearing apatite. Biomaterials, 28(6), 916-926.

Fleet, M.E., and Liu, X.Y. (2003) Carbonate apatite type A synthesized at high pressure: new space group (P(3)over-bar) and orientation of channel carbonate ion. Journal of Solid State Chemistry, 174(2), 412-417.

-. (2004) Location of type B carbonate ion in type A-B carbonate apatite synthesized at high pressure. Journal of Solid State Chemistry, 177(9), 3174-3182.

Fleet, M.E., Liu, X.Y., and Liu, X. (2011) Orientation of channel carbonate ions in apatite: Effect of pressure and composition. American Mineralogist, 96(7), 1148-1157.

Habas, M.P., Dovesi, R., and Lichanot, A. (1998) The B1 reversible arrow B2 phase transition in alkaline-earth oxides: a comparison of ab initio Hartree-Fock and density functional calculations. Journal of Physics: Condensed Matter, 10(31), 6897-6909.

Hay, P.J., and Wadt, W.R. (1985) Ab Initio effective core potentials for molecular calculations. Potentials for main group elements Na to Bi. Journal of Chemical Physics, 82, 284-298.

Hughes, J.M., Cameron, M., and Crowley, K.D. (1989) Structural variations in natural F, OH and Cl apatites. American Mineralogist, 74, 870-876.

Hughes, J.M., and Rakovan, J. (2002) The crystal structure of apatite, $Ca_5(PO_4)_3(F,OH,Cl)$. In M.J. Kohn, J. Rakovan, and J.M. Hughes, Eds. Phosphates, 48, p. 1–12. Mineralogical Society of America, Washington, D.C.

Lee, C.T., Yang, W.T., and Parr, R.G. (1988) Development of the Colle-Salvetti Correlation-Energy Formula into a Functional of the Electron-Density. Physical Review B, 37(2), 785-789.

Maslen, E.N., Streltsov, V.A., and Streltsova, N.R. (1993) X-Ray Study of the Electron-Density in Calcite, $CaCO_3$. Acta Crystallographica Section B-Structural Science, 49, 636-641.

Monkhorst, H.J., and Pack, J.D. (1976) Special points for Brillouin-zone integrations. Physical Review B, 8, 5188-5192.

Pascale, F., Zicovich-Wilson, C.M., Gejo, F.L., Civalleri, B., Orlando, R., and Dovesi, R. (2004) The calculation of the vibrational frequencies of crystalline compounds and its implementation in the CRYSTAL code. Journal of Computational Chemistry, 25(6), 888-897.

Peeters, A., DeMaeyer, E.A.P., VanAlsenoy, C., and Verbeeck, R.M.H. (1997) Solids modeled by ab initio crystal-field methods .12. Structure, orientation, and position of A-type carbonate in a hydroxyapatite lattice. Journal of Physical Chemistry B, 101(20), 3995-3998.

Peroos, S., Du, Z., and de Leeuw, N.H. (2006) A computer modelling study of the uptake, structure and distribution of carbonate defects in hydroxy-apatite. Biomaterials, 27, 2150-2161.

Prencipe, M., Pascale, F., Zicovich-Wilson, C.M., Saunders, V.R., Orlando, R., and Dovesi, R. (2004) The vibrational spectrum of calcite (CaCO3): an ab initio quantum-mechanical calculation. Physics and Chemistry of Minerals, 31(8), 559-564.

Rabone, J.A.L., and de Leeuw, N.H. (2005) Interatomic Potential Models for Natural Apatite Crystals: Incorporating Strontium and the Lanthanides. Journal of Computational Chemistry, 27, 253–266.

-. (2007) Potential routes to carbon inclusion in apatite materials: a DFT study. Physics and Chemistry of Minerals, 34, 495-506.

Saenger, A.T., and Kuhs, W.F. (1992) Structural disorder in hydroxyapatite. Zeitschrift Fur Kristallographie, 199, 123-148.

Stott, M.J., and Yin, X. (2003) α- and *β*-tricalcium phosphate: A density functional study. Physical Review B, 68(202505), 1-8.

Sturgeon, J.L., and Brown, P.W. (2009) Effects of carbonate on hydroxyapatite formed from $CaHPO_4$ and $Ca_4(PO_4)_2O$. Journal of Materials Science-Materials in Medicine, 20, 1787-1794.

Suda, H., Yashima, M., Kakihana, M., and Yoshimura, M. (1995) Monoclinic <--> Hexagonal Phase Transition in Hydroxyapatite Studied by X-ray Powder Diffraction and Differential Scanning Calorimeter Techniques. Journal of Physical Chemistry, 99(17), 6752-6754.

Suetsugu, Y., Shimoya, I., and Tanaka, J. (1998) Configuration of Carbonate Ions in Apatite Structure Determined by Polarized Infrared Spectroscopy. Journal of the American Ceramic Society, 81, 746-748.

Tosoni, S., Pascale, F., Ugliengo, P., Orlando, R., Saunders, V.R., and Dovesi, R. (2005) Quantum mechanical calculation of the OH vibrational frequency in crystalline solids. Molecular Physics, 103(18), 2549-2558.

Ugliengo, P., Viterbo, D., and Chiari, G. (1993) MOLDRAW: molecular graphic on a personal computer. Zeitschrift Fur Kristallographie, 207, 9-23.

Valenzano, L., Torres, F.J., Klaus, D., Pascale, F., Zicovich-Wilson, C.M., and Dovesi, R. (2006) Ab initio study of the vibrational spectrum and related properties of crystalline compounds; the case of CaCO3 calcite. Zeitschrift Fur Physikalische Chemie-International Journal of Research in Physical Chemistry & Chemical Physics, 220(7), 893-912.

Zahn, D., and Hochrein, O. (2008) On the composition and atomic arrangement of calcium-deficient hydroxyapatite: An ab-initio analysis. Journal of Solid State Chemistry, 181, 1712-1716.

- This page was left blank -

CHAPTER 8 – The vibrational features of hydroxylapatite and type A carbonated apatite: a first principle contribution.[7]

Abstract

In this work, the vibrational spectra of hexagonal hydroxylapatite OHAp (space group $P6_3$) and type A carbonated apatite [$Ca_{10}(PO_4)_6(CO_3)$, space group P1] have been calculated with an *ab initio* approach by density function method using the hybrid B3LYP functional and an all-electron polarized double-zeta quality Gaussian-type basis set using CRYSTAL09 computer program. The effect on the vibrational properties due to improving the Ca pseudopotential, usually adopted in previous studies on hydroxylapatite, towards the present all-electron basis set has also been briefly addressed. The anharmonic correction for hydroxyl groups in OHAp has also been considered. The results of the modeling are in good agreement with the available FTIR and Raman data present in literature and can be useful to experimental researchers to assign unequivocally the bands in infrared and Raman spectra to specific fundamental vibrational modes.

8.1 Introduction

Apatite minerals are an important group of minerals not only because they are commonly found in almost all type of rocks, but also because carbonate hydroxylapatite COHAp is the main component of the mineral phase of mammalian bones (Dorozhkin, 2009; Dorozhkin, 2010). The two natural polymorphs of hydroxylapatite are monoclinic [$P2_1/b$] and hexagonal [$P6_3/m$] and can be found mainly in minerals and bone tissues, respectively. At standard temperature and pressure, the monoclinic cell is more stable than the hexagonal one; the phase transition between the two polymorphs (order/disorder) takes place at 200°C. Nevertheless, the hexagonal OHAp allows extensive atomic substitution and non-stoichiometry in Ca, P and channel anion positions to entropically stabilize its structure (Suda et al., 1995). For example, anions such as fluoride, chloride and carbonate can easily enter in the *c*-axis channel, leading to fluoro-, chloro- and carbonate apatites, both as end-members and in mutual solid solutions (Elliott, 1998; Hughes and Rakovan, 2002).

[7] This chapter consists of a paper by Gianfranco Ulian, Giovanni Valdrè, Marta Corno and Piero Ugliengo, "The vibrational features of hydroxylapatite and type A carbonated apatite: a first principle contribution.", published in *American Mineralogist*, 98, 752-759.

The carbonate ion substitution in hydroxylapatite has been extensively studied, because the CO_3^{2-} ion is commonly present in natural bone tissues in substantial amount (about 4-6 wt. %). As a consequence, the inclusion of carbonate ion in apatite-based biomaterial could increase the biocompatibility of implanted prosthetic.

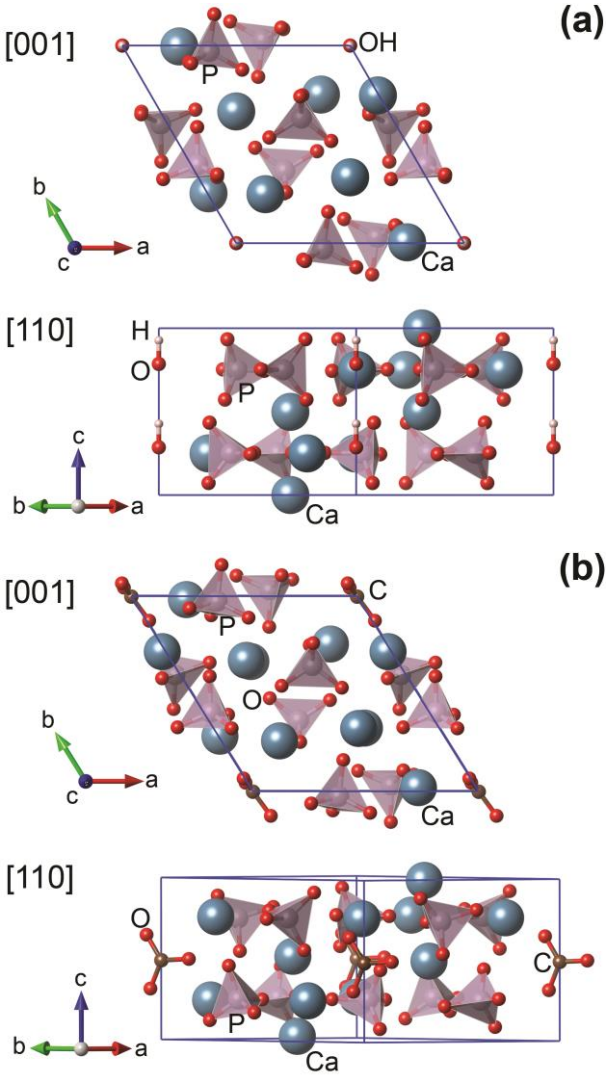

Figure 8.1. Optimized hydroxyl- (**a**) and carbonated apatite (**b**) crystallographic cell obtained from ab initio simulation (Ulian et al. 2013), viewed along different directions.

Carbonate ion can substitute for both OH in the *c*-axis channel of apatite (type A) and the phosphate group (type B), as already described by many authors (Astala and Stott, 2005; Fleet and Liu, 2007; Fleet and Liu, 2008; Fleet and Liu, 2003; Fleet and Liu, 2004; Fleet et al., 2004; Fleet et al., 2011; Kovaleva et al., 2009; Sturgeon and Brown, 2009). In a very recent paper, (Ulian and Valdrè, 2012) modelled the structures of both OHAp and type A carbonated apatite (CAp) by periodic *ab initio* simulation with DFT/B3LYP hybrid functional and with an all electron Gaussian basis set for all the atoms in the unit-cell. Figs. 8.1a and 8.1b report the optimized crystallographic cells of OHAp and CAp, respectively. They found that the carbonate ion is preferably oriented in the Ca^{2+} channel in a "closed" configuration (type A1 CAp), with a bisector of the CO_3^{2-} triangle perpendicular to the *c*-axis. This result was in agreement with both single crystal X-Ray Diffraction (XRD) data (Fleet and Liu, 2003; Fleet et al., 2011) and previous theoretical results (Peroos et al., 2006). However, the simulation with DFT/B3LYP hybrid functional with an all electron gaussian basis set for all the atoms in the unit cells of OHAp and CAp provided the closest structures to the experimental derived ones.

Alongside single-crystal XRD, two of the most employed tools to experimentally investigate the internal structure of a solid phase are Fourier-Transformed InfraRed (FTIR) and Raman spectroscopy. These techniques resolve specific vibrational mode of the different molecular groups in the sample and they have been extensively used for the characterization of both OHAp (Bertinetti et al., 2007;

Cuscó et al., 1998; Miller et al., 2001; Tsuda and Arends, 1994) and carbonated hydroxylapatite (CO-HAp) (Fleet, 2009; Fleet and Liu, 2008; Fleet and Liu, 2003; Fleet and Liu, 2004; Fleet et al., 2004; Petra et al., 2005; Suetsugu et al., 1998). From the position of the IR/Raman signals it is possible to obtain information on the chemical environment of each molecular group in the mineral. The most important IR vibrational mode in carbonated apatite is the CO_3^{2-} out-of-plane bending (labelled as ν_2). This vibrational mode falls at slightly different wavenumbers depending on the site (A or B) occupied by the carbonate ion in the apatite cell. From the relative intensities of the $\nu_2(CO_3)$ peaks it is possible to evaluate the relative amount of A and B sites in the sample (Fleet, 2009; Kolmas et al., 2011; Petra et al., 2005).

However, the interpretation of experimental vibrational spectra of both natural and synthetic samples can be complicated by several factors, for instance: (1) the presence of impurities from preliminary treatments and the synthesis process of the sample; (2) the nature and the morphology of the samples (powders or single crystals); (3) the presence of overtones and/or combination peaks, and (4) band broadening and overlap of signals.

One of the most reliable solution to overcome the problems cited above is the quantum mechanical simulation of the vibrational spectrum of the sample of interest. This approach was effectively adopted by many researchers in their theoretical investigations of the vibrational properties of hydroxylapatite, α-quartz, brucite, magnesite, calcite and dolomite (Corno et al., 2006; Pascale et al., 2004; Prencipe et al., 2004; Ugliengo et al., 2004; Valenzano et al., 2007; Valenzano et al., 2006). Furthermore, the comparison between the computed vibrational spectra with the experimental ones is another way to validate the chosen modelling method, other than to compare the modelled structures with those obtained by XRD.

The aim of the present work is to provide the simulated vibrational spectra of both OHAp and type A1 CAp, using the optimized geometries previously evaluated with DFT/B3LYP level of theory and a complete basis set for each atom in the structures (Ulian et al., 2012). The results from this kind of calculation can be used to unequivocally assign each signal to specific normal modes and can help the experimental researchers in identifying which bands in their spectra correspond to fundamental vibrational transitions.

8.2 Computational Details

All calculations have been performed on a Debian (Linux) Cluster with the *ab initio* CRYSTAL09 code (Dovesi et al., 2009), which implements the Hartree–Fock and Kohn–Sham self consistent field

method for the study of periodic systems. The graphical drawings have been carried out with the molecular graphics program VESTA (Momma and Izumi, 2008). The analysis of the vibrational modes were made with MOLDRAW (Ugliengo, 2009).

Basis set

Multielectron wave functions are described by linear combination of crystalline orbitals (CO), expanded in terms of Gaussian-type basis sets. For all the calculations, calcium has been described with a 86-511G(2d), used by other authors for calcite (Valenzano et al., 2006), with outer shell exponents α_{sp} = 0.453 bohr^{-2}, α_{d1} = 3.1910 and 0.8683 bohr^{-2} and α_{d2} = 0.2891 bohr^{-2}. The phosphorus atom is described by the basis 85-21G(d), α_{sp} = 0.48105 and 0.135 bohr^{-2} and α_{d} = 0.74583 bohr^{-2}, respectively. Oxygen and hydrogen are both represented by a 6-31G* basis set with the outer shell exponents α_{sp} = 0.2742 bohr^{-2} and α_{d} = 0.538 bohr^{-2}; and α_{sp} = 0.1613 and α_{p} = 1.1 bohr^{-2}, respectively. Finally, the carbon atom is described by a 6-21G* basis set with α_{sp} = 0.26 bohr^{-2} and α_{d} = 0.8 bohr^{-2}.

Hamiltonian and computational parameters

The Becke three-parameter (B3LYP) hybrid exchange functional (Becke, 1993) in combination with the gradient-corrected correlation functional of Lee, Yang, and Parr (Lee et al., 1988) has been adopted for all calculations. This functional has been already used for alkali oxides, α-quartz, calcite and hydroxylapatite (Dovesi et al., 1991; Pascale et al., 2004; Prencipe et al., 2004). The presence of some fraction of exact exchange increases the electronic localisation, which in turn increases the ionic nature of the materials, causing a systematic decrease of the lattice parameters and an increase of the elastic constants and bulk moduli. The exchange–correlation contribution is performed over a grid of points and is the result of a numerical integration of the electron density and its gradient. The adopted pruned grid is given by 75 points and 974 angular points, subdivided into 5 sub-intervals of 86, 194, 350, 974 and 350 points and obtained from the Gauss–Legendre quadrature and Lebedev schemes (Prencipe et al., 2004). This is a good compromise between accuracy and cost of calculation for geometry optimization and vibrational frequencies. The values of the tolerances that control the Coulomb and exchange series are the default provided by CRYSTAL09 (*ITOL1* to *ITOL4* = 6) (Dovesi et al., 2009), but we increased the pseudo-overlap parameter (*ITOL5*) from 12 to 14. The Hamiltonian matrix has been diagonalized (Monkhorst and Pack, 1976) using a shrinking factor of *IS* = 4 (Dovesi et al., 2009), that leads to 12 and 36 reciprocal lattice points (k-points) for OHAp and CAp, respectively.

Geometry

The cell parameters and fractional coordinates were optimized by the analytical gradient method in a recent work, adopting the same computational condition explained above (Ulian and Valdrè, 2012). Here we report a summary of the results in Table 8.1 for hydroxylapatite and type A1 carbonated apatite (CAp). For complete details, we suggest the reader to refer to the above referenced paper.

Table 8.1. B3LYP lattice parameters and mean geometric characteristics of initial models

	OHAp*	**CAp***
Symmetry	$P6_3$	P1
a (Å)	9.433	9.582
b (Å)	9.433	9.764
c (Å)	6.896	6.877
α (°)	90.0	89.3
β (°)	90.0	89.8
γ (°)	120.0	121.9
V_{cc} (Å^3)	532	546
Mean bond length (Å)		
P – O	1.55	1.54
O – H	0.97	-
C – O	-	1.29
Ca --- O (*c*-channel)	2.37	2.36
Mean bond angle (°)		
O – P – O	109.4	110.1
O – C – O	-	120.0

Notes: V_{cc} is the volume of the crystallographic cell. O (*c*-channel) refers to an oxygen atom of hydroxyl group and in OHAp cell or carbonate ion in type A1 CAp structure.
* (Ulian and Valdrè, 2012)

Vibrational features

In periodic systems and within the harmonic approximation, the phonon frequencies at Γ point are evaluated diagonalising the central zone (k = 0) mass-weighted Hessian matrix:

$$W_{ij}(k=0) = \sum_G \frac{H_{ij}^{0G}}{\sqrt{M_i M_j}}$$

H_{ij}^{0G} is the second derivative of the electronic and nuclear repulsion energy E evaluated at equilibrium **u=0** with respect to the displacement of atom A in cell 0 ($u_i = x_i - x_i^*$) and displacement of atom B in cell G ($u_j = x_j - x_j^*$) from their equilibrium position x_i^*, x_j^*:

$$\sum_G H_{ij}^{0G} = \sum_G \left[\frac{\partial^2 E}{\partial u_i^0 \partial u_j^G} \right]_0$$
$$i = 1,...,3N; \quad j = 1,...,3N$$

In CRYSTAL, the calculation of the Hessian at equilibrium is made by the analytical evaluation of the energy first derivatives, Φ_j of E with respect to the atomic displacements:

$$\Phi_j = \sum_G v_j^G = \sum_G \frac{\partial E}{\partial u_j^G} \quad j = 1,...,3N$$

while second derivatives at **u = 0** (where all first derivatives are zero) are calculated numerically using a "two-point" formula:

$$\left[\frac{\partial \Phi_j}{\partial u_i^0}\right]_0 \approx \frac{\Phi_j\left(0,...,u_i^0,...,0\right) - \Phi_j\left(0,...,u_i^0,...,0\right)}{u_i^0}$$

$$i = 1,...,3N; \quad j = 1,...,3N$$

More details on the vibrational calculation made by CRYSTAL can be found in literature (Pascale et al., 2004; Tosoni et al., 2005). The Hessian matrix eigenvalues provide the normal harmonic frequencies ω_h and it is obtained with 3N+1 SCF and gradient calculation. This method can be quite demanding for large unit cells, but point symmetry facilitates a remarkable time saving, because only the lines of the Hessian matrix referring to irreducible atoms need to be generated.

In addition, an anharmonic correction has been applied to the OH stretching mode in the OHAp cell. This three-step procedure is based on: (i) decoupling of the distance O–H, which is treated as a pure normal coordinate; (ii) calculation of the total energy of the system for a set of OH values around equilibrium (0.2/+0.3Å), followed by an interpolation by means of a sixth-order polynomial fit, and (iii) solution of the one-dimensional nuclear Schrödinger equation to obtain the three lowest eigenvalues, E_0, E_1 and E_2, from which one can calculate the fundamental frequency $\omega_{01} = E_1 - E_0$, the first overtone $\omega_{02} = E_2 - E_0$ and the anharmonicity constant of the OH mode, $\omega_e\chi_e = (2\,\omega_{01} - \omega_{02})/2$. This algorithm was proposed by Lindberg (Lindberg, 1988) and already adopted by other authors (Pascale et al., 2004; Ugliengo et al., 2004; Ulian and Valdrè, 2012).

8.3 Results and Discussions

Both hydroxyl- and carbonated apatite cells have 44 atoms and 44 x 3 = 132 associated degrees of freedom, of which 129 have vibrational character. The analysis of the vibrational modes has been conducted with the aid of (i) the visualization software MOLDRAW and (ii) the potential energy distribution (PED) computed by CRYSTAL09. These methodologies provide data that are particular useful to individuate different IR regions in the spectra, in particular for the phosphate ion vibrational bands.

Hydroxylapatite

Corno and co-workers (Corno et al., 2006) made a complete analysis of the vibrational modes for their OHAp model simulated with an all electron basis set except for the pseudopotential on the calcium atoms. In our simulations we followed their approach, but we used a complete all electron basis set for all the atoms of the OHAp cell. We compared our results with the experimental IR and Raman spectra present in literature.

In the OHAp structure the $P6_3$ symmetry subdivides the 132 vibrational modes in the different following irreducible representations:

$$\Gamma_{total} = 22A + 22B + 22E_1 + 22E_2$$

66 of these modes are active in the IR ($22A + 22E_1$) and 110 are active in Raman ($22A + 22E_1 + 22E_2$). The 22 B-symmetry modes are silent in both IR and Raman. The first A and E1 modes are associated with 3 acoustic (translation) modes and were not considered.

In Figure 8.2 we report the simulated infra-red vibrational spectrum of hydroxylapatite from 0 to 1300 cm^{-1}.

The lowest energy signals (100-400 cm^{-1}) are phonon modes, related to vibrations of the crystal lattice. The range from 500 to 1200 cm^{-1} in the spectra was mainly given by PO_4^{3-} ions bands. As already discussed by (Corno et al., 2006; Cuscó et al., 1998; Rehman and Bonfield, 1997; Tsuda and Arends, 1994), the free phosphate tetrahedron in aqueous solution gives four vibrational modes (irreducible representations A_1+E+2F): (i) the symmetric P-O stretching (ν_1, A_1) at 938 cm^{-1}; (ii) the symmetric OPO bending (ν_2, E) at 420 cm^{-1}, which are IR inactive; (iii) the asymmetric P-O stretching (ν_3, F) at 1017 cm^{-1} and (iv) the asymmetric OPO bending (ν_4, F) at 567 cm^{-1}.

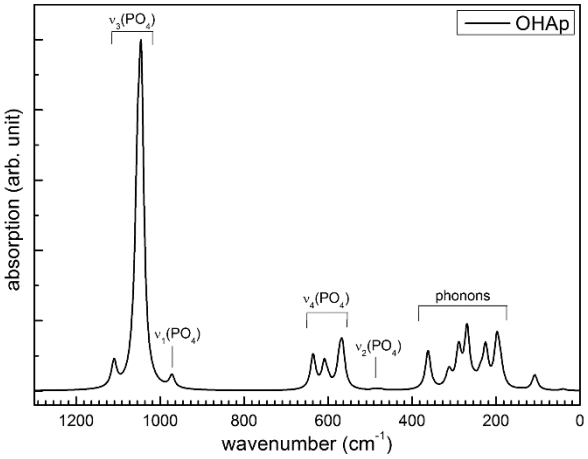

Figure 8.2. OHAp IR vibrational spectra, where the asymmetric (ν_3) and symmetric (ν_1) stretching and the asymmetric (ν_4) and symmetric (ν_2) bending modes of phosphate group are marked. The O-H stretching is not showed for the sake of clearness.

In molecular crystals, such as hydroxylapatite, the crystalline field induces distortions in the perfect phosphate tetrahedron. In particular, within the OHAp structure the PO_4^{3-} symmetry is reduced from T to C_6 point group. These effects activate the A_1 and E modes in the IR range and hence the PO_4^{3-} spectrum presents more than four bands originated from the doubly degenerate ν_2 and triply degenerate ν_4 and ν_3 modes. From the tables of symmetry correlation for the $P6_3$ space group, the predicted number of IR active bands is six for ν_3 and ν_4 modes, four for ν_2 and two for ν_1 modes. For the Raman spectrum, there are nine active bands for ν_3 and ν_4 modes, six for ν_2 and three for ν_1 modes. In the OHAp crystal the phosphate ion bands are blue shifted due to the interactions between the PO_4^{3-} distorted tetrahedron and the crystalline framework.

In Table 8.2, we reported our vibrational analysis (B-symmetry modes were not considered) together with other theoretical figures obtained from a previous simulation with pseudopotentials on calcium atoms (Corno et al., 2006) and from FTIR and Raman spectroscopy (Rehman and Bonfield, 1997; Tsuda and Arends, 1994). In the following we discuss in details each vibrational region of the simulated OHAp spectrum in comparison with the theoretical and experimental results.

Table 8.2. Harmonic frequencies for the B3LYP-simulated OHAp bulk structure.

			Calculated			Experimental		
Mode	**Symmetry**	**Active**	**B3LYP***	**Ampl. (IR)***	**B3LYP§**	**IR◊**	**Raman‡**	**Δν**
ν_2 (PO4)	A	IR, R	459	0.2	506		432	+27
	A	IR, R	489	40.4	527		454	+35
	E_1	IR, R	437	2.4	476			
	E_1	IR, R	475	34.6	515		432	+43
	E_2	R	440	0	482	462	449	-9
	E_2	R	457	0	515			
ν_4 (PO4)	A	IR, R	566	1095.5	599	566		
	A	IR, R	599	0.1	630	660-520	593	+6
	A	IR, R	621	4.2	656		609	+12
	E_1	IR, R	573	691.2	602			
	E_1	IR, R	600	166.7	632	632		
	E_1	IR, R	609	735.2	639	602		
	E_2	R	566	0	591		581	-15
	E_2	R	588	0	622		609	-21
	E_2	R	633	0	663		617	+16
ν_1 (PO4)	A	IR, R	972	2.62	991		962	+10
	E_1	IR, R	972	360.2	990	962		
	E_2	R	974	0	993		962	+12
ν_3 (PO4)	A	IR, R	1054	4686.4	1088	1190-976	1034	+20
	A	IR, R	1064	136.6	1111		1048	+16
	A	IR, R	1096	1.0	1127		1077	+19
	E_1	IR, R	1045	8207.8	1080		1043	+2
	E_1	IR, R	1068	97.6	1107	1042		
	E_1	IR, R	1110	755.8	1146	1091		
	E_2	R	1041	0	1081		1028	+13
	E_2	R	1077	0	1109		1055	+22
	E_2	R	1081	0	1126		1077	+4
ν $(OH)_{harm}$	A	IR, R	3757	-	3774			
ν $(OH)_{anharm}$	A	IR, R	3598	88.0	3603	3573	3572	+26

Notes: Ampl. (IR) is the calculated infrared transition amplitude. Δν has been evaluated from Raman spectroscopy.
* present work
§ (Corno et al., 2006)
◊ (Rehman and Bonfield, 1997)
‡ (Tsuda and Arends, 1994)

Symmetric OPO bending (ν_2).

Simulations conducted with B3LYP and pseudopotential approximation on Ca^{2+} ions (Corno et al., 2006) showed this mode in a range from 482 to 527 cm^{-1}. In the micro-Raman analysis by Cuscó et al. (1998) on a synthetic OHAp sample the symmetric bending mode spanned from 400 to 490 cm^{-1}

and two well resolved signals were found at 449 and 454 cm^{-1} by Tsuda and Arends (1994) using Raman spectroscopy on OHAp powders. The IR adsorption spectra of synthesized OHAp powder obtained by Zakharov et al. (Zakharov et al., 2004) showed two defined peaks at 462 and 474 cm^{-1}. Our symmetric OPO bending (ν_2) fell in the range 437-489 cm^{-1}, where we computed two silent modes (B symmetry) and six IR/Raman active vibrations, the most intense one being at 489 cm^{-1}.

Asymmetric OPO bending (ν_4).

Miller et al. (Miller et al., 2001) studied the crystallinity of synthetic OHAp by infrared micro-spectroscopy and focused the attention to the $\nu_4(PO_4)$ vibrational transitions, providing a detailed analysis of this spectral region. The authors found three main components at 560, 573 and 600 cm^{-1} and another band at 530-540 cm^{-1}, however assigned to acidic phosphate ions (HPO_4^{2-}) impurities. Cuscó and co-workers (1998) distinguished several bands between 570 and 625 cm^{-1}, while Zakharov et al. (2004) found two peaks at 571 and 601 cm^{-1}. Corno et al. (2006) evaluated the ν_4 signals in the range 591-663 cm^{-1}. We calculated 12 normal modes (three were silent) for the asymmetric OPO bending from 566 to 633 cm^{-1}.

Symmetric P-O stretching (ν_1).

Experimental results reported a single intense peak for the non-degenerate symmetric P-O stretch at 962 cm^{-1} both in IR (Rehman and Bonfield, 1997; Zakharov et al., 2004) and in Raman (Cuscó et al., 1998) spectra. In the B3LYP simulation of Corno and co-workers (2006) four modes have been computed for the ν_1 stretching, in the range between 990-993 cm^{-1}. We obtained the same four modes, but at lower wavenumbers: 971 cm^{-1} (B, silent), 972 cm^{-1} (A, Raman and IR), 972 cm^{-1} (E_1, Raman and IR) and 974 cm^{-1} (E_2, Raman).

Asymmetric P-O stretching (ν_3).

From the micro-Raman analysis of Cuscó et al. (1998) this vibrational mode spans over the 1020-1095 cm^{-1} range, while Zakharov and co-workers (Zakharov et al., 2004) distinguished four peaks in the IR spectrum (1087, ~1072, 1046, ~1032 cm^{-1}). In our simulation 12 modes were computed for the asymmetric P-O stretching (ν_3) in the spectral region between 1041-1110 cm^{-1}, with three silent modes. The same modes were previously obtained by Corno and co-workers (2006), but their ν_3 bands spanned the 1080-1146 cm^{-1} range.

Vibrations of OH groups.

We observed an IR/Raman band at 636 cm^{-1} (E_1 symmetry) and the Raman signal at 724 cm^{-1} (E_2 symmetry), assigned to OH librations. This mode has been also observed in OHAp IR spectrum at 630 cm^{-1} by Zakharov et al. (2004), but the similarities with experimental results are probably due to

some error cancellation (see below). The hydroxyl asymmetric stretching was measured in both IR and Raman spectroscopies around 3575 cm^{-1} (Cuscó et al., 1998; Rehman and Bonfield, 1997; Tsuda and Arends, 1994; Zakharov et al., 2004). In the simulation of Corno and co-workers (2006), this mode was at 3774 cm^{-1}, while with our method it is at 3757 cm^{-1}. When anharmonicity was taken into account (see the Computational Methods section), the mode shifted to lower wavenumbers, at 3603 cm^{-1} in the work of Corno et al. (2006) and at 3598 cm^{-1} in the present work. The OH^- symmetric stretching is a silent mode (B-symmetry). Other modes, such as the OH libration previously cited, are affected by anharmonicity but, unfortunately, the CRYSTAL code allows to apply the correction only to stretching ones. For this reason, it is difficult to establish a direct comparison between the calculated (with harmonic approximation) and the experimental OH modes.

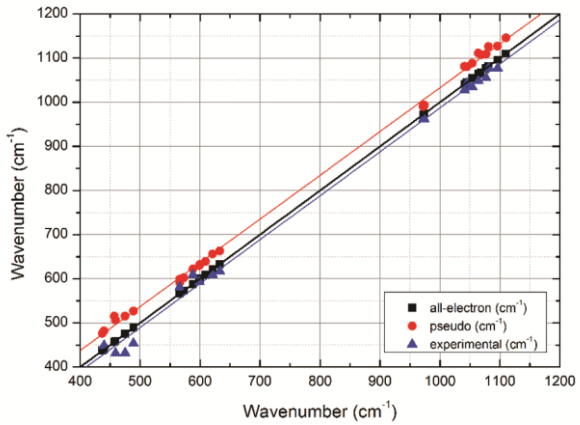

Figure 8.3. Correlation between experimental and computed vibrational frequencies using Ca-pseudopotential and all electron basis sets.

On the other hand, our simulation refers to a pure OHAp and obviously bands relative to impurities such as for example HPO_4^{2-}, that may be present in experimental samples, are absent.

The comparison between our vibrational frequencies and those relative to the modelling of Corno and co-workers (2006) showed that the pseudopotential approximation on Ca^{2+} ions over-estimates the experimental frequencies, with errors in a range of 30-80 cm^{-1}. By using an all electron basis set we observed a systematic deviation between the data (Figure 8.3), typical of the use of different basis set. This effect reduced the theoretical/experimental deviation to 15-35 cm^{-1}, obtaining a better agreement with the FTIR and Raman data of (Cuscó et al., 1998; Miller et al., 2001; Rehman and Bonfield, 1997; Tsuda and Arends, 1994; Zakharov et al., 2004).

Type A1 carbonated apatite

Because the optimized CAp cell does not have internal symmetry (space group *P1*), the 132 degrees of freedom are assignable only to the A (total-symmetric) irreducible representation:

$$\Gamma_{total} = 132A$$

This means that all the phosphate and lattice B- and E_2-symmetry modes observed for hydroxylapatite are now IR active. E_1 and E_2 modes gave doublets because they lost their degeneracy. These

reasons explain the more complexity of the type A1 CAp spectrum presented in Figure 8.4, when compared to the OHAp one.

We reported in Table 8.3 the results obtained from our simulated IR analysis alongside the experimental ones. As many calculations in the past were adopting a pseudopotential on the Ca ions (Corno et al., 2006) we compare them with the present all-electron results for the Cap A1 model.

The phosphate signals are almost unaffected by the different basis set, with shifts in the order of magnitude of experimental error. The differences arise on the carbonate ion normal modes because of its interaction with calcium ions.

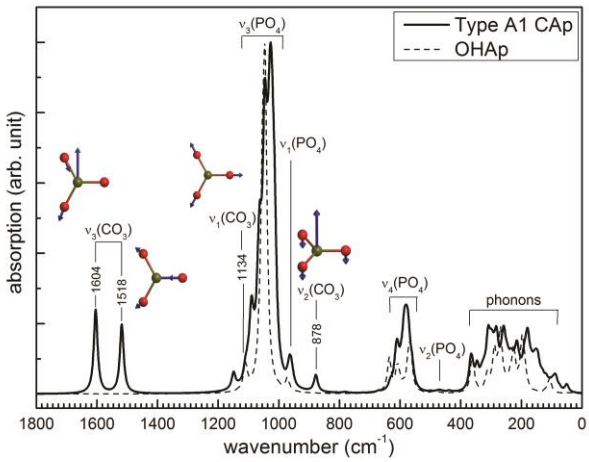

Figure 8.4. Simulated type A1 CAp IR vibrational spectra. Asymmetric (ν_3) and symmetric (ν_1) stretching and the out of plane (ν_2) bending modes of carbonate ion are marked. The OHAp spectrum (dashed line) is also reported to ease the comparison between the two structures.

In the following, the vibrational analysis of the type A1 CAp structure is focused on the all-electron basis set results and divided in two subsections: in the first one we discussed mainly the phosphate ions modes; in the second one on the carbonate ion signals.

Table 8.3. Harmonic frequencies for the B3LYP-simulated CAp bulk structure.

	B3LYP*		FTIR (experimental)			$\Delta\nu_{(CAp-FTIR)}$		
Mode	**OHAp**	**CAp**	**(a)**	**(b)**	**(c)**	**(a)**	**(b)**	**(c)**
ν_2 (PO_4)	475	471	469	470	-	+2	+1	-
ν_4 (PO_4)	566	562	-	564	566	-	-2	-4
	588	586	-	575	580	-	+11	+6
	609	610	603	604	604	+7	+6	+6
ν_1 (PO_4)	972	961	961	961	960	0	0	+1
ν_3 (PO_4)	1045	1047	1041	1044	1033	+6	+3	+14
	1054	1064	-	1064	-	-	0	-
	1110	1110	-	1110	1090	-	0	+20
ν_{4a} (CO_3)	-	670	-	670	-	-	0	-
ν_{4b} (CO_3)	-	781	-	750	-	-	+31	-
ν_2 (CO_3)	-	878	873	878	879	+5	0	-1
ν_1 (CO_3)	-	1134	-	-	-	-	-	-
ν_{3a} (CO_3)	-	1518	1470	1461	1458	+48	+57	+60
ν_{3b} (CO_3)	-	1604	1650	-	1538	-46	-	+66

Notes: All the frequencies are in wavenumbers (cm^{-1}). The results of the present work (*) are reported alongside the FTIR analysis of (a) Reman and Bonfield (1997), (b) Petra et al. (2005) and (c) Kolmas et al. (2011), respectively.

Phosphate ions vibrations (1200-500 cm^{-1}).

The symmetric phosphate OPO bending modes ν_2 usually give faint bands in the experimental IR spectra. Petra and co-workers (2005) found one signal at 470 cm^{-1}, while Rehman and Bonfield (1997) distinguished one peak at 469 cm^{-1}. In our simulation we obtained 12 normal modes between 421-498 cm^{-1}, with the most intense peak at 472 cm^{-1}.

According to the work of Kolmas et al. (2011), the asymmetric OPO ν_4 bendings fall in the range 562-630 cm^{-1}, where six bands have been decomposed and assigned in the following way: three are originated from apatite PO_4^{3-} at 562-566, 573-585 and 601-605 cm^{-1}; one was found at 616-623 cm^{-1} and was assigned to a poorly crystalline phosphate ion environment; the peak at 536-550 cm^{-1} was due to HPO_4^{2-} impurities and the signal at 630 cm^{-1} was assigned to an OH libration mode. Petra et al. (2005) individuated two main bands near 604 and 565 cm^{-1} and a shoulder at 575 cm^{-1}, while Costa and co-workers (Costa et al., 2012) distinguished two peaks at 600 and 560 cm^{-1}. In the work of Rehman and Bonfield (1997) a band was found at 603 cm^{-1}.

We computed 18 normal modes for the asymmetric OPO bending in the range 562-633 cm^{-1} with four intense signals at 562, 579, 586 and 610 cm^{-1}. The normal mode at 633 cm^{-1} is the same observed in OHAp (ν_4 + OH libration), but with lower intensity because of the absence of the hydroxyl groups contribution in the CAp model. This effect was observed also by Kolmas et al. (2011), where the area of the peak at 630 cm^{-1} was seen reduced from the OHAp sample to the COHAp one.

The symmetric P-O stretching (ν_1) presented a single peak at 961 cm^{-1} in the FTIR spectra obtained by Rehman and Bonfield (1997) and Petra et al. (2005), while it was at 960 cm^{-1} in the work of Kolmas and co-workers (2011) and Costa et al. (2012). In our simulation we obtained six overlapped modes of weak intensities in the range 956-967 cm^{-1}.

The asymmetric P-O stretching (ν_3) band fell in the 1020-1110 cm^{-1} range in the micro-FTIR analysis of Petra and co-workers (2005), who measured a maximum near 1030 cm^{-1} and strong signals at 1045, 1064 and 1110 cm^{-1}. Two maxima were found at ca. 1033 and 1090 cm^{-1} by Kolmas et al. (2011), while a single intense peak was observed at 1041 cm^{-1} by Rehman and Bonfield (1997) and at 1020 cm^{-1} by Costa et al. (2012). In the spectra presented in this work, we calculated the ν_3 modes in the 1149-1014 cm^{-1} region, where we computed 18 normal modes. The relative intensity of the peaks are very similar to those obtained for the OHAp structure. The strongest signal in the pure hydroxylapatite model (ν_3 at 1045 cm^{-1}, E_1 symmetry) divided in two peaks at 1047 and 1026 cm^{-1} in the type A1 CAp spectrum.

In general, the CO_3^{2-}/2OH^- substitution did not shifted significantly the phosphate ion vibrational modes (only ~15 cm^{-1}) and, despite the presence of more signals, the overall shape of the spectra is almost unchanged.

Carbonate ion vibrations.

The free CO_3^{2-} has four modes: bending in plane (ν_4, *E'* symmetry), bending out-of-plane (ν_2, *A''* symmetry), symmetric stretching (ν_1, *A'*$_1$ symmetry) and asymmetric stretching (ν_3, *E'* symmetry). In the free ion spectra, the only absent signal is the one relative to the symmetric stretching, because this mode does not cause dipole variations.

When the carbonate ion was placed in the apatite lattice, the *E'* modes (ν_3 and ν_4) lost their degeneracy because of the symmetry lowering and gave origin to two doublets.

The characteristic signal that evidences the carbonate ion presence in the apatite cell is the asymmetric C-O stretching (ν_3), whose doublet usually falls between 1400 and 1600 cm^{-1}. Detailed experimental vibrational analysis of the type A1 carbonate ion was provided by Fleet and Liu (2003), who measured the FTIR spectrum of a carbonate-rich carbonated apatite of composition 0.75CAp·0.25OHAp, with negligible amount of type B carbonate ion. The CO_3^{2-} ν_3 mode gave two peaks at 1461 and 1544 cm^{-1}. In the infra-red spectrum of the carbonated hydroxylapatite (COHAp) obtained by Rehman and Bonfield (1997) these signals are at 1470 and 1650 cm^{-1}, while they were found at 1458 and 1538 cm^{-1} in the Mg-COHAp sample of Kolmas and co-workers (2011). In two other experimental studies, a single peak was found at 1430 (Costa et al., 2012) and 1461 cm^{-1} (Petra et al., 2005) for a COHAp coating and for a bone sample treated with acetone to remove the organic phase, respectively. In an earlier theoretical work on static-lattice carbonated apatite (Peeters et al., 1997), the ν_3 mode was found at 1720 and 1332 cm^{-1}. We calculated the asymmetric C-O stretching doublet at 1518 and 1604 cm^{-1}, which is blue shifted by about 55 cm^{-1} if compared to the experimental results. Using pseudo-potential on Ca ions, the ν_3 signals were at 1555 and 1681 cm^{-1}, i.e. the all-electron basis set improved substantially the agreement of this bands with respect to experiment.

The out-of-plane bending mode (ν_2) is commonly used to evaluate the proportion of type A and B carbonate ion amount in the sample, because it falls at slightly different frequencies according to the site occupied by the carbonate (Fleet, 2009). For type A carbonate ion ν_2 has been found at 878 cm^{-1} (Costa et al., 2012; Fleet and Liu, 2003; Fleet et al., 2011; Kolmas et al., 2012; Petra et al., 2005), 873 cm^{-1} (Rehman and Bonfield, 1997) and at 871 cm^{-1} (Kolmas et al., 2011). In the work of Peeters and co-workers (1997) this mode was computed at 880 cm^{-1}, while in our simulated IR spectrum it is at 878 cm^{-1} and at 900 cm^{-1} with all electron and pseudo potential basis sets, respectively, again

showing a slight improvement with respect to experiment when the all-electron basis set is adopted for the Ca ions .

The OCO bending mode (ν_4) was measured at 650 and 750 cm^{-1} by Petra et al. (2005) and was calculated at 541 and 808 cm^{-1} by Peeters and co-workers (1997). We obtained two very weak peaks at 670 and 781 cm^{-1} with all electron basis set, while they were at 694 and 827 cm^{-1} with the pseudopotential on Ca ions, showing a better agreement to experiment when adopting the all-electron basis set for Ca ions .

In addition, we observed a weak signal related to the symmetric stretching of the carbonate ion (ν_1) at 1134 cm^{-1} (and 1140 cm^{-1} with pseudopotential on Ca atoms). In high-symmetric structures where the carbonate ion is placed in a similar environment, *i.e.* calcite and aragonite, this vibrational mode is visible only by Raman spectroscopy. Because of the interaction with the apatite lattice, the $\nu_1(CO_3)$ mode was active in IR, although its related signal has very low intensity and it is not clearly visible in Figure 7.4. It appears as a small shoulder on the $\nu_3(PO_4)$ band. The same result was obtained by Peeters and co-workers (Peeters et al., 1997) in their static-lattice model of carbonated apatite, but the symmetric stretching was calculated at 1043 cm^{-1}. We have not found any experimental evidence of this observation, probably because of the weak intensity of the carbonate ion symmetric stretching mode and the overlapping of the peak with the HPO_4^{2-} impurity bands commonly found in both synthetic and natural samples.

Compared to the "free" CO_3^{2-}, the type A1 carbonate ion establishes significant interactions with the surrounding calcium ions of the apatite channel. This is reflected in the amplitude of the IR shifts, especially for the high -frequency modes (ν_3 and ν_1).

Our carbonated apatite model refers to a perfectly periodic type A1 CAp end-member, with a CO_3^{2-} ion content fixed at 5.8 wt.%. It is not possible to make a direct peak-to-peak comparison between simulated and experimental spectra because the experimentally analyzed carbonated apatite samples may vary in composition because obtained from different sources, synthesis processes, type of minerals and also bone tissues. In the experimentally analyzed samples the carbonate ion amount may range between 1-12 wt.%, because of the possible simultaneous presence of type A and type B carbonate ions in the apatite cell. Usually there are hydroxyl groups, the presence of other ionic substitutions, *i.e.* Mg^{2+}/Ca^{2+} and the presence of type B CO_3^{2-} ions. The matrix effects can cause several problems in detecting weak signals, especially in bone samples.

However, the results that we obtained from the simulated IR spectra are in good agreement with the FTIR data reported in literature. Better accordance was found for the phosphate ion normal modes,

with an average difference of 10 cm^{-1}. Considering the carbonate ion, the computed ν_2 mode matches perfectly with experimental results, with deviations in the order of magnitude of the instrumental resolution (ca. 5 cm^{-1}). The most evident discordance was obtained for the carbonate ion asymmetric stretching mode (ν_3): our simulation gave the doublet blue shifted of about 50 cm^{-1} compared to the FTIR results. However, we observed that the separation between the two peaks (86 cm^{-1} in our spectrum) is in good agreement with the ones of Fleet and Liu (2003) and Kolmas et al. (2011), that are 83 and 80 cm^{-1}, respectively. This deviation is imputable to the different composition of the modelled structure (a CAp end-member) and the experimental samples (synthetic and natural).

Type A2 and planar carbonated apatite

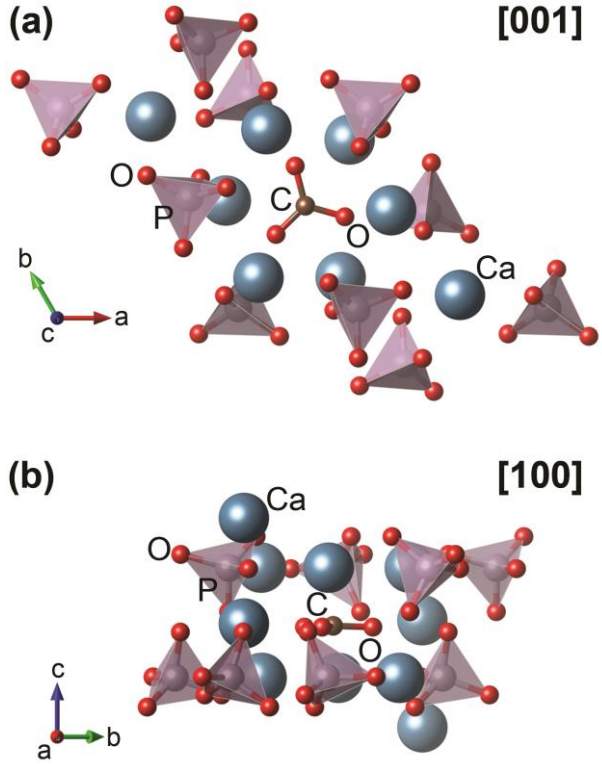

Figure 8.5. Optimized type A carbonated apatite with CO_3^{2-} in planar configuration, viewed from (a) [001] and (b) [100] directions.

We have reported in our previous work that the type A2 configuration, with a bisector of the CO_3^{2-} triangular plane parallel to the *c*-axis, is not energetically favourable and the carbonate ion rotated in the channel to reach the type A1 configuration (Ulian and Valdrè, 2012). For this reason, it was not possible to obtain a vibrational spectra of the type A2 CO_3^{2-} ion in the cell.

On the other hand, it was found that the planar configuration, with the CO_3^{2-} molecular plane perpendicular to the *c*-axis, represents a stationary point on the potential energy surface. This structure was geometrically optimized with the same computational parameters, with and without symmetry (space groups *P3* and *P1*, respectively). The graphical results are reported in Figure 8.5. Despite the geometry results, the electronic energy of the planar configuration was really high if compared to the A1 configuration (+165.78 kJ/mol and +164.78 kJ/mol for the *P3* and *P1* structure, respectively).

Then, to better understand the nature of this stationary point, we also evaluated the vibrational spectra of the planar CAp, with both *P1* and *P3* symmetries, obtaining two imaginary frequencies at -35 cm^{-1} and -59 cm^{-1}, respectively. These results are not surprising for such high-energy structures: the planar configuration is phononically instable at Γ point and then it is a saddle point on the potential

energy surface. The latter statement is justified by the analysis of the modes with imaginary frequency, because they are related to rotations of the plane of the CO_3^{2-} that bring the molecule into the A1 configuration. We excluded calculation artefacts, because of the very good convergence criteria, the high number of *k* sampling points and because the vibrational analysis was performed with and without symmetry constraints.

REFERENCES CITED

Astala, R., and Stott, M.J. (2005) First principles investigation of mineral component of bone: CO3 substitutions in hydroxyapatite. Chemistry of Materials, 17(16), 4125-4133.

Becke, A.D. (1993) Density-Functional Thermochemistry .3. The Role of Exact Exchange. Journal of Chemical Physics, 98(7), 5648-5652.

Bertinetti, L., Tampieri, A., Landi, E., Ducati, C., Midgley, P.A., Coluccia, S., and Martra, G. (2007) Surface structure, hydration, and cationic sites of nanohydroxyapatite: UHR-TEM, IR, and microgravimetric studies. Journal of Physical Chemistry C, 111, 4027-4035.

Corno, M., Busco, C., Civalleri, B., and Ugliengo, P. (2006) Periodic ab initio study of structural and vibrational features of hexagonal hydroxyapatite Ca10(PO4)6(OH)2. Physical Chemistry Chemical Physics, 8, 2464-2472.

Costa, D.O., Allo, B.A., Kalassen, R., Hutter, J.L., Dixon, S.J., and Rizkalla, A.S. (2012) Control of surface topography in biomimetic calcium phosphate coatings. Langmuir, 28, 3871-3880.

Cuscó, R., Guitian, F., de Aza, S., and Artus, L. (1998) Differentiation between hydroxyapatite and beta-tricalcium phosphate by means of mu-raman spectroscopy. Journal of the European Ceramic Society, 18(9), 1301-1305.

Dorozhkin, S.V. (2009) Calcium Orthophosphates in Nature, Biology and Medicine. Materials, 2, 399-398.

-. (2010) Bioceramics of calcium orthophosphates. Biomaterials, 31, 1465-1485.

Dovesi, R., Roetti, C., Freyria Fava, C., Prencipe, M., and Saunders, V.R. (1991) On the elastic properties of lithium, sodium an potassium oxide. An ab initio study. Chemical Physics, 156, 11-19.

Dovesi, R., Saunders, V.R., Roetti, C., Orlando, R., Zicovich-Wilson, C.M., Pascale, F., Civalleri, B., Doll, K., Harrison, N.M., Bush, I.J., D'Arco, P., and Llunell, M. (2009) CRYSTAL09 User's Manual. University of Torino, Torino.

Elliott, J.C. (1998) Recent studies of apatites and other calcium orthophosphates. In E. Brès, and P. Hardouin, Eds. Les matériaux en phosphate de calcium. Aspects fondamentaux, p. 25-66. Sauramps Medical, Montpellier.

Fleet, M.E. (2009) Infrared spectra of carbonate apatites: n2-Region bands. Biomaterials, 30, 1473-1481.

Fleet, M.E., and Liu, X. (2007) Coupled substitution of type A and B carbonate in sodium-bearing apatite. Biomaterials, 28(6), 916-926.

-. (2008) Type A-B carbonate chlorapatite synthesized at high pressure. Journal of Solid State Chemistry, 181(9), 2494-2500.

Fleet, M.E., and Liu, X.Y. (2003) Carbonate apatite type A synthesized at high pressure: new space group (P(3)over-bar) and orientation of channel carbonate ion. Journal of Solid State Chemistry, 174(2), 412-417.

-. (2004) Location of type B carbonate ion in type A-B carbonate apatite synthesized at high pressure. Journal of Solid State Chemistry, 177(9), 3174-3182.

Fleet, M.E., Liu, X.Y., and King, P.L. (2004) Accommodation of the carbonate ion in apatite: An FTIR and X-ray structure study of crystals synthesized at 2-4 GPa. American Mineralogist, 89(10), 1422-1432.

Fleet, M.E., Liu, X.Y., and Liu, X. (2011) Orientation of channel carbonate ions in apatite: Effect of pressure and composition. American Mineralogist, 96(7), 1148-1157.

Hughes, J.M., and Rakovan, J. (2002) The crystal structure of apatite, $Ca_5(PO_4)_3(F,OH,Cl)$. In M.J. Kohn, J. Rakovan, and J.M. Hughes, Eds. Phosphates, 48, p. 1–12. Mineralogical Society of America, Washington, D.C.

Kolmas, J., Jaklewicz, A., Zima, A., Bucko, M., Paszkiewicz, Z., Lis, J., Slosarczyk, A., and Kolodziejski, W. (2011) Incorporation of carbonate and magnesium ions into synthetic hydroxyapatite: The effect on physicochemical properties. Journal of Molecular Structure, 987(1-3), 40-50.

Kolmas, J., Szwaja, M., and Kolodziejski, W. (2012) Solid-state NMR and IR characterization of commercial xenogenic biomaterials used as bone substitutes. Journal of Pharmaceutical and Biomedical Analysis, 61, 136-141.

Kovaleva, E.S., Shabanov, M.P., Putlyaev, V.I., Tretyakov, Y.D., Ivanov, V.K., and Silkin, N.I. (2009) Bioresorbable carbonated hydroxyapatite $Ca_{10-x}Na_x(PO_4)_{6-x}(CO_3)_x(OH)_2$ powders for bioactive materials preparation. Central European Journal of Chemistry, 7(2), 168-174.

Lee, C.T., Yang, W.T., and Parr, R.G. (1988) Development of the Colle-Salvetti Correlation-Energy Formula into a Functional of the Electron-Density. Physical Review B, 37(2), 785-789.

Lindberg, B. (1988) A New Efficient Method for Calculation of Energy Eigenvalues and Eigenstates of the One-Dimensional Schrodinger-Equation. Journal of Chemical Physics, 88(6), 3805-3810.

Miller, L.M., Vairavamurthy, V., Chance, M.R., Mendelsohn, R., Paschalis, E.P., Betts, F., and Boskey, A.L. (2001) In situ analysis of mineral content and crystallinity in bone using infrared micro-spectroscopy of the v(4) PO43- vibration. Biochimica Et Biophysica Acta, General Subjects, 1527(1-2), 11-19.

Momma, K., and Izumi, F. (2008) VESTA: a three-dimensional visualization system for electronic and structural analysis. Journal of Applied Crystallography, 41, 653-658.

Monkhorst, H.J., and Pack, J.D. (1976) Special points for Brillouin-zone integrations. Physical Review B, 8, 5188-5192.

Pascale, F., Zicovich-Wilson, C.M., Gejo, F.L., Civalleri, B., Orlando, R., and Dovesi, R. (2004) The calculation of the vibrational frequencies of crystalline compounds and its implementation in the CRYSTAL code. Journal of Computational Chemistry, 25(6), 888-897.

Peeters, A., DeMaeyer, E.A.P., VanAlsenoy, C., and Verbeeck, R.M.H. (1997) Solids modeled by ab initio crystal-field methods .12. Structure, orientation, and position of A-type carbonate in a hydroxyapatite lattice. Journal of Physical Chemistry B, 101(20), 3995-3998.

Peroos, S., Du, Z., and de Leeuw, N.H. (2006) A computer modelling study of the uptake, structure and distribution of carbonate defects in hydroxy-apatite. Biomaterials, 27, 2150-2161.

Petra, M., Anastassopopulou, J., Theologis, T., and Theophanides, T. (2005) Synchrotron mirco-FT-IR spectroscopic evaluation of normal paediatric human bone. Journal of Molecular Structure, 733, 101-110.

Prencipe, M., Pascale, F., Zicovich-Wilson, C.M., Saunders, V.R., Orlando, R., and Dovesi, R. (2004) The vibrational spectrum of calcite (CaCO3): an ab initio quantum-mechanical calculation. Physics and Chemistry of Minerals, 31(8), 559-564.

Rehman, I., and Bonfield, W. (1997) Characterization of hydroxyapatite and carbonated apatite by photo acoustic FTIR spectroscopy. Journal of Materials Science-Materials in Medicine, 8(1), 1-4.

Sturgeon, J.L., and Brown, P.W. (2009) Effects of carbonate on hydroxyapatite formed from $CaHPO_4$ and $Ca_4(PO_4)_2O$. Journal of Materials Science-Materials in Medicine, 20, 1787-1794.

Suda, H., Yashima, M., Kakihana, M., and Yoshimura, M. (1995) Monoclinic <--> Hexagonal Phase Transition in Hydroxyapatite Studied by X-ray Powder Diffraction and Differential Scanning Calorimeter Techniques. Journal of Physical Chemistry, 99(17), 6752-6754.

Suetsugu, Y., Shimoya, I., and Tanaka, J. (1998) Configuration of Carbonate Ions in Apatite Structure Determined by Polarized Infrared Spectroscopy. Journal of the American Ceramic Society, 81, 746-748.

Tosoni, S., Pascale, F., Ugliengo, P., Orlando, R., Saunders, V.R., and Dovesi, R. (2005) Quantum mechanical calculation of the OH vibrational frequency in crystalline solids. Molecular Physics, 103(18), 2549-2558.

Tsuda, H., and Arends, J. (1994) Orientational micro-Raman spectroscopy on hydroxyapatite single crystals and human enamel crystallites. Journal of Dental Research, 73, 1703-1710.

Ugliengo, P. (2009) MOLDRAW: A molecular graphics program to display and manipulate molecular structures, H1 (32-bit).

Ugliengo, P., Pascale, F., Merawa, M., Labeguerie, P., Tosoni, S., and Dovesi, R. (2004) Infrared spectra of hydrogen-bonded ionic crystals: Ab initio study of Mg(OH)(2) and beta-Be(OH)(2). Journal of Physical Chemistry B, 108(36), 13632-13637.

Ulian, G., and Valdrè, G. (2012) Periodic *ab initio* bulk investigation of hydroxylapatite and type A carbonated apatite American Mineralogist, Submitted.

Valenzano, L., Noel, Y., Orlando, R., Zicovich-Wilson, C.M., Ferrero, M., and Dovesi, R. (2007) Ab initio vibrational spectra and dielectric properties of carbonates: magnesite, calcite and dolomite. Theoretical Chemistry Accounts, 117(5-6), 991-1000.

Valenzano, L., Torres, F.J., Klaus, D., Pascale, F., Zicovich-Wilson, C.M., and Dovesi, R. (2006) Ab initio study of the vibrational spectrum and related properties of crystalline compounds; the case of CaCO3 calcite. Zeitschrift Fur Physikalische Chemie-International Journal of Research in Physical Chemistry & Chemical Physics, 220(7), 893-912.

Zakharov, N.A., Polunina, I.A., Polunin, K.E., Rakitina, N.M., Kochetkova, E.I., Sokolova, N.P., and Kalinnikov, V.T. (2004) Calcium hydroxyapatite for medical applications. Inorganic Materials, 40(6), 641-648.

- This page was left blank -

CHAPTER 9 – *Ab initio* DFT investigation of structural and vibrational properties of type B and mixed A-B carbonated hydroxylapatite.[8]

Abstract

In nature hydroxylapatite [$Ca_{10}(PO_4)_6(OH)_2$] is mostly present with various stoichiometric defects. The most abundant is the carbonate ion that can occupy different crystallographic sites (namely A and B types), however its effects on the apatite structure is still object of debate.

Type A carbonated apatite was quantum mechanically simulated in a previous study, here we extend the simulation to bulk structural and vibrational features of Na-bearing type B and mixed type A-B carbonated hydroxylapatite [$Ca_{10-x}Na_x(PO_4)_{6-x}(CO_3)_{x+y}(OH)_{2(1-y)}$, space group P1]. The simulation has been performed by *ab initio* density functional methods. The geometry of the models (lattice parameters and internal coordinates) have been fully optimized exploring different positions of the sodium ion in the apatite unit-cell. The results, in agreement with XRD data, suggest that in each crystallographic cell in the biological mineral there is at least one calcium ion substitution or vacancy per cell. The carbonate ion presence in the apatite structure is in good agreement with biological/chemical data. Furthermore, there is also a very good agreement with FTIR data reported in literature.

9.1 Introduction

Hydroxylapatite [$Ca_{10}(PO_4)_6(OH)_2$; OHAp] is commonly found in all igneous rocks and in some metamorphic and sedimentary ones and, also as the main component of the inorganic phase of bone, dentin and enamel tissues (Dorozhkin, 2009c). For this reason, apatite minerals draw the attention of many researchers not only in mineralogy, but also in biology, biochemistry and medicine. OHAp is considered a key-biomaterial in cements and prosthetics for tissue repairing/reconstruction (Dorozhkin, 2009a; Dorozhkin, 2009b; Dorozhkin, 2009d).

In their first hierarchal level, biological hard tissues are characterized by the incorporation of minerals (inorganic phase) in a soft organic matrix of structural proteins, such as tropocollagen. The mineral phase is mainly given by hexagonal hydroxylapatite (space group $P6_3/m$), with parameters $a = b$ and

[8] This chapter consists of a paper by Gianfranco Ulian, Giovanni Valdrè, Marta Corno and Piero Ugliengo, "*Ab initio* DFT investigation of structural and vibrational properties of type B and mixed A-B carbonated hydroxylapatite.", in press in *American Mineralogist* (January 2014 issue).

a calcium channel where there are two hydroxyl groups oriented with the same direction along the *c*-axis. This polymorph is thermodynamically unstable if compared to the monoclinic phase (space group $P2_1/b$) typically found in rocks because of the proton order imposed by the same OH alignment in the apatite channel. The disorder/order transition have been evaluated at 200°C (Suda et al., 1995).

The biological hydroxylapatite is not a pure mineral, but presents vacancies and ionic inclusions/substitutions. The main substituting ion is the carbonate ion, with an average content of about 6% in weight. The carbonated hydroxylapatite (COHAp) accommodates the CO_3^{2-} ion either in place of both hydroxyl group in the *c*-axis channel of apatite (type A defect) or the phosphate group (type B) (Astala and Stott, 2005; Fleet, 2009; Fleet and Liu, 2007; Fleet and Liu, 2003; Fleet and Liu, 2004; Sturgeon and Brown, 2009; Suetsugu et al., 1998). The two types of defect usually coexist in a solid solution and the order of occurrence of A and B defects were extensively studied (Kovaleva et al., 2009). In recent years, the interest in those defective structures has increased, because it is known that chemical modification of OHAp, in particular the incorporation of carbonate ions, results in a considerable influence on the mineralization, demineralization and remineralization properties. Other properties, such as surface morphology and electrostatic potential, which influence interactions and adsorption processes at the mineral-organic interface in biological environment, could be affected by atomic substitutions, especially by the carbonate ion. Thus, obtaining accurate knowledge on the carbonate effects on both the apatite crystallographic cell and the surface leads to the possibility to design materials for prosthetic implants with improved biomimetic and biocompatible properties (Gibson and Bonfield, 2002; Lafon et al., 2008; LeGeros, 2002).

Many experimental and theoretical studies were conducted on both type A and type B carbonated defect to better understand the role of the CO_3^{2-} ion on the structural variation and its spatial orientation within the OHAp cell (Astala and Stott, 2005; Engin and Girgin, 2009; Fleet and Liu, 2007; Fleet and Liu, 2008; Fleet and Liu, 2004; Fleet and Liu, 2005; Fleet et al., 2004; Gibson and Bonfield, 2002; Kovaleva et al., 2009; Peeters et al., 1997; Peroos et al., 2006; Rabone and de Leeuw, 2007; Suetsugu et al., 1998). Recently, we successfully investigated, by periodic quantum mechanics (QM) approach based on the hybrid B3LYP functional with an all electron basis set, the structural and vibrational features of type A fully carbonated apatite (CAp) (Ulian et al., 2013a; Ulian et al., 2013b). The results showed that the preferred CO_3^{2-} orientation in the cell is the "closed" configuration (A1), with a bisector of the triangular plane perpendicular to the *c*-axis, in good agreement with experimental data reported in literature (Fleet and Liu, 2003). In type B COHAp, it is known that the carbonate ion occupies one of the tetrahedron sloping faces of the substituted PO_4^{3-}. This substitution requires charge compensation, which can be obtained in several ways, such as the substitution of one

of the calcium ion with a monovalent cation (sodium, potassium) or the inclusion of a small monovalent anion near the CO_3^{2-} (Peeros et al., 2006). The first example of coupled substitution is the most relevant, because Ca^{2+} ions can be easily substituted by both sodium and magnesium by 0.5 – 1.2 % wt. (Dorozhkin, 2009c), as it has been also experimentally observed in sodium-bearing apatites (Fleet and Liu, 2007). However, there is still some degree of disagreement on the effects of the substituent on the crystallographic cell parameters. Furthermore, the effect of the coupled mixed type A-B substitutions in the hexagonal OHAp cell is still unclear.

The aim of the present work is to complete the characterization of defective OHAp, considering type B and mixed type A-B defects. First we provide a detailed quantum mechanical (QM) analysis on the structural features of type B COHAp, adopting the same level of theory (B3LYP with all electron basis set) and computational parameters used for type A CAp. Then, we extended the modelling to type A-B carbonated hydroxylapatite, using the results obtained from the separated A1 and B substitutions. Finally, the structural results were used provide the simulated phonon properties of type A and type B carbonate ions in both B-COHAp and mixed A-B C(OH)Ap to further investigate the differences between defective carbonated hydroxylapatite and a fully carbonated one.

9.2 Computational Details

All simulations have been made on a Debian Cluster with 40 cores adopting the periodic *ab initio* CRYSTAL09 code (Dovesi et al., 2009). With this software it is possible to study periodic systems by the implemented Hartree–Fock and Kohn–Sham self-consistent field (SCF) method. The pictures of the structures and their inspections have been carried out with the molecular graphic software MOLDRAW (Ugliengo et al., 1993) and VESTA (Momma and Izumi, 2008).

Basis set

Multi electron wave functions are described by linear combination of crystalline orbitals (CO), expanded in terms of Gaussian-type basis sets. For all the calculations, calcium has been described with a 86-511G(2d), used by other authors for calcite (Valenzano et al., 2006) and by us in our previous work (Ulian et al., 2013a, 2013b), with outer shell exponents α_{sp} = 0.453 bohr^{-2}, α_{d1} = 3.1910 and 0.8683 bohr^{-2} and α_{d2} = 0.2891 bohr^{-2}. The phosphorus atom is described by the basis 85-21G(d), α_{sp} = 0.48105 and 0.135 bohr^{-2} and α_{d} = 0.74583 bohr^{-2}, respectively. For the sodium atom, an 8-511G basis set was used (Dovesi et al., 1991). Oxygen and hydrogen are both represented by a 6-31G* basis set with the outer shell exponents α_{sp} = 0.2742 bohr^{-2} and α_{d} = 0.538 bohr^{-2}; and α_{sp} = 0.1613 and α_{p}

= 1.1 $bohr^{-2}$, respectively. Finally, the carbon atom is described by a 6-21G* basis set with α_{sp} = 0.26 $bohr^{-2}$ and α_d = 0.8 $bohr^{-2}$ (Catti et al., 1993).

Hamiltonian and computational parameters

The Becke three-parameter (B3LYP) hybrid exchange functional (Becke, 1993) in combination with the gradient-corrected correlation functional of Lee, Yang, and Parr (Lee et al., 1988) has been adopted for all calculations. This functional has been already used for alkali oxides, α-quartz, calcite and hydroxylapatite (Dovesi et al., 1991; Pascale et al., 2005; Prencipe et al., 2004; Ulian et al., 2013a; Ulian et al., 2013b). The presence of some fraction of exact exchange increases the electronic localization, which in turn increases the ionic nature of the materials, causing a systematic decrease of the lattice parameters and an increase of the elastic constants and bulk moduli (Cora et al., 2004). The exchange–correlation contribution is performed over a grid of points and is the result of a numerical integration of the electron density and its gradient. The adopted pruned grid is given by 75 points and 974 angular points (75, 974-XLGRID), obtained from the Gauss–Legendre quadrature and Lebedev schemes (Prencipe et al., 2004). This is a good compromise between accuracy and cost of calculation for geometry optimization and vibrational frequencies. The values of the tolerances that control the Coulomb and exchange series are the default provided by CRYSTAL09 (*ITOL1* to *ITOL4* = 6) (Dovesi et al., 2009), but we increased the pseudo-overlap parameter (*ITOL5*) from 12 to 14. The Hamiltonian matrix has been diagonalized (Monkhorst and Pack, 1976) using a shrinking factor (*IS*) = 4. The same conditions have been adopted in our previous work on type A hydroxylapatite (Ulian et al., 2013a, 2013b).

Geometry

The geometry of the OHAp base-model used in this work was optimized within the $P6_3$ space group. For more details we suggest to refer to the paper of Ulian et al. (2013a). When carbonate ion defects were introduced in the structure, the subsequent optimization were carried without any symmetry constrain (*P1* symmetry).

Lattice constants and internal coordinates have been optimized within the same run using the analytical gradient method for the atomic positions and a numerical gradient for the unit-cell parameters. The Hessian matrix is upgraded with the Broyden–Fletcher–Goldfarb–Shanno algorithm. The tolerances for the maximum allowed gradient of the internal forces and the maximum atomic displacement for considering the geometry as converged have been set to 0.00006 hartree $bohr^{-1}$ and 0.00012 bohr, respectively.

Phonon calculations

In periodic systems and within the harmonic approximation, the phonon frequencies at Γ point are evaluated diagonalising the central zone (k = 0) mass-weighted Hessian matrix:

$$W_{ij}(k=0)=\sum_G \frac{H_{ij}^{0G}}{\sqrt{M_i M_j}}$$

H_{ij}^{0G} is the second derivative of the electronic and nuclear repulsion energy E evaluated at equilibrium **u=0** with respect to the displacement of atom A in cell 0 ($u_i = x_i - x_i^*$) and displacement of atom B in cell G ($u_j = x_j - x_j^*$) from their equilibrium position x_i^*, x_j^*:

$$\sum_G H_{ij}^{0G} = \sum_G \left[\frac{\partial^2 E}{\partial u_i^0 \partial u_j^G}\right]_0$$
$$i = 1,...,3N; \quad j = 1,...,3N$$

In CRYSTAL, the calculation of the Hessian at equilibrium is made by the analytical evaluation of the energy first derivatives, Φ_j of E with respect to the atomic displacements:

$$\Phi_j = \sum_G v_j^G = \sum_G \frac{\partial E}{\partial u_j^G} \quad j = 1,...,3N$$

while second derivatives at **u = 0** (where all first derivatives are zero) are calculated numerically using a "two-point" formula:

$$\left[\frac{\partial \Phi_j}{\partial u_i^0}\right]_0 \approx \frac{\Phi_j(0,...,u_i^0,...,0) - \Phi_j(0,...,u_i^0,...,0)}{u_i^0}$$
$$i = 1,...,3N; \quad j = 1,...,3N$$

More details on the vibrational calculation made by CRYSTAL can be found in literature (Pascale et al., 2004; Tosoni et al., 2005). The Hessian matrix eigenvalues provide the normal harmonic frequencies ω_h and it is obtained with 3N+1 SCF and gradient calculation.

Also, an anharmonic correction has been applied to the OH stretching mode in the type B COHAp cell. This three-step procedure is based on: (i) decoupling of the distance O–H, which is treated as a pure normal coordinate; (ii) calculation of the total energy of the system for a set of OH values around equilibrium (0.2/+0.3Å), followed by an interpolation by means of a sixth-order polynomial fit, and

(iii) solution of the one-dimensional nuclear Schrödinger equation to obtain the three lowest eigenvalues, E_0, E_1 and E_2, from which one can calculate the fundamental frequency $\omega_{01} = E_1 - E_0$, the first overtone $\omega_{02} = E_2 - E_0$ and the anharmonicity constant of the OH mode, $\omega_e\chi_e = (2\ \omega_{01} - \omega_{02})/2$. This algorithm was proposed by Lindberg (Lindberg, 1988) and already adopted by other authors (Pascale et al., 2004; Ugliengo et al., 2004; Ulian et al., 2013b).

9.3 Results and Discussions

Type B carbonated hydroxylapatite

In the type B defect formation in OHAp, the CO_3^{2-}/PO_4^{3-} substitution would lead to a positively charged cell. Many ways were proposed to restore the cell neutrality (Peroos et al., 2006), we chose the following charge balancing reaction:

$$PO_4^{3-}{}_{(cell)} + Ca^{2+}{}_{(cell)} + CO_3^{2-} + M^+ \rightarrow CO_3^{2-}{}_{(cell)} + M^+{}_{(cell)} + PO_4^{3-} + Ca^{2+}$$

where a Ca^{2+} is substituted by a monovalent ion, that could be any one of the alkaline elements. In this work we have chosen the sodium ion ($M^+ = Na^+$) because it possess an ionic radius close to that of calcium and thus it is sterically comparable. In fact, sodium-bearing apatites have been experimentally reported and were extensively studied by X-Ray Diffraction (XRD) and Fourier Transform Infrared (FTIR) analysis (Fleet and Liu, 2007; Kovaleva et al., 2009).

The modelling of type B COHAp involved the geometrically optimized OHAp structure that we have recently reported (Ulian et al., 2013a). Since there are six phosphate ions and ten calcium ions in a crystallographic cell of hydroxylapatite (Figure 9.1), the combined CO_3^{2-} and Na^+ substitution would lead to 60 models which are compatible with type B defect. However, since all the PO_4^{3-} are symmetry related within the *P6₃* space group, we fixed the CO_3^{2-}/PO_4^{3-} substitution on the P13 phosphate ion (see Figure 9.1). This operation reduces the symmetry to of the OHAp cell to *P1*. In this condition all the ten calcium ions are non-equivalent and a full analysis of the type B COHAp structure required ten models, one for each Ca/Na substitution.

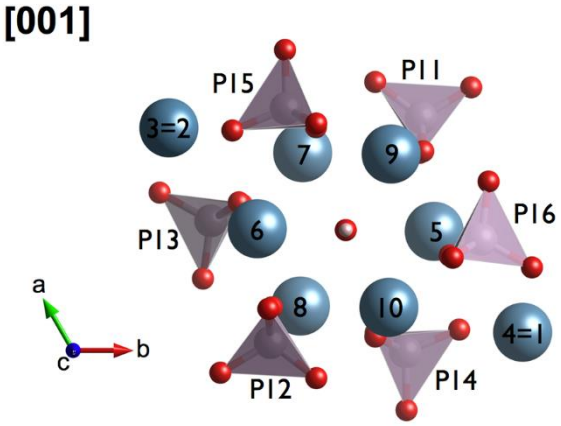

Figure 9.1. Views along the [001] direction of OHAp unit cell content with labelled potential substitution sites.

Thus, the rationale of the model creation was the following: (i) starting from the pure OHAp we removed the phosphate ion labelled as P13, (ii) then we placed the CO_3^{2-} on the bottom sloping face

of the removed tetrahedron and (iii) substituted a calcium with a sodium ion. Steps (i) and (ii) were the same for each model, while (iii) involved each Ca^{2+}: this method allowed to reduce the number of necessary models from 60 to just 10.

In Table 9.1 we reported the results of the geometrical optimization conducted on the type B COHAp structures.

Table 9.1. Optimization results for the type B COHAp substitution.

	OHAp*	**Na position**									
		1	**2**	**3**	**4**	**5**	**6**	**7**	**8**	**9**	**10**
Cell parameters											
a (Å)	9.433	9.377	*9.432*	9.376	9.398	9.402	*9.413*	9.373	9.397	9.429	9.386
b (Å)	9.433	9.346	*9.335*	9.335	9.310	9.364	*9.301*	9.320	9.353	9.338	9.324
c (Å)	6.896	6.924	*6.898*	6.910	6.899	6.913	*6.889*	6.926	6.915	6.895	6.903
α (°)	90	90.8	*90.4*	90.6	90.0	90.1	*90.1*	90.6	90.2	90.4	90.2
β (°)	90	90.0	*89.2*	90.3	90.0	90.3	*90.1*	90.2	90.1	89.7	90.2
γ (°)	120	120.6	*120.8*	120.3	120.5	121.0	*120.0*	120.8	121.1	120.8	120.3
Volume ($Å^3$)	531.5	522.3	*521.8*	521.9	520.1	521.6	*522.2*	519.5	520.7	521.2	521.4
Density (g/cm^3)	3.139	3.025	*3.028*	3.027	3.038	3.029	*3.025*	3.041	3.034	3.031	3.03
Mean bond lengths (Å)											
P - O	1.552	1.551	*1.552*	1.552	1.552	1.551	*1.551*	1.552	1.551	1.551	1.551
O - H	0.972	0.970	*0.971*	0.970	0.970	0.973	*0.971*	0.972	0.972	0.970	0.969
O-H --- O-H	2.477	2.232	*2.125*	2.406	2.110	2.036	*2.386*	1.994	2.058	2.312	2.666
C - O	-	1.295	*1.293*	1.294	1.295	1.294	*1.293*	1.294	1.294	1.294	1.295
Ca --- O	2.437	2.423	*2.445*	2.426	2.448	2.445	*2.446*	2.450	2.448	2.447	2.433
Na --- O	-	2.646	*2.555*	2.522	2.505	2.557	*2.477*	2.430	2.480	2.513	2.486
Na (--- $O_{PO4exited}$)	-	4.939	*2.762*	4.754	3.957	4.478	*2.342*	2.501	3.456	4.7844	5.346
Ca3 --- Ca3	4.178	4.073	*4.086*	4.069	4.090	4.084	*4.062*	4.064	4.070	4.073	4.088
Na --- C	-	3.354	*3.616*	3.326	3.423	3.146	*3.285*	3.373	3.456	5.800	6.177
Na --- O(CO3)	-	2.686	*2.775*	2.825	2.358	2.347	*2.589*	2.594	2.791	4.892	5.724
(Na--C)/(Na--O)	-	1.25	*1.30*	1.18	1.45	1.34	*1.27*	1.30	1.24	1.19	1.08
Mean bond angles (°)											
O - P -O	109.8	109.2	*109.3*	109.3	109.3	109.8	*110.0*	109.6	109.5	109.5	109.4
O - C -O	-	120.0	*120.0*	120.0	120.0	120.0	*120.0*	120.0	120.0	120.0	120.0
ΔE (kJ/mol)	-	9.3	*1.5*	18.4	18.2	28.8	*0.00*	13.9	39.3	46.3	50.2
Band Gap (eV)	7.71	7.76	*7.84*	7.64	7.79	7.96	*7.66*	7.93	7.87	7.60	7.76

Notes: values in italic indicate the most stable structures obtained. Numbers from 1 to 10 indicate the location of Na^+/Ca^{2+} substitution.
* (Ulian et al., 2013a)

According to the adopted computational parameters, all the presented data in this work have an uncertainty on each atomic position of about 0.00006 Å. Because of the same atomic composition, it was possible to directly compare the energy of the different models. The most stable one presents the Na^+ replacing Ca6 ion (Na6 model, see Figure 9.2b), followed by the Na2 model where Na^+ replaces Ca2 ion, which differs energetically from Na6 model by just +1.45 kJ/mol (Figure 9.2a). The relative

stability of the type B COHAp structure is probably due to a subtle interplay between the CO_3^{2-} and Na^+ relative distances and the distortion of the hosting structure to accommodate for the defect. In particular, the structure is stable when the sodium ion is in a position near to the oxygen vacancies related to the phosphate substitution, as it is possible to see in the results in Table 9.1. This observation would prove the hypothesis proposed by Fleet and Liu (2007). The actual energy values are high enough to conclude that only the Na2 and Na6 models exhibits significant populations in the absence of the thermal effects while all other cases are not present at room temperature.

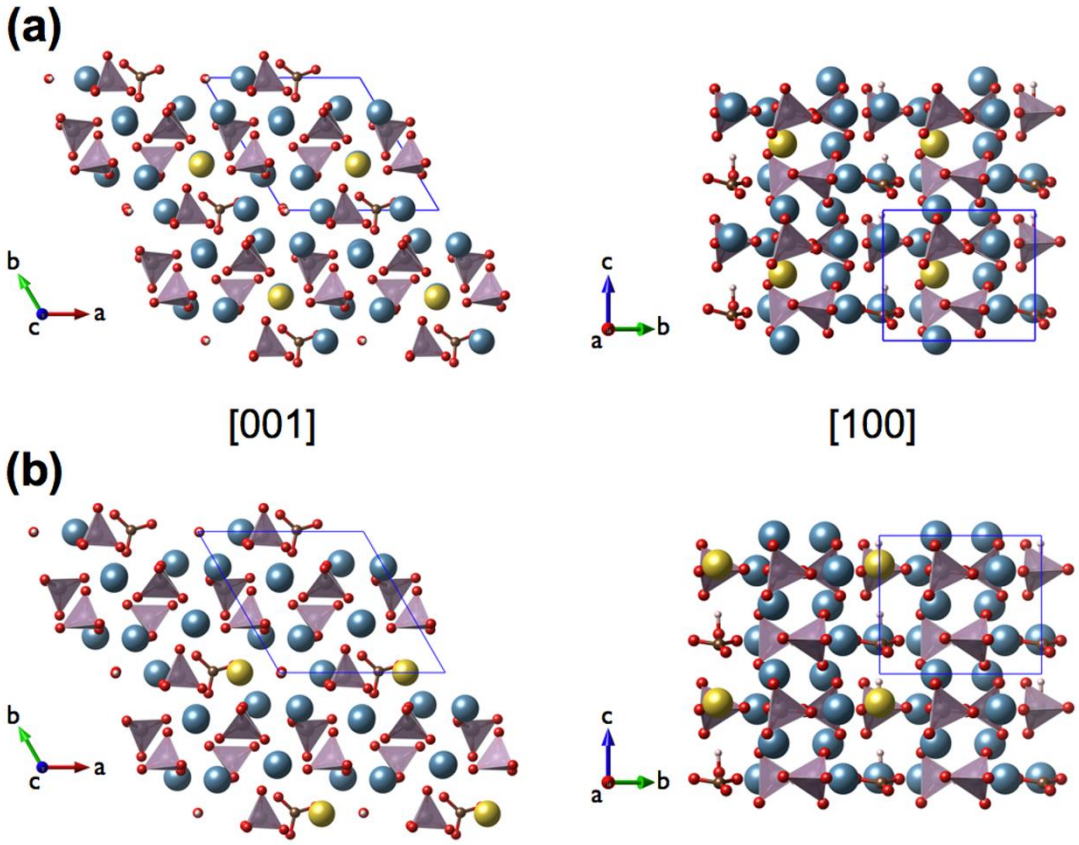

Figure 9.2. Optimization results for the two most stable type B COHAp, with (a) Na2/Ca2 and (b) Na6/Ca6 substitutions. Atoms are indicated in red for oxygen, pink for phosphate, cyan for calcium, white for hydrogen, ochre for carbon and yellow for sodium.

Compared to our previous results of pure OHAp model (Ulian et al., 2013a), the combined CO_3^{2-}/Na^+ substitutions cause a contraction of the crystallographic cell along the *a*- and *b*-dimensions, while the *c*-axis expands slightly. We noticed that the Ca3 --- Ca3 interaction distances slightly decreased by about 0.1 Å, which means that the calcium channel was also contracted by about 2.0%. These results are solely due to the carbonate ion, which is smaller than the substituted phosphate ion. The Na^+ ionic radius is close to the Ca^{2+} one and, as also suggested by previous studies (Peroos et al., 2006), its effects on cell variation are negligible. Angular distortions of the lattice are predicted to be small for the most stable Na2 and Na6 configurations, they remain below 0.8 degrees as compared to the OHAp parent structure.

Although the lattice parameters variations, the type B carbonate ion did not valuably affects the crystalline framework. The PO_4^{3-} tetrahedrons in the unit-cell were only slightly rotated to accommodate the CO_3^{2-} ion, but these rotations were negligible if compared to those of type A defect (Ulian et al., 2013a). The mean P-O and O-H bond lengths are almost the same in each model and they are very close to the OHAp values. We observed a reduction of the O-H---O-H interaction distances from 2.41 Å to 1.99 Å and in the case of Na5, Na7 and Na8 models it leaded to the formation of a hydrogen bond between the two OH groups in the unit-cell.

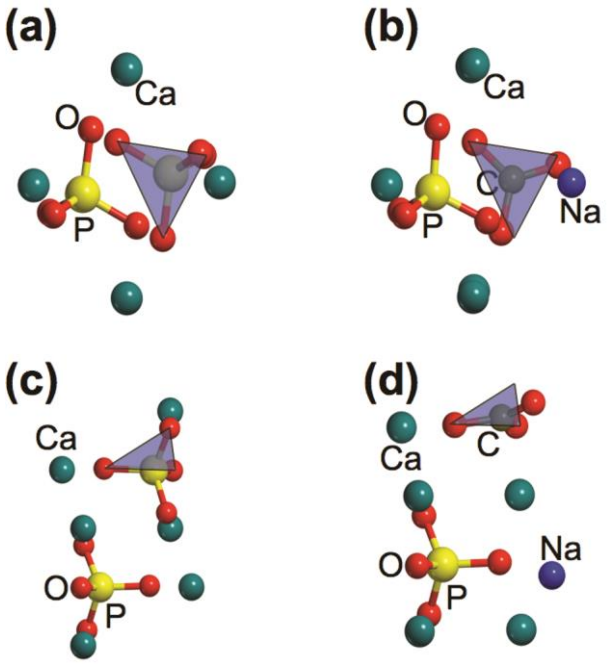

Figure 9.3. Views along (a,b) [001] and (c,d) [110] directions of the unit-cell phosphate ion in OHAp (a,c) interested in the type B CO_3^{2-} substitution (b,d). The sloping face in which the carbonate ion was introduced is maintained in the type B COHAp to show the optimization effect.

In Figure 9.3 we reported a section of the unit-cell involved in the PO_4^{3-}/CO_3^{2-} substitution. The highlighted phosphate tetrahedron face (Figure 9.3a,c) represents the initial carbonate ion position. After the geometry optimization of the type B COHAp (Figure 9.3b,d), we observed a rotation of the CO_3^{2-} molecular plane on the [001] and [110] directions by -15° and -46°, respectively (see Figure 9.3). Although there were minimal positional or angular variations between the ten models, the local geometry showed in Figure 9..3 was maintained. The observed carbonate ion position is in line with both previous theoretical studies made by molecular dynamics approach (Peroos et al., 2006) and experimental XRD refinement (Fleet and Liu, 2007), where the same molecular canting was observed.

Compared to XRD refinements reported in literature (Fleet and Liu, 2004; Kovaleva et al., 2009; Yahia and Jemal, 2010), the type B COHAp resulting from our quantum mechanical simulations is in good agreement with experimental results. The differences on the crystallographic lattices are ±0.050Å on *a* and *b* cell parameters and +0.010 on the *c* one. Generally, the simulated type B carbonated hydroxylapatite unit-cell volume is slightly contracted than the experimental by about $3Å^3$. This could be due to the presence also of type A carbonate or other defects in the experimental samples, as reported by the authors, and to the approximations in the quantum mechanical calculations.

Type A-B carbonated hydroxylapatite

In this section the focus is on the effect of coupled type A and B defects on the crystallographic cell of hydroxylapatite. We have considered various configurations and mutual distances of the defects in both a single cell and in a supercell.

Single-cell of type A-B carbonated apatite

We initially considered a single unit-cell of OHAp in which both type A and B carbonate ions are included, accordingly to the reactions:

$$2OH^-_{(cell)} + CO_3^{2-} \rightarrow (A1)CO_3^{2-}{}_{(cell)} + 2OH^-$$

$$PO_4^{3-}{}_{(cell)} + Ca^{2+}{}_{(cell)} + CO_3^{2-} + Na^+ \rightarrow (B)CO_3^{2-}{}_{(cell)} + Na^+{}_{(cell)} + PO_4^{3-} + Ca^{2+}$$

The resulting structure has chemical formula $Ca_9Na(PO_4)_5(CO_3)_2$, with a carbonate ion content of 12.3 wt.% and without any OH^- groups. The two models have been created with the same CO_3^{2-} positions in A and B sites but with sodium ion substituting Ca2 and Ca6 sites. This choice was made taking into account the previous results on the stability of type B COHAp. The orientation of the carbonate ion in the apatite channel (type A1) was selected as the same of that reported in a previous work (Ulian et al., 2013a), which was the most stable one. The results of the optimization are reported in Table 9.2.

The coupled substitution caused a small compression of the lattice parameters *a* and *b* and an expansion of the *c* one. However, the contraction on the *a* and *b*-dimensions is smaller than the one observed for the pure type B carbonated apatite: this is due to the type A carbonate ion in the calcium channel, which causes an expansion on *a* and *b*-dimensions and this explains the observed effect on the unit cell. The obtained values are in good agreement with the XRD data on a Na-bearing type A-B COHAp sample with similar CO_3^{2-} content (Fleet and Liu, 2007). The bond lengths and angles are not significantly different. During the geometry optimization process, the type A1 CO_3^{2-} ion rotated counterclockwise on its plane of about 180°, bringing the C – O bond perpendicular to the [001] direction near the type B carbonate ion. It is worth noting that this rotation brought the type A1 carbonate ion first in the A2 configuration, then after the optimization again in A1 configuration. The model with Ca6/Na6 substitution is more stable than that with Ca2/Na2. This result is in agreement with the data of the type B carbonate defect in apatites reported in the previous section.

Table 9.2. Optimization results for type A-B CAp in comparison with experimental data

Defect A-B (Na)	**Experimental***	**B3LYP**	
Single Cell	**XRD**	**Na2**	**Na6**
Cell parameters			
a (Å)	9.3855	9.4085(+0.023)	9.3951(+0.010)
b (Å)	9.3855	9.4111(+0.026)	9.3371(-0.048)
c (Å)	6.9142	6.9210(+0.007)	6.9038(-0.010)
α (°)	90.0	89.0(-1.0)	89.6(-0.4)
β (°)	90.0	90.9(+0.9)	90.4(+0.4)
γ (°)	120.0	120.1(+0.1)	119.8(-0.2)
Volume ($Å^3$)	527.5	530.1(+2.6)	525.8(-1.7)
Density (g/cm^3)	3.120	3.066(-0.054)	3.091(-0.029)
% CO_3 wt.	11.1	12.3(+1.2)	12.3(+1.2)
% Na wt.	2.01	2.35(+0.34)	2.35(+0.34)
Mean bond lengths			
P – O	1.513	1.544(+0.031)	1.552(+0.039)
C - O (A)	-	1.294	1.295
C - O (B)	-	1.295	1.296
C – C	-	3.854	3.881
Ca --- O (A)	2.360	2.378(+0.018)	2.422(+0.062)
Na --- O	-	2.568	2.395
Ca3 --- Ca3	4.212	4.306(+0.094)	4.257(+0.045)
Na --- C (A)	-	5.138	2.818
Na --- C (B)	-	3.649	3.187
Na --- O(CO_3)	-	2.732	2.287
(Na--C)/(Na--O)	-	1.336	1.394
Mean bond angles			
O - P –O	109.4	110.1(+0.7)	110.0(+0.6)
O - C -O (A)	120.0	120.0(+0.0)	120.0(+0.0)
O - C -O (B)	120.0	120.0(+0.0)	120.0(+0.0)
Energy			
ΔE (kJ/mol)	-	+19.06	0.00

Notes: values in parenthesis are the deviations from experimental results. Na2 and Na6 indicate the location of Na^+/Ca^{2+} substitution.
* (Fleet and Liu, 2007)

Supercell of type A-B carbonated apatite

The single cell of type A-B CAp described in the previous paragraph is a good starting point to analyse the interaction between type A1 and type B carbonate ions. However, in that structure the relative distances between the CO_3^{2-} ions is almost fixed to about 3 Å because of their contiguity within the same unit-cell, which allows to study only their short-range interactions. It would be interesting to study a case in which the defects are less close by adopting a supercell approach. The adoption of the canonical unit cell forces the removal of all OH groups in order to accommodate the mixed A-B type defects, while OH groups are experimentally found in both natural and synthetic carbonated apatites.

In order to take into account the above mentioned considerations, i.e., both the non-contiguity of type A and type B defects and the experimental observations of the presence of the OH groups, we modelled a "supercell". We doubled the *a* and *b* cell parameters, obtaining a structure that was 2 x 2 x 1 the original one, with four unit-cells of OHAp and chemical formula $Ca_{40}(PO_4)_{24}(OH)_8$ (Figure 9.4a). This larger model allowed to place the type A and B defects in different contiguous unit-cells, thus to consider different carbonate ions relative distances. To create the mixed A-B COHAp we initially made the type A1 CO_3^{2-} substitution: the four unit-cells are equivalent due to the symmetry of the supercell, so the choice is indifferent. The substitution resulted in a type A COHAp, a structure without any internal symmetry given by a solid solution of three OHAp unit-cells and a type A1 CAp one. Fixing this partial model, the type B carbonate ion could be placed in one of the three remaining hydroxylapatite unit-cells, thus defining three models that are:

(i) with the type B defect in the unit-cell contiguous to the type A1 CAp one along the *b*-axis (labelled as AB-1 in Figure 9.4b);

(ii) with the type B defect placed along the *ab* diagonal (labelled as AB-2 in Figure 9.4b);

(iii) with the type B defect placed along the *a*-axis (labelled as AB-3 in Figure 9.4b).

In each model, the sodium ion of the type B defect always substituted a Ca6 ion in the unit-cell.

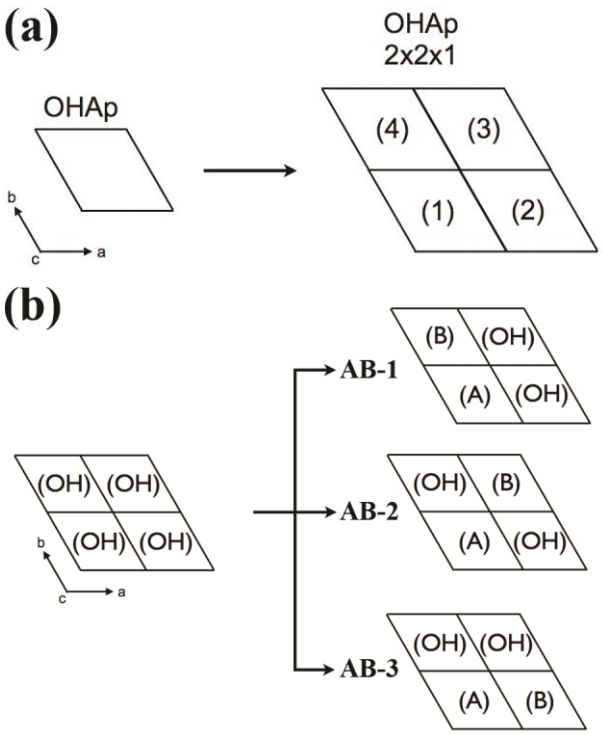

Figure 9.4. Substitution scheme for type A-B COHAp. (a) Generation of the supercell and (b) generation of the three type A-B models. A and B refers to the carbonate defect types and OH to the pure hydroxylapatite.

The resulting structures are then solid solutions of two OHAp, one type A1 CAp and one Na-bearing type B COHAp unit-cells, with chemical formula $Ca_{39}Na(PO_4)_{23}(CO_3)(OH)_6(CO_3)$ (normalized to $Ca_{9.75}Na_{0.25}(PO_4)_{5.75}(CO_3)_{0.25}(OH)_{1.5}(CO_3)_{0.25}$) and a carbonate ion content of 3.01 wt.%. The results have been reported in Table 9.3.

To ease the interpretation and in order to make a direct comparison with previous results and with XRD experimental data, the lattice parameters *a* and *b* have been normalized with respect to the models with type A and B defects in a single unit cell. The three models AB-1, AB-2 and AB-3 have CO_3 --- CO_3 distances that increase following the trend AB-3 < AB-1 < AB-2, where periodicity was

also took into account. The type A1 carbonate ion in the first and second model rotates about the *c-axis* as to follow the type B CO_3^{2-} ion.

Table 9.3. Optimization results for type A-B COHAp

Defect A-B (Na)	**Experimental***	**B3LYP**		
2 x 2 x 1 unit-cell	**XRD**	**AB-1**	**AB-2**	**AB-3**
Cell parameters				
a (Å)	9.397	9.451(+0.054)	9.413(+0.016)	9.486(+0.089)
b (Å)	9.397	9.482(+0.085)	9.466(+0.069)	9.400(+0.003)
c (Å)	6.889	6.897(+0.008)	6.903(+0.014)	6.906(+0.017)
α (°)	90.0	89.5(-0.5)	89.5(-0.5)	89.9(-0.1)
β (°)	90.0	90.1(+0.1)	90.4(+0.4)	90.0(+0.0)
γ (°)	120.0	120.6(+0.6)	120.1(+0.1)	120.1(+0.1)
Volume ($Å^3$)	526.8	532.0(+5.2)	532.2(+5.4)	532.5(+5.7)
Density (g/cm^3)	3.150	3.112(-0.038)	3.111(-0.039)	3.109(-0.041)
% CO_3 wt.	3.5	3.01(-0.49)	3.01(-0.49)	3.01(-0.49)
% Na wt.	0.81	0.58(-0.23)	0.58(-0.23)	0.58(-0.23)
Mean bond lengths				
P - O	-	1.548	1.548	1.548
O - H	-	0.972	0.971	0.971
O-H --- O-H	-	2.537	2.491	2.440
C - O (A)	-	1.287	1.287	1.288
C - O (B)	-	1.294	1.295	1.296
C - C	-	8.108	8.693	5.988
Ca --- O (A)	-	2.415	2.339	2.371
Na --- O	-	2.403	2.421	2.407
Ca3 --- Ca3	-	4.237	4.343	4.239
Na --- C (A)	-	8.591	9.921	7.363
Na --- C (B)	-	3.122	3.330	3.104
Na --- O(CO3)	-	2.322	2.484	2.483
(Na--C)/(Na--O)	-	1.345	1.341	1.250
Mean bond angles				
O - P -O	-	109.4	108.9	108.9
O - C -O (A)	-	120.0	120.0	120.0
O - C -O (B)	-	120.0	120.0	120.0
Energy				
ΔE (kJ/mol)	-	0.00	20.71	9.18

Notes: values in parenthesis are the deviations from experimental results.
* Single-crystal XRD refinement of sample LM006, (Fleet and Liu, 2007)

The average bond lengths and angles are almost unaffected by the different carbonate ions relative distances. However, it seems that the structure stability increases in the following order AB-1 > AB-3 > AB-2. This trend does not follow the CO_3 --- CO_3 distances as it has could be expected. At low distance (AB-3) there could be some direct coulomb repulsion between carbonate ions that decreased the structure stability. At high distance (AB-2) the instability is amplified, probably because of the

lack of interaction. Then, the most stable structure must lie between these two limit distances considered. Given the relative small energy differences between the most favourable structures (AB-1 and AB-3), it may be suggested that the experimental structure refers to a "geometrical" mix of these two structures or, more precisely, of all structures that are within k_BT of the energetically most favourable structure, where k_B is the Boltzmann's constant and T is the temperature. As observed before, the coupled substitution caused a slight expansion of the *c* parameter, but the *a*- and *b*-dimensions showed different behaviours according to the type B defect location in the models. In particular, there is a full expansion along every lattice axis in the AB-1 model, which may explain its stability. The mean bond lengths and angles of the crystalline framework were not significantly affected. It is worth noting that provided XRD data are somehow incomplete and thus a full comparison between the interatomic distances and angles was not possible. However, we reported the crystallographic information framework (CIF) data files for all the structures obtained from our simulations, which were used to measure the internal geometry of the models, to help others in interpreting their results.

In general, all the structural results are in good agreement with the experimental data (see Table 9.4). The calculated lattice parameters show small variations between the different carbonated (hydroxyl)apatite models, with a larger deviation on the type A defective structure, but the evaluated data are consistent with experimental evidence. In each model but the single-cell type A-B CAp the calcium ion content is higher than the relative one in biological tissues, but in good agreement with that of synthetic apatites (Fleet and Liu, 2007). This is not surprising, because Ca^{2+} ions can be easily substituted by both sodium and magnesium by 0.5 – 1.2 % wt. (Dorozhkin, 2009c). Thus, the type A-B CAp model suggests that in each crystallographic cell in the biological mineral there is at least one calcium ion substitution or vacancy per cell. The phosphorus weight content is in line with the experimental data. In particular, it seems that in the bone tissue there is in average one type B defect per unit cell. On the other hand, the enamel has a higher P content than the other hard tissues, which suggests the presence of less type A and B carbonate ion in the structure. The carbonate ion presence in the apatite structure is in good agreement with biological/chemical data, with an exception for the single-cell type A-B CAp model. The Na^+ content is more represented by the type A-B supercell models, because in both type B COHAp and single-cell of mixed A-B CAp it is more than two times the experimental values.

Table 9.4. Comparison between C(OH)Ap models and natural hard tissues

	Theoretical models					Experimental§		
	OHAp*	**Type A1 CAp***	**Type B Na-COHAp†**	**Type A-B Na-CAp†**	**Type A-B Na-COHAp†**	**Bone**	**Dentin**	**Enamel**
Cell parameters								
a (Å)	9.433	9.582	9.3982	9.4027	*9.4493*	9.41	9.421	*9.441*
b (Å)	9.433	9.764	9.3327	9.3707	*9.4486*	9.41	9.421	*9.441*
c (Å)	6.896	6.877	6.9071	6.9134	*6.9028*	6.89	6.887	*6.880*
α (°)	90	89.3	90.3	89.3	*89.6*	90.0	90.0	*90*
β (°)	90	89.8	90.0	90.7	*90.2*	90.0	90.0	*90*
γ (°)	120	121.9	120.6	120.0	*120.3*	120.0	120.0	*120*
Volume (Å^3)	531.5	546	521.3	527.4	*532.2*	528.4	529.4	*531.1*
% wt.								
Ca^{2+}	39.89	38.81	37.87	36.79	*39.07*	34.80	35.1	*36.5*
P	18.05	18.05	16.26	15.84	*17.86*	15.20	16.9	*17.7*
CO_3^{2-}	-	5.82	6.30	12.26	*3.01*	7.40	5.6	*3.5*
Na^+	-	-	2.41	2.35	*0.58*	0.90	0.6	*0.5*

* (Ulian et al., 2013a)
† present work
§ (Dorozhkin, 2009c)

Simulated infrared properties of carbonate ions

Type B carbonated hydroxylapatite

The type B COHAp unit-cell does not have internal symmetry, thus its (43 x 3) - 3 = 126 vibrational modes belong only to the A irreducible representation (IRREP):

$$\Gamma_{total} = 126\ A$$

The vibrational modes can be subdivided in three regions: lattice modes (< 400 cm-1), phosphate ion vibrations (500 – 1200 cm^{-1}) and carbonate ion modes (600 – 1800 cm^{-1}). In the following we discuss in details each vibrational region of the simulated type B COHAp spectrum.

FTIR and Raman spectra of the free phosphate tetrahedron in aqueous solution present four vibrational modes (irreducible representations A_1+E+2F): (i) the symmetric P-O stretching (ν_1, A_1) at 938 cm^{-1}; (ii) the symmetric OPO bending (ν_2, E) at 420 cm^{-1}, which are IR inactive; (iii) the asymmetric P-O stretching (ν_3, F) at 1017 cm^{-1} and (iv) the asymmetric OPO bending (ν_4, F) at 567 cm^{-1} (Corno et al., 2006; Rehman and Bonfield, 1997; Tsuda and Arends, 1994). When the PO_4^{3-} ion is in a molecular crystals, such as hydroxylapatite, the crystalline field induces distortions of the perfect phosphate tetrahedron, reducing its symmetry. In particular, within both type A and type B defective COHAp structures the phosphate ion lies in a framework which does not have any symmetry feature. This lead to the loss of degeneracy of the highly symmetric phonon modes and to the activation of all

the silent ones (B symmetry) previously described (Corno et al., 2006; Ulian et al., 2013b), thus to the presence of more signals in the infrared spectra.

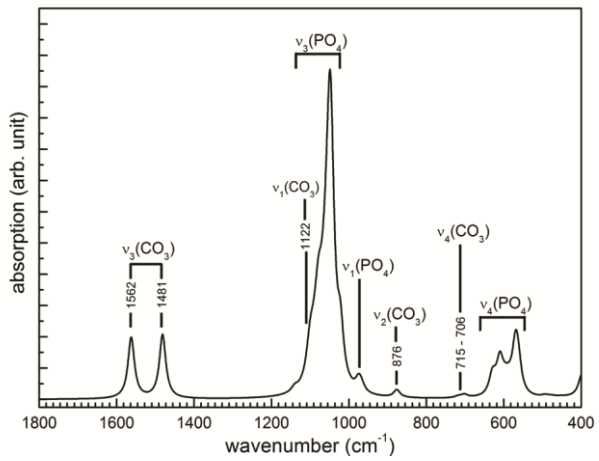

Figure 9.5. Simulated vibrational spectra of the most stable type B COHAp structure (Na6 model).

The spectrum presented in Figure 9.5 is related to the Na6 model of type B COHAP, the most stable structure obtained. The asymmetric phosphate ions, $\nu_3(PO_4)$, at 1022-1140 cm^{-1} stretching signal is the most intense in the spectrum. This band is more complex than that of pure OHAp, because it is composed by 18 active modes originated by the degeneracy loss of E_1 and E_2 vibrational modes. Despite the complexity, the $\nu_3(PO_4)$ band in type B COHAp is very similar to that of OHAp, more than that of type A CAp (Ulian et al., 2013b). The P-O symmetric stretching (ν_1) signal can be found in the 876 – 977 cm^{-1} range, composed by six phonon modes. The OPO asymmetric (ν_4) and symmetric (ν_2) bending modes are located in the 562 – 630 cm^{-1} (medium intensity) and 426 – 494 cm^{-1} (very low intensity) ranges, respectively. In general, the CO_3^{2-}/PO_4^{3-} substitution caused a slight broadening of the phosphate vibrational band, leaving the high-intensity signal positions almost unchanged: this means that the type B carbonate defect in OHAp interacts poorly with the crystalline framework. Taking into account this consideration, the complete vibrational analysis has been conducted only on the most stable type B COHAp model (Na6). Similar PO_4^{3-} phonon modes in the other nine theoretical type B COHAp structures were assumed.

Regarding the hydroxyl groups, the O-H stretching mode falls at two different wavenumbers, 3774 cm^{-1} and 3759 cm^{-1}. The first signal is relative to the stretching of an hydroxyl group near to the charge-balancing sodium ion at a distance of 2.35 Å. The other peak is very close to the O-H signal of pure hydroxylapatite, at 3757 cm^{-1} (Ulian et al., 2013b). When anharmonicity was taken into account (see the Computational Methods section), the two stretching modes shifted to lower wavenumbers, at 3693 cm^{-1} and 3597 cm^{-1} respectively, in good agreement with the FTIR result of Fleet and Liu (2007). The 500 – 700 cm^{-1} region of the type B COHAp spectrum has more signals than that of type A CAp, because of the presence of eight OH libration modes. These phonon signals concur in the formation of two peaks at 622 – 630 cm^{-1} (four modes of medium-intensity) and 701 – 722 cm^{-1} (four modes of very-low intensity), close to the results obtained for pure hydroxylapatite (an IR/Raman band at 636 cm^{-1}, E_1 symmetry, and the Raman signal at 724 cm^{-1}, E_2 symmetry). As we have

reported in our previous work, OH libration are affected by anharmonicity and, unfortunately, the CRYSTAL09 code allows to apply the correction only to the stretching ones (Ulian et al., 2013b), preventing the direct comparison between the theoretical (with harmonic approximation) and the experimental OH modes.

The free CO_3^{2-} in aqueous solution has four modes: asymmetric stretching (ν_3, *E'* symmetry), symmetric stretching (ν_1, *A'1* symmetry). bending out-of-plane (ν_2, *A''* symmetry) and bending in plane (ν_4, *E'* symmetry). In the IR spectrum, the the *A'1* symmetry mode relative to the symmetric stretching is inactive, because it does not cause dipole variations. In the apatite framework, the symmetry reduction causes the loss of degeneracy of *E'* modes, giving origin to two doublets and to the activation of the symmetric stretching mode.

The characteristic carbonate bands in apatite lattice are the asymmetric stretching (ν_3) and the out-of-plane bending (ν_2). The simulated peaks occurred in the Na6 model spectrum (Figure 9.5) at 1481 and 1562 cm^{-1} for the ν_3 vibration and at 876 cm^{-1} for the ν_2 one. We compared the type B CO_3^{2-} modes with those of the simulated type A1 CAp spectra reported in a previous paper (Ulian et al., 2013b). The asymmetric stretch doublet of type B was at lower frequencies than that of type A1. However, they maintained a similar separation (81 cm^{-1} in type B and 86 cm^{-1} in type A1). The $\nu_2(CO_3)$ mode fell very close to the same band observed for the type A1 CAp (878 cm^{-1}).

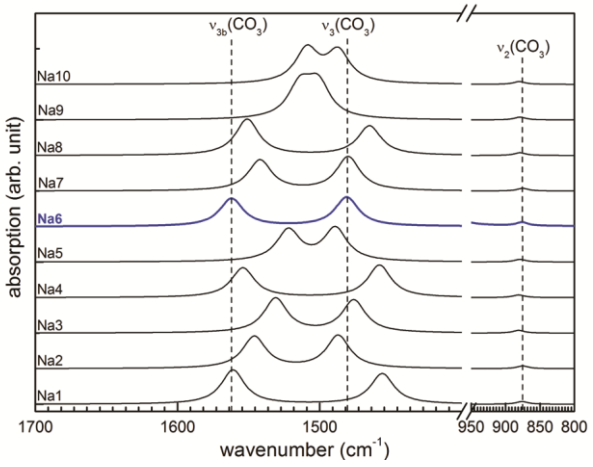

Figure 9.6. Simulated ν_3 and ν_2 bands of carbonate ion in the type B COHAp models. Dotted lines are centered on the Na6 model results.

The CO_3^{2-} vibrational modes in the other nine optimized models have been obtained separately with the FRAGMENT keyword (Dovesi et al., 2009). The related spectra are reported in Figure 9.6 and the frequency values in Table 9.5. The carbonate asymmetric stretch doublets (ν_3) are at different frequencies with respect to the Na6 model. A consistent comparison is possible using this method because repeating the frequency calculation on the Na6 model with the FRAGMENT keyword returned almost the same values obtained with the full calculation. This result further confirms the low interaction of the type B carbonate ion with the crystalline framework. We observed a systematic red shift of the ν_{3b} signal, with different entity from one structure to another. The ν_3 band follow this trend in four cases (Na1, Na3, Na4 and

Na8 models), but in the remnant structures it is blue shifted. In this latter case this leaded to a reduction of the doublet separation, which is very noticeable in Na5, Na9 and Na10 spectra. This effect was due to the different Ca^{2+}/Na^{+} substitutions in the unit-cell. Considering that in experimental samples the sodium ion occupies different positions simultaneously, this result could explain a significant band broadening of this mode ($\nu_{3max} - \nu_{3min} \approx 45$ cm^{-1}).

Table 9.5. Carbonate ion phonon frequencies in type B COHAp

Band	Na1	Na2	Na3	Na4	Na5	Na6	Na7	Na8	Na9	Na10
$\nu_4(CO_3)$	-4	-1	-8	-4	-8	706	-12	-13	-5	-7
$\nu_4(CO_3)$	-3	-3	-6	-8	-2	715	9	2	-4	-8
$\nu_2(CO_3)$	0	-1	5	5	3	876	-1	3	3	4
$\nu_1(CO_3)$	-9	1	-3	-16	-5	1109	-3	-4	-3	-10
$\nu_3(CO_3)$	-25	6	-5	-23	8	1481	-1	-16	20	6
$\nu_{3b}(CO_3)$	-1	-16	-31	-8	-40	1562	-20	-11	-48	-53

Notes: Values (cm^{-1}) are reported as deviation from the most stable type B COHAp structure (Na6).

The $\nu_2(CO_3)$ band fell at almost the same frequency in each model (876 cm^{-1}), which means that the sodium ion position did not interfered with this vibrational mode. The symmetric stretching (ν_1) and the in-plane bending (ν_4) modes are also slightly affected by the different Na^{+} ion position, with the signals red shifted when compared to the Na6 model.

Type A-B carbonated (hydroxyl)apatite

In this section the focus is on the effects of the CO_3^{2-} --- CO_3^{2-} relative distance on the IR signal positions. The results are collected in Table 9.6.

Compared to the to the type A1 CAp simulated in a previous work (Ulian et al., 2013b), in the fully carbonated cell of type A1-B CAp all the signals but the ν_1 one are red shifted (Figure 9.7a).

When the different solid solution of hydroxylapatite and carbonate defects were considered, we observed an inversion of the order of $\nu_{3a}(CO_3)$ modes at different CO_3^{2-} relative distances (Figure 9.7b). When the two defects are very close, *i.e.* in the single unit-cell of type A-B CAp, there is first

Table 9.6. Carbonate ion phonon frequencies in different type A-B models

Band	AB-Na6	AB-1	AB-2	AB-3	B-Na6
$\nu_{4a}(CO_3)$ (A)	660	666	676	666	-
$\nu_{4b}(CO_3)$ (A)	759	784	775	771	-
$\nu_2(CO_3)$ (A)	890	889	882	889	-
$\nu_1(CO_3)$ (A)	1086	1128	1124	1125	-
$\nu_3(CO_3)$ (A)	1442	1503	1517	1501	-
$\nu_{3b}(CO_3)$ (A)	1589	1612	1608	1613	-
$\nu_{4a}(CO_3)$ (B)	693	693	692	701	706
$\nu_{4b}(CO_3)$ (B)	721	719	713	718	715
$\nu_2(CO_3)$ (B)	875	879	879	861	876
$\nu_1(CO_3)$ (B)	1091	1099	1095	1092	1109
$\nu_{3a}(CO_3)$ (B)	1463	1472	1473	1462	1481
$\nu_{3b}(CO_3)$ (B)	1545	1568	1548	1553	1562

Notes: Values are in wavenumber (cm^{-1}).

the ν_{3a}(A) mode, then the ν_{3a}(B) one (at 1442 and 1436 cm^{-1}, respectively); in type A-B COHAp, either AB-1, AB-2 and AB-3 models, the order is reversed (1470 cm^{-1} for ν_{3a}(B) and 1505 cm^{-1} for ν_{3a}(B)). The order of occurrence of the $\nu_{3b}(CO_3)$ signal is not affected by the positions of the type A and type B defect in the apatite cell. The out-of-plane bending (ν_2) falls almost at the same position in the supercell models of type A-B carbonated hydroxylapatite.

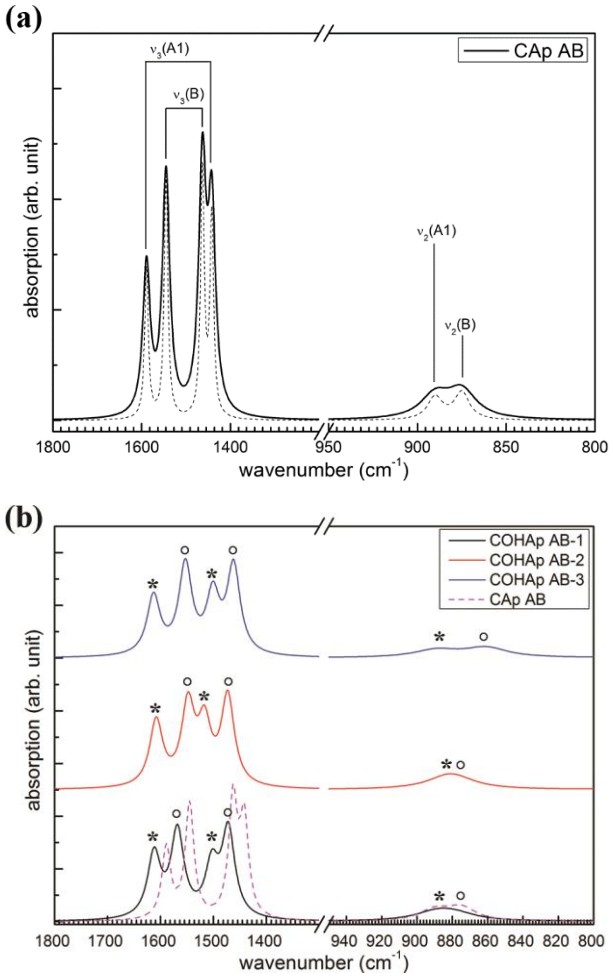

Figure 9.7. Phonon spectra of mixed type A-B C(OH)Ap structures (a) in single unit-cell and (b) in 2x2x1 supercell. The dotted line in (a) is the same type A-B CAp spectrum, with sharper signals. For the sake of clearness, in the spectra reported in (b) the A1 and B modes have been labeled as (*) and (°), respectively.

Respect to both singly type A1 and type B defects, the symmetric stretching mode (ν_1) is slightly red shifted ($\Delta\nu \approx 10$ cm^{-1}) in the AB-1, AB-2 and AB-3 models, while the effect is larger in the AB-Na6 one ($\Delta\nu > 15$ cm^{-1}). In the type AB supercell models the carbonate ion modes are shifted to different position, with no apparent behavior. In particular, the ν_2 signals can be quite well resolved in AB-3 or slightly overlapped in AB-1 and AB-2 models.

We compared our phonon results with experimental Raman/FTIR analysis reported in literature for a variety of samples (Table 9.7). Both natural and synthetic samples were experimentally investigated (Fleet et al., 2011; Penel et al., 2005; Petra et al., 2005; Sturgeon and Brown, 2009; Yahia and Jemal, 2010). There is a very good agreement on the $\nu_2(CO_3)$ mode to each simulated structure, both with singly and coupled type A1 and type B defects, with only negligible variations from +1 to +9 cm^{-1}.

This is an important result, because the quantification of the carbonate content in apatite is usually made from the intensity of the out-of-plane band and our approach adequately describe this region of the spectrum. Differences are present in the asymmetric stretch region (1400-1500 cm^{-1}). Our $\nu_3(CO_3)$ doublet for type B carbonate ion was blue shifted of about +70 cm^{-1} and presented a larger separation between the two signals (81 cm^{-1}) than the experimental ones (~50 cm^{-1}). This observation can be extended to type A1 ν_3 signals, but the difference from experimental results is less than the one found

for the type B phonon mode. The effect on the ν_3 modes could be related to the adopted computational methods, since there is a systematic shift of the calculated signals. A configuration where the CO_3^{2-} ion is placed in the Ca^{2+} channel with a bisector of the carbonate triangular plane parallel to the **c**-axis (type A2) was reported (Fleet et al., 2011). It was found by FTIR analysis an asymmetric stretching mode doublet relative to the A2 carbonate ion at 1569 and 1507 cm^{-1}. This CO_3^{2-} configuration was found unstable in our previous work on type A defect, spontaneously shifting toward the A1. For this reason, we do not have any evidence of the signal reported by Fleet et al. (2011).

Table 9.7. Comparison between theoretical and experimental phonon results for C(OH)Ap structures.

Band	**Theoretical**				**Experimental**				
	A1[a]	*B-Na6*[b]	*AB-Na6*[b]	*AB-1*[b]	*Raman*[c]	*Micro-FTIR*[d]	*FTIR*[e]	*FTIR*[f]	*FTIR*[g]
$\nu_{4a}(CO_3)$ (A)	670	-	660	666	676	670	-	-	-
$\nu_{4b}(CO_3)$ (A)	781	-	759	784	754	750	-	-	-
$\nu_2(CO_3)$ (A)	878	-	890	889	-	878	-	880	-
$\nu_1(CO_3)$ (A)	1134	-	1086	1128	1103	-	-	-	-
$\nu_3(CO_3)$ (A)	1518	-	1442	1503	-	-	1449	1457	-
$\nu_{3b}(CO_3)$ (A)	1604	-	1589	1612	-	-	1541	1550	1558
$\nu_{4a}(CO_3)$ (B)	-	706	693	693	689	670	-	-	
$\nu_{4b}(CO_3)$ (B)	-	715	721	719	718	750	-	-	
$\nu_2(CO_3)$ (B)	-	876	875	879	-	871	873	876	873
$\nu_1(CO_3)$ (B)	-	1109	1091	1099	1073	-	-	-	-
$\nu_{3a}(CO_3)$ (B)	-	1481	1463	1472	-	-	1406	1418	1423
$\nu_{3b}(CO_3)$ (B)	-	1562	1545	1568	-	-	1474	1462	1473

Notes: all values are in wavenumbers (cm^{-1}).
a (Ulian et al., 2013b)
b present work
c (Penel et al., 2005)
d (Petra et al., 2005)
e (Fleet and Liu, 2008)
f (Fathi et al., 2008)
g (Sturgeon and Brown, 2009)

Despite these small deviations, there is a general good agreement with the experimental results, especially with those of synthetic carbonated hydroxylapatite samples (Fathi et al., 2008; Fleet and Liu, 2007; Sturgeon and Brown, 2009). Both natural and synthetic samples present different concentration of type A and type B defects and their distribution within the lattice is not clearly known. An important aspect may be given by the presence and the content in the apatite cell of various type of defects, substituent and/or vacancies, especially for bone tissues samples. When modeling a structure different strategies have been proposed to restore the neutrality of the apatite cell when a type B carbonate ion is included (Astala and Stott, 2005; Peroos et al., 2006). We have chosen the $Ca^{2+} \rightarrow Na^{+}$ substitution because the sodium ion was observed in biological apatites and its ionic radius is

very close to that of calcium ion. This approach affected the COHAp lattice and phonon modes as we reported, while other possible ways were not covered in the present work. As an example, the inclusion of an OH group in the cell near the carbonate ion may produce different responses. However, that simulation will be the subject of a future work.

REFERENCES CITED

Astala, R., and Stott, M.J. (2005) First principles investigation of mineral component of bone: CO3 substitutions in hydroxyapatite. Chemistry of Materials, 17(16), 4125-4133.

Becke, A.D. (1993) A New Mixing of Hartree-Fock and Local Density-Functional Theories. Journal of Chemical Physics, 98(2), 1372-1377.

Catti, M., Pavese, A., Dovesi, R., and Saunders, V.R. (1993) Static lattice and electron properties of MgCO3 (Magnesite) calculated by ab-initio periodic Hartree-Fock methods. Physical Review B, 47, 9189-9198.

Cora, F., Alfredsson, M., Mallia, G., Middlemiss, D.S., Mackrodt, W.C., Dovesi, R., and Orlando, R. (2004) The performance of hybrid density functionals in solid state chemistry. In N.M.J.E. Kaltsoyannis, Ed. Principles and Applications of Density in Inorganic Chemistry Ii, 113, p. 171-232.

Corno, M., Busco, C., Civalleri, B., and Ugliengo, P. (2006) Periodic ab initio study of structural and vibrational features of hexagonal hydroxyapatite Ca10(PO4)6(OH)2. Physical Chemistry Chemical Physics, 8, 2464-2472.

Dorozhkin, S.V. (2009a) Calcium orthophosphate-based biocomposites and hybrid biomaterials. Journal of Materials Science, 44(9), 2343-2387.

-. (2009b) Calcium Orthophosphate Cements and Concretes. Materials, 2, 221-291.

-. (2009c) Calcium Orthophosphates in Nature, Biology and Medicine. Materials, 2, 399-398.

-. (2009d) Nanodimensional and Nanocrystalline Apatites and Other Calcium Orthophosphates in Biomedical Engineering, Biology and Medicine. Materials, 2, 1975-2045.

Dovesi, R., Roetti, C., Freyria Fava, C., Prencipe, M., and Saunders, V.R. (1991) On the elastic properties of lithium, sodium an potassium oxide. An ab initio study. Chemical Physics, 156, 11-19.

Dovesi, R., Saunders, V.R., Roetti, C., Orlando, R., Zicovich-Wilson, C.M., Pascale, F., Civalleri, B., Doll, K., Harrison, N.M., Bush, I.J., D'Arco, P., and Llunell, M. (2009) CRYSTAL09 User's Manual. University of Torino, Torino.

Engin, A., and Girgin, I. (2009) Synthesis of hydroxyapatite by using calcium carbonate and phosphoric acid in various water-ethanol solvent systems. Central European Journal of Chemistry, 7(4), 745-751.

Fathi, M.H., Hanifi, A., and Mortazavi, V. (2008) Peparation and bioactivity evaluation of bone-like hydroxyapatite nanopowder. Journal of Materials Processing Technology, 202, 536-542.

Fleet, M.E. (2009) Infrared spectra of carbonate apatites: n2-Region bands. Biomaterials, 30, 1473-1481.

Fleet, M.E., and Liu, X. (2007) Coupled substitution of type A and B carbonate in sodium-bearing apatite. Biomaterials, 28(6), 916-926.

-. (2008) Type A-B carbonate chlorapatite synthesized at high pressure. Journal of Solid State Chemistry, 181(9), 2494-2500.

Fleet, M.E., and Liu, X.Y. (2003) Carbonate apatite type A synthesized at high pressure: new space group (P(3)over-bar) and orientation of channel carbonate ion. Journal of Solid State Chemistry, 174(2), 412-417.

-. (2004) Location of type B carbonate ion in type A-B carbonate apatite synthesized at high pressure. Journal of Solid State Chemistry, 177(9), 3174-3182.

-. (2005) Local structure of channel ions in carbonate apatite. Biomaterials, 26(36), 7548-7554.

Fleet, M.E., Liu, X.Y., and King, P.L. (2004) Accommodation of the carbonate ion in apatite: An FTIR and X-ray structure study of crystals synthesized at 2-4 GPa. American Mineralogist, 89(10), 1422-1432.

Fleet, M.E., Liu, X.Y., and Liu, X. (2011) Orientation of channel carbonate ions in apatite: Effect of pressure and composition. American Mineralogist, 96(7), 1148-1157.

Gibson, I.R., and Bonfield, W. (2002) Novel synthesis and characterization of an AB-type carbonate-substituted hydroxyapatite. Journal of Biomedical Materials Research, 59(4), 697-708.

Kovaleva, E.S., Shabanov, M.P., Putlyaev, V.I., Tretyakov, Y.D., Ivanov, V.K., and Silkin, N.I. (2009) Bioresorbable carbonated hydroxyapatite $Ca_{10-x}Na_x(PO_4)_{6-x}(CO_3)_x(OH)_2$ powders for bioactive materials preparation. Central European Journal of Chemistry, 7(2), 168-174.

Lafon, J.P., Champion, E., and Bernache-Assollant, D. (2008) Processing of AB-type carbonated hydroxyapatite Ca10-x(PO4)(6-x)(CO3)(x)(OH)(2-x-2y)(CO3)(y) ceramics with controlled composition. Journal of the European Ceramic Society, 28(1), 139-147.

Lee, C.T., Yang, W.T., and Parr, R.G. (1988) Development of the Colle-Salvetti Correlation-Energy Formula into a Functional of the Electron-Density. Physical Review B, 37(2), 785-789.

LeGeros, R.Z. (2002) Properties of osteoconductive biomaterials: Calcium phosphates. Clinical Orthopaedics and Related Research, 395, 81-98.

Lindberg, B. (1988) A New Efficient Method for Calculation of Energy Eigenvalues and Eigenstates of the One-Dimensional Schrodinger-Equation. Journal of Chemical Physics, 88(6), 3805-3810.

Momma, K., and Izumi, F. (2008) VESTA: a three-dimensional visualization system for electronic and structural analysis. Journal of Applied Crystallography, 41, 653-658.

Monkhorst, H.J., and Pack, J.D. (1976) Special points for Brillouin-zone integrations. Physical Review B, 8, 5188-5192.

Pascale, F., Zicovich-Wilson, C.M., Gejo, F.L., Civalleri, B., Orlando, R., and Dovesi, R. (2004) The calculation of the vibrational frequencies of crystalline compounds and its implementation in the CRYSTAL code. Journal of Computational Chemistry, 25(6), 888-897.

Pascale, F., Zicovich-Wilson, C.M., Orlando, R., Roetti, C., Ugliengo, P., and Dovesi, R. (2005) Vibration frequencies of $Mg_3Al_2Si_3O_{12}$ pyrope. An ab initio study with the CRYSTAL code. Journal of Physical Chemistry B, 109(13), 6146-6152.

Peeters, A., DeMaeyer, E.A.P., VanAlsenoy, C., and Verbeeck, R.M.H. (1997) Solids modeled by ab initio crystal-field methods .12. Structure, orientation, and position of A-type carbonate in a hydroxyapatite lattice. Journal of Physical Chemistry B, 101(20), 3995-3998.

Penel, G., Delfosse, C., Descamps, M., and Leroy, G. (2005) Composition of bone and apatitic biomaterials as revealed by intravital Raman microspectroscopy. Bone.

Peroos, S., Du, Z., and de Leeuw, N.H. (2006) A computer modelling study of the uptake, structure and distribution of carbonate defects in hydroxy-apatite. Biomaterials, 27, 2150-2161.

Petra, M., Anastassopopulou, J., Theologis, T., and Theophanides, T. (2005) Synchrotron mirco-FT-IR spectroscopic evaluation of normal paediatric human bone. Journal of Molecular Structure, 733, 101-110.

Prencipe, M., Pascale, F., Zicovich-Wilson, C.M., Saunders, V.R., Orlando, R., and Dovesi, R. (2004) The vibrational spectrum of calcite (CaCO3): an ab initio quantum-mechanical calculation. Physics and Chemistry of Minerals, 31(8), 559-564.

Rabone, J.A.L., and de Leeuw, N.H. (2007) Potential routes to carbon inclusion in apatite materials: a DFT study. Physics and Chemistry of Minerals, 34, 495-506.

Rehman, I., and Bonfield, W. (1997) Characterization of hydroxyapatite and carbonated apatite by photo acoustic FTIR spectroscopy. Journal of Materials Science-Materials in Medicine, 8(1), 1-4.

Sturgeon, J.L., and Brown, P.W. (2009) Effects of carbonate on hydroxyapatite formed from $CaHPO_4$ and $Ca_4(PO_4)_2O$. Journal of Materials Science-Materials in Medicine, 20, 1787-1794.

Suda, H., Yashima, M., Kakihana, M., and Yoshimura, M. (1995) Monoclinic <--> Hexagonal Phase Transition in Hydroxyapatite Studied by X-ray Powder Diffraction and Differential Scanning Calorimeter Techniques. Journal of Physical Chemistry, 99(17), 6752-6754.

Suetsugu, Y., Shimoya, I., and Tanaka, J. (1998) Configuration of Carbonate Ions in Apatite Structure Determined by Polarized Infrared Spectroscopy. Journal of the American Ceramic Society, 81, 746-748.

Tosoni, S., Pascale, F., Ugliengo, P., Orlando, R., Saunders, V.R., and Dovesi, R. (2005) Quantum mechanical calculation of the OH vibrational frequency in crystalline solids. Molecular Physics, 103(18), 2549-2558.

Tsuda, H., and Arends, J. (1994) Orientational micro-Raman spectroscopy on hydroxyapatite single crystals and human enamel crystallites. Journal of Dental Research, 73, 1703-1710.

Ugliengo, P., Pascale, F., Merawa, M., Labeguerie, P., Tosoni, S., and Dovesi, R. (2004) Infrared spectra of hydrogen-bonded ionic crystals: Ab initio study of Mg(OH)(2) and beta-Be(OH)(2). Journal of Physical Chemistry B, 108(36), 13632-13637.

Ugliengo, P., Viterbo, D., and Chiari, G. (1993) MOLDRAW: molecular graphic on a personal computer. Zeitschrift Fur Kristallographie, 207, 9-23.

Ulian, G., Valdrè, G., Corno, M., and Ugliengo, P. (2013a) Periodic ab initio bulk investigation of hydroxylapatite and type A carbonated apatite with both pseudopotential and all electron basis sets for calcium atoms. American Mineralogist, Accepted, in press March 2013.

-. (2013b) The vibrational features of hydroxylapatite and type A carbonated apatite: a first principle contribution. American Mineralogist, 98(4), 752-759.

Valenzano, L., Torres, F.J., Klaus, D., Pascale, F., Zicovich-Wilson, C.M., and Dovesi, R. (2006) Ab initio study of the vibrational spectrum and related properties of crystalline compounds; the case of CaCO3 calcite. Zeitschrift Fur Physikalische Chemie-International Journal of Research in Physical Chemistry & Chemical Physics, 220(7), 893-912.

Yahia, F.B.H., and Jemal, M. (2010) Synthesis, structural analysis and thermochemistry of B-type carbonate apatites. Thermochimica Acta, 505(1-2), 22-32.

CHAPTER 10 – General Conclusions

The purpose of this thesis was to investigate the structural and physical-chemical properties of different minerals involved in ceramic structural and biomedical industry. Due to the magnitude of materials belonging to both fields, the analysis were limited to cases of upmost relevance, i.e. to phyllosilicates (talc, pyrophyllite and muscovite), hydroxylapatite and its carbonate-defective forms, respectively.

The selected investigation method is described in literature as "Quantum Mineralogy", i.e. the adoption of quantum-mechanical (QM) theory, formulas and computer codes to study the crystallographic and the physical-chemical properties of mineral (solid) phases. To this aim, a comparison between different *ab initio* QM approaches within Density Functional Theory (DFT) and periodic boundary conditions (PBC) was performed to select one method that provides the best results in comparison with experimental data. Such operation was necessary to both establish a set of coherent and comparable results between different mineralogical systems and to allow the subsequent prediction of mineral properties. The comparison promoted the use of Gaussian-type orbitals (GTO) as atomic basis set and the hybrid DFT functional B3LYP to take into account the exchange-correlation contribution. In the simulations of layered structures, as in the case of phyllosilicates, a dispersion correction to evaluate weak interaction forces is mandatory and it was included with rescaled C_6 and R_6 parameters for the hybrid functional (B3LYP-D* method).

Then, the bulk properties of two phyllosilicate end-members were obtained: tri-octahedral talc and di-octahedral pyrophyllite. Also, one mica group mineral was considered, the muscovite. The structures, phonon properties and mechanical behaviours were calculated and compared with experimental data, which is sometimes lacking or very scarce in literature. Simulations of the minerals at different lattice volumes were conducted to calculate their equation of state (EoS) It was found that the QM EoS resembles the one obtained experimentally by single-crystal X-Ray Diffraction, while it shows some deviations from X-Ray Powder Diffraction results. It was supposed that this observation is due to the PBC adopted to solve the Schrödinger equation, wich does not consider the random crystal orientations in powdered samples.

Furthermore, the calculation of vibrational properties at each volumetric (pressure) condition allowed the inclusion of the thermal behaviour of the considered minerals by the quasi-harmonic approximation. *P-T-V* and thermo-chemical (isochoric and isobaric heat capacities, entropy) data was collected, obtaining for the first time three-dimensional diagrams of these properties. The results are in good

agreement with those found in literature and provide predictions of the mineral behaviours at conditions still not fully explored by experimental means because of the complex experimental set up.

Regarding bioceramic materials, a study of hydroxylapatite (OHAp) and different models of carbonated (hydroxyl)apatite unit-cells was conducted to investigate the carbonate ion effects on OHAp lattice and physical-chemical properties. To our knowledge, this is the first time that the pure hydroxylapatite, type A, type B and mixed type A-B carbonated (hydroxyl)apatite were simulated with an all electron basis set for each atom in the structure. The geometric parameters obtained were in perfect agreement with the experimental results reported in literature. The use of a full-potential basis set provided lesser deviation from both X-Ray/Neutron Diffraction and FTIR/Raman data than the adoption of pseudopotential on calcium atoms.

We found that the preferred orientation of the type A carbonate ion in the apatite lattice is that of the close configuration, i.e., with C – O bond perpendicular to the c-axis. We observed also that the CO_3^{2-} interacts with the surrounding calcium ions in very similar a way to that found in calcite ($CaCO_3$). In the case of CAp, it has been proved that the CO_3^{2-} planar configuration represents a saddle point in the potential energy surface of the CAp structure because there is a phonon instability provided by three negative modes related to the rotation of the CO_3^{2-} molecular plane.

In the case of type B carbonate ion, it has been observed that it occupies one of the tetrahedral faces of the substituted phosphate ion. The charge-balancing ion (Na in the present work) stabilizes the structure when it substitutes a calcium atom near to the oxygen vacancy created by the extracted PO_4^{3-} ion, in excellent agreement with experimental single-crystal XRD data.

The mixed A-B defect was considered in both single and lager unit-cells to mimic some different solid solutions similar to the real biomineral and to explore their relative stabilities. Due to the small energy differences between some of the considered models, it can be asserted that the carbonated hydroxylapatite mineral is a geometrical mix of these structures. However, It was observed that different relative positions of type A and type B defects have a great impact on the phonon signals of the carbonate ion in the apatite cells. This could be the reason of the broadening of the IR/Raman peaks observed in experiments.

In general, the results obtained in this thesis represent a valuable starting point for subsequent investigations on the chosen minerals. From the bulk structure, it is possible to simulate slab models to study the surface atomic morphologies and physical properties, such as the electrostatic potential map and the chemical reactivity of both pure and defective minerals. In particular, work is in progress to study the interactions between water and relevant biomolecule (nucleic acids and amino acids) and mineral phases.

Appendix – Basis sets adopted

A.1 Premise

CRYSTAL performs *ab initio* calculations on periodic systems adopting the linear combination of atomic orbitals (LCAO) approximation. Within this approximation, the crystalline orbitals (CO) are treated as linear combinations of Bloch functions (BF),

$$\psi_i(\mathbf{r};\mathbf{k}) = \sum_{\mu} a_{\mu i}(\mathbf{k})\,\phi_{\mu}(\mathbf{r};\mathbf{k}) \tag{A2.1}$$

$$\phi_{\mu}(\mathbf{r};\mathbf{k}) = \sum_{\mathbf{g}} \varphi_{\mu}(\mathbf{r}-\mathbf{A}_{\mu}-\mathbf{g})\,e^{i\mathbf{k}\cdot\mathbf{g}} \tag{A2.2}$$

defined in terms of local functions, indicated as atomic orbitals (AO). Those local functions are expressed as linear combination of a certain number of Gaussian type functions (GTF).

$$\varphi_{\mu}(\mathbf{r}-\mathbf{A}_{\mu}-\mathbf{g}) = \sum_{j}^{n_G} d_j G(\alpha_j;\mathbf{r}-\mathbf{A}_{\mu}-\mathbf{g}) \tag{A2.3}$$

These functions are characterized by the same centre **A**, with fixed coefficients, *d*, and exponents, α, all of them defined in the input. In Equations A2.1-3 we have:

- **r**, the coordinate of an electron;
- **g**, the direct lattice vector;
- *k*, a point I the reciprocal space defined by a lattice vector;
- **A**, the coordinate of an atom in the reference cell;
- *a*, the variational coefficients which multiply the Bloch functions;
- *d*, the coefficiens of the primitive Gaussians in the contraction, fixed for a given basis set.

The atomic orbitals belonging to a given atom are grouped into shells. The shell can contain either all AOs with the same quantum numbers, n and l (for instance 3s, 2p, 3d shells), or all the AOs with the same principal quantum number n and different l (sp shells; exponent of s and p gaussians are the same). A single, normalized, s-type GTF, the adjoined gaussian, is associated with each shell. The exponent of the adjoined gaussian is the smallest exponent of the gaussians in the contraction. The adjoined gaussian is used to estimate the AO overlap and select the level of approximation to be adopted for the evaluation of the integrals (Dovesi et al., 2009).

All the basis sets adopted in this thesis are general ones, that is, exponent and contraction coefficients are defined by the user. In the following, an example of the basis set input is reported to explain the reader how to read it. Then, the basis sets for each atom used are listed, subdivided in chapters.

```
1[a] 3[b]
0[c]  0[d]   3[e]  1.[f]  1.00[g]
   0.1873113696D+02[h]  0.3349460434D-01[i]
   0.2825394365D+01  0.2347269535D+00
   0.6401216923D+00  0.8137573262D+00
0   0   1   0.   1.00
   0.1612777588D+00  0.1000000000D+01
0   2   1   0.   1.
   1.1  1.
```

a. conventional atomic number (hydrogen in this case)
b. number of shells (3)
c. type of basis set (0 means user-defined shell)
d. shell type
- 0 = 1 s AOs
- 1 = 1 s + 3 p AOs
- 2 = 3 p AOs
- 3 = 5 d AOs
- 4 = 7 f AOs

e. number of primitive Gaussian Type Functions
f. formal electron charge attributed to the shell
g. scale factor
h. exponent of the normalized primitive GTF
i. contraction coefficient of the normalized primitive GTF

A.2 Basis sets used in Chapter 2–4 for Talc

Silicon atom [1]

```
14 5
0 0 8 2.0 1.0
 149866.0    0.0001215
  22080.6    0.0009770
   4817.5    0.0055181
   1273.5    0.0252000
    385.11   0.0926563
    128.429  0.2608729
     45.4475 0.4637538
     16.2589 0.2952000
0 1 8 8.0 1.0
    881.111  -0.0003   0.0006809
    205.84   -0.0050   0.0059446
     64.8552 -0.0368   0.0312000
     23.9    -0.1079   0.1084000
     10.001   0.0134   0.2378000
      4.4722  0.3675   0.3560066
      2.034   0.5685   0.3410000
      0.9079  0.2065   0.1326000
0 1 3 4.0 1.0
      2.6668 -0.0491   0.0465000
      1.0780 -0.1167  -0.1005000
      0.3682  0.2300  -1.0329000
0 1 1 0.0 1.0
      0.193   1.0      1.0
0 3 1 0. 1.
      0.610   1.0
```

Oxygen atom [2]

```
8 6
0 0 8 2.0 1.0
   8020.   0.001080
   1338.   0.008040
    255.4  0.053240
     69.22 0.168100
     23.90 0.358100
      9.264 0.385500
      3.851 0.146800
      1.212 0.072800
0  1  4  6.  1.0
   49.43   -0.008830  0.009580
   10.47   -0.091500  0.069600
   3.235   -0.040200  0.206500
   1.217    0.379000  0.347000
0  1  1  0.  1.0
   0.486    1.      1.
0  1  1  0.  1.0
   0.1925     1.      1.
0  3  1  0.  1.
   2.0  1.
0  3  1  0.  1.
   0.500  1.
```

Hydrogen atom [3]

```
1 3
0 0    3 1. 1.00
 0.1873113696D+02  0.3349460434D-01
 0.2825394365D+01  0.2347269535D+00
 0.6401216923D+00  0.8137573262D+00
0 0     1 0. 1.00
 0.1612777588D+00  0.1000000000D+01
0 2 1 0. 1.
 1. 1  1.
```

Magnesium atom [4]

```
12  5
0 0 8 2.0 1.0
 68370.0     0.0002226
  9661.0     0.001901
  2041.0     0.011042
   529.6     0.05005
   159.17    0.1690
    54.71    0.36695
    21.236   0.4008
     8.791   0.1487
0 1 5 8.0 1.0
  143.7     -0.00671    0.00807
   31.27    -0.07927    0.06401
    9.661   -0.08088    0.2092
    3.726    0.2947     0.3460
    1.598    0.5714     0.3731
0 1 1 2.0 1.0
    0.688    1.0        1.0
0 1 1 0.0 1.0
    0.28     1.0        1.0
0  3  1  0.  1.
   0.500  1.
```

1 (Nada et al., 1996)
2 (Valenzano et al., 2007)
3 (Gatti et al., 1994)
4 (Valenzano et al., 2007)

A.3 Basis sets used in Chapter 5–6 for Pyrophyllite and Muscovite

Silicon atom [1]

```
14 5
0 0 8 2.0 1.0
 149866.0    0.0001215
  22080.6    0.0009770
   4817.5    0.0055181
   1273.5    0.0252000
    385.11   0.0926563
    128.429  0.2608729
     45.4475 0.4637538
     16.2589 0.2952000
0 1 8 8.0 1.0
    881.111  -0.0003   0.0006809
    205.84   -0.0050   0.0059446
     64.8552 -0.0368   0.0312000
     23.9    -0.1079   0.1084000
     10.001   0.0134   0.2378000
      4.4722  0.3675   0.3560066
      2.034   0.5685   0.3410000
      0.9079  0.2065   0.1326000
0 1 3 4.0 1.0
      2.6668 -0.0491   0.0465000
      1.0780 -0.1167  -0.1005000
      0.3682  0.2300  -1.0329000
0 1 1 0.0 1.0
      0.193   1.0      1.0
0 3 1 0. 1.
      0.610   1.0
```

Oxygen atom [2]

```
8 6
0 0 8 2.0 1.0
   8020.   0.001080
   1338.   0.008040
    255.4  0.053240
     69.22 0.168100
     23.90 0.358100
      9.264 0.385500
      3.851 0.146800
      1.212 0.072800
0  1  4  6.  1.0
   49.43   -0.008830  0.009580
   10.47   -0.091500  0.069600
   3.235   -0.040200  0.206500
   1.217    0.379000  0.347000
0  1  1  0.  1.0
   0.486    1.      1.
0  1  1  0.  1.0
   0.1925     1.      1.
0  3  1  0.  1.
   2.0  1.
0  3  1  0.  1.
   0.500  1.
```

Hydrogen atom [3]

```
1 3
0 0    3 1. 1.00
 0.1873113696D+02  0.3349460434D-01
 0.2825394365D+01  0.2347269535D+00
 0.6401216923D+00  0.8137573262D+00
0 0     1 0. 1.00
 0.1612777588D+00  0.1000000000D+01
0 2 1 0. 1.
 1. 1  1.
```

Aluminium atom [5]

```
13  5
0  0  8  2.  1.
   70510.0       0.000226
   10080.0       0.0019
    2131.0       0.0110
     547.5       0.0509
     163.1       0.1697
      54.48      0.3688
      19.05      0.3546
       5.402     0.0443
0 1 5 8. 1.
     139.6      -0.01120     0.0089
      32.53     -0.1136      0.0606
      10.23     -0.0711      0.1974
       3.810     0.5269      0.3186
       1.517     0.7675      0.2995
0 1 1 3. 1.
       0.59      1.        1.
0 1 1 0. 1.
       0.35      1.        1.
0 3 1 0. 1.
       0.51      1.
```

Potassium atom [5]

```
19   6
0   0   8   2.   1.
    172500.   0.000220
    24320.    0.00192
    5140.     0.01109
    1343.9    0.04992
    404.5     0.1702
    139.4     0.3679
    54.39     0.4036
    22.71     0.1459
0   1   6   8.   1.
    402.0     -0.00603      0.00841
    93.5      -0.0805       0.0602
    30.75     -0.1094       0.2117
    11.91      0.258        0.3726
    5.167      0.684        0.4022
    1.582      0.399        0.186
0   1   5   8.   1.
    17.35    -0.0074       -0.0321
    7.55     -0.129        -0.062
    2.939    -0.6834        0.1691
    1.19      1.08          1.500
    0.674     1.03          1.060
0   1   1   1.   1.
    0.389     1.             1.
0   1   1   0.   1.
    0.216     1.             1.
0   3   3   0.   1.
    3.94      0.160
    1.072     0.313
    0.394     0.406
```

1 (Nada et al., 1996)
2 (Valenzano et al., 2007)
3 (Gatti et al., 1994)
4 (Catti et al., 1994)
5 (Dovesi et al., 1991)

A.4 Basis sets used in Chapter 7–9 Hydroxyl- and carbonated-(hydroxyl)apatite

Calcium atom [1]

```
20 7
0  0  8  2.  1.
 191300.    0.0002204
  26970.    0.001925
   5696.    0.01109
   1489.4   0.04995
    448.3   0.17014
    154.62  0.3685
     60.37  0.4034
     25.09  0.1452
0 1 6 8. 1.
    448.6   -0.00575  0.00847
    105.7   -0.0767   0.06027
     34.69  -0.1122   0.2124
     13.50   0.2537   0.3771
      5.820  0.688    0.401
      1.819  0.349    0.198
0 1 5 8. 1.
     20.75  -0.0020  -0.0365
      8.40  -0.1255  -0.0685
      3.597 -0.6960   0.1570
      1.408  1.029    1.482
      0.726  0.944    1.025
0 1 1 2. 1.
      0.453  1.       1.
0 1 1 0. 1.
      0.295  1.       1.
0 3 2 0. 1.
      3.1910  0.160
      0.8683  0.313
0 3 1 0. 1.
      0.2891  0.406
```

Phosphorous atom [2]

```
15 5
0 0  8  2.  1.
      202703.      0.0001
      22413.1      0.0013
      4625.08      0.0068
      1312.41      0.0275
      425.149      0.0951
      146.409      0.2667
      51.8363      0.4781
      18.5913      0.2971
0 1  5 8. 1.
     339.375    0.00089   0.00287
      94.9248  -0.03549   0.02778
23.125   -0.153     0.172
       6.9753   0.355     0.4215
       2.275    0.9102    0.4109
0 1  2 5.  1.
       1.219   -0.3715    0.09158
       0.48105  1.271     0.9349
0 1  1  0.  1.
       0.135    1.        1.
0 3 1 0. 1.
       0.74583  1.
```

Oxygen atom [3]

```
8   4
0   0   6   2.   1.00
     5484.6717        0.0018
     825.2349         0.0140
     188.0470         0.0684
     52.9645          0.2327
     16.8976          0.4702
     5.7996           0.3585
0   1   3   6.   1.00
     15.5396         -0.1108     0.0709
     3.5999          -0.1480     0.3398
     1.0138           1.1308     0.7272
0   1   1   0.   1.00
     0.2742           1.          1.
0   3   1   0.   1.00
     0.538            1.
```

Hydrogen atom [4]

```
1   3
0   0    3   1.   1.00
   0.1873113696D+02  0.3349460434D-01
   0.2825394365D+01  0.2347269535D+00
   0.6401216923D+00  0.8137573262D+00
0   0   1   0.   1.00
   0.1612777588D+00  0.1000000000D+01
0   2   1   0.   1.
   1.1  1.
```

Carbon atom [5]

```
6   4
0   0   6.   2.0   1.0
    3048.0          0.001826
    456.4           0.01406
    103.7           0.06876
    29.23           0.2304
    9.349           0.4685
    3.189           0.3628
0   1   2.   4.0   1.0
    3.665           -0.3959     0.2365
    0.7705          1.216       0.8606
0   1   1.   0.0   1.0
    0.26            1.0         1.0
0   3   1.   0.0   1.0
     0.8 1.0
```

Sodium atom [6]

```
11    4
0   0   8   2.   1.
    56700.          0.000225
    8060.           0.00191
    1704.           0.0105
    443.6           0.05006
    133.1           0.1691
    45.8            0.3658
    17.75           0.3998
    7.38            0.1494
0   1   5   8.   1.
    119.0           -0.00673    0.00803
    25.33           -0.0798     0.0639
    7.80            -0.0793     0.2074
    3.00            0.3056      0.3398
    1.289           0.5639      0.3726
0   1   1   1.   1.
     0.548          1.          1.
0   1   1   0.   1.
     0.273          1.          1.
```

1 (Valenzano et al., 2006)
2 (Corno et al., 2006)
3 (Corno et al., 2006)
4 (Corno et al., 2006)
5 (Dovesi et al., 1991)
6 (Catti et al., 1993)

REFERENCES CITED

Catti, M., Pavese, A., Dovesi, R., and Saunders, V.R. (1993) Static lattice and electron properties of MgCO3 (Magnesite) calculated by ab-initio periodic Hartree-Fock methods. Physical Review B, 47, 9189-9198.

Catti, M., Valerio, G., Dovesi, R., and Causa, M. (1994) Quantum-mechanical calculation of the solid-state equilibrium MgO + alpha-Al_2O_3 $MgAl_2O_4$ (spinel) versus pressure. Physical Review B, 49(20), 14179-14187.

Corno, M., Busco, C., Civalleri, B., and Ugliengo, P. (2006) Periodic ab initio study of structural and vibrational features of hexagonal hydroxyapatite Ca10(PO4)6(OH)2. Physical Chemistry Chemical Physics, 8, 2464-2472.

Dovesi, R., Roetti, C., Freyria Fava, C., Prencipe, M., and Saunders, V.R. (1991) On the elastic properties of lithium, sodium an potassium oxide. An ab initio study. Chemical Physics, 156, 11-19.

Dovesi, R., Saunders, V.R., Roetti, C., Orlando, R., Zicovich-Wilson, C.M., Pascale, F., Civalleri, B., Doll, K., Harrison, N.M., Bush, I.J., D'Arco, P., and Llunell, M. (2009) CRYSTAL09 User's Manual. University of Torino, Torino.

Gatti, C., Saunders, V.R., and Roetti, C. (1994) Crystal-field effects on the topological properties of the electron-density in molecular-crystals - the case of urea. Journal of Chemical Physics, 101(12), 10686-10696.

Nada, R., Nicholas, J.B., McCarthy, M.I., and Hess, A.C. (1996) Basis sets for ab initio periodic Hartree-Fock studies of zeolite/adsorbate interactions: He, Ne, and Ar in silica sodalite. International Journal of Quantum Chemistry, 60(4), 809-820.

Valenzano, L., Noel, Y., Orlando, R., Zicovich-Wilson, C.M., Ferrero, M., and Dovesi, R. (2007) Ab initio vibrational spectra and dielectric properties of carbonates: magnesite, calcite and dolomite. Theoretical Chemistry Accounts, 117(5-6), 991-1000.

Valenzano, L., Torres, F.J., Klaus, D., Pascale, F., Zicovich-Wilson, C.M., and Dovesi, R. (2006) Ab initio study of the vibrational spectrum and related properties of crystalline compounds; the case of CaCO3 calcite. Zeitschrift Fur Physikalische Chemie-International Journal of Research in Physical Chemistry & Chemical Physics, 220(7), 893-912.